

**Interactions between Stress, Environment, and Microstructure causing Irradiation-assisted
Stress Corrosion Cracking in Austenitic Stainless Steels**

by

Michael R. Ickes

BS, Chemical Engineering, University of Pittsburgh, 2010

MS, Materials Science and Engineering, 2015

Submitted to the Graduate Faculty of
The Swanson School of Engineering in partial fulfillment
of the requirements for the degree of
Doctor of Philosophy

University of Pittsburgh

2022

UNIVERSITY OF PITTSBURGH
SWANSON SCHOOL OF ENGINEERING

This dissertation was presented

by

Michael Ickes

It was defended on

March 14, 2022

and approved by

Dr. Arash Parsi, PhD, Principal Scientist, Westinghouse Electric Company

Dr. Tom Congedo, PhD, Professor, Department of Nuclear Engineering

Dr. Heng Ban, PhD, Professor, Department of Mechanical Engineering and Materials Science

Dissertation Director: Dr. Jung-Kun Lee, PhD, Professor, Department of Mechanical

Engineering and Materials Science

Copyright © by Michael Ickes

2022

Interactions between Stress, Environment, and Microstructure causing Irradiation-assisted Stress Corrosion Cracking in Austenitic Stainless Steels

Michael Ickes, PhD

University of Pittsburgh, 2022

Irradiation-assisted stress corrosion cracking is a costly degradation mechanism for austenitic stainless steel components in nuclear reactors. This cracking phenomenon involves a complex interaction between the microstructure of the irradiated steel, the high temperature water environment, and the stresses applied to the material. The exact mechanisms involved in this cracking mode are not fully understood.

The series of experiments described in this document are intended to elucidate the relationship between these variables in irradiation-assisted stress corrosion cracking. The experiments are generally focused on austenitic stainless steels irradiated in pressurized water reactors allowing high-quality and relevant research to be performed. In some experiments, such materials available at Westinghouse Churchill Site were machined into specimens and sent to the University of Michigan's Irradiated Materials Testing Laboratory for mechanical testing in simulated reactor coolant conditions. The influence of applied stress, radiation dose, and high temperature water chemistry on both crack initiation and propagation is studied. Crack initiation and growth studies will be conducted in high temperature water containing either LiOH or KOH additions (otherwise the environments will be the same, including pH) which will determine if cracking behavior differs in the presence of the two different alkali ions.

The results of these experiments provide insight into the conditions required to initiate and propagate IASCC. This understanding is beneficial to the nuclear industry, where mitigating

maintenance costs associated with IASCC could provide substantial economic benefits. It can also inform the design of future reactors to avoid this failure mode.

Table of Contents

Acknowledgements & Disclaimers	XX
Dedication	XXII
Acronyms & Abbreviations	I
1.0 Introduction And Motivation.....	1
1.1 Benefits Of Nuclear Energy	2
1.2 Negative Impact Of Brittle Failure On Nuclear Power Plant Performance ..	6
2.0 Technical Background.....	9
2.1 SCC Of Austenitic Stainless Steel	9
2.2 Irradiation Assisted Stress Corrosion Cracking Of Austenitic Stainless Steels	
11	
2.2.1 Environmental Effects on Cracking	14
2.2.2 Irradiation Effect on Environment.....	15
2.2.3 Irradiation Effect on Stress	15
2.2.4 Irradiation Effect on Mechanical Behavior	16
2.2.5 Irradiation Effect on Microchemistry and Phase Stability	17
2.2.6 Effect of Alkali Ions on IASCC	18
2.2.7 Combined Effects Testing Strategy in this Thesis Work	19
3.0 Hypothesis.....	21
4.0 Analysis Of IASCC-Induced Bolt Failures In PWRS.....	22
4.1 Motivation And Experimental Objectives.....	22
4.2 Methodology	25

4.2.1	Visual Examination and Light Optical Microscopy.....	25
4.2.2	SEM Fractography.....	25
4.2.3	Surface Contaminant Analysis.....	26
4.2.4	Dye Penetrant Testing.....	26
4.2.5	Hardness Testing.....	27
4.2.6	Optical Emissions Spectroscopy.....	27
4.2.7	Radionuclide Analysis.....	27
4.2.8	Mechanical Testing of Whole Bolts.....	28
4.2.9	Tensile Testing.....	28
4.2.10	Metallography.....	30
4.3	Results.....	31
4.3.1	Visual Examination and Light Optical Microscopy.....	31
4.3.2	SEM Fractography.....	33
4.3.3	Surface Contaminant Analysis.....	54
4.3.4	Dye Penetrant Testing.....	54
4.3.5	Hardness Testing.....	54
4.3.6	Results of Chemical Composition Analysis.....	55
4.3.7	Radionuclide Analysis.....	56
4.3.8	Results of Mechanical Testing of Whole Bolts.....	57
4.3.9	Tensile Testing Results.....	58
4.3.10	Metallography.....	61
4.4	Discussion.....	66
5.0	IASCC Crack Growth Rate.....	70

5.1	Motivation And Experimental Objectives.....	70
5.2	Methodology.....	71
5.2.1	Material.....	71
5.2.2	Test Method.....	73
5.3	Results.....	77
5.3.1	CGR Testing of 4D2.....	77
5.3.2	CGR Testing of 4D1.....	80
5.3.3	Fractographic Examination of 4D1 and 4D2.....	83
5.3.4	CGR Testing of 1FB.....	87
5.3.5	CGR Testing of 1FA.....	89
5.4	Discussion.....	90
6.0	IASCC Crack Initiation Experiments.....	94
6.1	Motivation And Experimental Objectives.....	94
6.2	Methodology.....	95
6.2.1	Material and Specimen Manufacture.....	95
6.2.2	IASCC Initiation Testing.....	117
6.3	Results.....	119
6.4	Discussion.....	127
7.0	Proton-Irradiation Of Additively Manufactured Materials.....	129
7.1	Experimental Objectives.....	129
7.2	Methodology.....	133
7.2.1	Material and Specimen Fabrication.....	133
7.2.2	Sample Irradiation.....	134

7.2.3	Testing Procedure.....	137
7.2.4	Sample Evaluation.....	138
7.3	Results.....	141
7.3.1	Constant Extension Rate Tests.....	141
7.3.2	Sample Evaluation.....	143
7.4	Discussion	159
8.0	Summary And Conclusions.....	162
	Bibliography	166

List of Tables

Table 1. Stress/Dose categorization for baffle-former bolts.....	35
Table 2. Quantitative fractographic data	35
Table 3. Results of Chemical Composition Analysis (in weight percent).....	56
Table 4. Results of Radionuclide Analysis	57
Table 5. Results of Miniature Tensile Testing.....	59
Table 6. Water chemistries used in CGR tests.....	74
Table 7. Text Matrix for CGR Experiment.....	76
Table 8. Summary of the representative CGR results, and the environments they were measured in.	93
Table 9. Chemistry of Baffle-former Bolt Materials (from Reference 36).....	98
Table 10. Identification of baffle-former bolts to be assessed for use in this project.....	99
Table 11. Final Irradiated 4-point Specimen Identities, Dimensions, and Dose Rates	116
Table 12. TEM Specimens Prepared from Baffle-former Bolt Material	117
Table 13. Results for specimens tested in KOH	119
Table 14. Results for Specimens Tested in LiOH.....	122
Table 15. Test Matrix for SCC susceptibility test.....	133
Table 16. Yield strength determined from CERT.....	142
Table 17. EDS results on the as-received surface of the samples.....	143
Table 18. Variables in IASCC Investigated in this Work.....	165

List of Figures

Figure 1. Electricity Generation in the US.....	3
Figure 2. Land use of electricity generation methods (Reference 2).....	4
Figure 3. Capacity factor of alternative energy sources	5
Figure 4. Mortality rate in various electric power generation facilities (Reference 3).....	5
Figure 5. Westinghouse 4-loop downflow reactor internals assembly	7
Figure 6. Westinghouse 4-loop downflow baffle-former assembly bolts.....	8
Figure 7. Intact Baffle-former Bolt (Left) and Failed Type 347 Baffle-former Bolts in a U.S. 4-loop Downflow PWR.....	8
Figure 8. Elements of Stress Corrosion Cracking - Adapted from Reference 8.....	10
Figure 9. Measured Grain Boundary Chromium Depletion – Adapted from Reference 13.....	12
Figure 10. Grain Boundary Separation in Irradiated Material under Strain – Adapted from Reference 17	13
Figure 11. Slip at Grain Boundaries. (a) is an Example of Continuous Slip, and (b) is an Example of Discontinuous Slip. Adapted from Reference 16	14
Figure 12. Torque required to remove a baffle-former bolt from three French CP0 plants (adapted from Reference 24).	16
Figure 13. Elements transmuting with the potential for phase stability issues in stainless steel (Reference 28).....	18
Figure 14. Baffle-former bolt inspection map for D.C. Cook Unit 2 in 2016 (Reference 31)	24
Figure 15. Dimensions (in inches) of tensile specimens.....	29
Figure 16. Orientation of tensile specimens within baffle-former bolt	29

Figure 17. Picture of tensile specimen B83-B	30
Figure 18. Example sectioning diagram for baffle bolt metallography	31
Figure 19. Photograph of IP2 bolt B35.....	32
Figure 20. New lens (left) compared to lens used for baffle-former bolt examination (right).....	32
Figure 21. S1 Bolt B77 Light Optical Microscope View of Fracture Surface	38
Figure 22. S1 Bolt G77 SEM Overall View of Fracture Surface	39
Figure 23. Overall Image of E22 Fracture at Head-to-shank Region.....	40
Figure 24. IP2 bolt C37 – Overall fracture surface (head side). IG crack regions are service-induced cracking, while ductile tearing resulted from laboratory tensile testing.	41
Figure 25. IP2 bolt F2, IG cracking and secondary cracking	42
Figure 26. SEM Micrograph of E23 Head Fracture – Area 1, IG Cracking Extending into the Head	43
Figure 27. IP2 bolt E65, IG cracking and fine particles on grain boundaries. Red arrows indicate unknown surface spots.....	44
Figure 28. IP2 bolt D5, TG cracking with striations and holes	45
Figure 29. IP2 bolt F2, TG cracking showing striations and secondary cracking	46
Figure 30. Secondary crack branching on the TG portion of the bolt S-R2C6 fracture surface ..	47
Figure 31. SEM Micrograph of E23 Head Fracture – Area 3, TG Cracking with Slip Bands	48
Figure 32. TG Cracking in Bolt E22 Feathery cracking with slip bands, limited secondary cracking, no striations.....	49
Figure 33. TG Cracking with Slip Bands in Bolt E22	50
Figure 34. SEM Micrograph of E22 Shank Fracture, Striations and Secondary Cracking in Area of TG Fracture.....	51

Figure 35. SEM Micrograph of E23 Head Fracture – Area 5, Transition between TG and IG Cracking.....	52
Figure 36. IP2 bolt G103, Blocky microvoid coalescence, showing numerous holes into the fracture surface.....	53
Figure 37. Stress-strain curves for bolt pull tests.....	58
Figure 38. Stress-strain curves for miniature tensile tests	60
Figure 39. Tensile properties of PWR-irradiated austenitic stainless steels versus irradiation damage	60
Figure 40. IP2 E37-H flow lines near head-to-shank transition (etched)	63
Figure 41. Transverse cross-section of IP2 bolt C52 showing aligned features in head-to-shank transition region (etched)	64
Figure 42. Transverse cross-section of DCC2 bolt E23 showing aligned features in head-to-shank transition region	65
Figure 43. TGSCC at a constant strain rate of $4.7E-8$:s in PWR water from Reference 41	68
Figure 44. TGSCC generated at constant load in PWR water from Reference 44	68
Figure 45. TGSCC on SSRT specimen 3B1 from Reference 47	69
Figure 46. Mechanism of TG IASCC, with locally enhanced slip provided by dislocation channeling - Figure adapted from Reference 50.....	69
Figure 47. (Left) Piece 4D, Held by Manipulator in Westinghouse Churchill Site High Level Cell (Right) Diagram Showing RCT Placement inside Baffle-plate Piece (right). The radiological field from this piece was ~10 Rad/hour at a distance of 30 centimeters.....	72
Figure 48. Dimensions of RCT specimens to be used in this project. Dimensions in inches unless otherwise noted.	72

Figure 49. View of CNC Machine through Shielded Hot Cell Window.	73
Figure 50. Autoclave control station at the University of Michigan IMTL.....	75
Figure 51. Flow diagram of CGR test autoclave loop	75
Figure 52. Application of current in the direct current potential drop method, after Reference .	76
Figure 53. Crack length, outlet conductivity and K for specimen 4D2 in 340°C hydrogenated water (a) during pre-cracking stage, (b) after decreasing K , (c) during the water chemistry switch from Li to K, (d) during the water chemistry switch from K to Li and back to K.	80
Figure 54. Crack length, outlet conductivity and K of 4D1 specimen in 340°C hydrogenated water (a) during pre-cracking stage, (b) during the water chemistry switch of Li – K – Li – K under EOC condition, (c) during the water chemistry switch from K to Li and back to K under BOC condition.	82
Figure 55. Fracture surface with marked ligaments on both sides of (a) specimen 4D2, (b) specimen 4D1.....	84
Figure 56. (a) Ligament #2 on the fracture surface of 4D2, (b) ligament #4 on the fracture surface of 4D1 (crack grew from bottom to top).....	86
Figure 57. Pre-crack, IGSCC and sudden fracture in air regimes on the fracture surface of (a) 4D2, (b) 4D1 (crack grew from bottom to top).	87
Figure 58. Crack length, outlet conductivity and K vs. test time of 1FB in 340°C hydrogenated water during (a) pre-cracking stage, (b) the water chemistry switch of Li – K – Li – K under BOC condition.	88
Figure 59. Crack length, outlet conductivity and K vs. test time of 1FA in 340°C hydrogenated water during (a) pre-cracking stage, (b) the water chemistry switch of K – Li – K under BOC condition.	90

Figure 60. Left - Specimen Geometry (Dimensions in millimeters) Right – Specimens Inside 12.7mm Diameter Baffle-former Bolt Shank (conceptual sketch)	96
Figure 61. Areas to be investigated by this experiment shown in green boxes, relative to data generated by testing Type 316 O-rings irradiated in PWRs (Figure adapted from Reference 59)97	
Figure 62. Baffle-former bolt (left) showing cross-section of 4-point bend specimen milled into the threaded end, and (right) the 4-point bend specimens cut free from the bolt.	101
Figure 63. Machining of 4-point bend samples from unirradiated practice bolt	101
Figure 64. Approximate locations for specimen machining for Salem 1 bolt D28. The 18 dpa sampling location is at the end of the threaded portion of the bolt, obscured by the nut used for ID purposes.	102
Figure 65. Approximate locations for specimen machining for DC Cook 2 S-R6C6	103
Figure 66. Approximate location for specimen machining for DC Cook 2 S-R2C6.....	103
Figure 67. Tormach CNC Machine Installed in Cell M	104
Figure 68. View within CNC machine, within M Cell, showing milling of 4-point bend cross section into threaded end of bolt.....	104
Figure 69. View within CNC machine, within M Cell, showing 4 point bend specimens being cut free from the bolt	105
Figure 70. Effect of electropolishing showing difference between (left) as polished specimen and (right) specimen after 15 seconds of electropolishing	106
Figure 71. Effect of electropolishing showing difference between (right) as polished specimen and (left) specimen after 60 seconds of electropolishing, with the etching of stringers indicated by red arrows.....	107
Figure 72. Sample for TEM Lamella Extraction in Protective Case	109

Figure 73. Specimen (left) before and (right) after wide-area ion beam polishing	109
Figure 74. Selection of carbon deposition regions, attempting to center grain boundaries under the mask prior to ion milling for lamella preparation.....	110
Figure 75. Trenches cut around carbon deposits	111
Figure 76. Six undercut lamellas	112
Figure 77. Undercut lamella containing some apparent inclusions	113
Figure 78. Lamella attached to lift-out needle prior to placement on grid (light optical image)	113
Figure 79. Lamella placed on grid (light optical image)	114
Figure 80. Lamella deposited on grid after final thinning (viewed via SEM).....	115
Figure 81. Design of test fixtures used for 4-point bend testing. The left image shows a CAD drawing of the overall fixture assembly with a specimen inserted, while the right image shows a cross-section of the fixture with the specimen removed. From Reference 58.....	118
Figure 82. Shielded autoclave station at the University of Michigan, showing (a) the user controls, (b) the supporting piping and resin columns, and (c) the insulated autoclave system sitting atop the load frame. Photographs courtesy of University of Michigan.....	118
Figure 83. An example crack from specimen D28-H-3 at 26.4 dpa, viewed in back scatter mode after testing at 60% and 70% of the irradiated yield stress in KOH water chemistry	120
Figure 84. Images of 4-point bend specimens after testing in KOH water chemistry. The dashed red boxes indicate regions of uniform surface stress.....	121
Figure 85. An example crack from specimen D28-H-1 at 26.4 dpa, viewed in back scatter mode (top) and secondary electron mode (bottom) after testing at 80% of the irradiated yield stress in LiOH water chemistry.....	122

Figure 86. Images of 4-point bend specimens after testing in LiOH water chemistry. The dashed red boxes indicate regions of uniform surface stress.....	123
Figure 87. Average crack length (μm) and crack length per unit area ($\mu\text{m}/\text{mm}^2$) for samples tested in KOH water chemistry (left) and LiOH water chemistry (right).....	124
Figure 88. Comparison of crack initiation stress at the investigated dose rates for KOH and LiOH water chemistries	124
Figure 89. Images in (left) backscatter mode and (right) secondary electron mode of the progression of crack initiation at a location on sample D28-H-2.....	126
Figure 90. Comparison of data generated in this program to literature data	127
Figure 91. Illustration of the laser powder bed fusion (LPBF) process from Reference 62.....	130
Figure 92. Etched metallographic cross-section of Inconel 718 fabricated by selective laser melting in an argon environment showing the melt pool structure resulting from rapid laser melting and cooling. Arrow indicates build direction. From Reference 64.....	131
Figure 93. SEM images showing (a) the melt pool structure present in a LPBF Type 316L sample after etching with Vilella’s reagent for thirty minutes and (b) the texture of the etched material at the intersection of two melt pools. From Reference 65.....	132
Figure 94. Dimensions of Samples	134
Figure 95. Stage Design.....	135
Figure 96. SRIM Results indicating depth of irradiation.....	136
Figure 97. Tensile samples and TEM bars mounted on irradiation stage. Picture courtesy of the University of Michigan.....	137
Figure 98. Sample mounting for automated image capture of gauge sections	139
Figure 99. Tescan LYRA-3 at Westinghouse Churchill Site.....	139

Figure 100. CERT Results in Argon.....	141
Figure 101. CERT Results in PWR water	142
Figure 102. Example of image of surface of as-irradiated binder jet tensile sample.....	145
Figure 103. Example image of surface of as-irradiated LPBF tensile sample.....	146
Figure 104. Example image of surface of irradiated binder jet CERT sample after 4% strain in argon. The strain direction was horizontal in this image.	147
Figure 105. Example image of surface of LPBF sample strained to 4% in argon, with slip steps and cracks visible. The strain direction was horizontal in this image.	148
Figure 106. Example image of surface of wrought sample strained to 4% in argon, with slip steps visible. The strain direction was horizontal in this image.	150
Figure 107. Example image of surface of binder jet sample strained to 4% in simulated PWR water, with hydrothermal oxide deposits decorating the surface and cracking observed. Strain direction was left to right in this image.....	151
Figure 108. SEM image for EDS map of irradiated binder jet sample strained to 4% in simulated PWR water. This image was taken in backscatter mode.	152
Figure 109. EDS maps of irradiated binder jet sample strained to 4% in simulated PWR water.	153
Figure 110. Example image of surface of LPBF sample strained to 4% in simulated PWR water. The red box indicates area of higher magnification shown in Figure 111. Strain direction was left to right in this image.	154
Figure 111. Enlarged image of region indicated in Figure 110 on the surface of LPBF sample strained to 4% in simulated PWR water, showing fine scale cracking emanating from crack tip of larger crack. Strain direction was left to right in this image.....	155

Figure 112. Example image of surface of LPBF sample strained to 4% in simulated PWR water showing isolated fine cracking. This region was far way from any larger cracks such as that visible in Figure 110. Strain direction was left to right in this image. 156

Figure 113. Example image of surface of wrought sample strained to 4% in simulated PWR water. Strain direction was left to right in this image..... 157

Figure 114. Results of quantitative sample cracking evaluation as a function of environment during straining and material type..... 158

Figure 115. Trends in quantitative cracking evaluation results 160

Figure 116. Oxide partially obscuring cracks on LPBF sample strained in PWR water 161

Acknowledgements & Disclaimers

The opinions expressed in this document are those of the author and do not necessarily represent those of Westinghouse Electric Company or the funding agencies listed here.

Section 4.0 describes work sponsored by American Electric Power, Entergy, and the Electric Power Research Institute. Grateful thanks are owed to the many Churchill technicians who conducted this work including Fran Gradich, Jason Boyle, Steph Deal, Steph Duncan, Pete Boyko, Audrey Sutton, and especially Bob Rees.

Section 5.0 describes work sponsored by the Electric Power Research Institute. Special thanks are owed to Matt Fitz for the machining of the specimens used in this work.

Section 6.0 of this document is based upon work supported by the Department of Energy Nuclear Science User Facility Program under User Facility Agreement No. 19-16567. Special thanks are again owed to Matt Fitz for the machining of the specimens used in this work, and to Fran Gradich and Lizzie Shumaker for their efforts in polishing these. Gratitude is also owed to Arash Parsi for guidance with conducting the focused ion beam operations, and to Lucille Giannuzzi for assistance with the lamella lift-outs and final polishing.

Section 7.0 of this document was supported by the U.S. Department of Energy, Office of Nuclear Energy under DOE Idaho Operations Office Contract DE-AC07-051D14517 as part of a Nuclear Science User Facilities experiment.

The author is also grateful to the members of his PhD committee, especially Jung-Kun Lee for his extensive guidance and many hours of discussion during the author's time as a student at the University of Pittsburgh.

Sections 5.0, 6.0, and 7.0 include substantial work performed at the University of Michigan by the team led by Gary Was, to whom the author is grateful for years of productive collaboration. Thanks are owed to his team including Kai Chen, Lijin Dong, Abdullah Alsinglawi, and Ovidiu Toader.

Loving thanks are also owed to my wife Erin, for being supportive of this process through so many years of graduate school.

Disclaimer: Portions of this document were prepared as an account of work sponsored by an agency of the United States Government. Neither the U.S. Government nor any agency thereof, nor any of their employees, makes any warranty, expressed or implied, or assumes any legal liability or responsibility for the accuracy, completeness, or usefulness of any information, apparatus, product, or process disclosed, or represents that its use would not infringe privately owned rights. References herein to any specific commercial product, process, or service by trade name, trade mark, manufacturer, or otherwise, does not necessarily constitute or imply its endorsement, recommendation, or favoring by the U.S. Government or any agency thereof. The views and opinions of authors expressed herein do not necessarily state or reflect those of the U.S. Government or any agency thereof.

Dedication

In loving memory of Dr. Mike Burke, a great mentor and friend

21 June 1953 – 2 April 2021

Acronyms & Abbreviations

AES	Atomic emissions spectroscopy
AOI	Area of Interest
BWR	Boiling water reactor
CERT	Constant Extension Rate Test
CGR	Crack growth rate
CNC	Computer-Numeric Control
DCC2	DC Cook Unit 2
DCPD	Direct current potential drop
DOE	Department of Energy
dpa	Displacements per atom
ECP	Electrochemical potential
EDS	Energy-dispersive X-ray spectroscopy
IASCC	Irradiation-assisted stress corrosion cracking
IG	Intergranular
IMTL	University of Michigan Irradiated Materials Testing Laboratory
<i>K</i>	Stress intensity (MPa \sqrt{m})
LOM	Light optical microscopy
LPBF	Laser powder bed fusion
LWR	Light water reactor

NSUF	Nuclear Science User Facility
OES	Optical emissions spectroscopy
OPS	Oxide polishing suspension
PWR	Pressurized water reactor
RA	Reduction in area
RCT	Round compact tension specimen
RIS	Radiation-induced segregation
SEM	Scanning electron microscope
SCC	Stress corrosion cracking
SSRT	Slow strain rate test
TEM	Transmission electron microscope
TG	Transgranular
UT	Ultrasonic test
UTS	Ultimate tensile strength
YS	Yield stress

1.0 Introduction and Motivation

The nuclear reactor environment is a harsh one for materials. In commercial power reactors this environment includes high temperatures, intense radiation fields, and contact with potentially corrosive coolants. Austenitic stainless steels were chosen as the primary material of construction of light water reactor (LWR) internals in this environment due to excellent corrosion resistance, favorable fabrication processes, high fracture toughness, and radiation tolerance. In spite of these favorable initial properties, many years or decades of service in close proximity to the nuclear chain reaction occurring in nuclear fuel assemblies in the reactor core can cause degradation of material properties and performance. Ultimately, this degradation can result in brittle failure of the normally ductile austenitic stainless steels. This unexpected type of failure mode is detrimental to the performance of nuclear power plants.

The author's professional experience as a metallurgist at Westinghouse Electric Company has dealt directly with attempting to understand, predict, and prevent the occurrence of such brittle failure in nuclear power plant components. The author has performed both fracture mechanics analyses on hypothetical flaws in power plant components as well as failure analyses on components which failed in service in nuclear power plants, in addition to numerous mechanical property testing campaigns on ex-reactor or other neutron-irradiated materials. This has led to developing significant expertise in the area of fracture of steels in nuclear power plant environments, and also provides the motivation for furthering the scientific understanding of the responsible phenomena. The desired benefit of such study is to support preventing or reducing the occurrence of unexpected failures of steels in nuclear power plant service, allowing them to continue to provide low-emissions electricity as economically as possible.

1.1 Benefits of Nuclear Energy

Concern over the emission of carbon dioxide and other greenhouse gases as a result of the use of fossil fuels for energy has become a major concern due to predicted effects of the resulting global warming. The implementation of nuclear power is currently the most viable strategy for meeting increasing energy demands while preventing greenhouse gas emissions.

In the United States, nuclear power is currently the largest source of non-fossil fuel electricity (Figure 1). Among electricity generation methods, nuclear power uses land the most efficiently (Figure 2). Nuclear power is the most reliable of the generation methods as measured by capacity factor (Figure 3). The capacity factor is the fraction of time that the power plant is providing electricity to the grid, accounting for time when a power source is inoperable due to maintenance for example, or unavailability of sunlight or wind in the case of solar and wind power sources. Nuclear power is also the safest form of electrical power generation (Figure 4) causing the fewest deaths per Watt-hour.

Solar power represents an attractive solution; however currently concentrated solar power concepts are not operating to their expectations, with lower efficiency and higher operating and maintenance costs than expected (Reference 1). Hydroelectric power is an excellent source of carbon-free electricity, however, there is limited potential for this electricity supply, as there are a limited amount of suitable locations for deployment, many of which have already been realized. Photovoltaic solar power represents an excellent choice for decentralized, low duty generation, especially when coupled with battery storage. However, large scale deployments of this technology are problematic in the same way that wind power installations are, requiring large areas of land and power generation is intermittent.

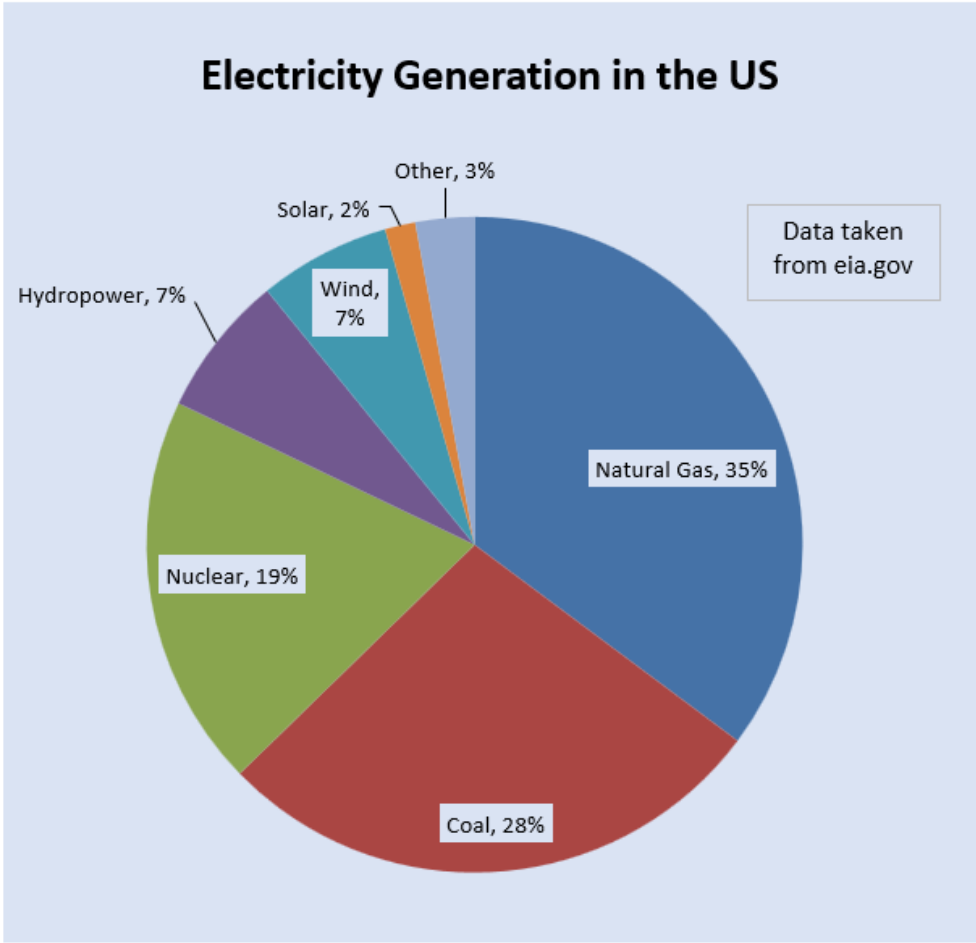
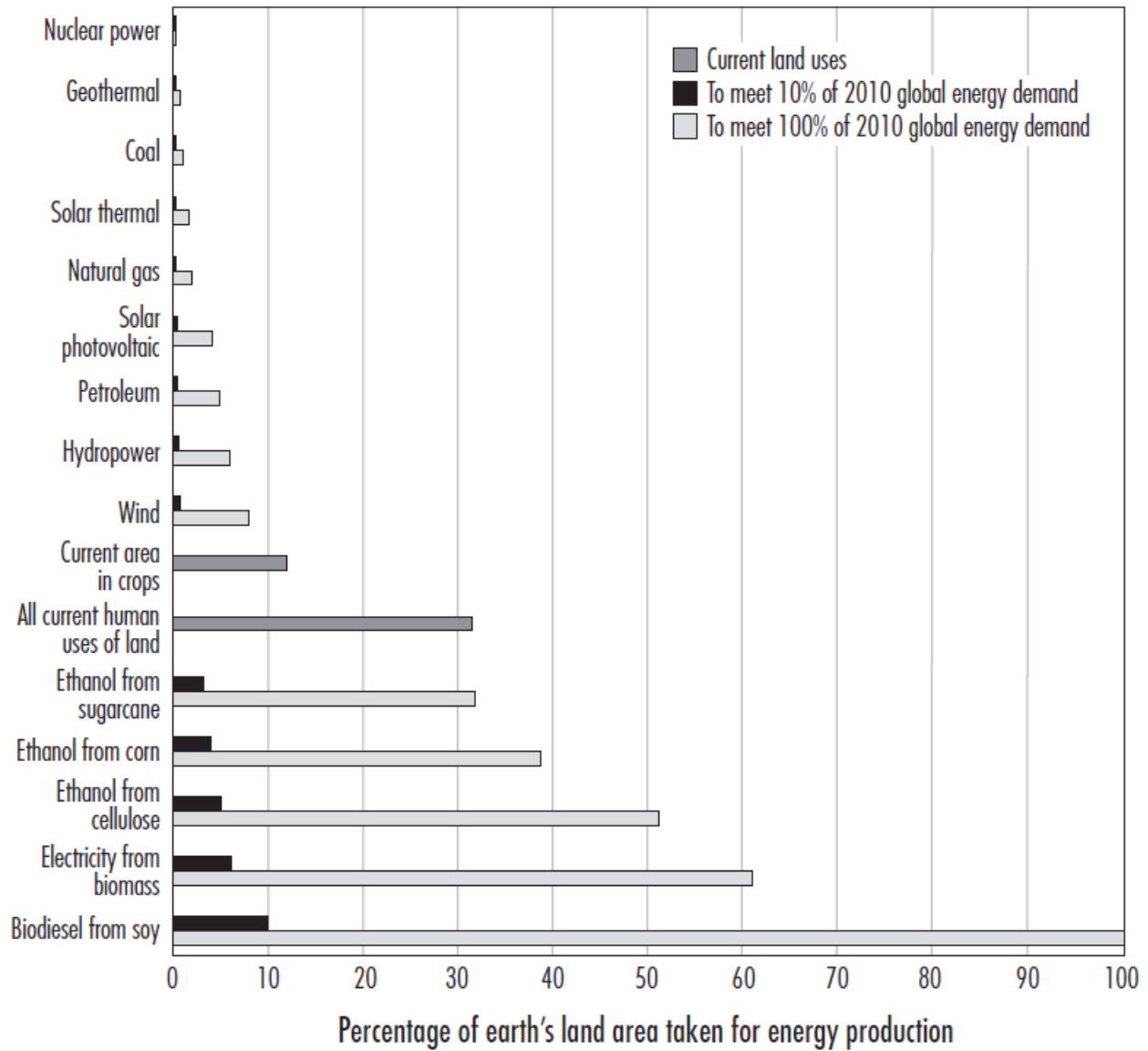


Figure 1. Electricity Generation in the US



Sources: Land intensiveness data from McDonald et al. (2009); land area data from Melillo et al. (2009); global energy demand data from EIA (2009a).

Figure 2. Land use of electricity generation methods (Reference 2)

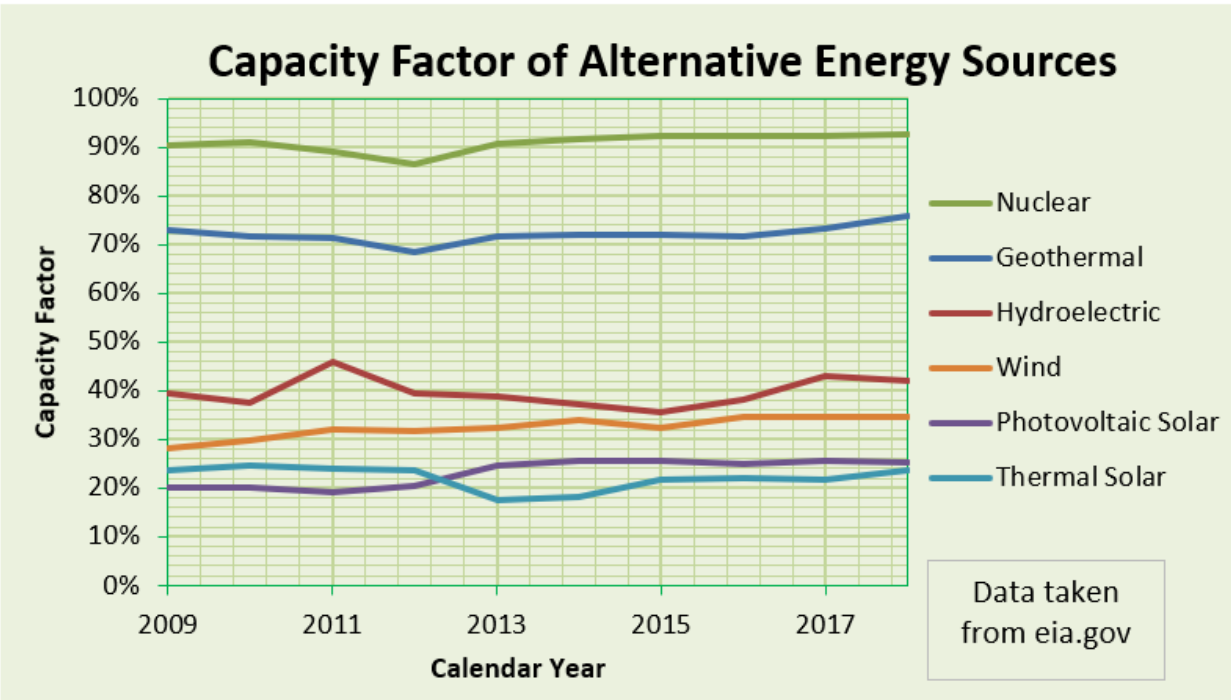


Figure 3. Capacity factor of alternative energy sources

Energy source	Mortality rate (deaths per billion kWh)
Coal – global average	100 (50% of global electricity)
Coal – China	160 (75% of China's electricity)
Coal – U.S.	15 (44% of U.S. electricity)
Oil	36 (36% of global energy, 8% of global electricity, none in U.S.)
Natural gas	4 (20% of global electricity)
Biofuel/biomass	24 (21% of global energy)
Solar (rooftop)	0.44 (<1% of global electricity)
Wind	0.15 (~1% of global electricity)
Hydro – global average	1.4 (15% of global electricity, 171,000 Banqiao dead)
Nuclear – global average	0.04 (17% of global electricity, with Chernobyl & Fukushima – none in US)

Figure 4. Mortality rate in various electric power generation facilities (Reference 3)

1.2 Negative Impact of Brittle Failure on Nuclear Power Plant Performance

Nuclear power plants conduct refueling and maintenance outages typically every 18 or 24 months. These outages are expensive operations and tight schedules are targeted to minimize impact on the power plant's economic performance. One activity that is conducted as a part of some refueling and maintenance outages is the inspection of baffle-former bolts. To conduct such an operation, the reactor assembly (Figure 5) must be shut down, disassembled, and de-fueled. The baffle-former plates fasten the baffle plates, which guide water through the fuel assemblies, to former plates, as shown in a detail in Figure 6.

In 2016, substantial degradation of Type 347 baffle-former bolts was observed in pressurized water reactors (PWRs) due to irradiation-assisted stress corrosion cracking (IASCC) (Reference 4), with some examples shown in Figure 7. The baffle-former bolts are located inside the reactor near the core, and so their inspection and replacement requires the reactor to be shut down, opened up, and the fuel removed. The work must be conducted in a radiologically controlled area, and results in some amount of radiation dose to personnel. Because the extent of degradation observed in 2016 was not anticipated, the affected power plants underwent extended refueling and maintenance outages detrimental to their performance. Better prediction of IASCC allows for proactive rather than reactive maintenance activities, which can be performed with less impact on the duration of maintenance outages (which are often quoted to cost greater than one million dollars per day in equipment, personnel, and lost generation costs), improving the economics and reliability of PWRs. IASCC inspections are conducted as required at every operating light water reactor; while a majority of light water reactors throughout the world have reported IASCC-related degradation to some extent, all light water reactors are affected by the inspection requirements.

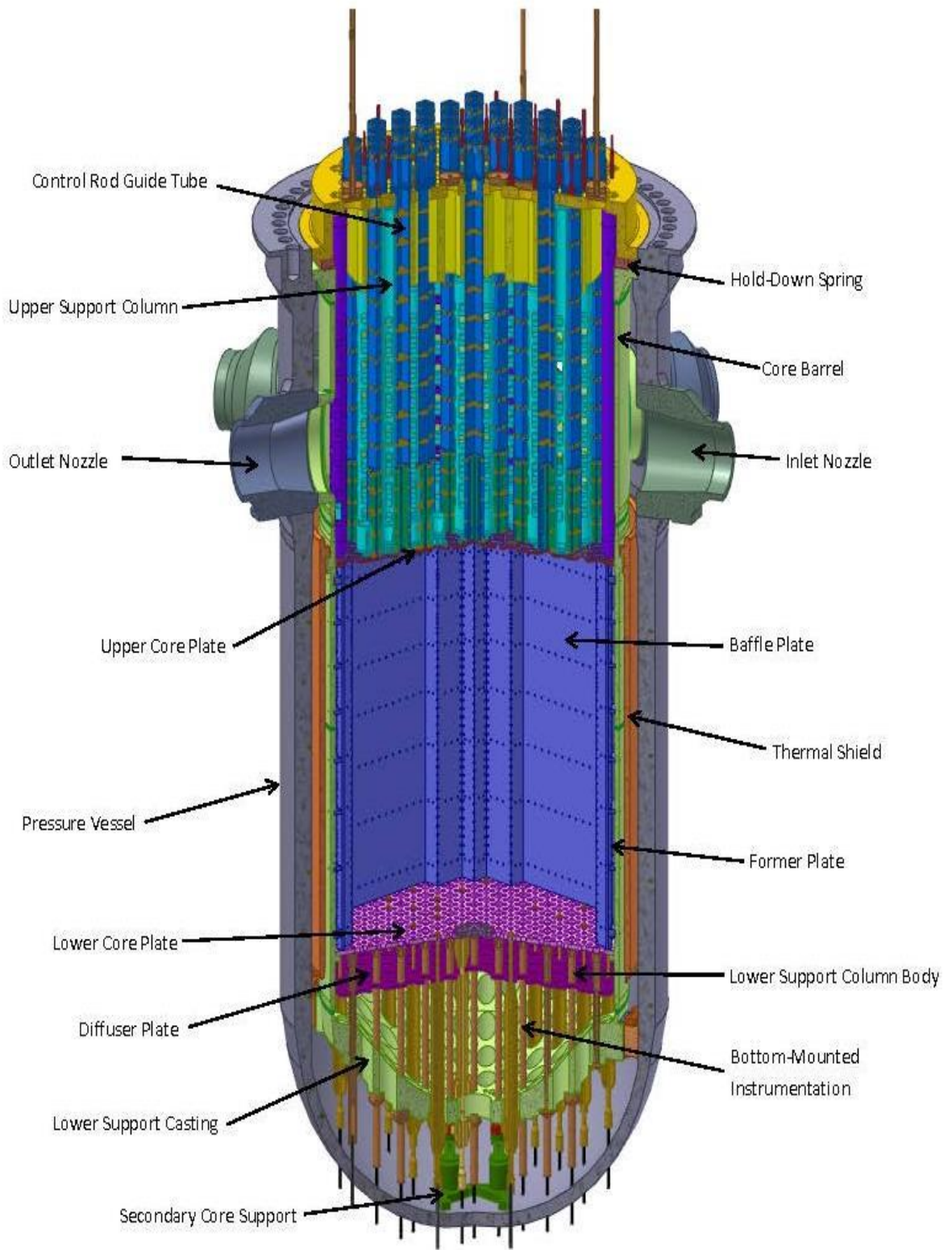


Figure 5. Westinghouse 4-loop downflow reactor internals assembly

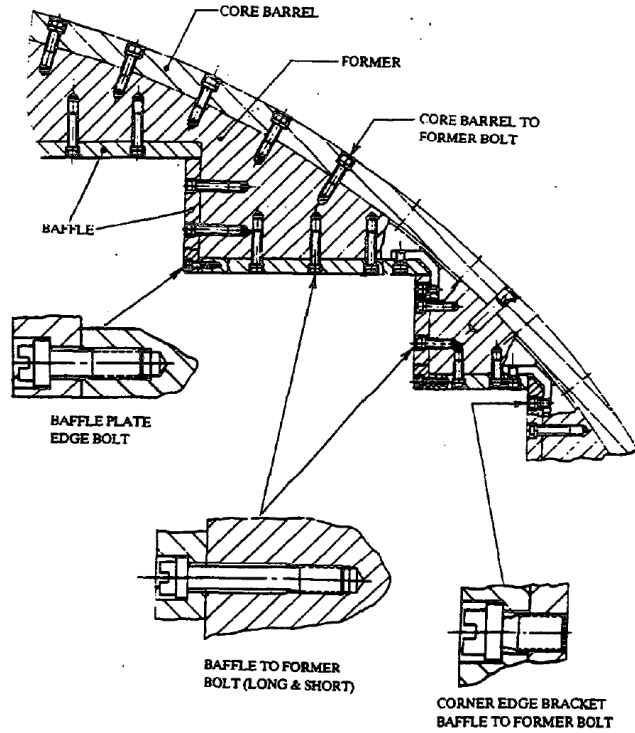


Figure 6. Westinghouse 4-loop downflow baffle-former assembly bolts



Figure 7. Intact Baffle-former Bolt (Left) and Failed Type 347 Baffle-former Bolts in a U.S. 4-loop Downflow PWR

2.0 Technical Background

The authoritative reference on irradiation damage in metals and alloys is the textbook by Was (Reference 7), however some points relevant to stress corrosion cracking (SCC) and IASCC will be reviewed here along with the relevant available data from the literature. IASCC is a form of SCC. For SCC to occur, three conditions must be met: a susceptible material, an aggressive environment, and stress.

The radiation environment can affect SCC behavior by influencing all three of the required factors. Irradiation damage to the material can make it susceptible (via radiation hardening, radiation embrittlement, and radiation-induced segregation). Radiation can make the environment more aggressive by causing localized heating (potentially boiling) and radiolysis of the coolant. Radiation can also affect the stress state of a component. This can be due to volumetric growth of material due to irradiation-induced void swelling, or reduction of existing stresses such as bolt preload due to irradiation-induced stress relaxation. IASCC can then be defined as SCC where irradiation acts in one or more of these ways to modify one of the three critical conditions for SCC.

2.1 SCC of Austenitic Stainless Steel

SCC is a material degradation mechanism that can cause non-ductile and even catastrophic failure of components under specific conditions. SCC occurs when an aggressive environment lowers the stress required for formation of a crack in a susceptible material. Without all three

factors present (stress, susceptible material, aggressive environment), a stress corrosion crack will not form. This is shown schematically in Figure 8.



Figure 8. Elements of Stress Corrosion Cracking - Adapted from Reference 8

Austenitic stainless steels are the material of choice for light water reactor (LWR) internals components because of their high fracture toughness and corrosion resistance. While typically austenitic stainless steels are not greatly susceptible to SCC in LWR conditions, this nonetheless can occur when off-normal conditions are present. One condition where austenitic stainless steel can become susceptible to SCC is grain boundary sensitization, when the steel is exposed to a high temperature for a sufficient length of time, allowing dissolved carbon to form chromium carbides at the grain boundaries, a risk during welding processes for example. This reduction of chromium

in its metallic form at the grain boundaries reduces the corrosion resistance at these locations, allowing for intergranular attack of the material (Reference 8). SCC can also occur in austenitic stainless steels under the presence of chlorides in combination with oxygen (Reference 10). The author has also identified SCC in austenitic stainless steel due to sulfur contamination (Reference 11). Specific to the LWR environment, the presence of excessive cold work can also cause increased susceptibility to SCC (References 12, 13). Sensitization, chlorides, and cold work are all factors that are carefully controlled and avoided in fabricating and operating LWRs, however in the massive engineering structure that is an LWR system, deviations from the prescribed practices can occur.

2.2 Irradiation Assisted Stress Corrosion Cracking of Austenitic Stainless Steels

IASCC is a special case of SCC, where radiation acts to increase one or more of the factors influencing SCC (material, environment, stress). IASCC was not a known degradation mechanism when the first LWRs were designed. IASCC was first observed in stainless steel control rod cladding. Its incidence was reduced by reducing phosphorus and silicon content in the stainless steel, and ultimately stainless steel was replaced in this application by zirconium alloys (Reference 14). IASCC was later observed in boiling water reactor (BWR) core shrouds (References 13, 14) and later in pressurized water reactor (PWR) baffle-former bolts. The observation of IASCC in PWRs was particularly significant because PWRs maintain dissolved hydrogen in the reactor coolant system, which maintains oxygen at very low levels. For a time, this was thought to make PWRs highly resistant to IASCC.

The mechanism of IASCC in BWR environments has been correlated to radiation-induced segregation (RIS). RIS results in the preferential segregation of chromium away from the grain boundary, and of nickel and silicon to the grain boundary (Reference 15). This lowers the corrosion resistance of the grain boundary, allowing for intergranular attack to occur. An example of elemental segregation at material grain boundaries is shown in Figure 9, measured from a sample of an IASCC crack in a BWR core shroud using an EDS in a TEM sample.

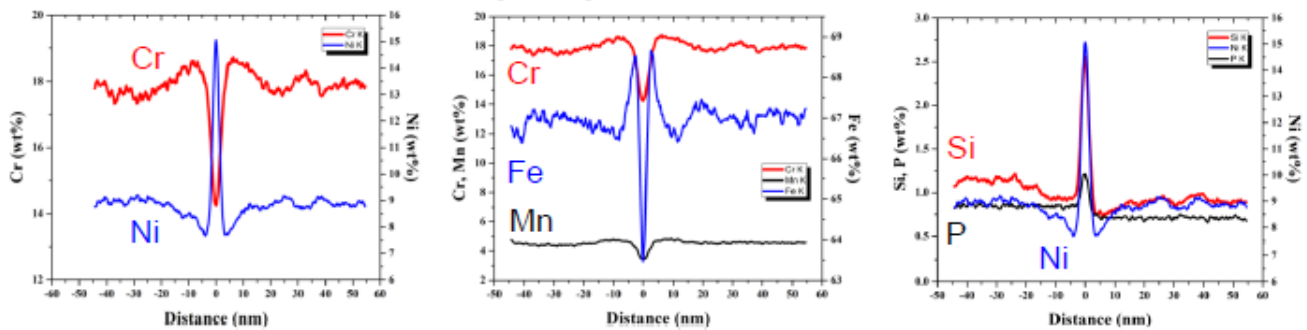


Figure 9. Measured Grain Boundary Chromium Depletion – Adapted from Reference 13

The RIS mechanism alone is not sufficient to account for IASCC in PWR environments. In the PWR environment, IASCC is attributed in part to highly localized strain (due to irradiation hardening of the material) occurring at grain boundaries (Reference 16). When sufficient material hardening occurs strain can cause grain boundaries with sufficient misorientation to separate – allowing for intergranular attack to occur (Reference 17). This grain boundary separation is shown in Figure 10. In Figure 10, the top row of images are SEM images, while the lower row are grain misorientation maps with grain boundary character. Three different regions of a strained specimen are shown, where region a is unstrained material, region b is at 2% strain, and region c is at 5% strain. Such grain boundary separation can be initiated by a loss of continuous slip across a grain

boundary (Reference 16). An example of continuous versus discontinuous slip is shown in Figure 11.

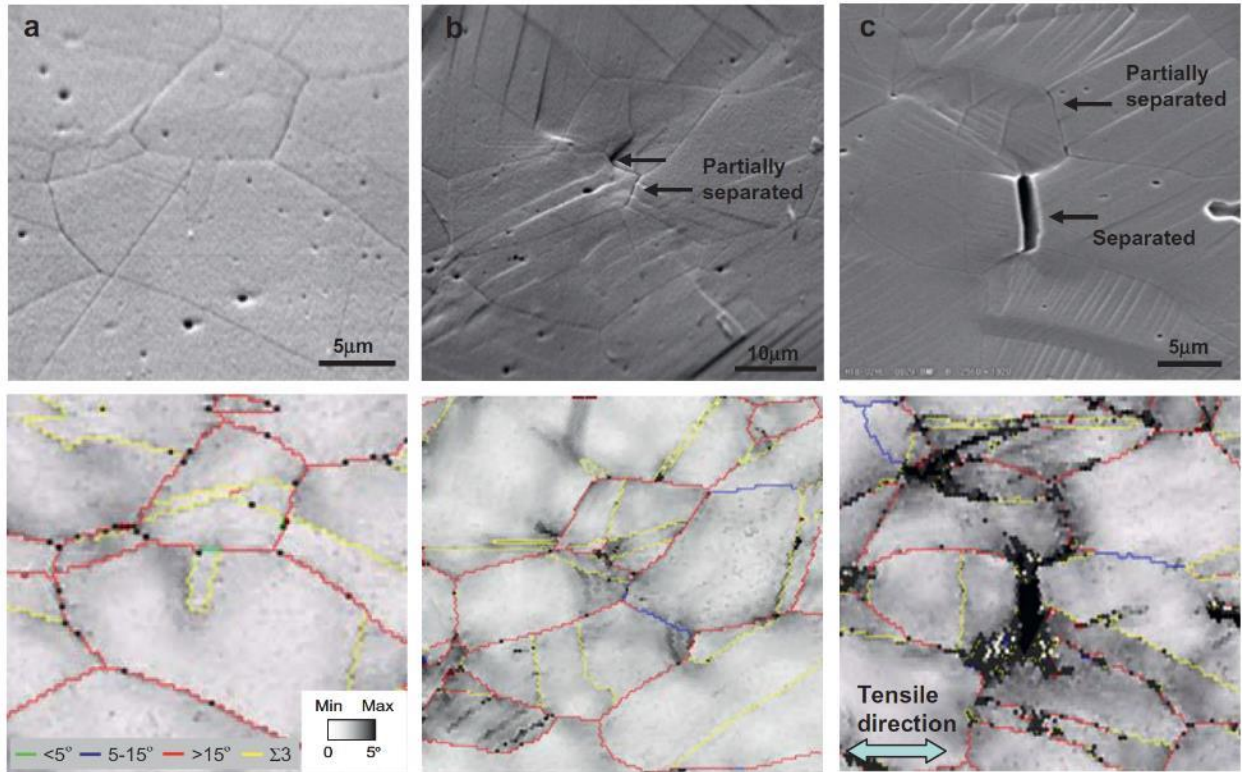


Figure 10. Grain Boundary Separation in Irradiated Material under Strain – Adapted from Reference 17

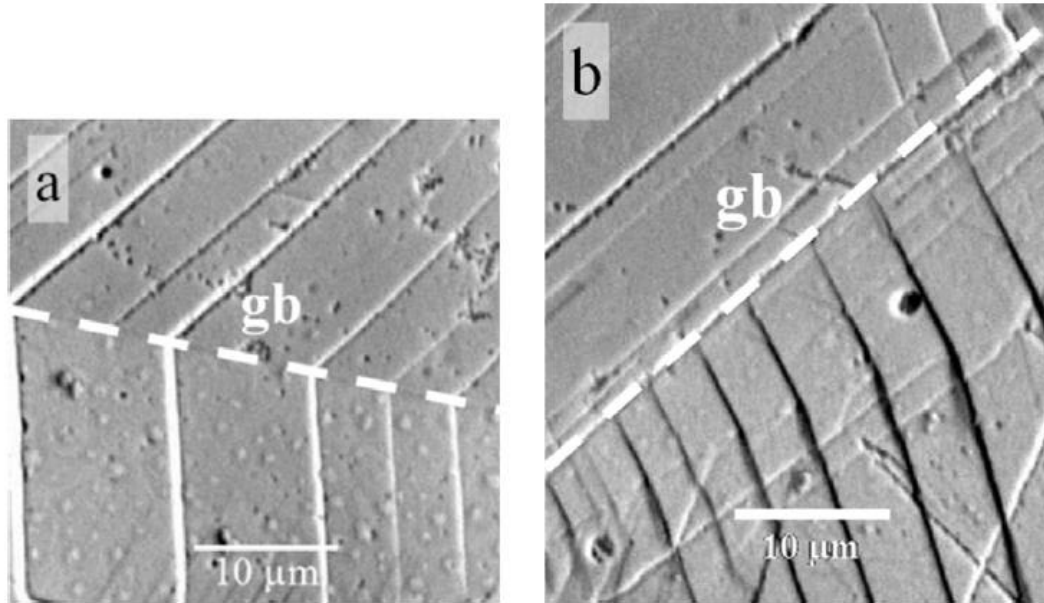


Figure 11. Slip at Grain Boundaries. (a) is an Example of Continuous Slip, and (b) is an Example of Discontinuous Slip. Adapted from Reference 16

2.2.1 Environmental Effects on Cracking

It is well established that there is an effect of the environment on cracking (Reference 8, 10, 12, 15, 18, 19, 20 21, 22). The particular magnitude and mechanisms of this effect in the LWR environment are knowledge gaps that are of significant interest to the Nuclear Regulatory Commission (References 18, 22) and the nuclear industry at large (Reference 8). While the LWR coolant environment clearly has a detrimental effect on crack initiation rates (Reference 14) it can be very difficult to single out critical variables and even more so to identify the mechanism by which they affect cracking behavior. High temperature water itself can cause SCC (Reference 8) but it would seem that even minor chemical additions can strongly affect the cracking behavior. The impact of added elements can be beneficial, in the case of the addition of zinc to PWR water

(Reference 19) or noble metals like platinum to BWR water (Reference 20). Impurity elements like chlorine, sulfur, or lead, inadvertently added to reactor water, have the potential to be highly detrimental to cracking behavior.

2.2.2 Irradiation Effect on Environment

Separately from material effects, irradiation can affect the material's environment, making it more aggressive. Radiolysis increases the ECP of the reactor water which is more favorable for crack growth by the decomposition of water molecules generating a variety of reaction products including hydroxyl radicals, peroxide, and molecular hydrogen (Reference 14). Radiolysis products can affect the stability of oxide species in the irradiated area. Reference 23 implicates radiolysis-generated hydrogen peroxide in repressing formation of the chromium-rich spinel-type inner oxide on Type 316 stainless steel in a combined irradiation-corrosion experiment.

2.2.3 Irradiation Effect on Stress

Radiation creep (or irradiation-assisted stress relaxation) affects reactor components by relieving stresses. On fasteners like the baffle-former bolts, the result is a loss of most of the torque on the bolt. This loss of torque reduces the efficiency of the bolted joint, potentially allowing the bolt to be exposed to stresses other than the tensile preload of the bolt.

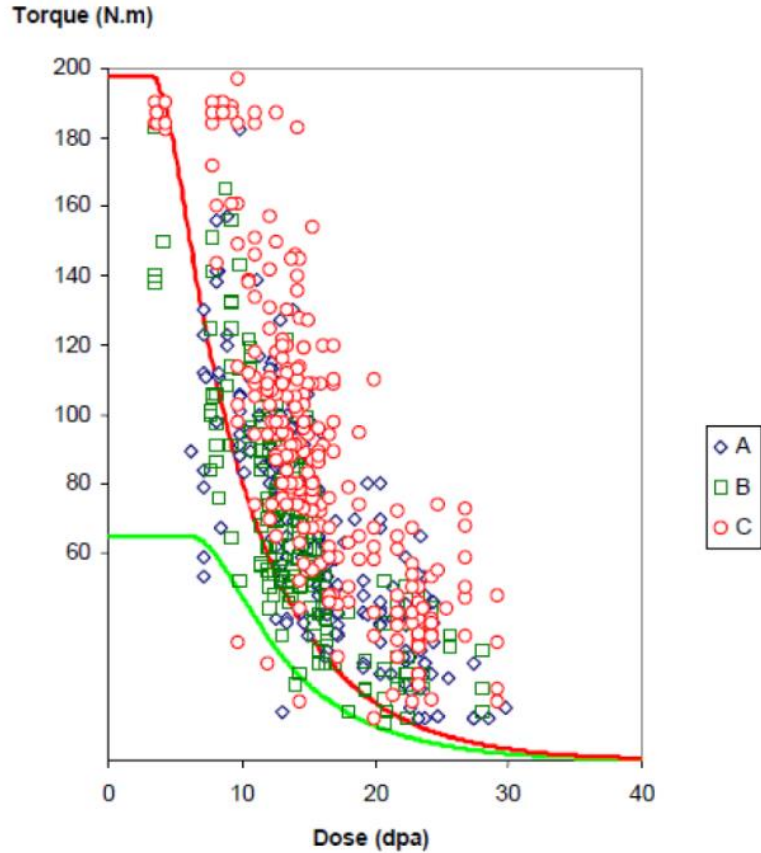


Figure 12. Torque required to remove a baffle-former bolt from three French CP0 plants (adapted from Reference 24).

2.2.4 Irradiation Effect on Mechanical Behavior

Irradiation can affect the deformation behavior of austenitic stainless steels by causing a transition from a wavy slip mode to a planar slip mode. In a planar slip mode, deformation is confined to a specific slip system giving rise to a sharper crack. In wavy slip, the deformation is dispersed on several slip systems leading to a blunt crack (Reference 25). The radiation-induced defects tend to confine deformation, resulting in a planar slip mode and a sharper crack tip than

would exist in unirradiated material. The sharper crack results in a higher stress concentration factor, further localizing stresses and facilitating cracking.

Irradiation also causes substantial hardening of the bulk material (see subsection 4.3.5 or 4.3.9 for example). At the level of individual grains, hardening the grains reduces their ability to deform locally, giving rise to higher intergranular stresses. This is especially true at high-angle grain boundaries where continuous slip is not possible (recall Figure 11, Reference 16).

2.2.5 Irradiation Effect on Microchemistry and Phase Stability

Irradiation can, through radiation induced segregation and radiation enhanced diffusion, cause phase instability in austenitic stainless steels (Reference 26). The formation of martensite and γ' is typical for austenitic stainless steels under neutron irradiation (Reference 37 for example).

Related to intergranular cracking, the aforementioned RIS causing depletion of chromium at the grain boundary (as shown in Figure 9) is of substantial interest. However, issues can also arise from transmutation of elements such as manganese, which have non-negligible thermal neutron cross-sections and will transmute to other elements (Figure 13). As manganese is an austenite stabilizer, its loss results in reduced austenite stability. Some amount of chromium also undergoes a transmutation reaction to vanadium, reducing the amount of chromium available in the alloy (Reference 28). Radiation may cause destabilization of manganese sulfide, a common inclusion in stainless steels, releasing sulfur into the bulk alloy and potentially facilitating IASCC (Reference 29).

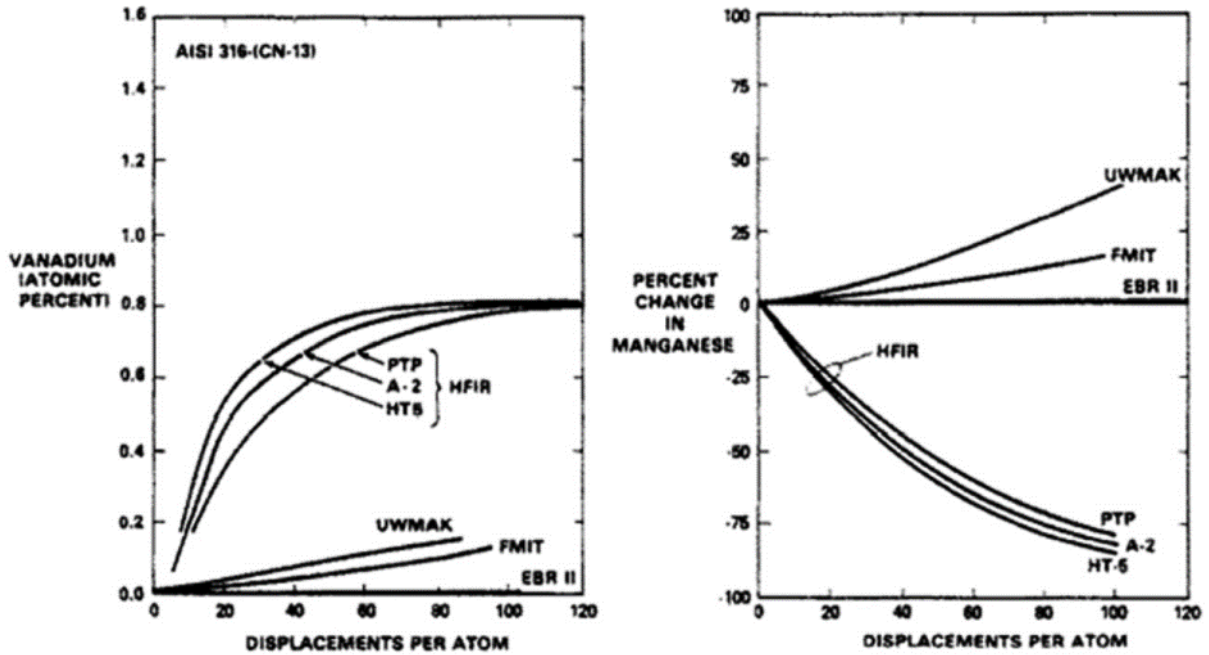


Figure 13. Elements transmuting with the potential for phase stability issues in stainless steel (Reference 28)

2.2.6 Effect of Alkali Ions on IASCC

Some U.S. nuclear power plants are also considering a change in primary coolant water chemistry as a potential cost savings measure. Currently, the primary coolant is water at approximately 2500 psi and 500-650°F containing additions of boron (added as boric acid) to assist in controlling the nuclear reaction, and a lithium hydroxide (LiOH) addition to control pH. Currently, LiOH depleted in Li-6 (due to its high neutron capture cross section) is used. The supply chain security of isotopically depleted LiOH is tenuous and mired in geopolitical uncertainties. The change would be to use potassium hydroxide, which does not require isotopic refinement. (Reference 5). While there are economic benefits to using a KOH water chemistry, differences in cracking performance in the water chemistry could exist. Comparing material exposed to KOH and LiOH water chemistries, potassium remains in the exterior oxide layer on the metal surface

while lithium has been observed to penetrate into the inner oxide layer and along grain boundaries (Reference 6). KOH also has a greater dissociation constant in high temperature water than LiOH, allowing much more of it to be dissolved in a given volume of water. In crevice conditions (potentially present at a crack tip), this could lead to a concentration of hydroxyl ions which could create caustic conditions which could lead to SCC. Therefore, investigation of IASCC behavior in KOH PWR is an important step to be completed prior to its implementation.

2.2.7 Combined Effects Testing Strategy in this Thesis Work

Of the work presented in this thesis, only that presented in Section 4.0, analyzing IASCC failures of nuclear power plant components in service, captured the complete range of factors that influence IASCC. The work presented in Sections 5.0 6.0 and 7.0 utilize irradiated materials, applied stress, and simulated PWR water and so are able to generate SCC which wouldn't be possible without the irradiation damage to the material, which is commonly called IASCC. However, these experiments lack the influence of a substantial radiation field. While the irradiated specimens themselves produce some amount of gamma and beta radiation, this is quite insignificant compared to that of an active PWR core such material would see in PWR service. As discussed previously, radiolysis of the PWR cooling water can occur. However, the hydrogen overpressure of 35 cc/kg applied to PWR water is "completely effective in suppressing the oxidizing (and reducing) products of water radiolysis." (Reference 14).

Further, the absence of radiation field also excludes the possibility for irradiation-assisted stress relaxation. The effect of this phenomenon on crack initiation and growth at the microstructural level is not likely to be significant, as it takes several dpa (which would take years

to accumulate in PWR structural materials) to achieve significant stress relaxation (recall Figure 12).

Another absent effect will be the high flux of vacancies and interstitials present in material under neutron irradiation, which contribute to irradiation-enhanced diffusion. As microstructural-level processes such as oxidation of a grain boundary or crystallographic plane contribute to SCC processes, and oxidation is a diffusion-based process, it is possible that this effect could effect crack initiation and growth behavior.

It should be noted that the tests conducted on the materials in Sections 5.0 6.0 and 7.0 are intended to accelerate IASCC testing, both by testing at the highest relevant temperature levels and by using stress levels greater than are representative of typical PWR operating conditions. These practices are, however, standard in SCC and IASCC testing (Reference 27).

3.0 Hypothesis

The hypothesis is:

The extent of environmental assistance in causing cracking in irradiated austenitic stainless steel in light water reactor environments varies depending on the extent of irradiation damage to the material, the alkali ions in the water, and the stress applied to it.

For classic IASCC, environmental assistance is required. Environmental assistance required for fracture of irradiated materials may also be reduced in conditions of elevated or alternating stresses such as in the case of corrosion fatigue. In the case of highly embrittled materials, environmental assistance may be very minimal or not needed at all. Study of the extent of environmental influence on fracture is not new, however, the examination of the extent of environmental influence on IASCC has received less attention. The use of materials neutron-irradiated in commercial PWRs, the use of Type 347 stainless steel, and the investigation of the role of alkali ions are unique aspects of this work.

4.0 Analysis of IASCC-Induced Bolt Failures in PWRs

This section describes work sponsored by the Electric Power Research Institute, American Electric Power, and Entergy. These experiments were conducted in collaboration with Joshua McKinley, Jung-Kun Lee, Jean M. Smith, Andrew M. Ruminski, and Michael A. Burke. This work was published in the Journal of Nuclear Materials, and the published article should be referred to for the full details of the work:

Michael R. Ickes, Joshua McKinley, Jung-Kun Lee, Jean M. Smith, Andrew M. Ruminski, Michael A. Burke, “Irradiation-assisted stress corrosion cracking of Type 347 and Type 316 steels irradiated in commercial pressurized water reactors,” Journal of Nuclear Materials, Volume 536, 1 August 2020. <https://doi.org/10.1016/j.jnucmat.2020.152182> (Reference 30)

4.1 Motivation and Experimental Objectives

As described in subsection 1.2, in 2016 baffle-former bolts fabricated from Type 347 and Type 316 stainless steels were found to have indications of potential degradation in far greater numbers than was anticipated after decades of service installed in PWR reactor core internals. The ultrasonic (UT) inspection technique, which was well qualified and proven at other plants, had in this instance appeared to have identified intact bolts as degraded, confounding interpretation of the inspection results and resulting in more bolts being replaced than may have been necessary. However in spite of this, the number of degraded bolts (identified as degraded by being fractured in two pieces upon removal) identified in 2016 inspection campaigns (Reference 31) was an order

of magnitude greater than identified during any previously planned aging management inspection of this component (References 32, 33). To attempt to identify contributing factors to the failures, a subset of the bolts removed during the following bolt replacement campaign were provided to the Westinghouse Churchill Site hot cell facility for failure analysis.

BFB UT Indications Map

D.C.Cook unit 2, Oct.2016

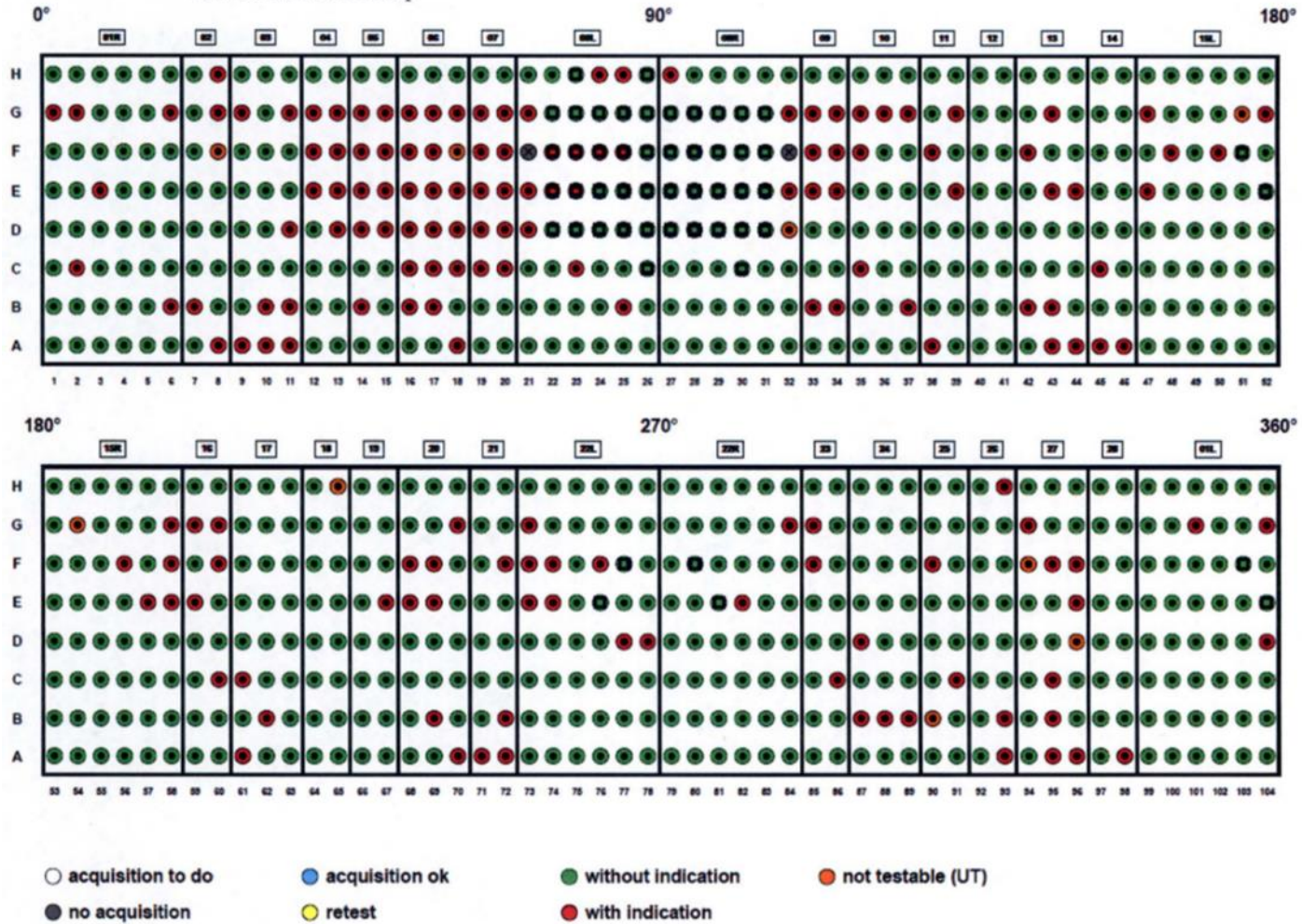


Figure 14. Baffle-former bolt inspection map for D.C. Cook Unit 2 in 2016 (Reference 31)

4.2 Methodology

Each as-received bolt had radiological readings of 1000 to over 9000 Rad/hour on contact, necessitating the use of strict radiological controls. The Westinghouse Churchill Site hot cell facility's heavily shielded high level cell allowed the work described in this document to be conducted while keeping exposure to personnel to below local administrative limits and allow working safely with these highly irradiated materials.

The baffle-former bolts were stored in individually-labelled containers in the heavily shielded high level hot cell at the Westinghouse Churchill Site facility and were machined as-needed for testing. Equipment was set up in the adjoining low level cell as needed for each task.

4.2.1 Visual Examination and Light Optical Microscopy

The light optical microscopy was conducted using a Keyence VHX-5000 digital microscope installed in the low level hot cell, and included examinations of fracture surfaces, as well as examinations of the intact bolts for indications of cracking.

4.2.2 SEM Fractography

The SEM fractography was conducted on a Tescan Vega-3 XMU SEM. This SEM is located in a shielded cell directly above the high level cell. Samples are transferred between the two using a small sample elevator. This enabled examination of as-received baffle-former bolts

without removing them from the shielded hot cell system. Due to the high radiological activity of samples typically examined in this SEM, no EDS detector is installed as it would be ineffective in the radiation field due to excessive detector dead time. The fracture surfaces were cleaned ultrasonically in combination with and an organic solvent (DuPont™ Vertrel® XF – decafluoropentane) immediately prior to loading the samples into the SEM to remove debris from the surfaces.

A Tescan Lyra-3 GMU dual beam FIB/SEM system with an Oxford Instruments EDS detector was used to conduct EDS on a small (~1 mg) sample of one bolt as the radiological fields associated with the small sample were sufficiently low to allow use of this unshielded piece of equipment.

4.2.3 Surface Contaminant Analysis

Bolt pieces were ultrasonically cleaned in deionized water for 24 hours. The resulting solution was run through a silver filter and analyzed using EDS.

4.2.4 Dye Penetrant Testing

Bolts that had UT indications but were removed from the reactor intact were subject to dye penetrant testing. Magnaflux Zyglol® dye penetrant was applied and allowed to dwell per manufacturer's instructions for 20 minutes, and then examined under ultraviolet light. As no indications of cracking were identified using this approach, this process was repeated with longer dwell times of several hours. No cracks were identified by dye penetrant testing.

4.2.5 Hardness Testing

Hardness testing specimens were prepared from baffle-former bolt shanks by milling flats on opposite sides of the shank along its length. This gave a flat and level surface for hardness testing along the length of the bolt. Since the fluence received by the bolt varies along the length of the bolt (highest at the head and lowest at the threaded end) the effect of radiation on hardness can be investigated. Rockwell Hardness (Rockwell C) were conducted using a Wilson Rockwell hardness tester.

4.2.6 Optical Emissions Spectroscopy

Small (~1 mg) samples were removed from the bolts, carefully weighed, and then dissolved in a mixture of hydrochloric, nitric, and fluoric acids in a MARS 5 microwave digestion system. The digested samples were analyzed using an Agilent VDV 5800 ICP-OES by optical emissions spectroscopy (OES).

4.2.7 Radionuclide Analysis

Small (~1 mg) samples were removed from the bolts, carefully weighed, and beta spectroscopy was then performed on the samples. Specifically, Ni-63 activity was measured using the RP300 method (Reference 34). The amount of Ni-63 present, the amount of total nickel present (obtained from ICP-OES), and the service history of the bolt can be used together, via a set of hand calculations, to estimate neutron fluence for the sample material.

4.2.8 Mechanical Testing of Whole Bolts

For bolts which had UT indications but were delivered to the laboratory intact, it was desired to conclusively determine if any cracking was present in the bolt. Three original bolts without UT indications were loaded in tension to 414 MPa in the bolt shank (bounding original design loads). For additional bolts, it was decided to load the bolts to failure. This was achieved by applying tensile loading at a crosshead extension of 0.635 mm/minute to the bolt until failure. Consideration of the bolt geometry and fixture geometry allowed the determination of an approximate gauge length. This, along with the crosshead displacement data, was used to develop approximate stress-strain curves for the whole bolt tests.

4.2.9 Tensile Testing

Miniature tensile specimens were machined from IP2 E28 and S1 B83, both of which are Type 347 bolts. The dimensions of the specimen are given in Figure 15. The specimens were extracted from the shank and threaded portion of the bolts, as shown in Figure 16. An example of a finished tensile specimen is shown in Figure 17

Specimen E28-A was tested at a crosshead extension rate of 0.0012 in/minute (0.030 mm/minute). Due to the extensive necking during this test, subsequent tests were conducted at a faster extension rate to expedite the process. Specimens B83-A, B83-B, and E28-B were tested at a crosshead extension rate of 0.0036 in/minute (0.91 mm/minute). All of the miniature tensile tests were conducted at room temperature. Data recording had begun after a load of 10 pounds (44.5 N) was reached to minimize the amount of fixture settling that was captured in the data. A

miniaturized clip-gauge extensometer was used to measure extension of the miniature tensile specimens along the gauge length.

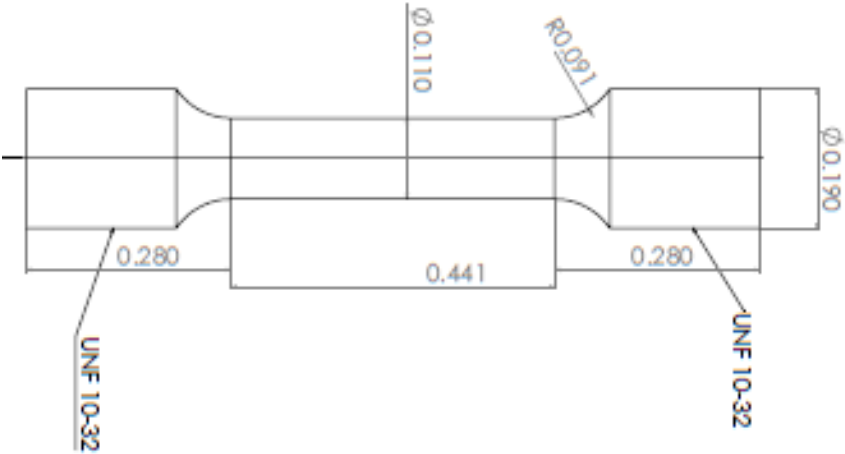


Figure 15. Dimensions (in inches) of tensile specimens

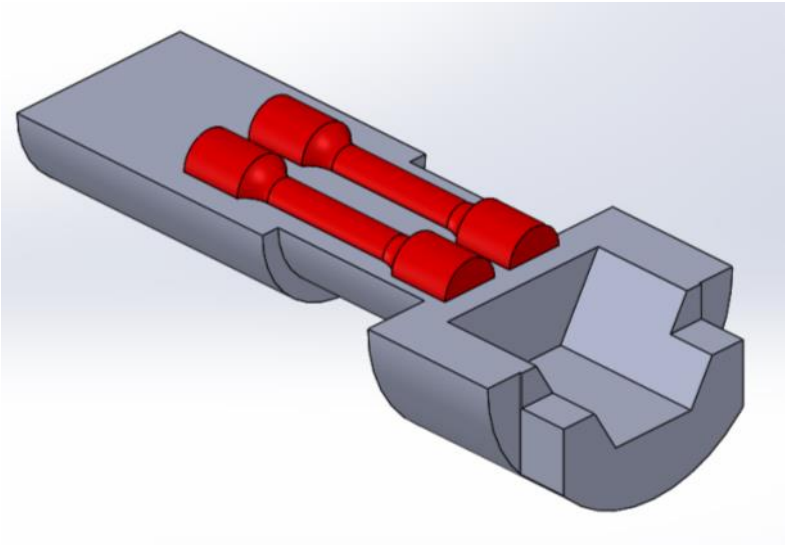


Figure 16. Orientation of tensile specimens within baffle-former bolt

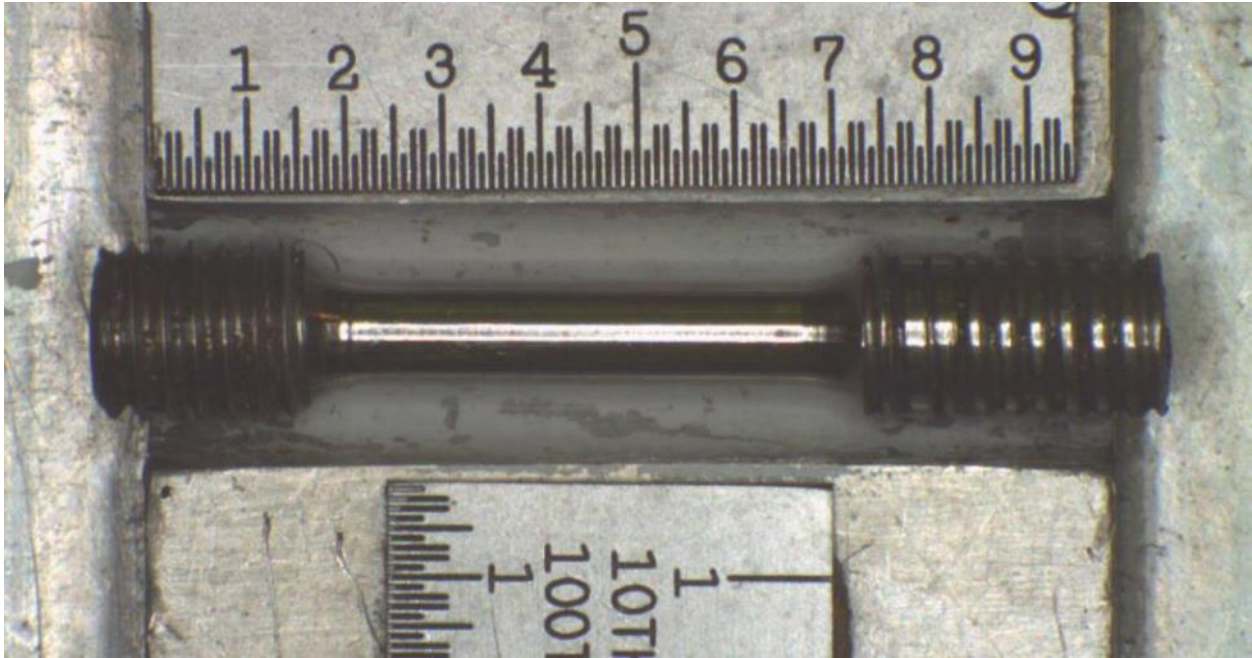


Figure 17. Picture of tensile specimen B83-B

4.2.10 Metallography

The focus on the metallography of the IP2 and S1 bolts was to identify any microstructural differences between intact bolts with and without UT indications – that is, if flow lines or inclusions were responsible for UT reflections that may have been the source of UT indications. Metallography on the DCC2 bolts was intended to investigate crack morphology.

The bolts were sectioned as desired (example sectioning diagram shown in Figure 18), mounted in epoxy, ground flat and polished to a mirror finish using OP-S silica slurry, and characterized using the Keyence VHX5000 digital optical microscope. After examination in the as-polished condition, the mounts were electro-polished in a 10% oxalic acid solution for 1-3 minutes at 3-6 volts and examined again.

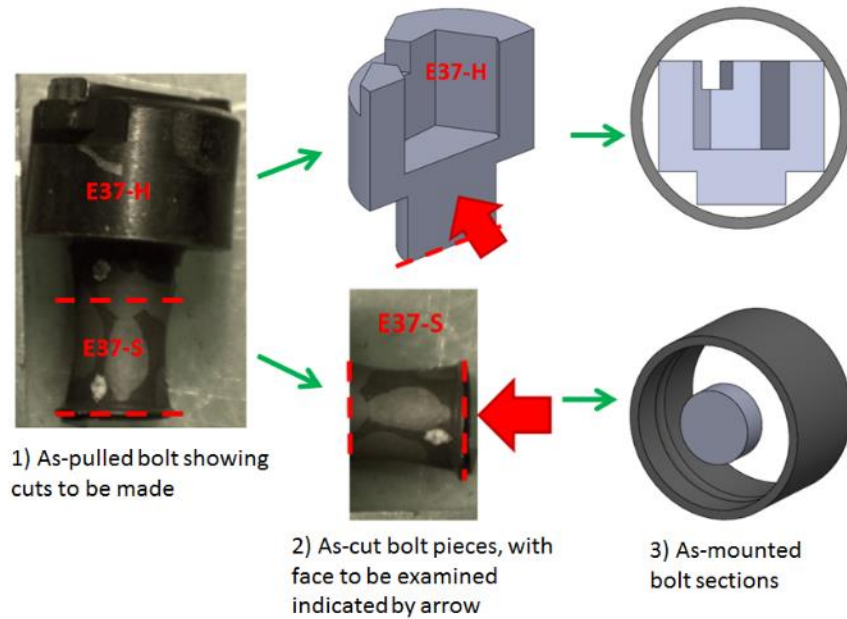


Figure 18. Example sectioning diagram for baffle bolt metallography

4.3 Results

4.3.1 Visual Examination and Light Optical Microscopy

The bolts were covered primarily with a dark grey, adherent oxide layer. Near the head to shank radius of the Type 347 bolts, the oxide layer tended to be thicker with some brown coloring (Figure 19) and was observed to be friable. This thick friable oxide was absent from the Type 316 replacement bolts. Some shiny regions appear on the fracture surface, which are regions that were damaged during extraction. In many instances, the crack grew towards the head of the bolt. The significant radiation field from the bolts (10 to 100 Sieverts per hour at 30 cm) caused substantial darkening of the lens of the LOM (Figure 20).

Bolts that contained UT indications from IP2 and S1 but without apparent cracks were investigated at higher magnifications (50-1000X) at the head-to-shank region in an attempt to identify surface cracks. Of the bolts examined, only IP2 C37 showed a small, tight crack in this region. The extent of this crack was later revealed by pull testing and subsequent fractography.



Figure 19. Photograph of IP2 bolt B35



Figure 20. New lens (left) compared to lens used for baffle-former bolt examination (right)

4.3.2 SEM Fractography

SEM examination of fracture surfaces revealed the presence of intergranular (IG) cracking, which is characteristic of IASCC (References 7 and 14). Also observed were transgranular (TG) cracking, mixed-mode cracking consisting of both IG and TG features, and ductile rupture. IG and TG are brittle failure modes, displaying little to no ductility, while ductile rupture was identified by regions of microvoid coalescence (also known as dimpled rupture). The amount of each morphology varied from bolt to bolt, from completely IG to predominantly TG. Figure 21 shows, for example, S1 bolt B77 which contains two distinct regions: one of IG and mixed TG and IG cracking and a second region of flat TG cracking. Figure 22 shows S1 bolt G77 with a circumferential region of IG, mixed IG and TG, and TG regions and a substantial central region of ductile tearing. Figure 23 shows the almost-entirely TG fracture of DCC2 bolt E22, with three distinct regions of different TG cracking morphologies and no ductile rupture. Figure 24 shows the fracture surface of IP2 bolt C37 (pull tested in the lab at room temperature) showing a narrow rim of IG cracking around the circumference. This cracking had been previously identified by high-magnification examination of the head-to-shank region via LOM.

A categorization generalizing the best estimate stress during crack propagation for each bolt was developed, with these categories defined in Table 1. Category ‘A’ corresponds to relatively low stress (the bolt failure was relatively isolated within the assembly; none or only one of its ‘nearest neighbors’ had failed) and high irradiation dose (well above the IASCC threshold described in Reference 60). Category ‘B’ corresponds to relatively high stress bolts (the bolt was located in a cluster of failures, causing increased load on nearby intact bolts) and high irradiation dose. Category ‘C’ corresponds to relatively high stress and low irradiation dose (near the lower

limit for IASCC as described in Reference 60). The loading here is generally assumed to be steady-state during power plant operation.

Table 2 summarizes the fractographic data, including the approximate percentage area of each failure type. This table gives a calculated approximate dose for each bolt, along with the stress category assigned per Table 1. The table also describes the ‘Inspection and Extraction’ data for each bolt. ‘Red’ indicates that the bolt displayed UT inspection indications greater than the inspection acceptance criteria; that is, the inspection identified a potentially degraded condition. ‘Green’ indicates the bolt did not have UT indications greater than the inspection acceptance criteria, indicating no degradation identified by the inspection. Bolts that were already protruding from their installed location were assumed broken and not inspected by UT. Bolts indicated as ‘intact’ were able to be removed from the reactor baffle wall in one piece, while bolts indicated as ‘broken’ were removed from the baffle wall in two pieces, presumably having fractured during service. It is apparent that the inspection technique was not completely accurate at identifying degradation, as ‘green’ bolts (no UT inspection indications) did come out broken in some instances (F25, F45, and F48) while some ‘red’ bolts (with UT indications) such as B74 and E37 had no apparent service-induced degradation. It should also be further noted that the sample of bolts examined in this study, and particularly the relationship between UT inspection accuracy and bolt structural integrity, are not representative of the entire inspection population. Instead, the subset of bolts shipped to the laboratory intentionally included bolts with unusual results like F25, F45, and F48 so the cause of this discrepancy could be understood.

Table 1. Stress/Dose categorization for baffle-former bolts

Stress/Dose Category	Dose Criterion	Stress Criterion
A	>> 10 dpa	0 or 1 failed nearest neighbors
B	>> 10 dpa	>1 failed nearest neighbors
C	< 10 dpa	>1 failed nearest neighbors

Table 2. Quantitative fractographic data

Plant	Baffle Bolt Location	Steel Grade	Inspection & Extraction Data	Estimated dpa	Stress/Dose Category	Quantitative Fractography (%)			
						IG	TG	Mixed	Ductile
IP2	B74	347	Red- Intact*	27	-	0	12	0	88
IP2	C37	347	Red- Intact*	18	-	9	0	3	87
IP2	D5	347	Red- Broken	27	B	4	3	85	8
IP2	D73	347	Red- Broken	20	B	0	11	81	8
IP2	E26	347	Protruding (broken) - no UT	33	B	12	41	34	12
IP2	E28	347	Red- Broken	33	B	6	24	62	8
IP2	E37	347	Red- Intact*	18	-	0	12	0	88
IP2	E65	347	Red- Broken	41	B	66	26	7	0
IP2	E78	347	Protruding (broken) - no UT	33	A	49	18	25	8
IP2	F2	347	Red- Broken	33	B	46	20	15	19
IP2	F25	347	Green - Broken	33	A	97	3	0	0
IP2	F45	347	Green - Broken	41	A	100	0	0	0
IP2	F48	347	Green - Broken	27	A	26	2	65	7
IP2	F57	347	Red- Broken	33	A	44	12	43	2
IP2	G100	347	Red- Broken	27	B	45	2	3	50
IP2	G103	347	Red- Broken	33	B	12	11	54	23
S1	B77	347	Protruding (broken) - no UT	28	B	23	37	40	0
S1	G77	347	Red- Broken	28	B	35	13	39	14
DCC2	E22	316	Red- Broken	4	C	1	99	0	0
DCC2	E23	316	Red- Broken	5	C	40	60	0	0
DCC2	E28	316	Green- Intact*	5	-	0	0	0	100

*Pull tested to failure in room temperature air

IG cracking was observed to frequently occur with secondary cracking (Figure 25). IG cracking was also observed to extend into the load bearing surface of the bolt (Figure 26). In some regions of IG cracking dark spots (marked with red arrows) were observed on grain facets (Figure 27). These could not be conclusively identified. EDS was not possible due to the high radiation field of the material. These spots could possibly be entrained slag particles from the steel fabrication or coarse carbide particles.

The features of the TG cracking varied by appearing with or without secondary cracking or striations and in some instances included features such as ratchet marks and river lines. For example, Figure 28 and Figure 29 show TG cracking with striations and secondary cracking, Figure 30 shows TG cracking with secondary cracking and no striations, and Figure 31 and Figure 32 show TG cracking with slip bands, without striations and very limited secondary cracking. The slip bands at times appeared very well-ordered, even stairway-like (Figure 33). Striations were rare and in all cases very fine, such as shown in Figure 34. It is noted that typical isolated IASCC failures of baffle-former bolts have been reported as being IG in nature (References 30, 35, 36, and 37) similar to the appearance of the relatively isolated failures of E78, F25, F45, and F48 in this work. The baffle-former bolts that have failed in large clusters examined in these investigations have initiated by an IG mode but also included TG cracking. Note that in Table 2, bolts E 78, F48 and F57 may appear as outliers because these appear in the ‘low stress’ group, but do not contain a majority of IG cracking. In fact, while much of these fracture surfaces are indicated as ‘mixed,’ the mixture in this case has strong intergranular characteristics with occasional transgranular features. The quantitative fractography of these two bolts was also challenged by damage to the fracture surfaces during extraction.

The transitions between IG and TG cracking were at times abrupt and associated with secondary cracks (such as in Figure 35) or took place over regions of mixed TG and IG cracking. Also identified on several fracture surfaces of IP2 bolts was microvoid coalescence (Figure 36) with a flatter morphology consistent with ductile tearing. This morphology appeared in between regions of TG cracking as shown in the previous figures and the final ductile fracture of the remaining bolt cross section (which appeared as typical microvoid coalescence).

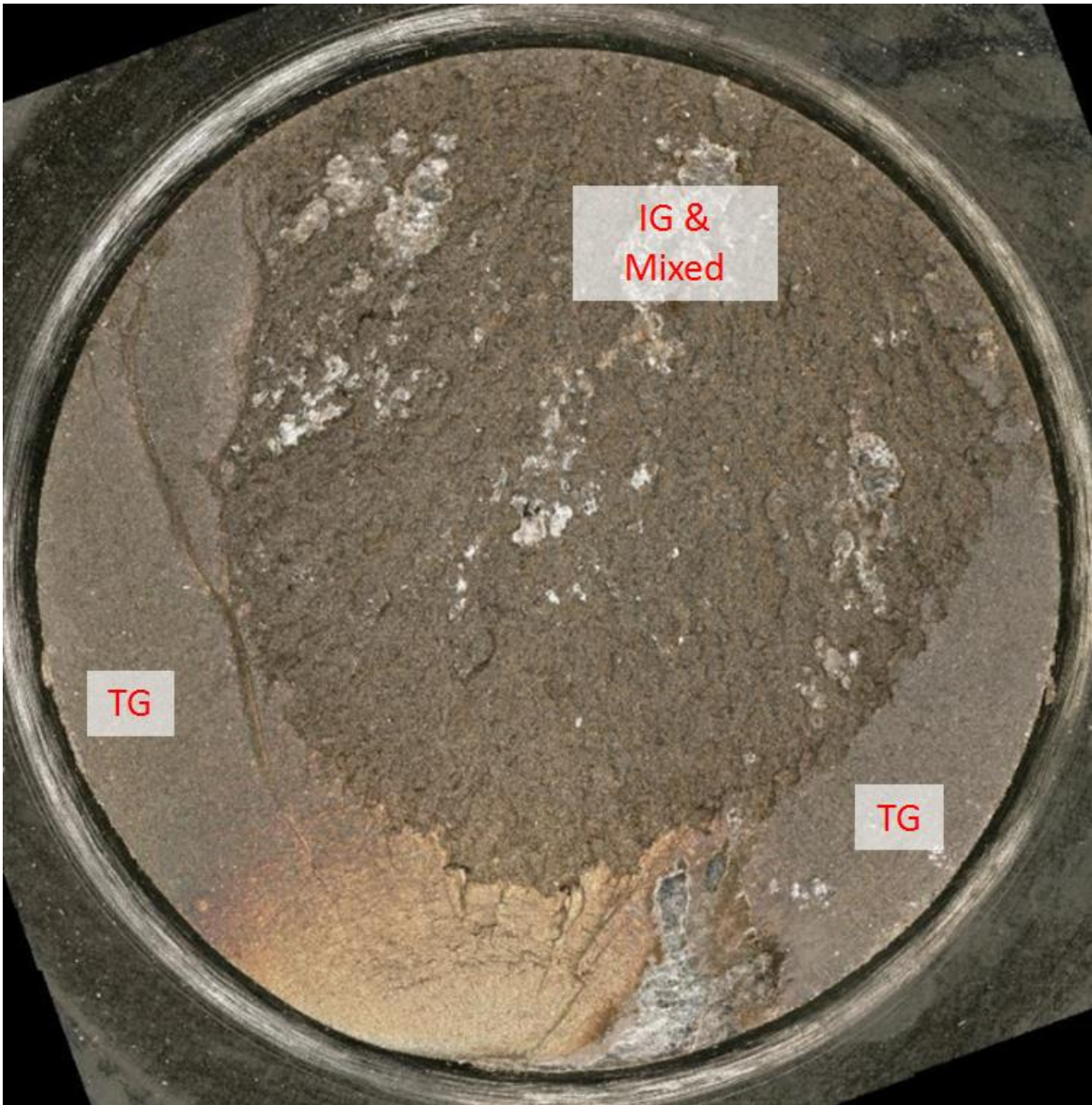


Figure 21. S1 Bolt B77 Light Optical Microscope View of Fracture Surface

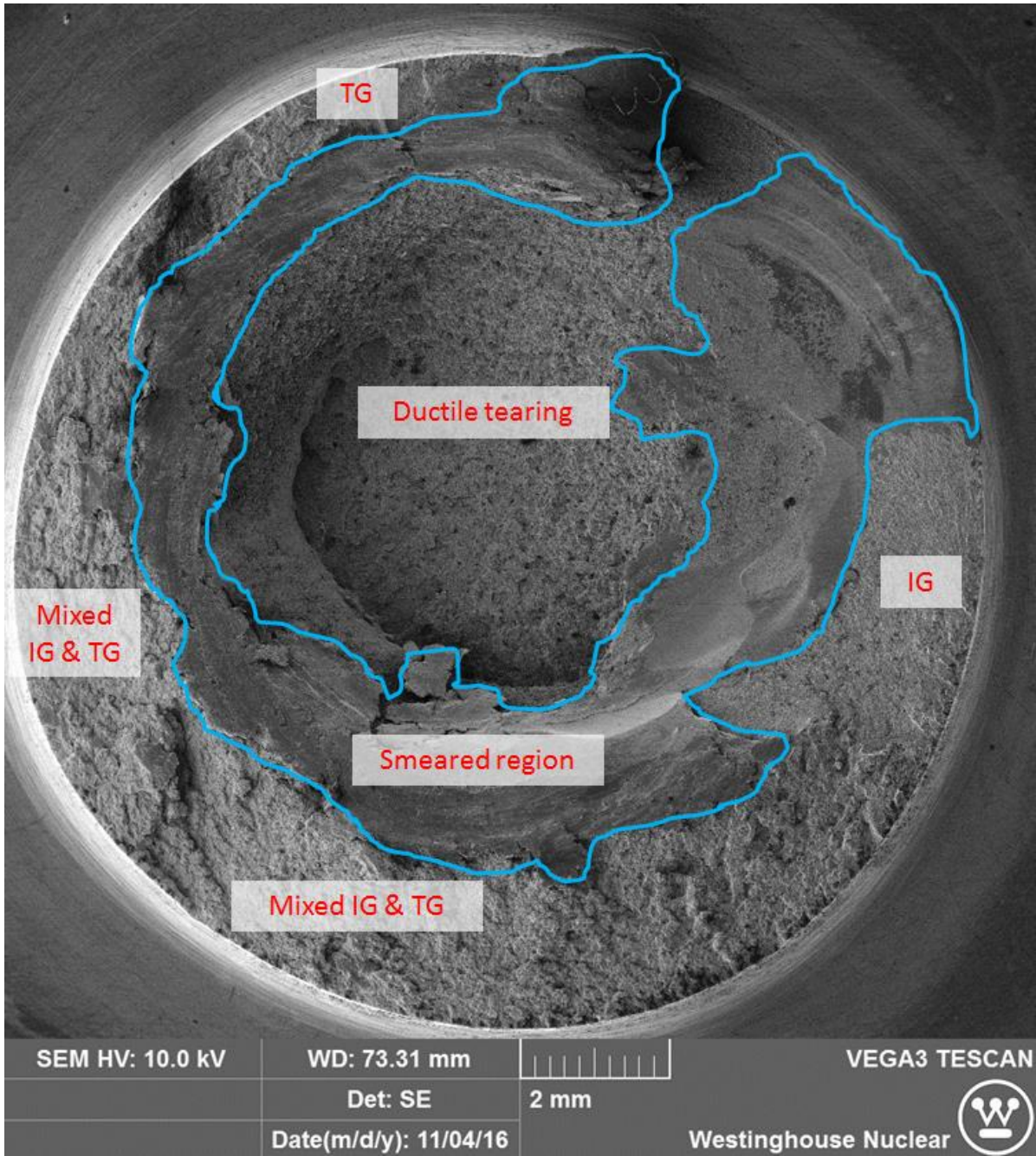


Figure 22. S1 Bolt G77 SEM Overall View of Fracture Surface

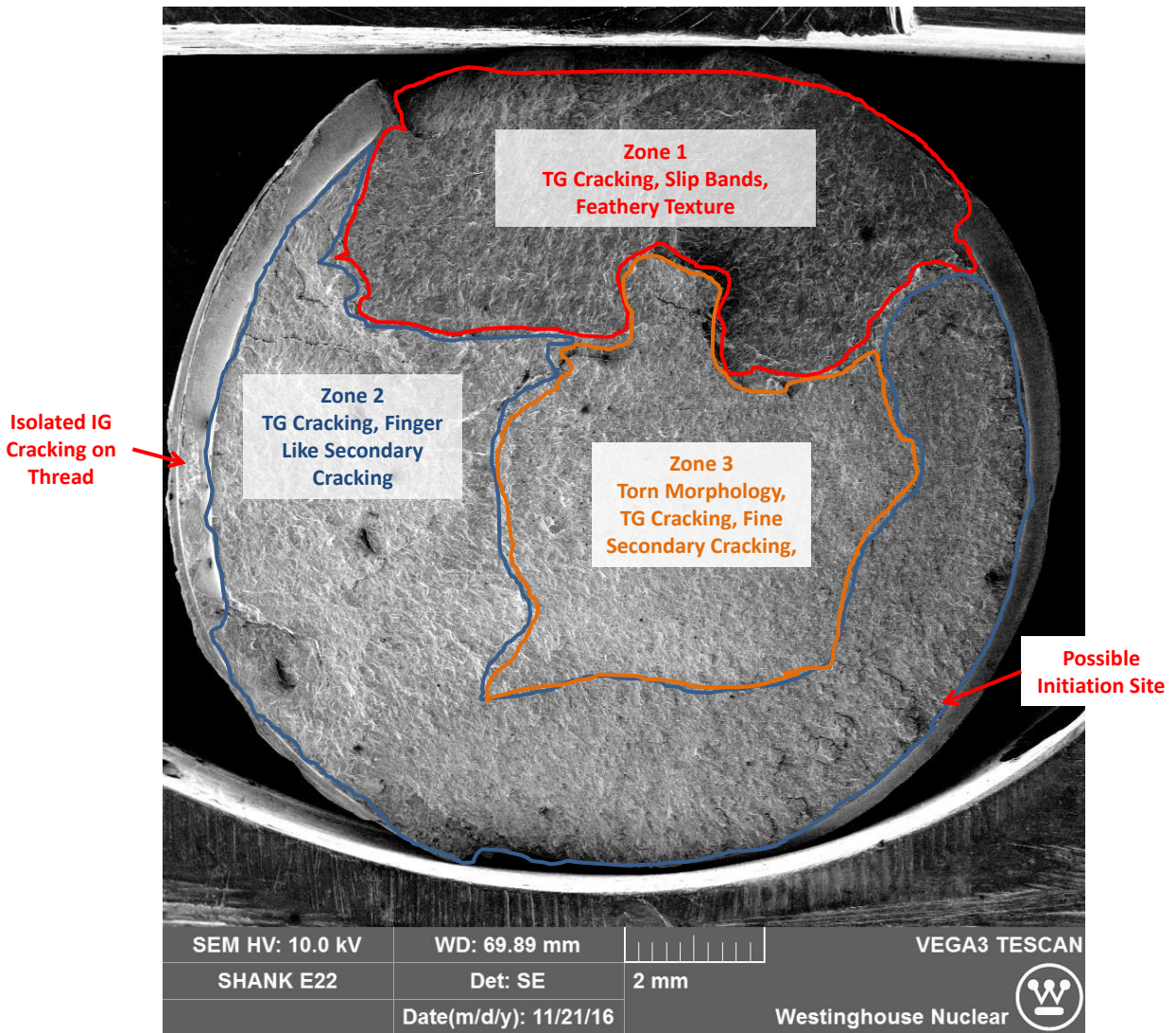


Figure 23. Overall Image of E22 Fracture at Head-to-shank Region

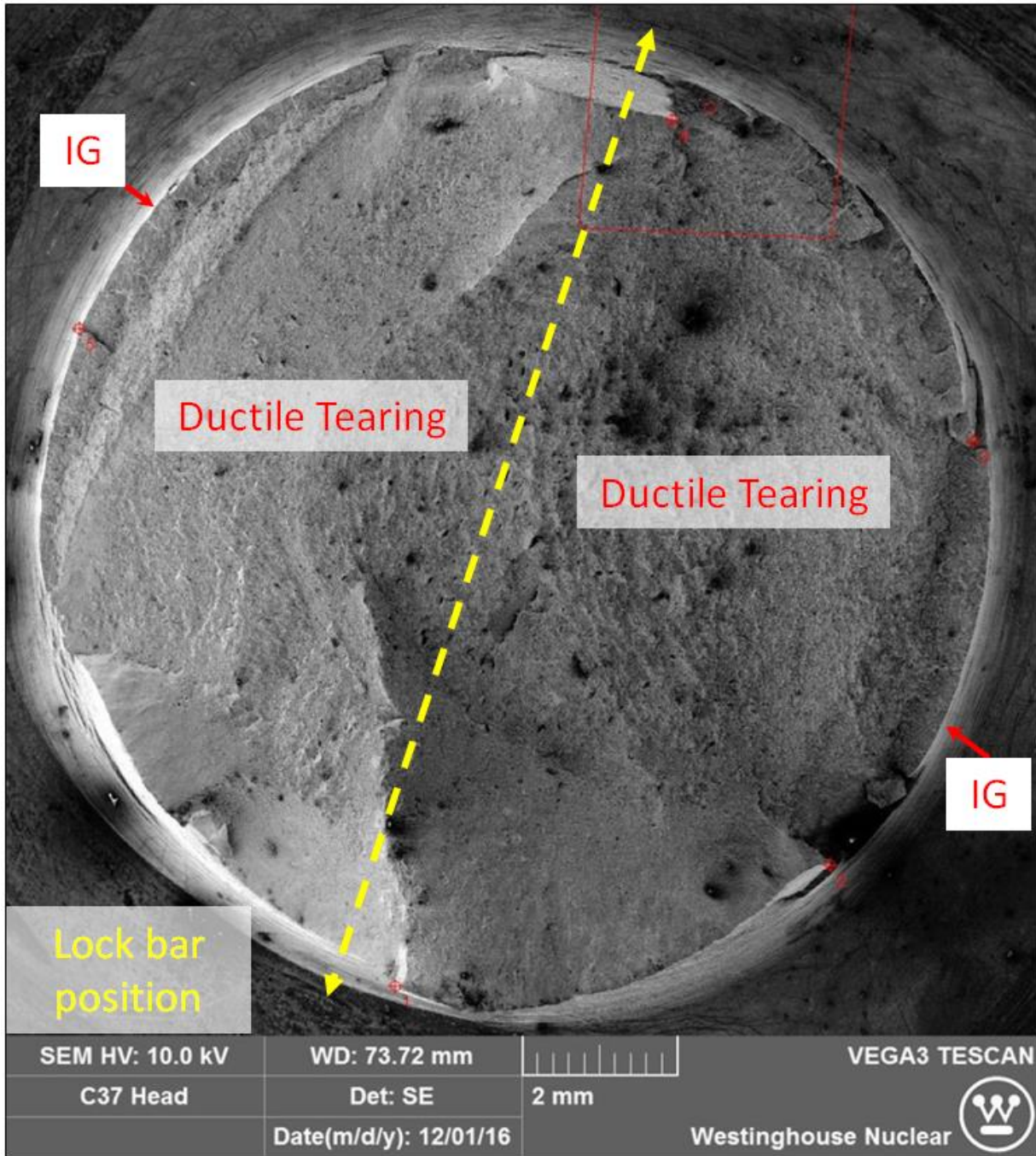


Figure 24. IP2 bolt C37 – Overall fracture surface (head side). IG crack regions are service-induced cracking, while ductile tearing resulted from laboratory tensile testing.

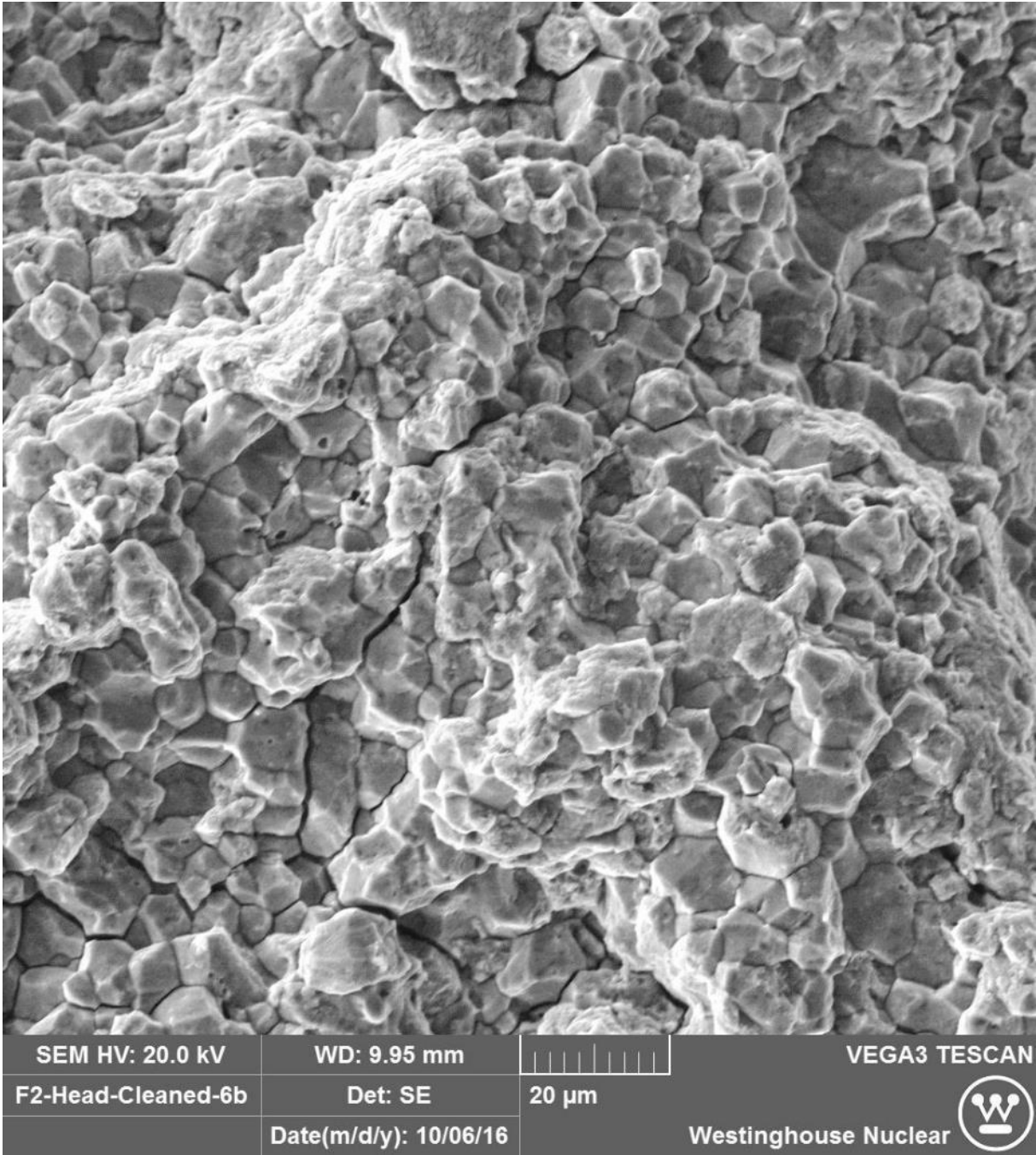


Figure 25. IP2 bolt F2, IG cracking and secondary cracking

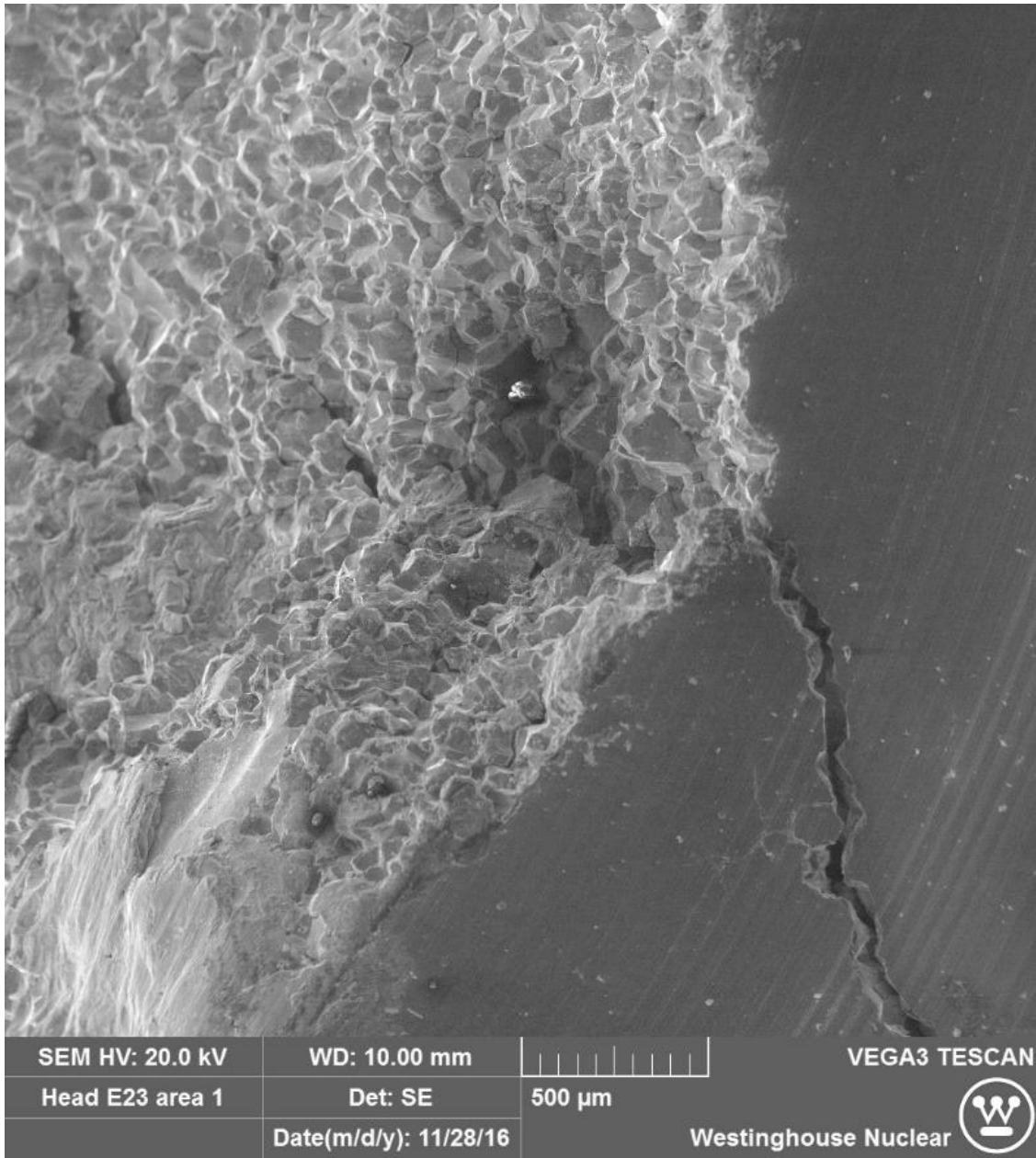


Figure 26. SEM Micrograph of E23 Head Fracture – Area 1, IG Cracking Extending into the Head

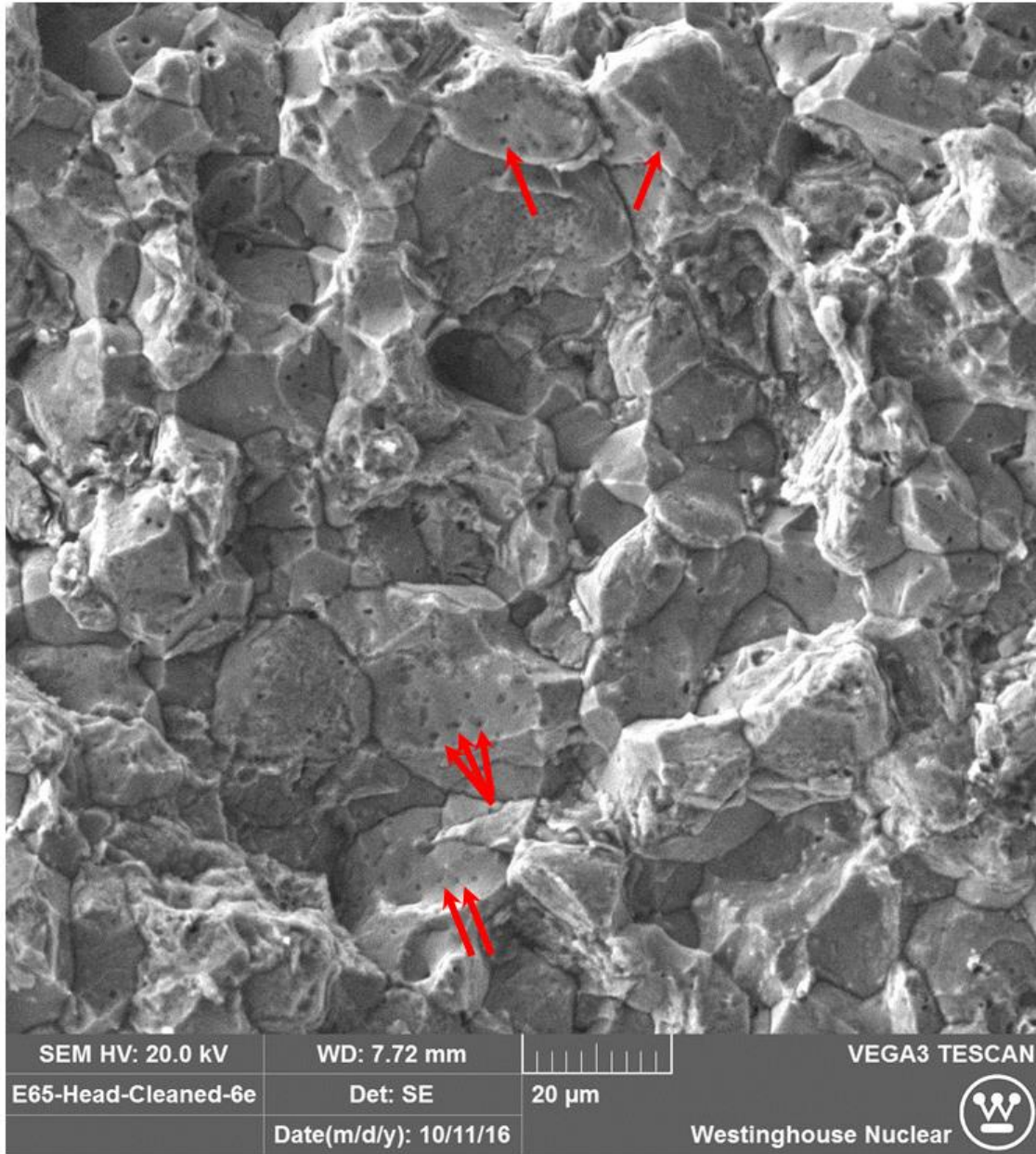


Figure 27. IP2 bolt E65, IG cracking and fine particles on grain boundaries. Red arrows indicate unknown surface spots

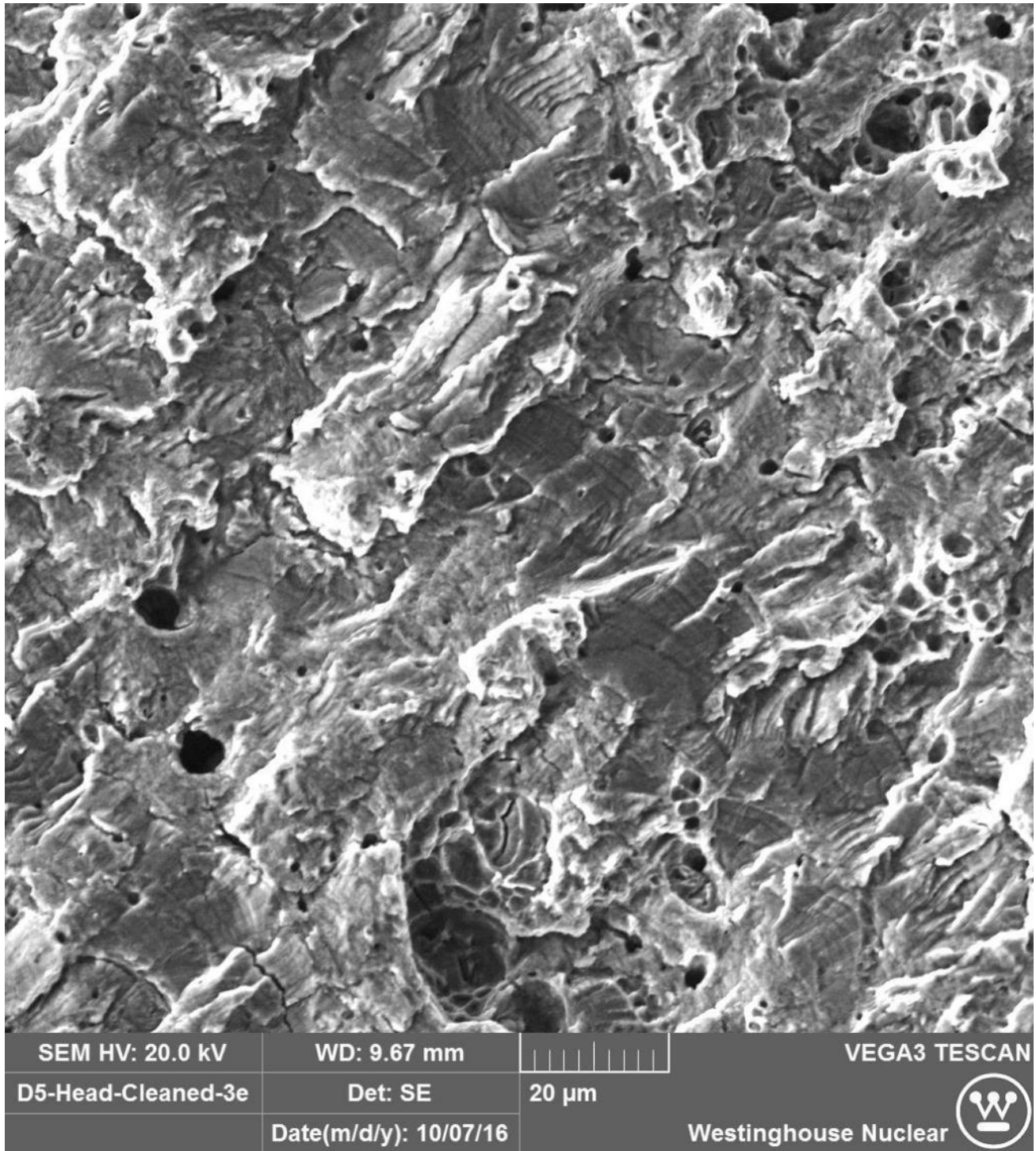


Figure 28. IP2 bolt D5, TG cracking with striations and holes

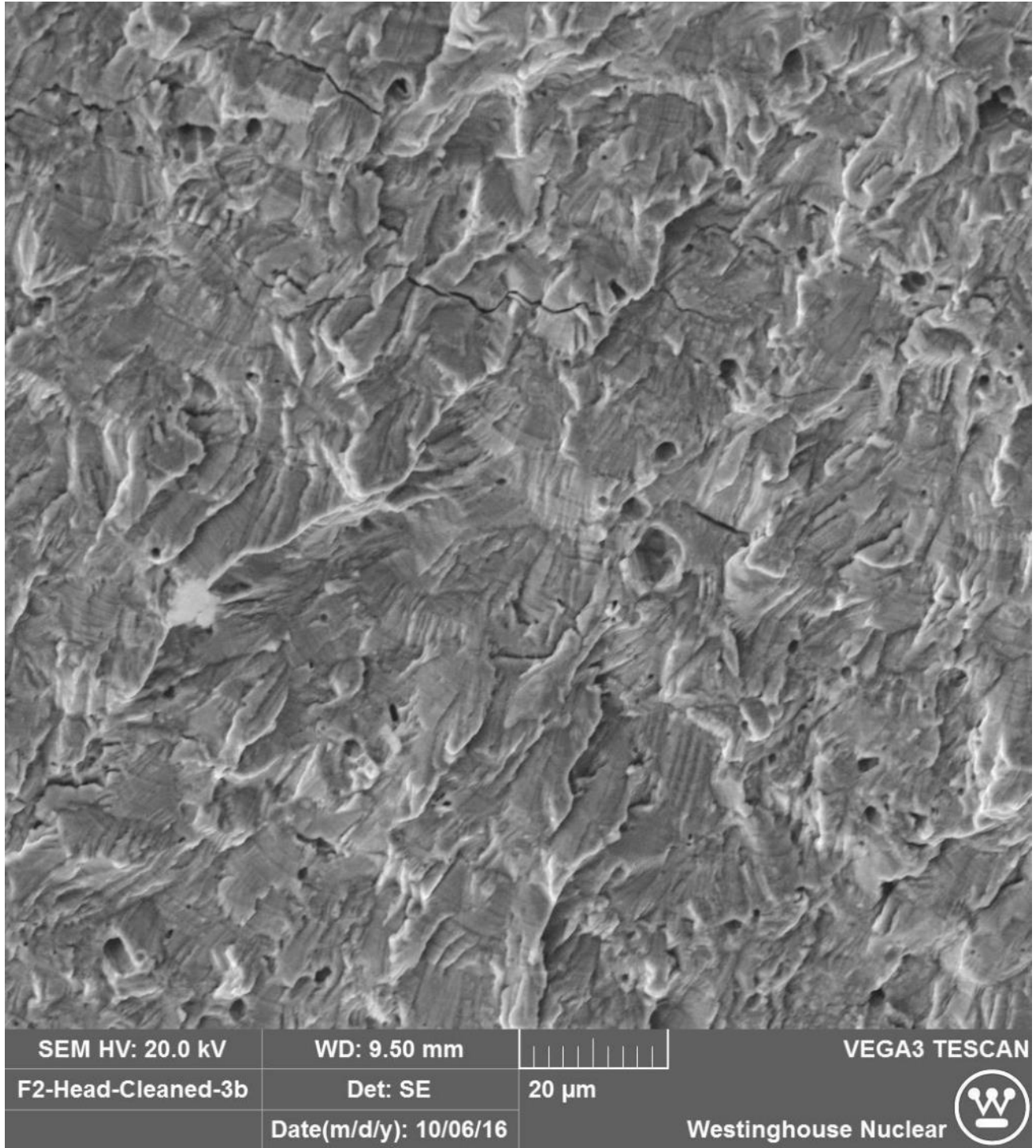


Figure 29. IP2 bolt F2, TG cracking showing striations and secondary cracking

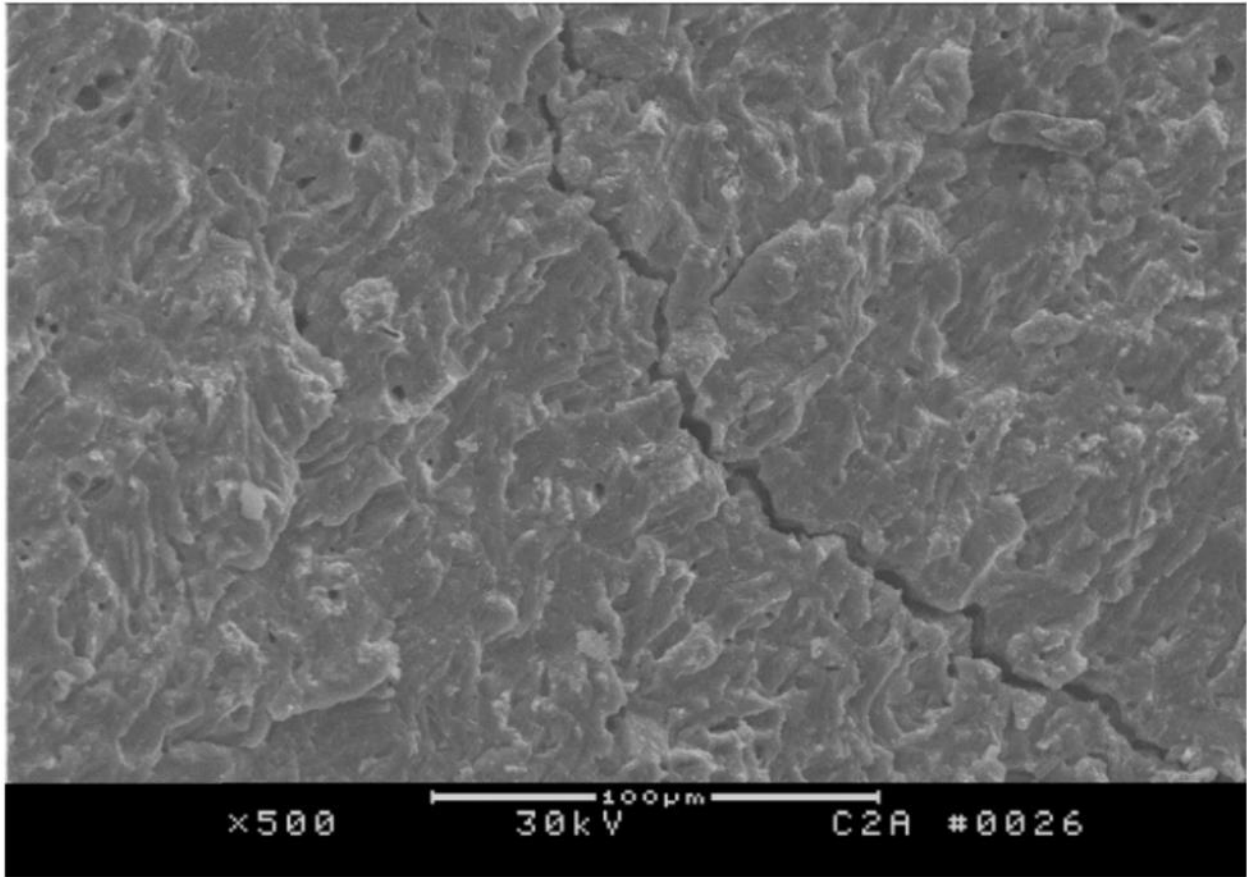


Figure 30. Secondary crack branching on the TG portion of the bolt S-R2C6 fracture surface

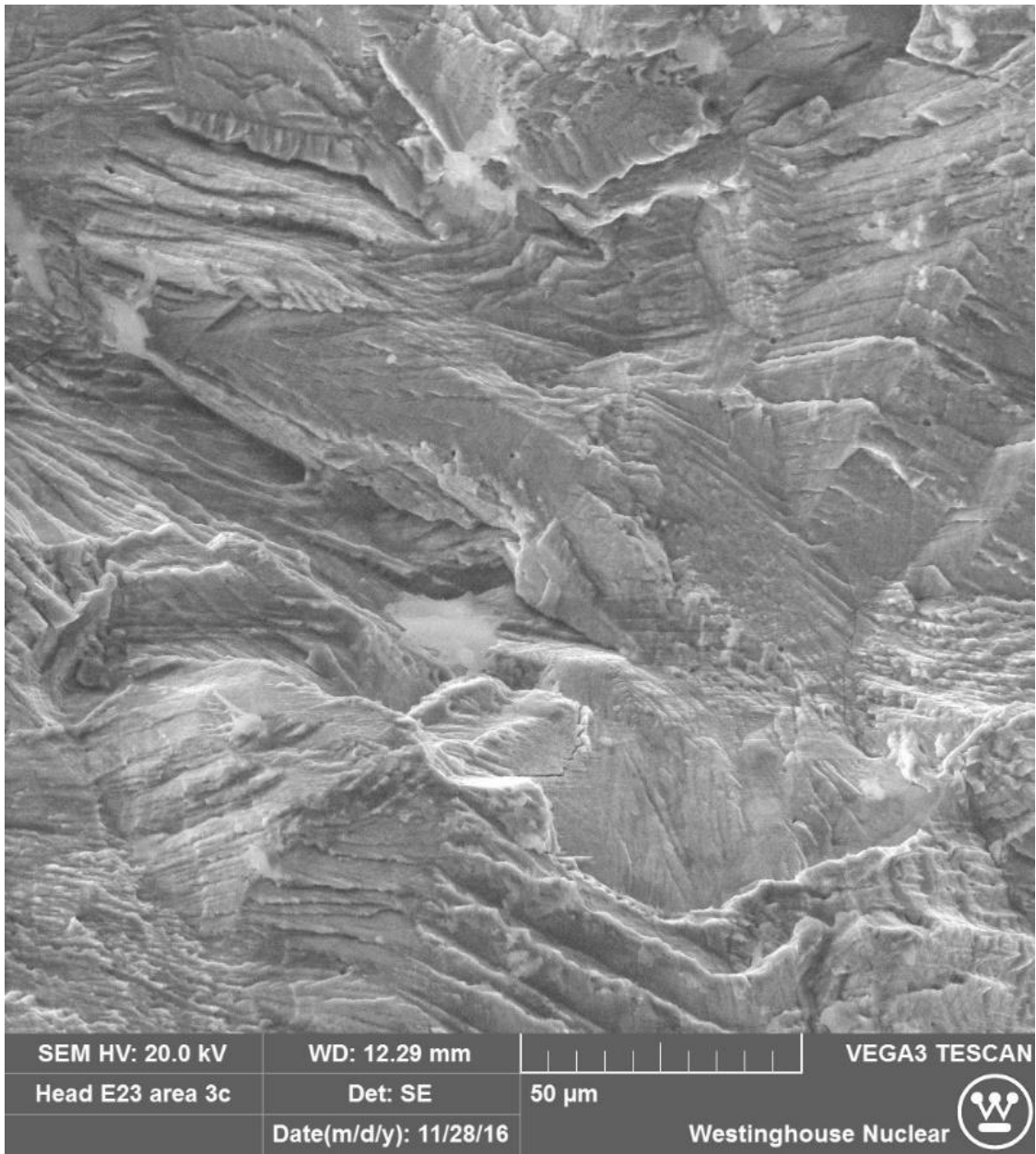


Figure 31. SEM Micrograph of E23 Head Fracture – Area 3, TG Cracking with Slip Bands



Figure 32. TG Cracking in Bolt E22 Feathery cracking with slip bands, limited secondary cracking, no striations



Figure 33. TG Cracking with Slip Bands in Bolt E22

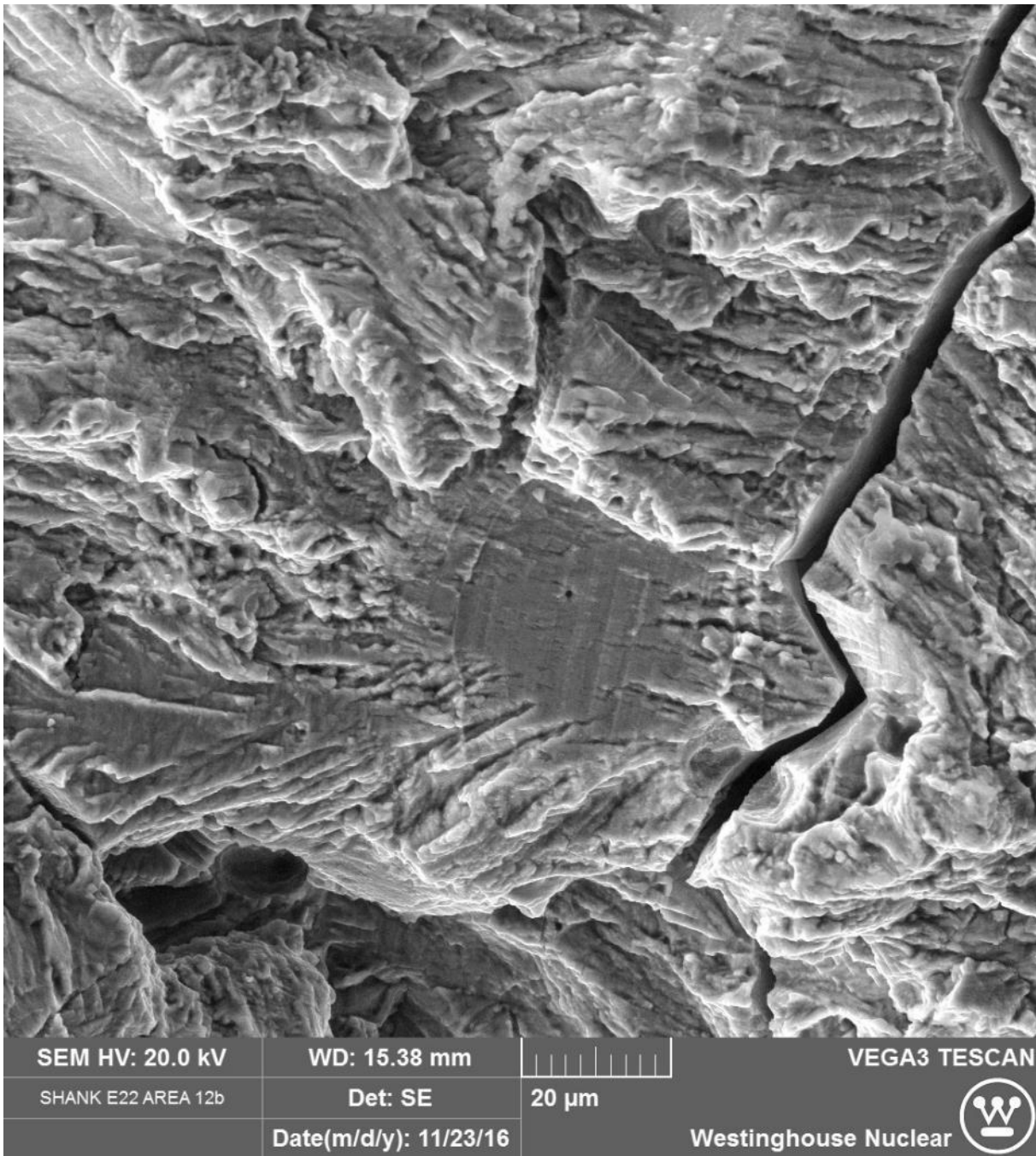


Figure 34. SEM Micrograph of E22 Shank Fracture, Striations and Secondary Cracking in Area of TG Fracture

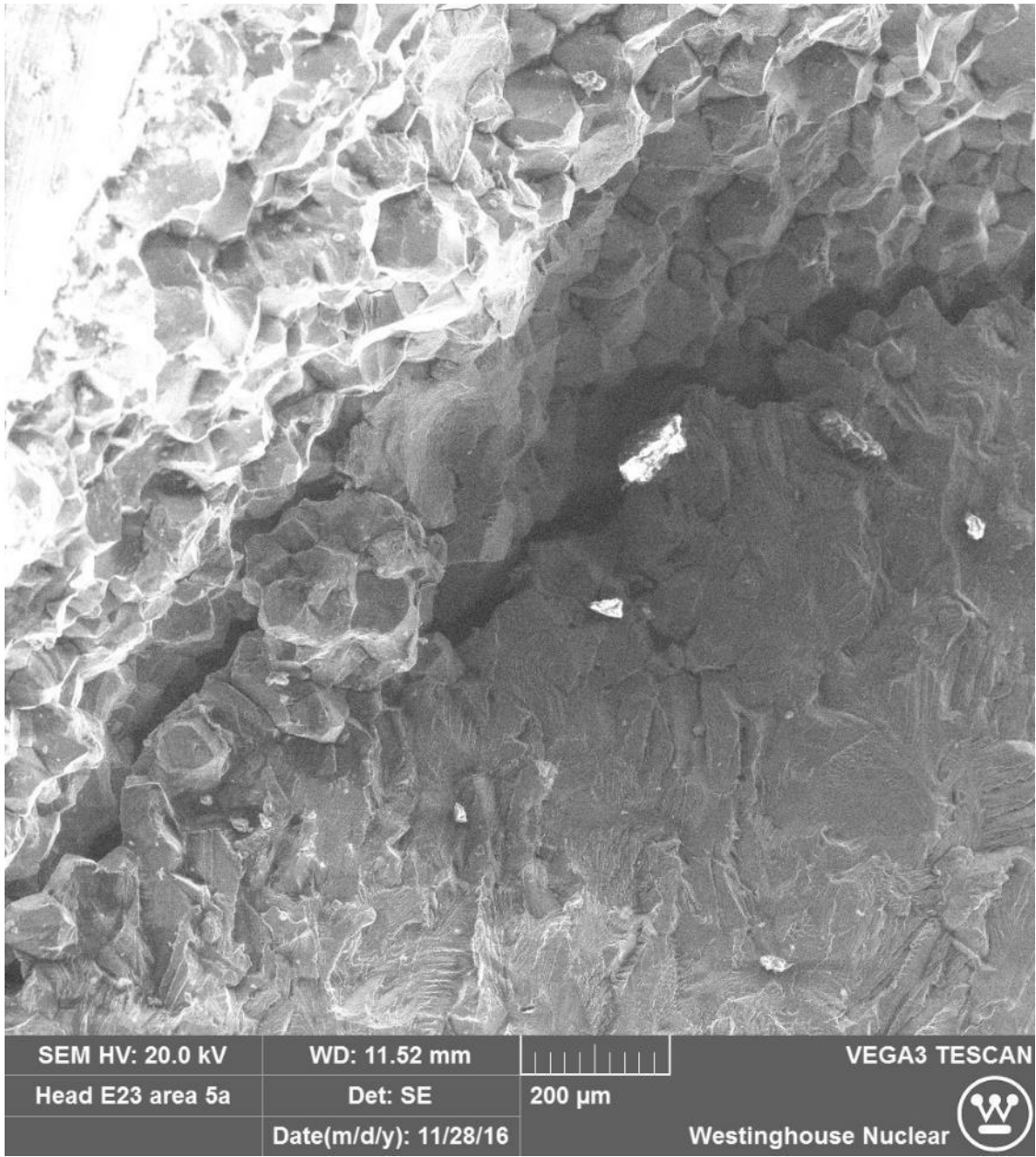


Figure 35. SEM Micrograph of E23 Head Fracture – Area 5, Transition between TG and IG Cracking

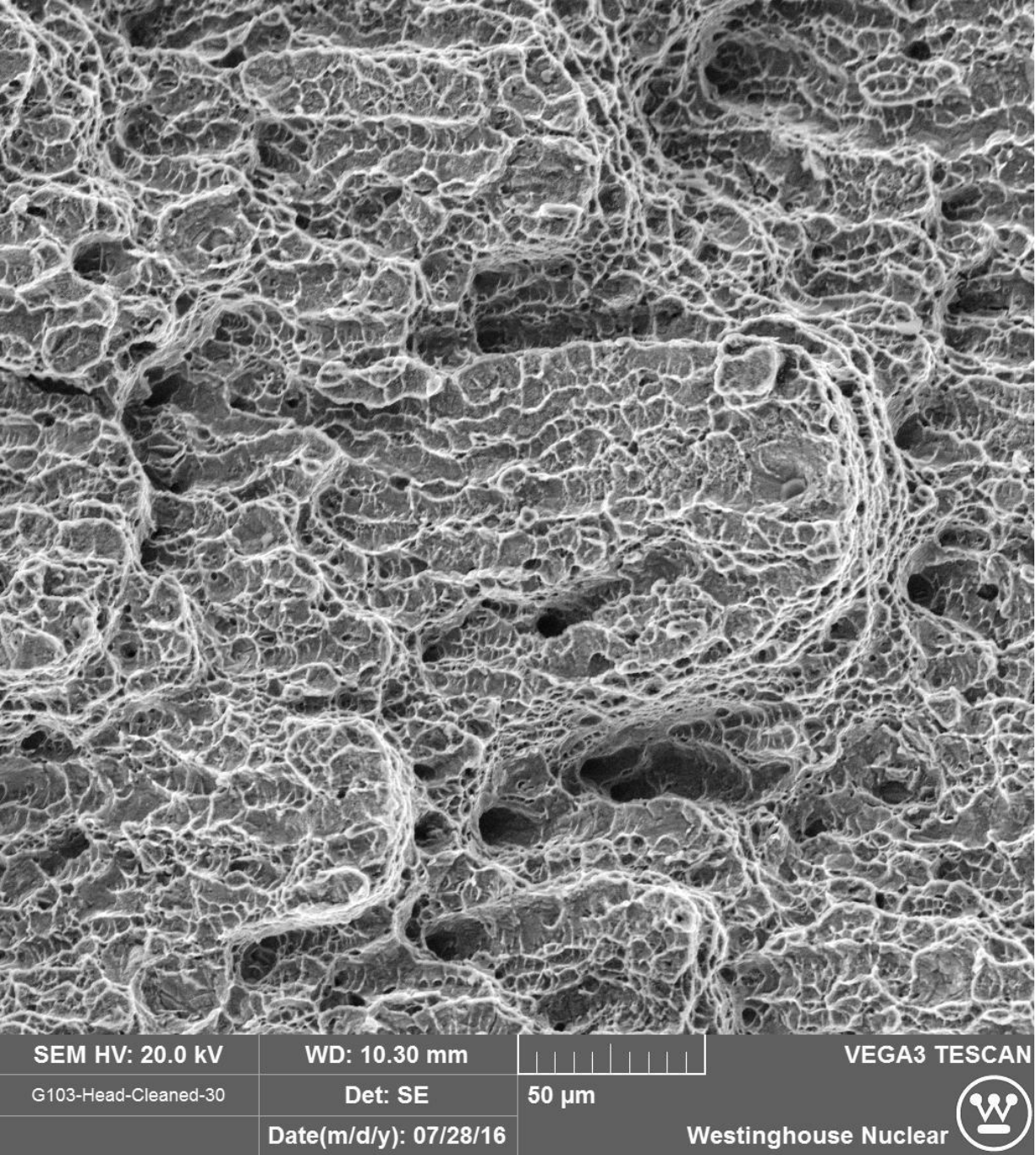


Figure 36. IP2 bolt G103, Blocky microvoid coalescence, showing numerous holes into the fracture surface.

4.3.3 Surface Contaminant Analysis

Analysis of surface debris did not identify any contaminants on bolts from IP2 or S1. However, some amount of chlorides were identified on bolt E23 from DCC2. Given that this bolt was exposed to several environments between extraction from the reactor and the laboratory examination (the spent fuel pool, the shipping cask, and the hot cell environment) the detection of this contaminant does not conclusively prove that it contributed to the fracture of the bolt. As tight water chemistry monitoring and control is employed at PWRs and no off-normal chemistry conditions were reported at these plants, chlorides or other impurities are not suspected as the cause of the bolt failures.

4.3.4 Dye Penetrant Testing

Dye penetrant testing did not identify any indications of cracking in the intact bolts with UT indications sent to the lab, including in IP2 bolt C37. C37 had previously been identified to have a tight crack by LOM, which was confirmed by fractography after pull testing. Because the dye penetrant method was not able to identify tight IASCC cracks, it was not further employed.

4.3.5 Hardness Testing

Rockwell hardness tests showed a gradient in hardness, with higher hardness values measured at the head of the bolt and decreasing towards the threads. This is expected as it coincides with the fluence gradient present in baffle-former bolts (described in Reference 38), which decreases by a factor of 1.5 to 2.5 along the length of the bolt from head to end. For the

originally installed bolts with approximately 23 dpa of neutron exposure at the head of the bolt, hardness values ranged from 41 HRC to 32 HRC. For the replacement bolts with approximately 4 dpa of neutron exposure at the bolt head hardness values ranged from 27 HRC to 22 HRC. For reference, unirradiated Type 316 stainless steel used in this application would be too soft (less than 15 HRC) to measure on a Rockwell C hardness scale, and would be less than 88 HRB on a Rockwell B hardness scale.

4.3.6 Results of Chemical Composition Analysis

Results of the chemical analysis are shown in Table 3. Chemical analysis of samples taken from the under-head area of the bolt (near the location of most service-induced failures) confirmed that the alloy chemistry met the Type 347 stainless steel specifications with the exception of a few measurements that indicated higher-than-allowable amounts of silicon. As the sample size of the material gathered was very small (due to radiological considerations), silicon is a minority element in the chemical composition, and silicon is a common environmental contaminant, these measurements do not conclusively show that the silicon in the bolt material was above the Type 347 specification.

Table 3. Results of Chemical Composition Analysis (in weight percent)

Plant / Document	Heat / Bolt	Fe	Ni	Cr	Mn	Mo	Nb/Cb	Ta	Co	Si
Specification	ASTM A-193	-	9.00-13.00	17.00-19.00	2.00 max	-	Nb + Ta \geq 10 x C content		-	1.00 max
CMTR	X11014	Bal	10.46	18.10	1.63	0.33	0.96	0.0X ⁽¹⁾	-	0.75
	10879	Bal	10.68	17.95	1.34	0.33	0.70	0.06	0.11	0.55
	39653	Bal	9.80	18.46	1.83	0.19	0.81	0.0X ⁽¹⁾	0.06	0.75
IP2	E37	67.79	10.30	17.80	1.28	0.25	0.74	0.02	0.07	1.06
	F45	67.22	10.38	17.93	1.44	0.26	0.95	0.00	0.05	1.15
	E28	66.99	10.49	18.11	1.50	0.22	0.96	0.00	0.06	1.12
	E65 (EDS)	67.4	9.0	19.3	2.0	0.3	0.9	-	-	0.7
	E65	66.36	10.24	18.80	1.45	0.32	0.94	0.00	0.05	1.2
	C37	68.51	10.22	18.00	1.28	0.27	0.65	0.00	0.08	0.71
S1	B83	68.14	10.40	17.76	1.28	0.30	0.74	0.00	0.07	0.91
	D2	67.21	10.35	17.81	1.48	0.26	0.94	0.00	0.06	1.25
	D92	68.35	10.21	17.76	1.26	0.26	0.68	0.00	0.06	0.94
DCC2 ⁽²⁾ (analyzed by ICP-OES/MS)	N-R4C4	69.4	10.0	17.5	1.7	0.1	1.1	0.1	-	-
	E-R4C6	66.9	10.9	19.2	1.7	0.1	0.8	0.0	-	-
	W-R3C5	66.4	11.2	19.7	1.7	0.1	0.8	0.0	-	-
	W-R3C5	66.8	10.9	19.6	1.7	0.1	0.8	0.0	-	-

Table 3 Notes:

- (1) Last digit for amount of tantalum is not visible on CMTR.
- (2) Additional minor elements were analyzed, see Reference 39.

4.3.7 Radionuclide Analysis

Samples taken from the same locations as those used for chemical analysis were subject to radionuclide analysis, which determined that the effective range of thermal (<0.025 eV) neutron exposures in the examined bolts was between 14 and 27 dpa at the underside of the bolt head near where cracks were observed to initiate. This analysis did not include any of the replacement bolts sent to the laboratory for testing. The trend in neutron exposures was consistent with expectations based on baffle-former geometry relative to fuel assemblies; that is, the highest neutron exposures were for bolts closest to the reactor core. The results of the radionuclide analysis are shown in Table 4. The nickel content of E65 was measured by both ICP-OES and EDS, and dpa values were

calculated using the two slightly different measured chemistries. All other values are based on ICP-OES chemistry only. The measurements found that there was approximately 0.02 to 0.04 weight percent of Ni-63 in the samples. The uncertainty on the fluence values was determined to be approximately +/- 15%. These results confirm that the materials were all within a radiation damage range where IASCC can potentially occur.

Table 4. Results of Radionuclide Analysis

Bolt	IP2 E37	IP2 F45	IP2 E28	IP2 E65 (EDS)	IP2 E65 (OES)	IP2 C37	S1 B83	S1 D2	S1 D92
Effective dpa	14	26	27	27	24	14	17	20	22

4.3.8 Results of Mechanical Testing of Whole Bolts

Three original bolts without UT indications from D.C. Cook Unit 2 were loaded in tension to 414 MPa in the bolt shank (bounding original design loads) without failure. Mechanical loading to failure in air at room temperature was conducted on eight whole bolts which displayed UT indications, and one bolt (DCC2 E28) which did not have a UT indication. Approximate stress-strain curves for these bolts are shown in Figure 37. The effects of radiation hardening were evident from these results with the extent of hardening varying with radiation exposure, as was expected. Eight of the nine bolts showed no signs of service-induced cracking after being pulled to failure, while one bolt (C37) was found to have two fine diametrically opposed IG cracks on the perimeter of the bolt, near the head-to-shank radius (Figure 24). However, the approximate stress-strain curve for C37 does not differ significantly from the bolts that were completely uncracked. The bolt H104, which was installed at the top level of the baffle former assembly and out of the

active core region, had significantly higher ductility than the other bolts which were in the active core region. The replacement bolt DCC2 E28 was only in service for six years, and also showed higher ductility than the originally installed bolts that had been in service for ~30-40 years.

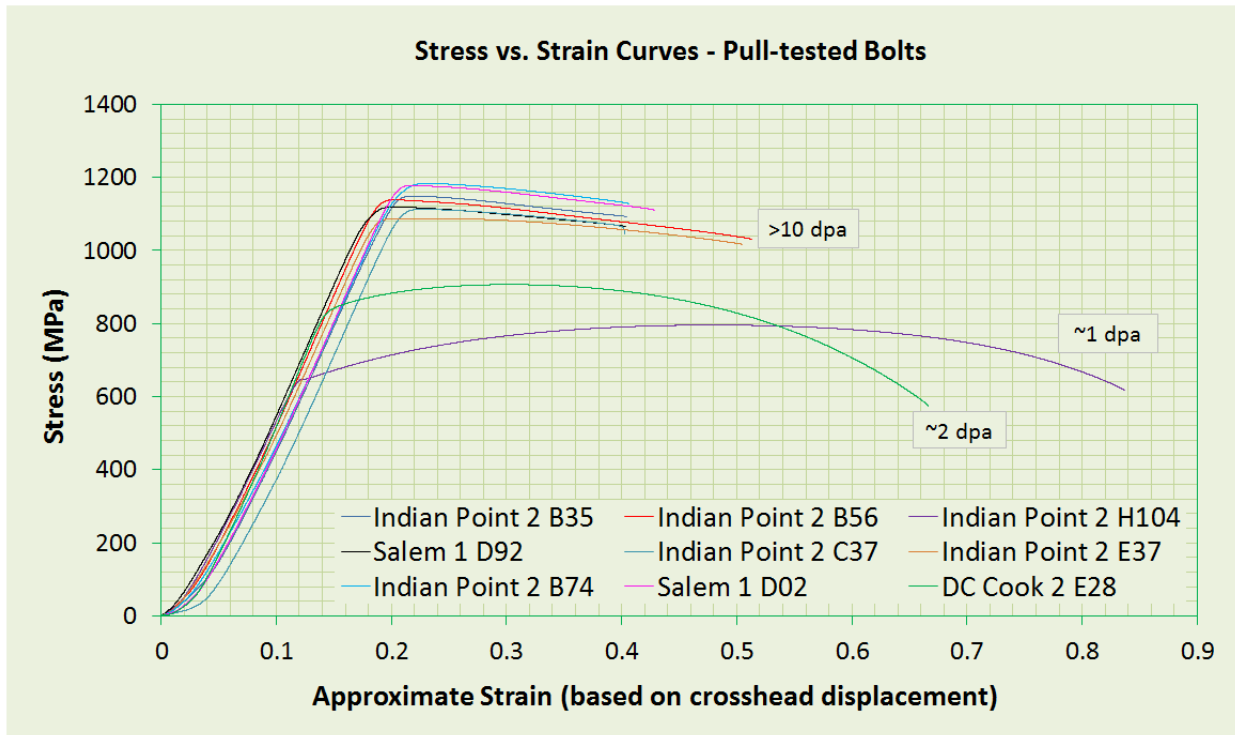


Figure 37. Stress-strain curves for bolt pull tests

4.3.9 Tensile Testing Results

Four miniature tensile samples of material extracted from the shanks of two bolts were also tested. The tensile samples were 25 mm long, 5 mm diameter cylindrical specimens with an 11 mm gauge length and a 2.8 mm gauge diameter and fastened into the load line via threaded ends. The specimens were tested at room temperature in air. The resulting engineering stress-strain curves are shown in Figure 38. Sample E28 (27 dpa) showed the highest level of hardening, with

a 136% increase in yield strength to 1172 MPa from initial properties as indicated by the CMTR. Despite this hardening, the bolt material maintains appreciable ductility as shown by the elongation and reduction of area (RA) values (see Table 5). These data are compared to tensile results from other tensile data (References 37, 40, 60) on material extracted from Westinghouse-designed reactor internals in Figure 39. These results, combined with those from 4.2.8, indicate that the tensile properties are consistent with those expected for highly irradiated austenitic stainless steels. This helps to rule out the potential for a metallurgical irregularity that would have made these materials more susceptible to IASCC than others previously tested.

Table 5. Results of Miniature Tensile Testing

Tensile Specimen	RA	Uniform Elongation	Total Elongation	YS	UTS	Dpa
CMTR	67.9%	-	42.3%	510 MPa	683 MPa	0
B83A	47%	0.8%	7%	1078 MPa	1086 MPa	17
B83B	42%	0.6%	7%	1085 MPa	1100 MPa	17
E28A	44%	0.4%	6%	1165 MPa	1173 MPa	27
E28B	45%	0.4%	6%	1173 MPa	1178 MPa	27

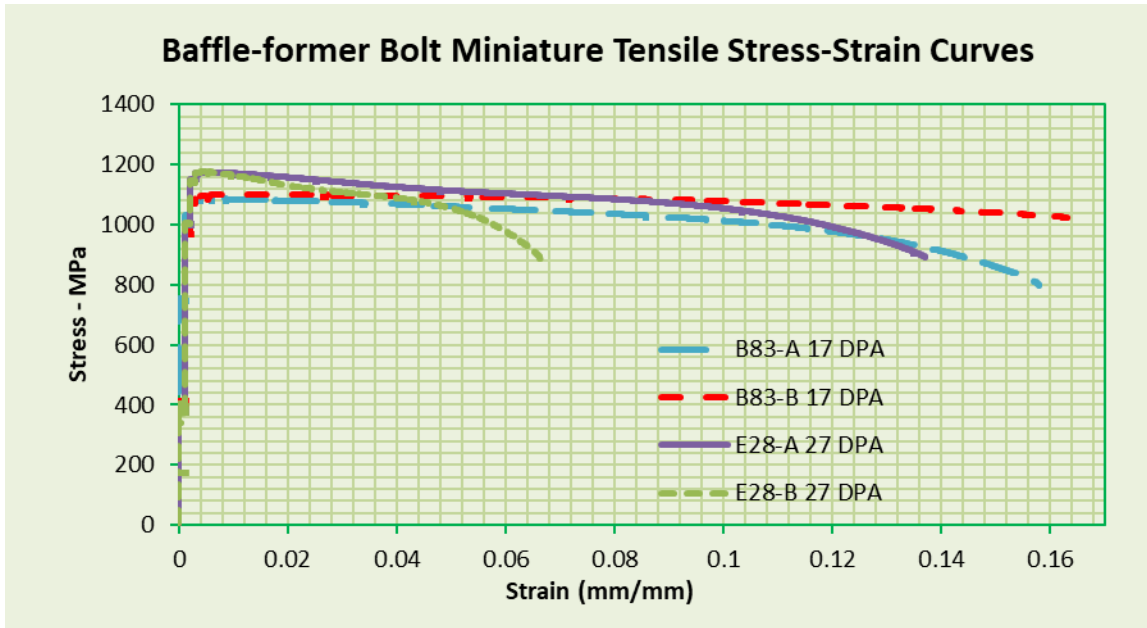


Figure 38. Stress-strain curves for miniature tensile tests

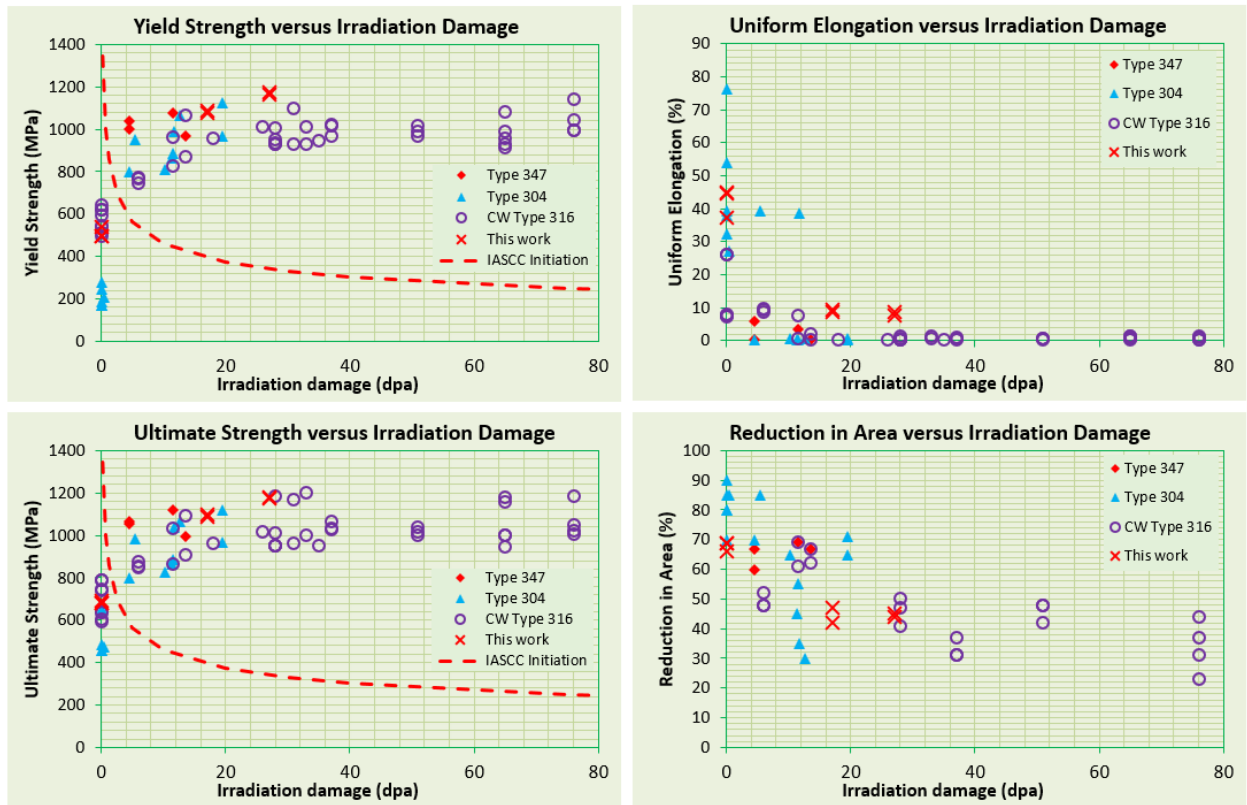


Figure 39. Tensile properties of PWR-irradiated austenitic stainless steels versus irradiation damage

4.3.10 Metallography

Cross-sections were taken from four different bolts from IP2 and S1 for metallography. Three bolts had UT indications and one did not. Flow lines (Figure 40) and aligned microstructural features (Figure 41) were observed in all cases. These features are consistent with the hot forging process used to create the bolt head geometry. No attempt was made to determine the chemical composition of these features due to the radiation field from the samples. Inclusions greater than 1.6 mm, which would be expected to produce a UT indication, were not observed. However, the presence of numerous aligned inclusions, flow lines, and variable grain sizes all challenge the assumption of a homogenous material typically required for application of ultrasonic inspection techniques. The existence of these features in bolts with and without recordable UT indications makes it unlikely that these microstructural features were responsible for the large number of bolts that exhibited recordable UT indications but were found to be intact on removal.

Metallography was also performed on DCC2 bolts (both original Type 347 and replacement Type 316). The original Type 347 DCC2 bolts exhibited branched cracking in areas of both IG and TG cracking indicative of an environmentally-assisted mechanism. Stringer-like inclusions, likely MnS, were also observed. The replacement Type 316 bolts also exhibited branched cracking in both IG and TG cracking areas. Grain boundary ditching could clearly be observed (Figure 42).

Metallography allowed the bolt heads to be examined in cross-section. It was at this time noticed that the bolts from IP2 and S1 had a smaller head-to-shank radius than the DCC2 bolts, which would increase the stress concentration factor and so increase susceptibility to IASCC. This was unexpected as the DCC2 bolts were the first clustered failures to be detected.

An important result of this metallographic investigation was also identifying differences in the metallurgical structures of steels from different eras. The Type 347 bolts from IP2 and S1 were fabricated in the 1960s, while the replacement Type 316 bolts were fabricated in the 2010 timeframe. The newer bolts contain substantially fewer inclusions than the older bolts, due to more modern steelmaking practices resulting in a cleaner product. This has potential implications for IASCC behavior, as such inclusions (like MnS) are potential contributors to IASCC initiation (Reference 58).

At the completion of these investigations, the 32 Type 347 IP2 bolts remain in storage at the Westinghouse Churchill Site facility. These IP2 bolts have been donated to the Idaho National Laboratory Nuclear Fuels and Materials Library and are open for study through the Department of Energy via programs such as the Nuclear Science User Facility program.

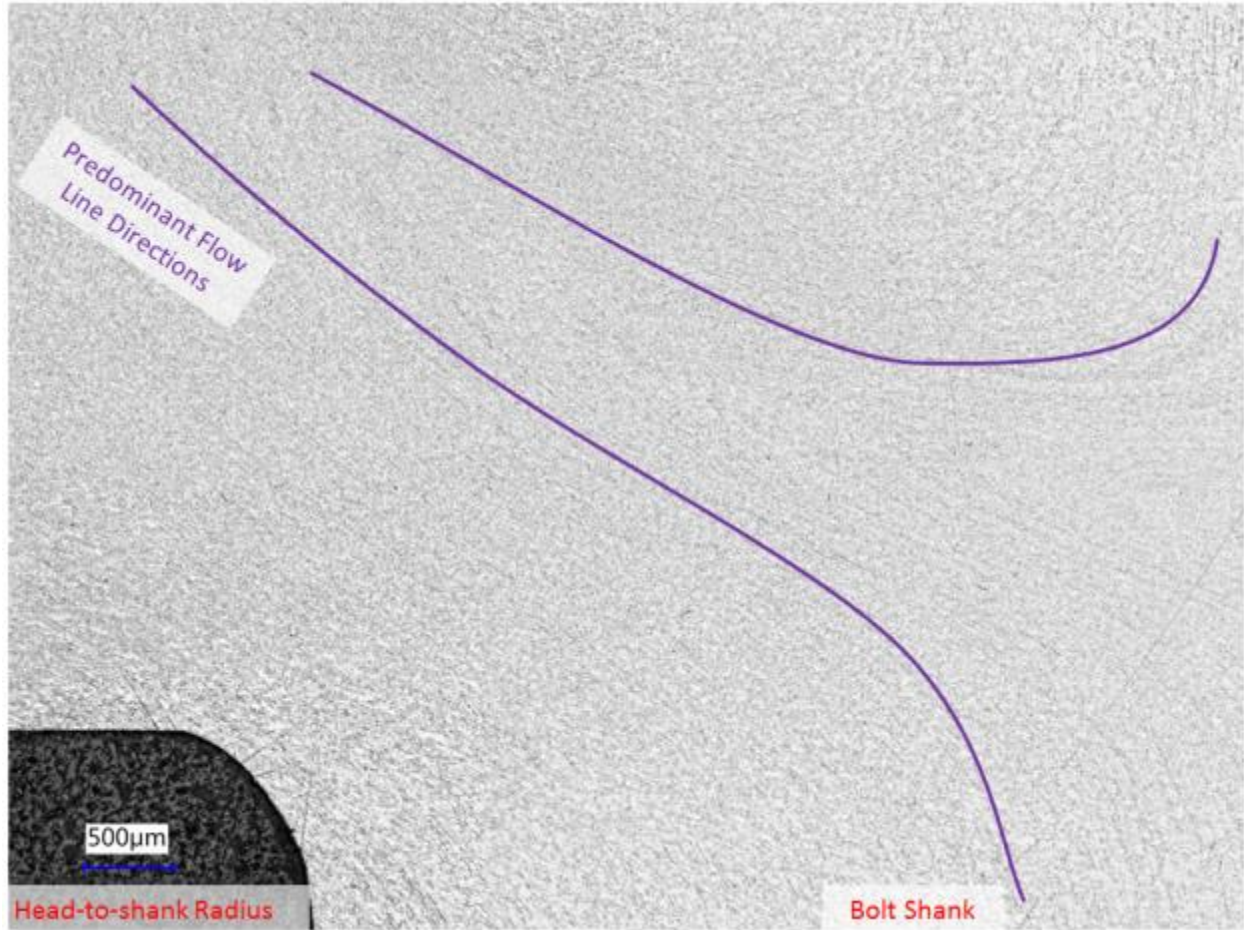


Figure 40. IP2 E37-H flow lines near head-to-shank transition (etched)

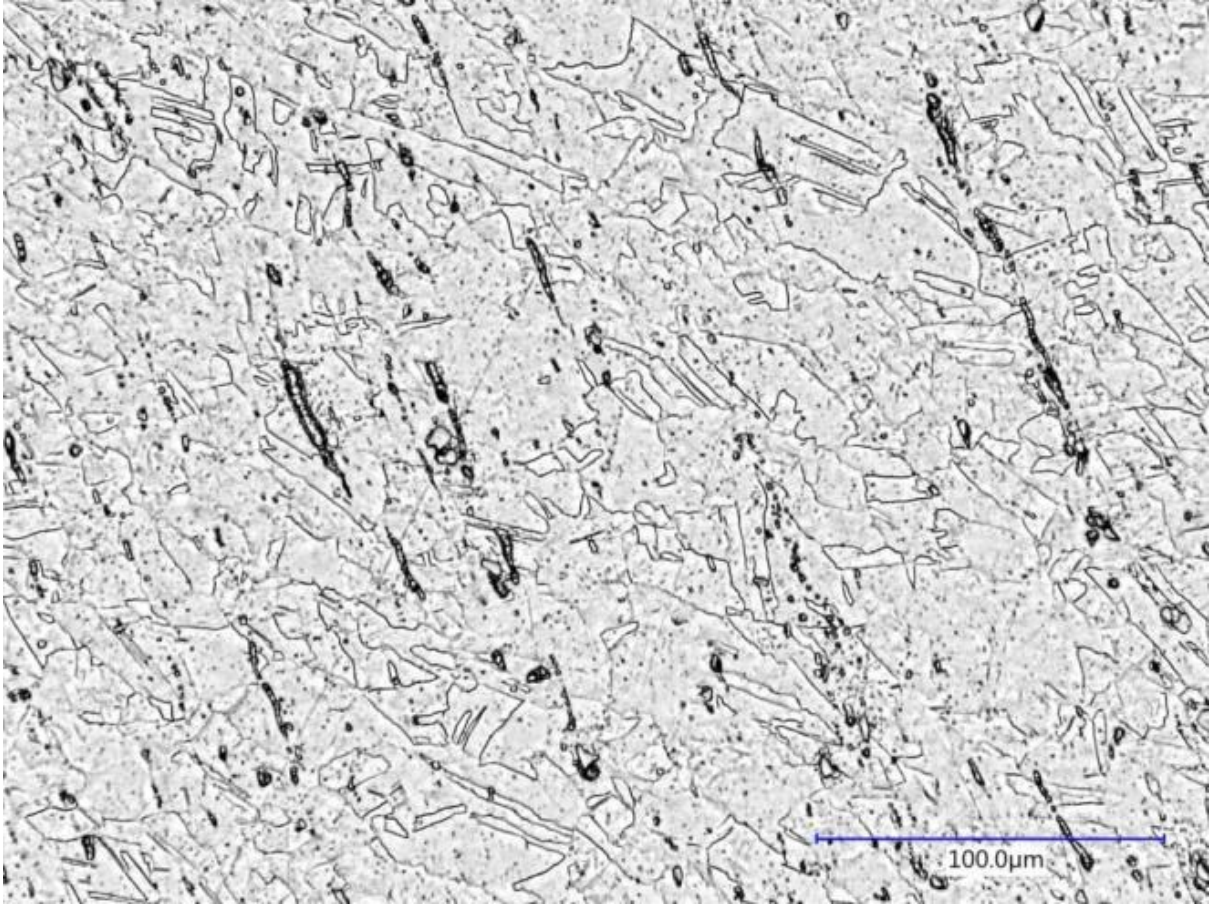


Figure 41. Transverse cross-section of IP2 bolt C52 showing aligned features in head-to-shank transition region (etched)

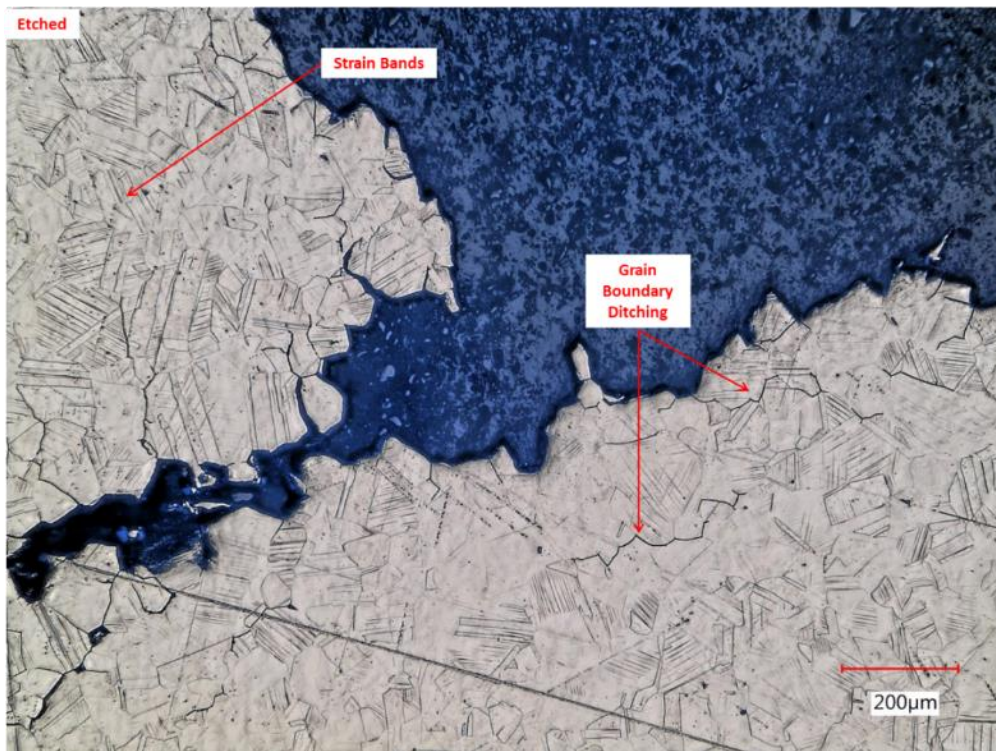
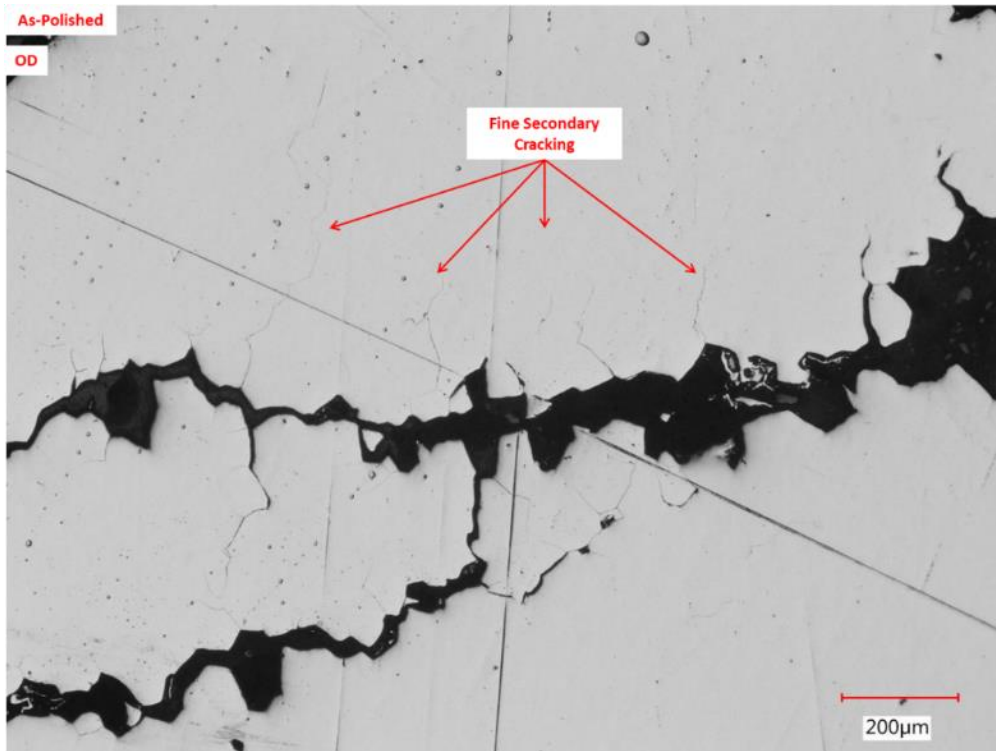


Figure 42. Transverse cross-section of DCC2 bolt E23 showing aligned features in head-to-shank transition region

4.4 Discussion

The significance of this work to the nuclear industry is that IASCC was identified as the initiating degradation mode in the baffle-former bolts. The results of the mechanical property testing, chemical composition analysis, and metallography did not reveal any features that would be expected to significantly enhance the material's susceptibility to IASCC. This led to further investigations of plant-specific design, inspection practices, and operational practices (beyond the scope of this thesis) that may have been able to mitigate such failures.

The scientific aspects of this work which are of interest are the observation of transgranular cracking associated with IASCC, and the characterization of a large volume of PWR-irradiated material which has now been made available for study through the DOE NSUF program.

The aspect relevant to this thesis is the observation of transgranular cracking in IASCC associated with components which failed under the higher stress. Typically, IASCC has been associated with an intergranular fracture mode when identified in LWR service (References 35, 36, 37). Observations of transgranular fracture are typically associated with fatigue or chloride-induced stress corrosion cracking in austenitic steels. However, it has been shown that transgranular SCC can occur in heavily cold worked unirradiated austenitic stainless steels at constant loads (References 41, 42, 43, 44, 45, 46). While not representative of steels used for nuclear construction due to the excessive cold work, which is prohibited by regulation in nuclear construction (47), these studies do illustrate the role of localization of stress in driving transgranular SCC. Further, the fracture surfaces generated during such experiments strongly resemble those observed on the baffle-former bolts (Figure 43 and Figure 44).

Similarly-appearing TG fractures have appeared during slow strain rate testing (SSRT) of neutron-irradiated austenitic stainless steel (Figure 45, from Reference 48). The SSRT specimens

had a tendency to initiate with an intergranular morphology, which transitioned to transgranular as specimen cross-section was reduced, and terminated in microvoid coalescence as local stress was increased on the remaining material. This failure progression also appears similar to that observed on baffle-former bolts (Figure 22).

While localization of stress and strain has been linked to IASCC previously (References 49 and 50), this had not been extended to transgranular IASCC before. The transgranular IASCC behavior may follow a mechanism similar to the hydrogen-enhanced localized plasticity model (Figure 46, from Reference 51), where further localization of stress is provided by dislocation channeling behavior and irradiation embrittlement.

The observation of transgranular fracture is therefore interpreted as the mechanical behavior of the material becoming more dominant in the cracking process than the time-dependent environmentally-driven behavior.

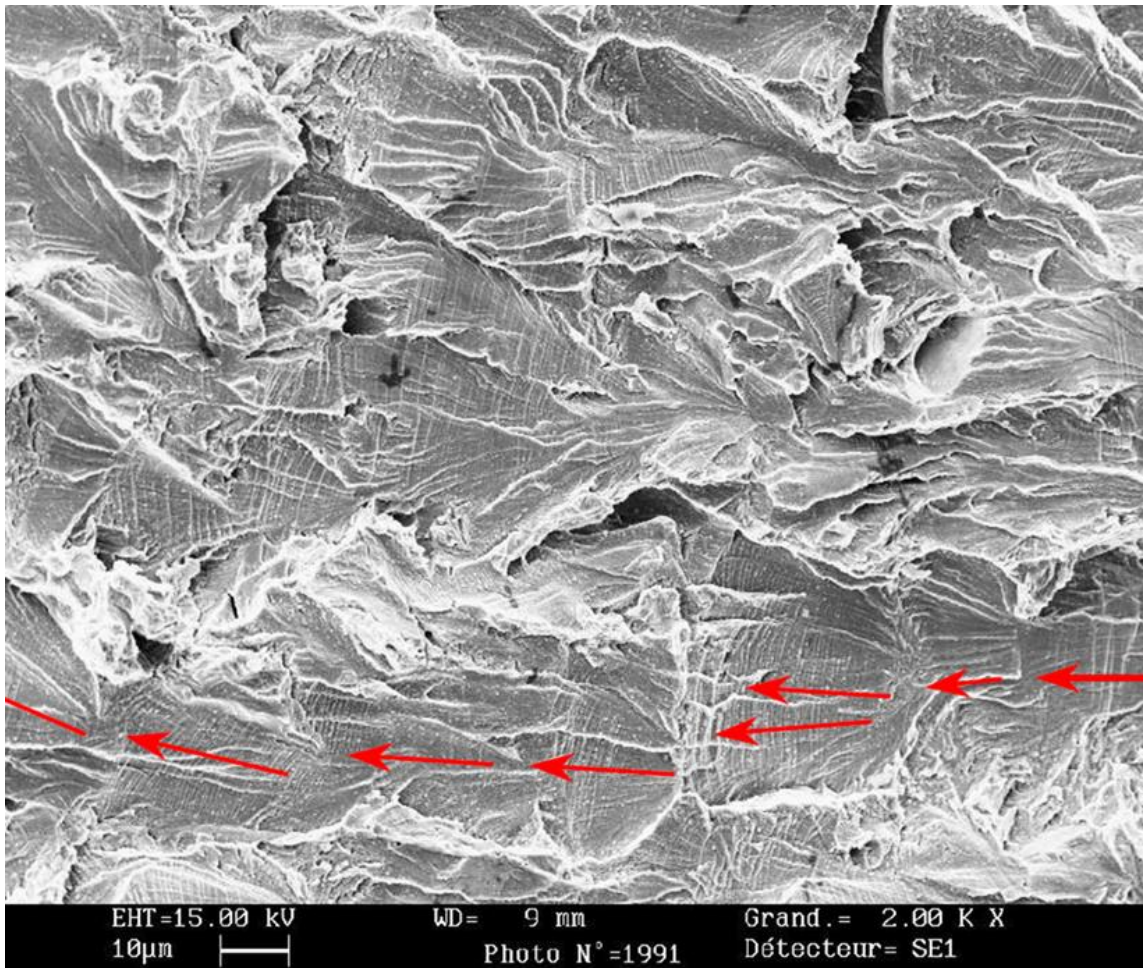


Figure 43. TGSCC at a constant strain rate of $4.7E-8:s$ in PWR water from Reference 41

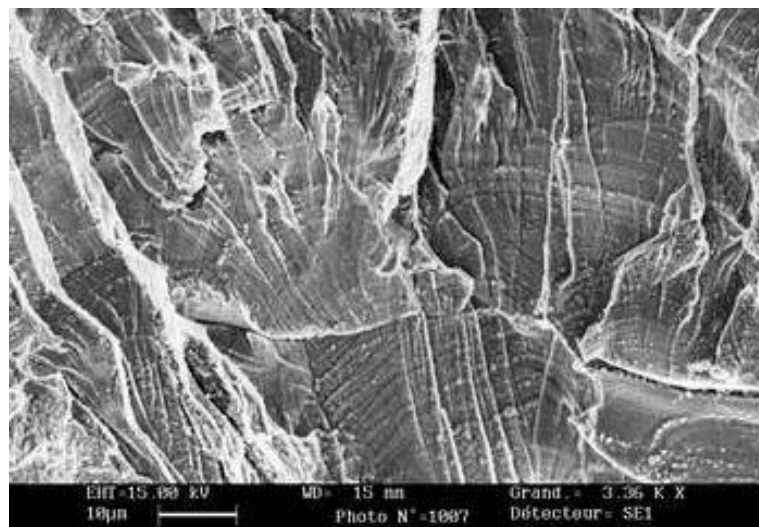


Figure 44. TGSCC generated at constant load in PWR water from Reference 44

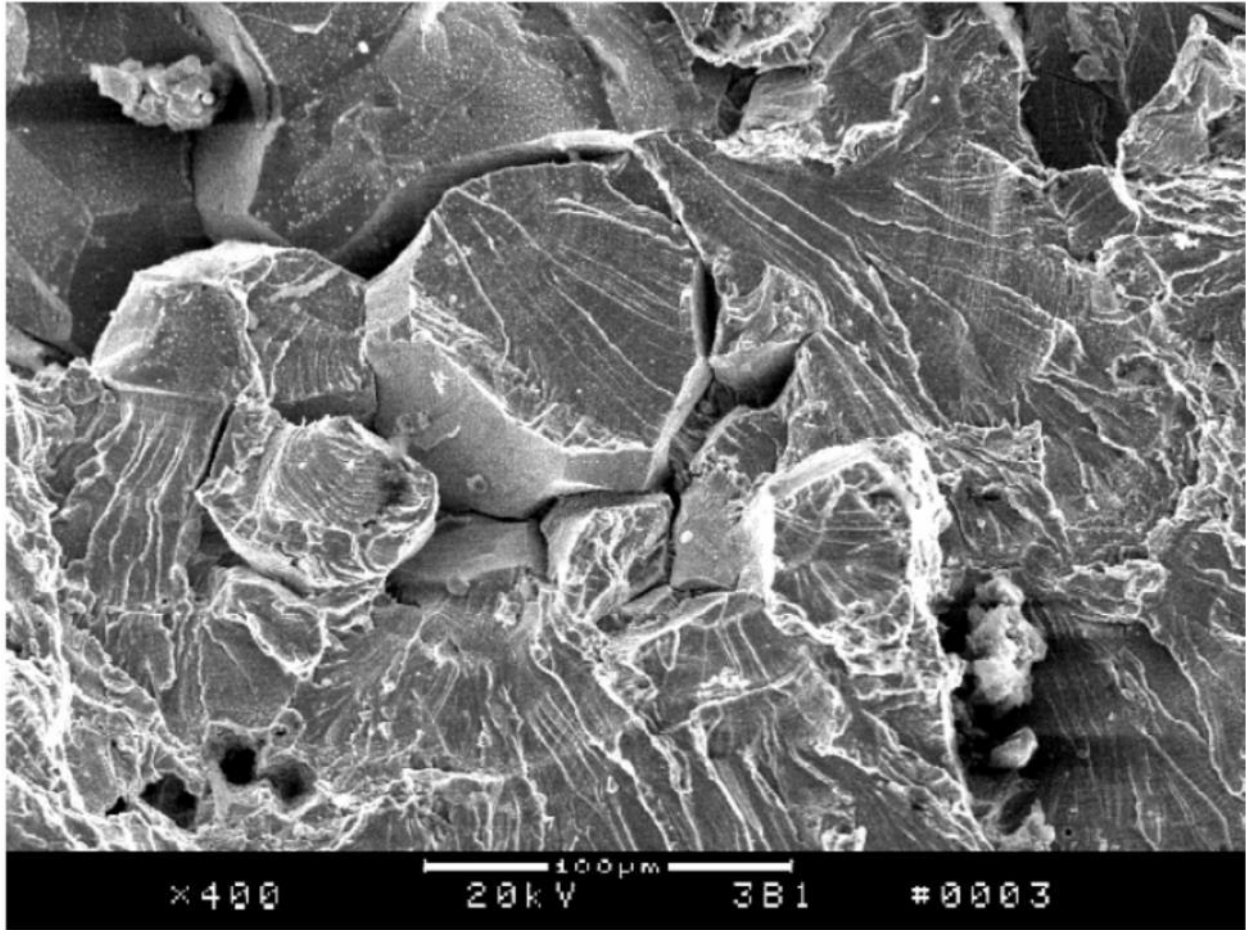


Figure 45. TGSCC on SSRT specimen 3B1 from Reference 48

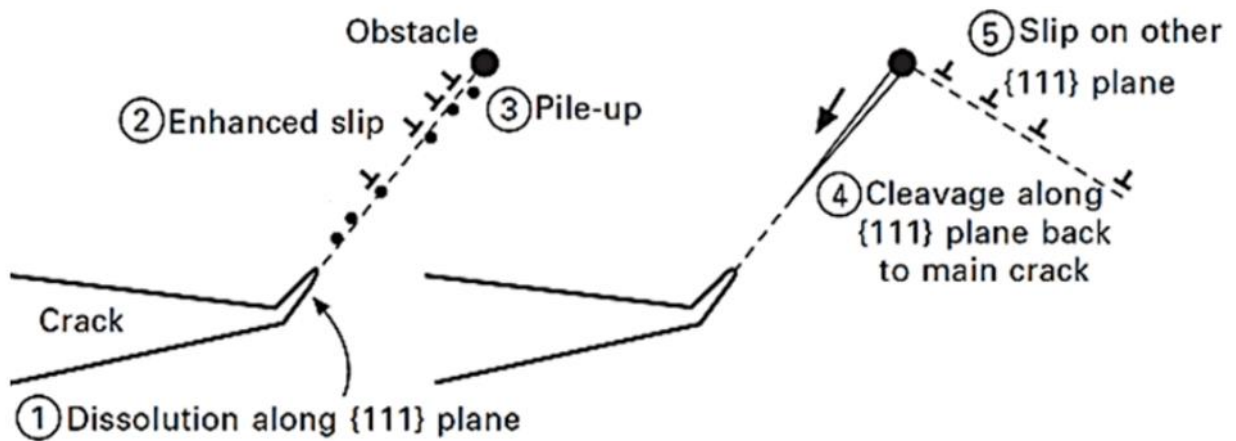


Figure 46. Mechanism of TG IASCC, with locally enhanced slip provided by dislocation channeling - Figure adapted from Reference 51

5.0 IASCC Crack Growth Rate

This section describes work sponsored by the Electric Power Research Institute. These experiments were conducted in collaboration with Mike Burke, Kai Chen, and Gary Was. This work was published in the Journal of Nuclear Materials, and the published article should be referred to for the full details of the work:

Kai Chen, Michael R. Ickes, Michael A. Burke, Gary S. Was, “The effect of potassium hydroxide primary water chemistry on the IASCC behavior of 304 stainless steel,” Available online 9 October 2021, <https://doi.org/10.1016/j.jnucmat.2021.153323> (Reference 52)

5.1 Motivation and Experimental Objectives

The objective of this experiment was to compare IASCC growth behavior in simulated PWR water with pH maintained with LiOH versus KOH. The U.S. nuclear industry is considering changing PWR primary water chemistries to use KOH in place of LiOH, as a means to ensure a stable supply chain and secure cost savings. This experiment will specifically investigate the impact of these alkali ions on the crack growth rate (CGR).

5.2 Methodology

5.2.1 Material

This experiment utilized neutron-irradiated Type 304 stainless steel. The material used to fabricate the test specimens was extracted from a baffle plate from a decommissioned Westinghouse-designed reactor. This material has been extensively characterized previously, as is documented in References 40, 53, 54, and 55.

Material remaining from these testing programs existed as two small remnant pieces of baffle plate (one example shown in Figure 47), each containing enough material to make two round compact tension (RCT) specimens. The dimensions of the specimen design are shown in Figure 48. A CNC milling machine was customized for use in the hot cell environment, and installed in one of the hot cells at Westinghouse Churchill Site (Figure 49).

Two specimens were fabricated from baffle plate piece '4D' and these were designated 4D1 and 4D2. These two specimens should be essentially identical. Per Reference 54, the piece 4D material is approximately 15 dpa. Two RCTs were similarly fabricated from baffle plate piece 1F, and these specimens were designated 1FA and 1FB. Per Reference 54, the piece 1F material is approximately 9 dpa. Despite the small size of these specimens, the radiation field of each specimen was approximately 500 millirem per hour at a distance of 30 centimeters. Because of this substantial field, heavily shielded shipping, handling, and testing capabilities was needed for the experiment.

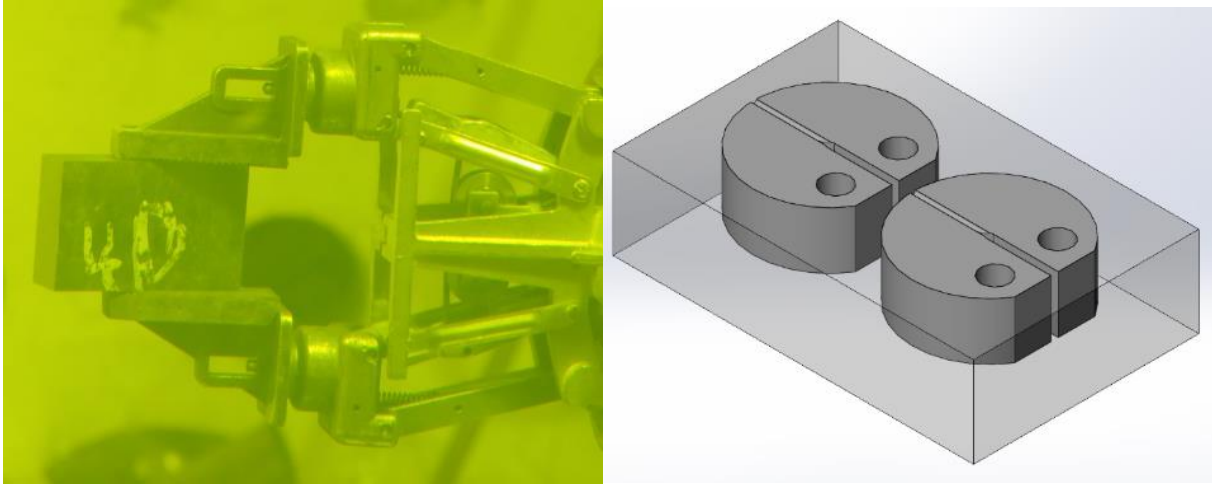


Figure 47. (Left) Piece 4D, Held by Manipulator in Westinghouse Churchill Site High Level Cell (Right) Diagram Showing RCT Placement inside Baffle-plate Piece (right). The radiological field from this piece was ~10 Rad/hour at a distance of 30 centimeters.

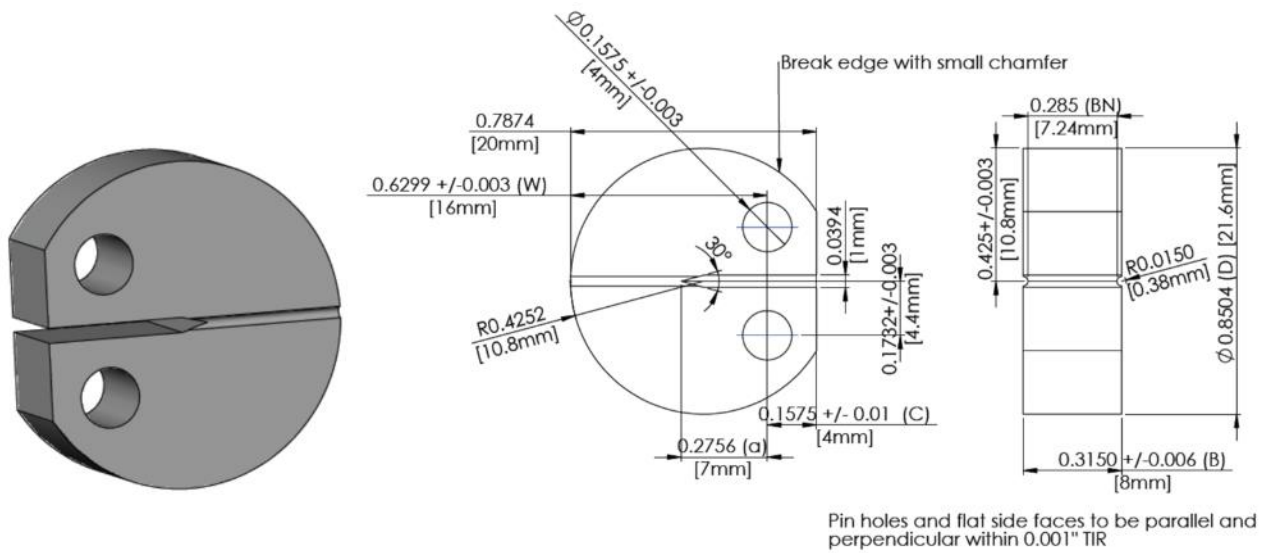


Figure 48. Dimensions of RCT specimens to be used in this project. Dimensions in inches unless otherwise noted.

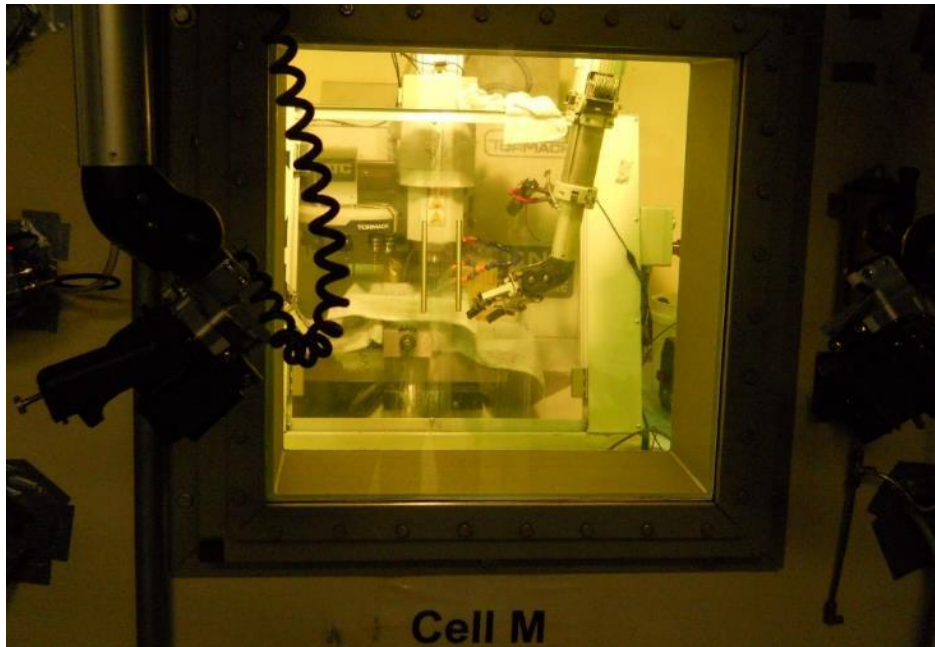


Figure 49. View of CNC Machine through Shielded Hot Cell Window.

5.2.2 Test Method

The ability to test neutron-irradiated materials in simulated PWR water requires highly specialized laboratory facilities which exist in only a few places worldwide. One such facility is the University of Michigan Irradiated Material Testing Laboratory (IMTL) which was used to conduct the IASCC CGR tests for this experiment.

The RCT specimens, weighing in total less than 100 grams, were shipped from Westinghouse Churchill Site near Pittsburgh, Pennsylvania to the University of Michigan IMTL in a lead-shielded steel cask weighing approximately 12,000 kilograms. This prevented radiological exposure of personnel handling the cask.

The IMTL hot cell was configured to host the autoclave system which would contain the RCT specimen. The controls for this system were outside the hot cell as shown in Figure 50, with a flow diagram for the autoclave system shown in Figure 51. One RCT specimen at a time was

installed in the autoclave loading fixtures. Wires were spot welded to the RCT specimen in the IMTL hot cell to allow in-situ monitoring of crack length by the direct current potential drop (DCPD) method. In the DCPD method, current is passed through the specimen allowing the resistance of the specimen to be measured. As the crack grows, the resistance of the specimen increases, increasing the potential drop across the specimen which can be measured and related to crack length. A diagram illustrating the DCPD method is shown in Figure 52.

After the autoclave system was filled with water it was then brought to controlled water chemistry conditions and heated to temperature. The target conditions were 340°C with a pH_T (at 300 °C) between 6.95 and 7.30 depending on whether Beginning of Cycle (BOC) or End of Cycle (EOC) conditions were being studied. The water chemistries used in the CGR tests are given in Table 6. Fatigue loading was used to begin a crack. The cycling frequency was gradually reduced over a 24 hour period until a constant load condition was introduced.

Table 6. Water chemistries used in CGR tests

Condition	B (ppm)	Li or K (ppm)	pH @ 300°C
BOC	1000	2.00 (Li)	6.95
		11.27 (K)	
EOC	200	1.28 (Li)	7.3
		7.21 (K)	

After a satisfactory amount of stable crack growth was measured, the water chemistry was changed between LiOH and KOH (or vice versa in the case of specimen 1FA). Once an amount of stable crack growth was measured under the new water chemistry, it was then further reversed. The test matrix for the specimens is shown in Table 7.

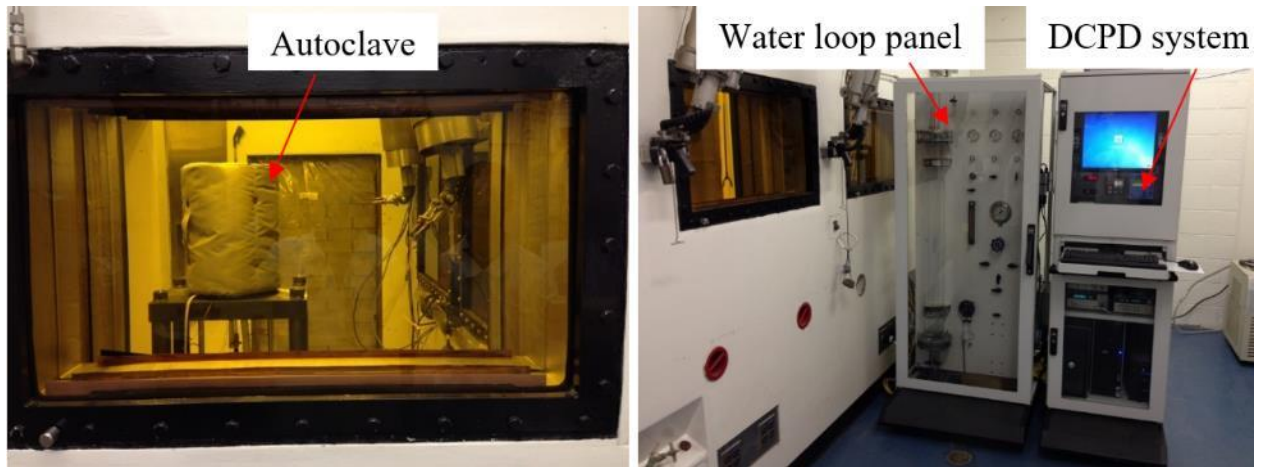


Figure 50. Autoclave control station at the University of Michigan IMTL

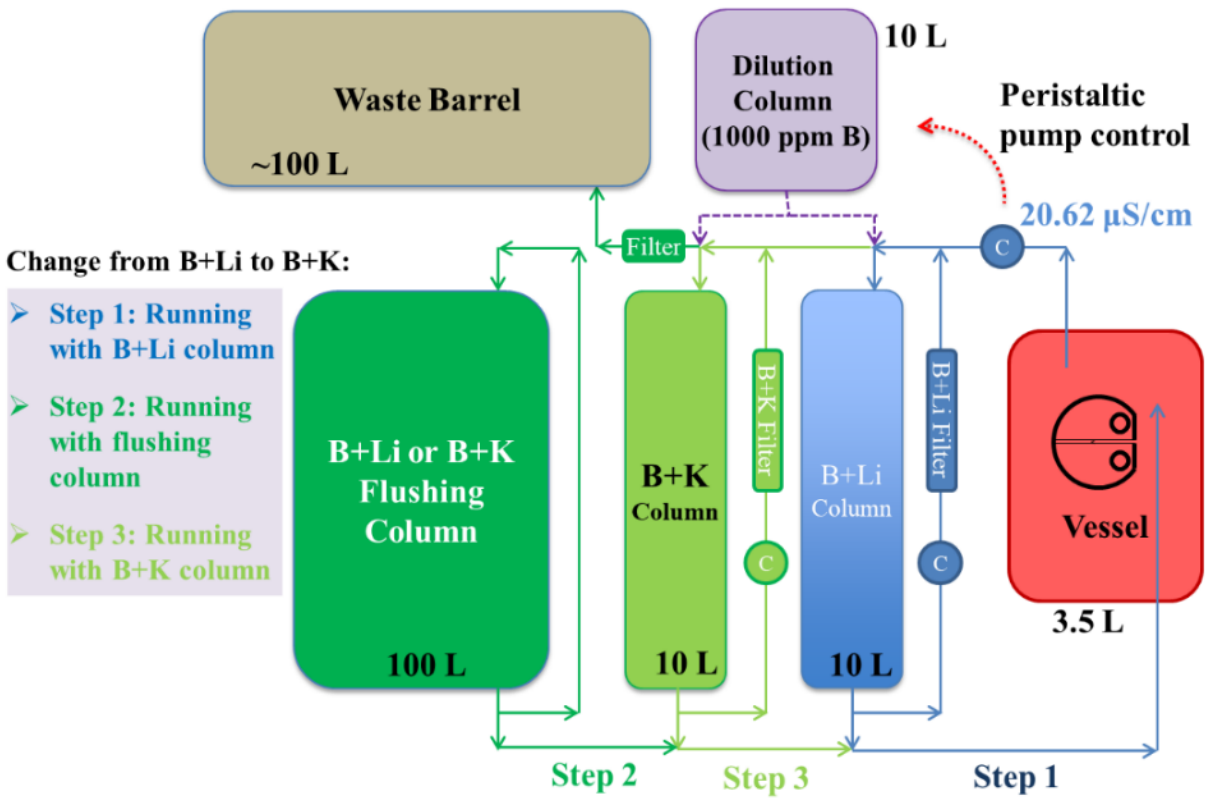


Figure 51. Flow diagram of CGR test autoclave loop

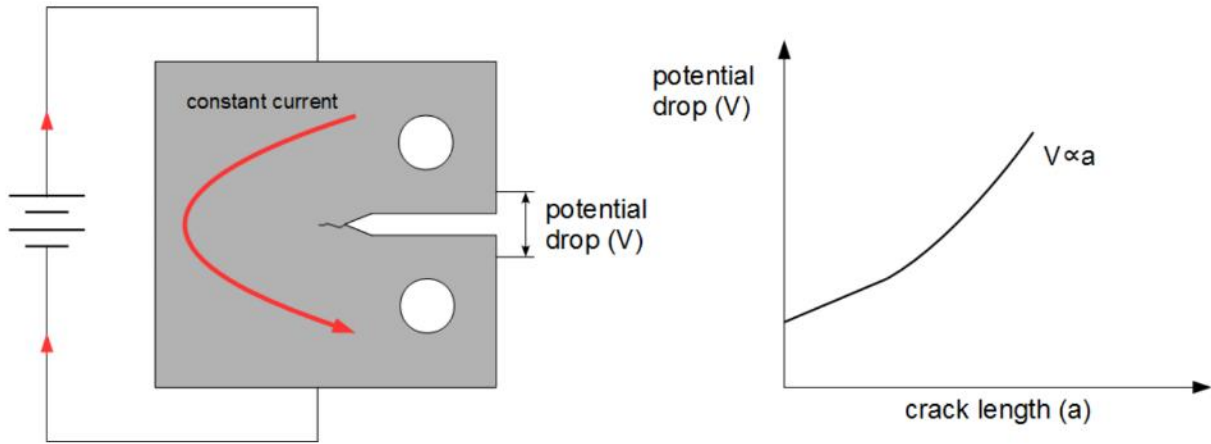


Figure 52. Application of current in the direct current potential drop method, after Reference 56.

Table 7. Text Matrix for CGR Experiment

Specimen	Radiation Dose (dpa)	Starting Environment	Investigated K values (MPa \sqrt{m})
4D2	15	LiOH	18, 14
4D1	15	LiOH	18, 14
1FB	9	LiOH	18
1FA	9	KOH	18

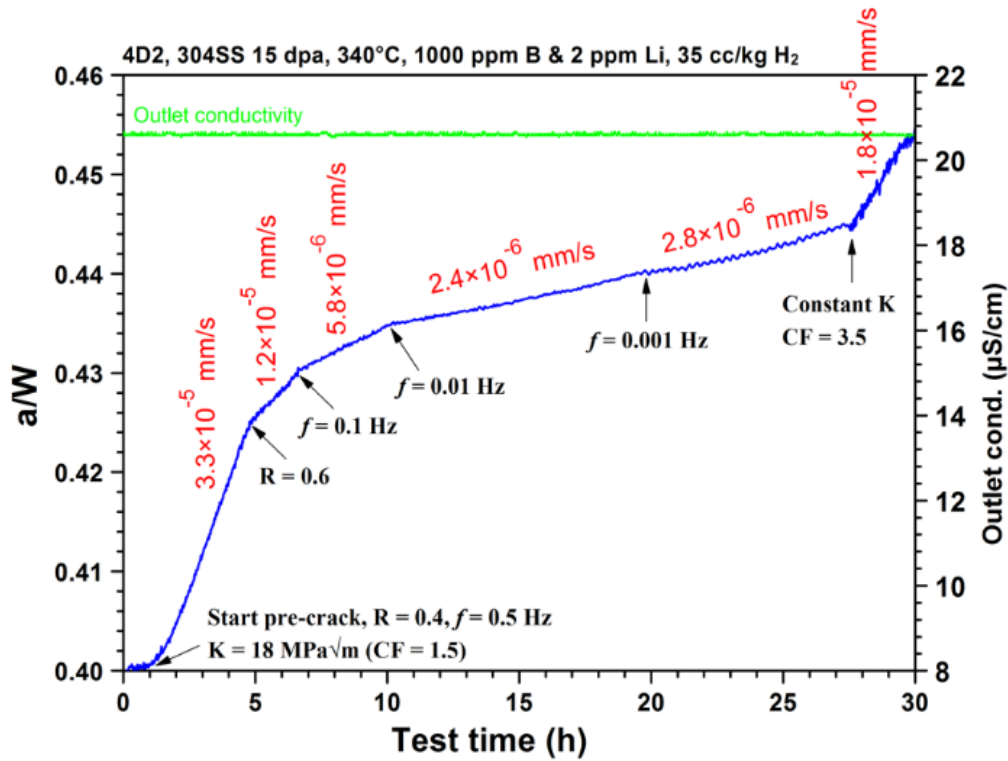
5.3 Results

Four CGR tests were completed using material fabricated from the neutron-irradiated Type 304 stainless steel. The crack growth rates measured in this experiment at $18 \text{ MPa}\sqrt{\text{m}}$ were relatively fast compared to the size of the specimen, and so these tests were only hundreds of hours long instead of the expected thousands of hours. Crack initiation for each specimen occurred within a few hours, which is rapid for a stainless steel, indicating this material had a high susceptibility to cracking under the tested conditions.

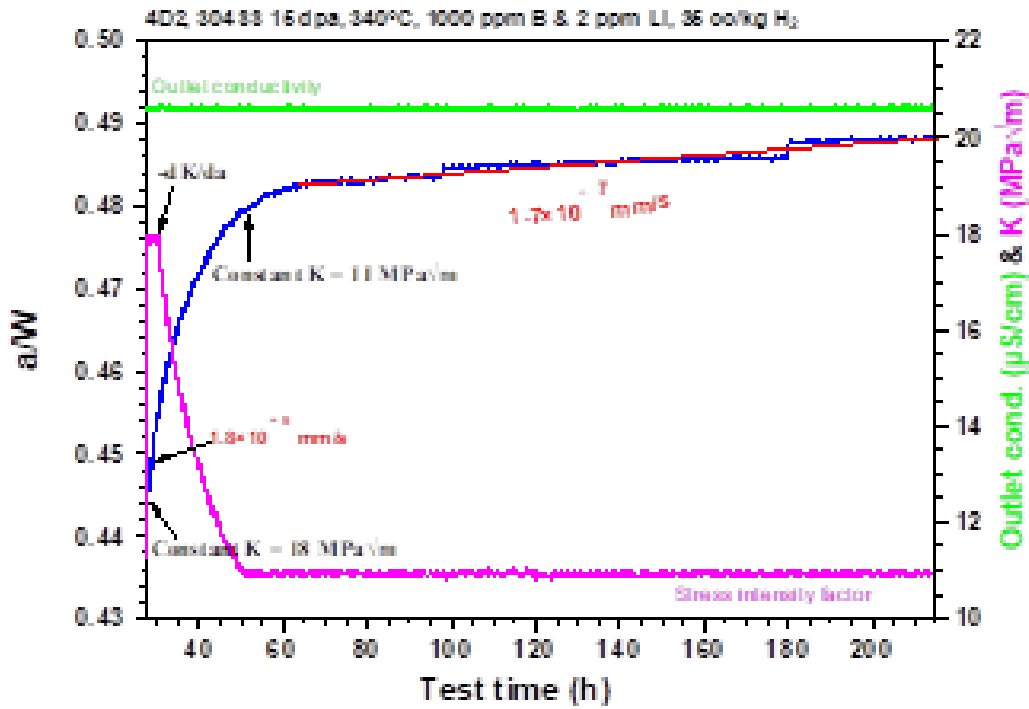
5.3.1 CGR Testing of 4D2

The CGR test results for specimen 4D2 are given in Figure 53. On the Y axis of this figure, 'a' represents crack length, while 'W' indicates the original length of the specimen, and so 'a/W' represents the normalized crack length (see Figure 48 for starting specimen dimensions). The blue line represents the crack length as a function of time, and in Figure 53 (a) the various crack growth rates are indicated in mm/s for the pre-cracking stages of the CGR test. The reduction in frequency f is indicated on the plots, and then fatigue cycling is stopped and the crack is allowed to grow at a constant stress intensity K. At this point, the crack growth rate increases. This is because the average stress intensity at constant load is higher than during the variable load present during fatigue pre-cracking. In Figure 53 (b) it can be seen that at the initial constant K value of $18 \text{ MPa}\sqrt{\text{m}}$ the crack growth rate was quite high, and the usable length of the specimen would have been consumed before water chemistry changes could be conducted as planned. The applied stress intensity (pink line) was then lowered to $11 \text{ MPa}\sqrt{\text{m}}$ and the crack growth rate stabilized at $1.7 \times 10^{-7} \text{ mm/s}$. The crack seemed to have stalled and so as can be seen in Figure 53 (c) by the step

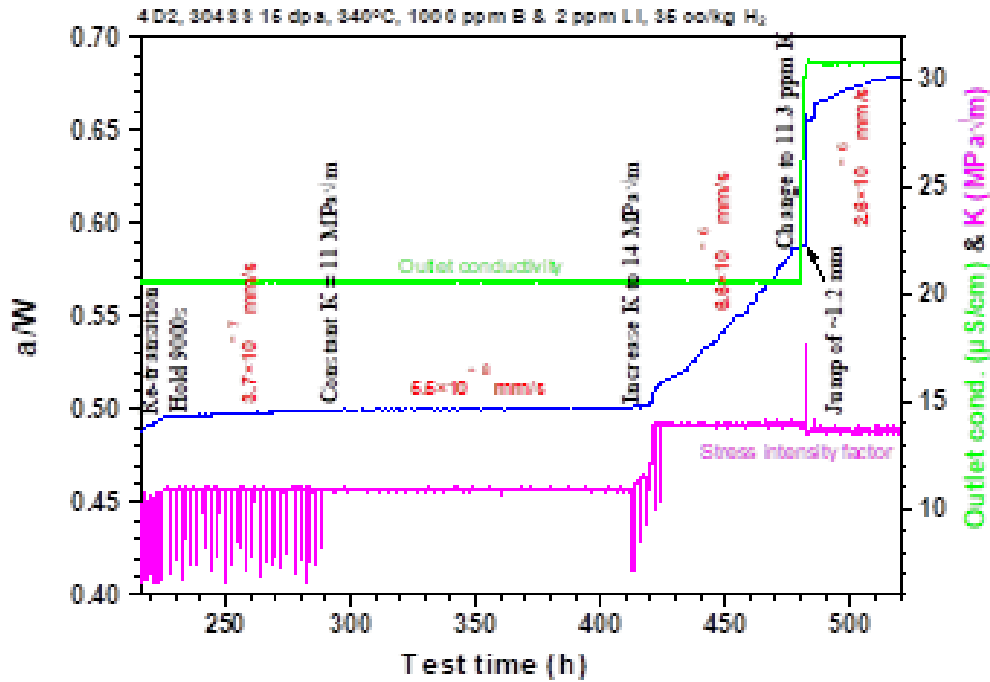
changes in the stress intensity factor that cycling was introduced to attempt to restore crack growth. An increase in K to $14 \text{ MPa}\sqrt{\text{m}}$ resulted in increased crack growth rates; after this change in stress intensity factor, the first water chemistry change was attempted. A few hours after this water chemistry change, an apparent jump in the crack length of 1.2 mm occurred. The crack length as recorded by DCPD underwent two apparent ‘jumps’ as shown in (c) and (d) of Figure 53, which were relatively close to changes in water chemistry when examining the plots. It should be noted however that there were still several hours between the chemistry change and the apparent crack jump.



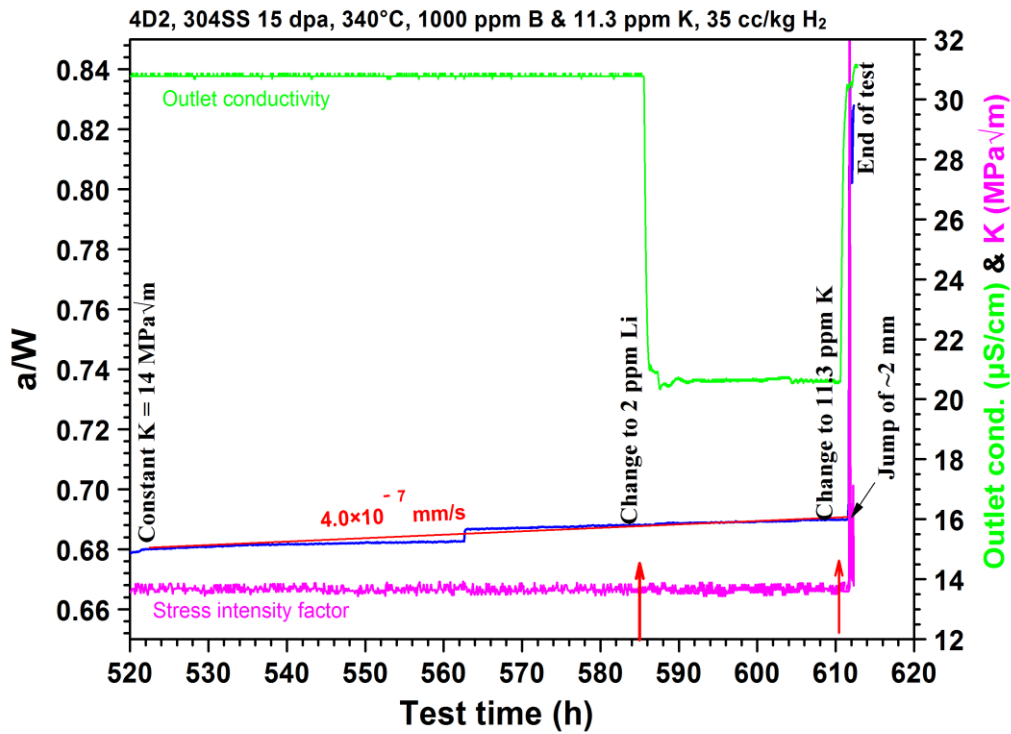
(a)



(b)



(c)



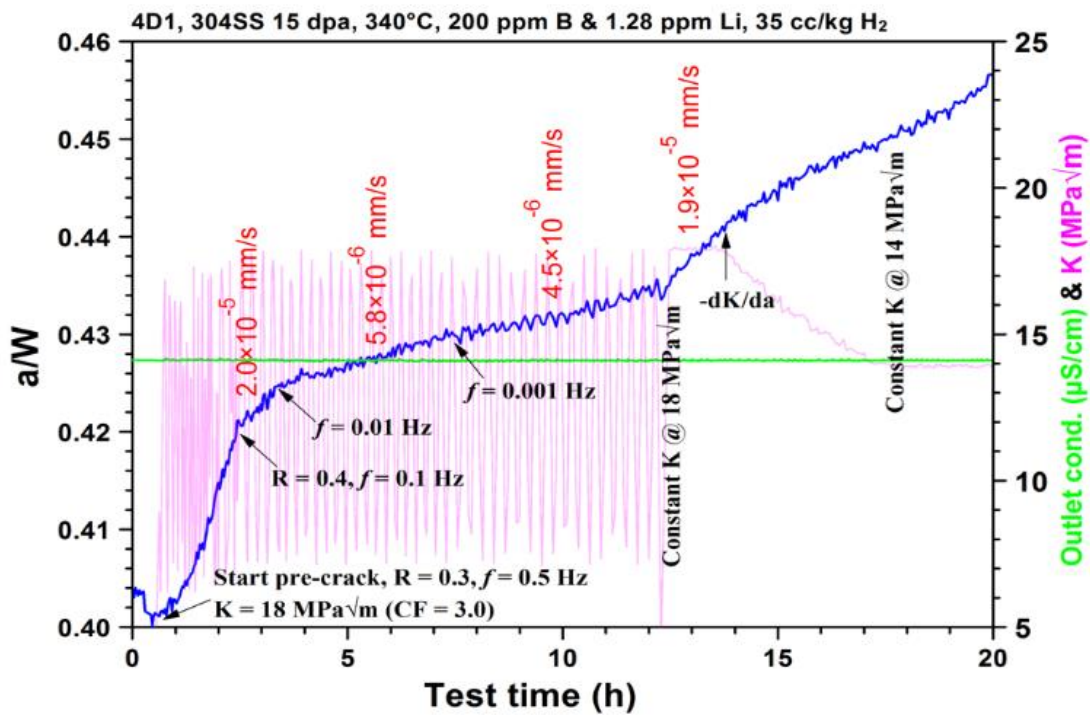
(d)

Figure 53. Crack length, outlet conductivity and K for specimen 4D2 in 340°C hydrogenated water (a) during pre-cracking stage, (b) after decreasing K , (c) during the water chemistry switch from Li to K, (d) during the water chemistry switch from K to Li and back to K.

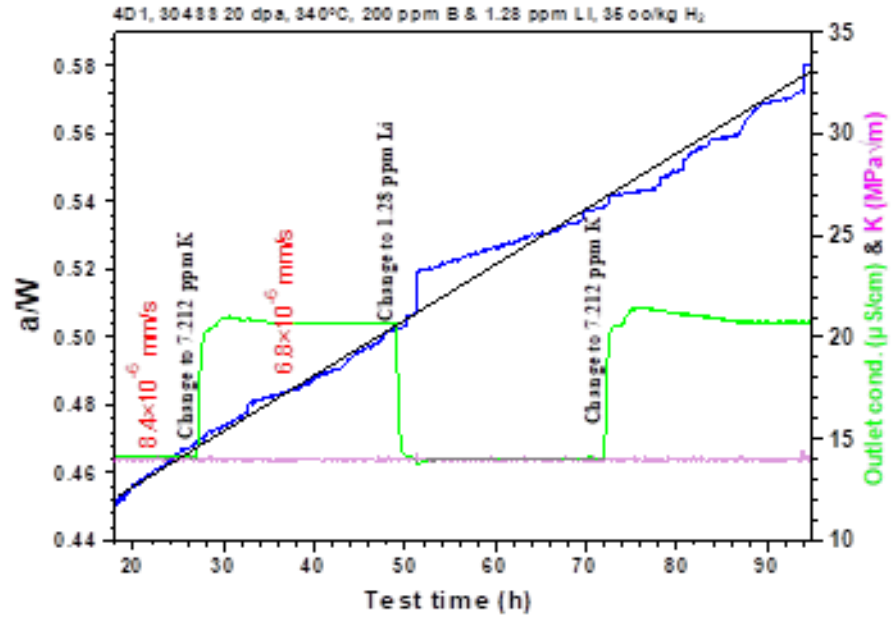
5.3.2 CGR Testing of 4D1

The CGR test results are shown in Figure 54. In Figure 54 (a), again, the pre-cracking stage is distinguished by the rapidly changing stress intensity factor utilized in the initial ~12 hours of the test. In Figure 54 (b), stable crack growth rates were established, and, three water chemistry changes were conducted without incident. During this test, several water chemistry changes were conducted without apparent jumps in crack length. However, such jumps were observed during

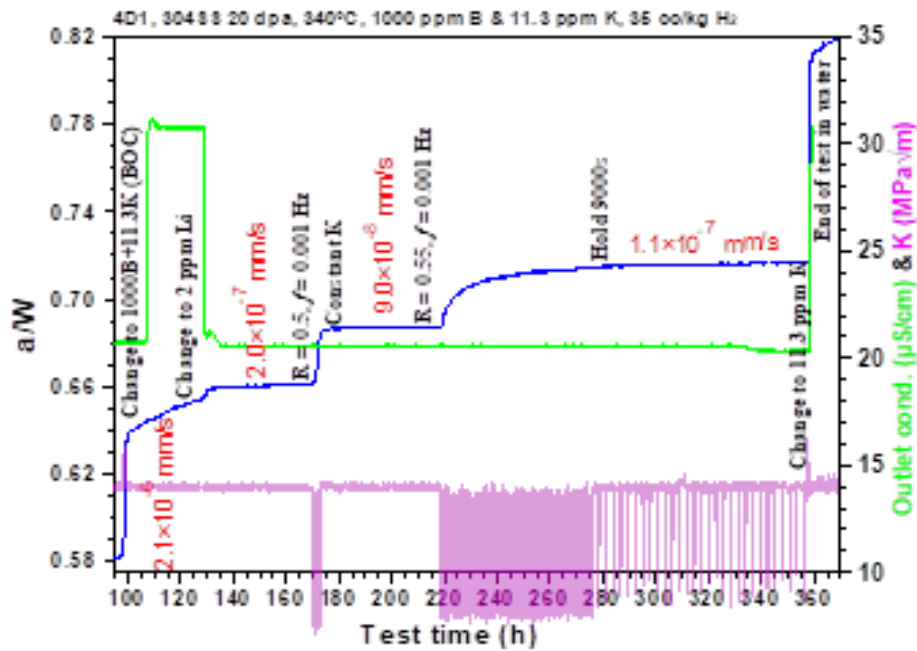
other parts of the CGR test and the test was ultimately terminated by one. Figure 54 (c) an apparent crack length jump occurred. Two water chemistry changes were conducted following this. About 30 hours later, a second apparent crack length jump occurred. After this, the crack growth appeared to stall. Cycling was introduced in an attempt to restore crack growth. A change in water chemistry was conducted. A crack length jump occurred shortly afterwards which terminated the test.



(a)



(b)



(c)

Figure 54. Crack length, outlet conductivity and K of 4D1 specimen in 340°C hydrogenated water (a) during pre-cracking stage, (b) during the water chemistry switch of Li – K – Li – K under EOC condition, (c) during the water chemistry switch from K to Li and back to K under BOC condition.

5.3.3 Fractographic Examination of 4D1 and 4D2

After the completion of CGR testing specimens 4D1 and 4D2 were cooled to room temperature, and fatigue cracked in air to fully fracture the CGR specimen and allow for fractography. The fracture surfaces of both specimens was entirely intergranular. Typically it would be expected that transgranular cracking would be observed during fatigue portions of the test at the beginning, and either transgranular cracking or ductile tearing during the post-test fracture in room temperature air.

The fractographs for specimen 4D2 are given in (Figure 55). A notable feature of the fracture surface was the appearance of lifted-up areas of the crack surface. On the surface of some of these lifted up areas are regions without any apparent oxide deposits on the surface (Figure 56). This would suggest that this region is a ligament which was initially bypassed by the primary fracture and remained intact until a later portion of the test or even until the final fracture of the specimen in room temperature air. Generally similar features were observed in specimen 4D1. The overall features of the two specimens are summarized in Figure 57.

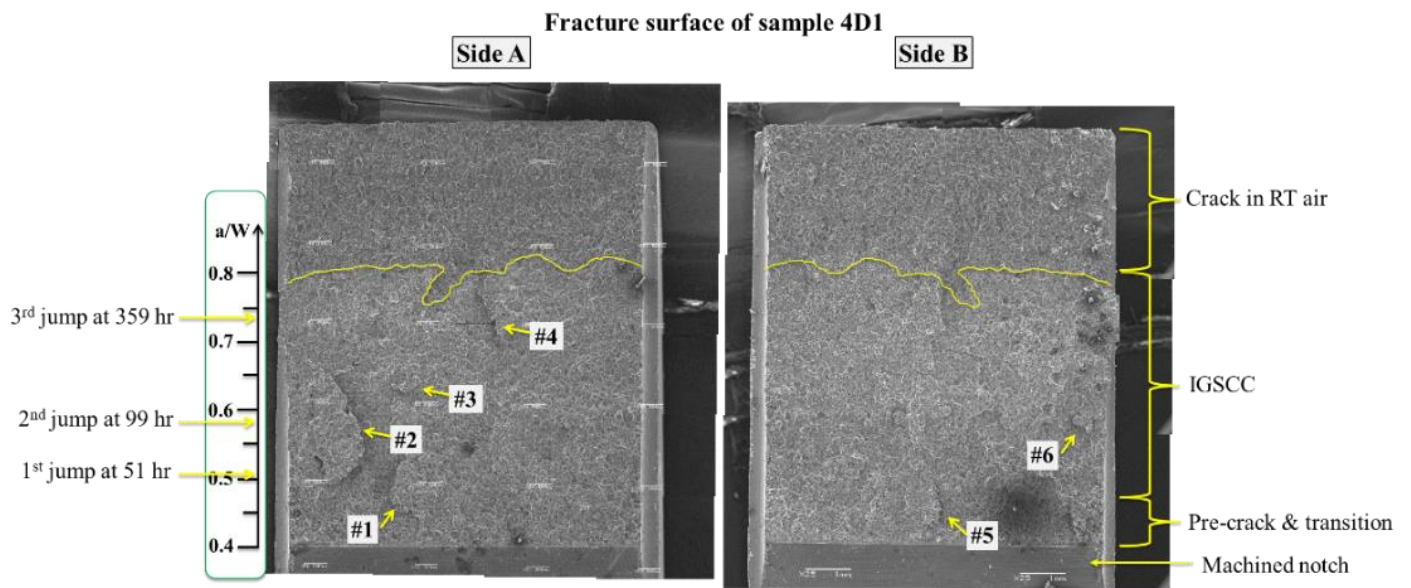
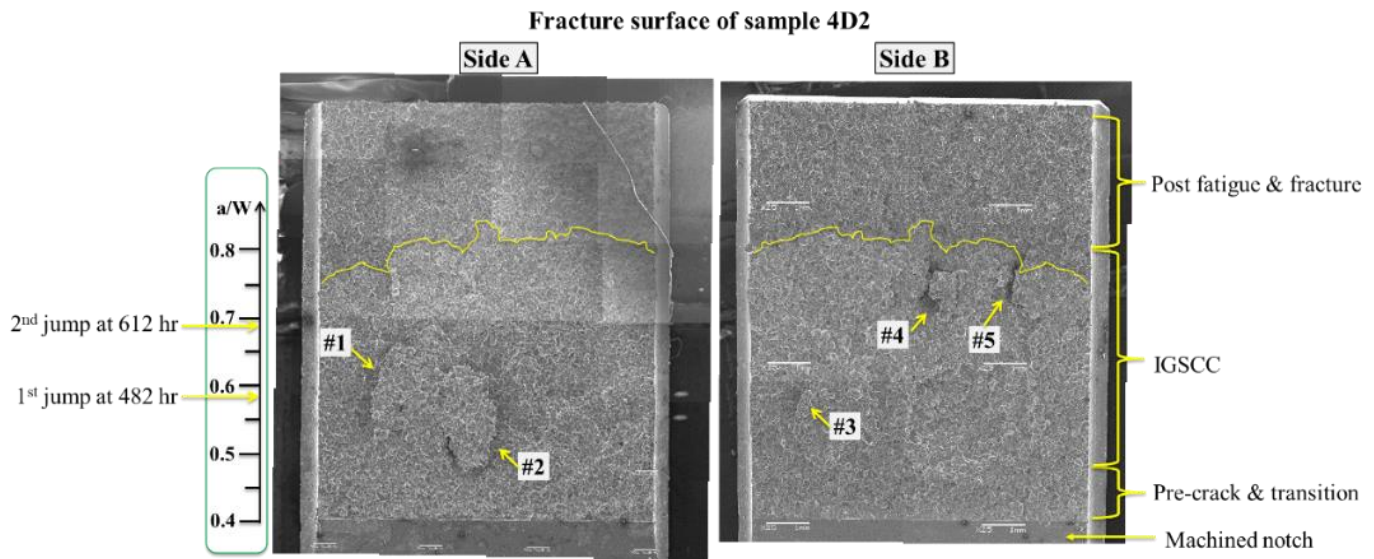
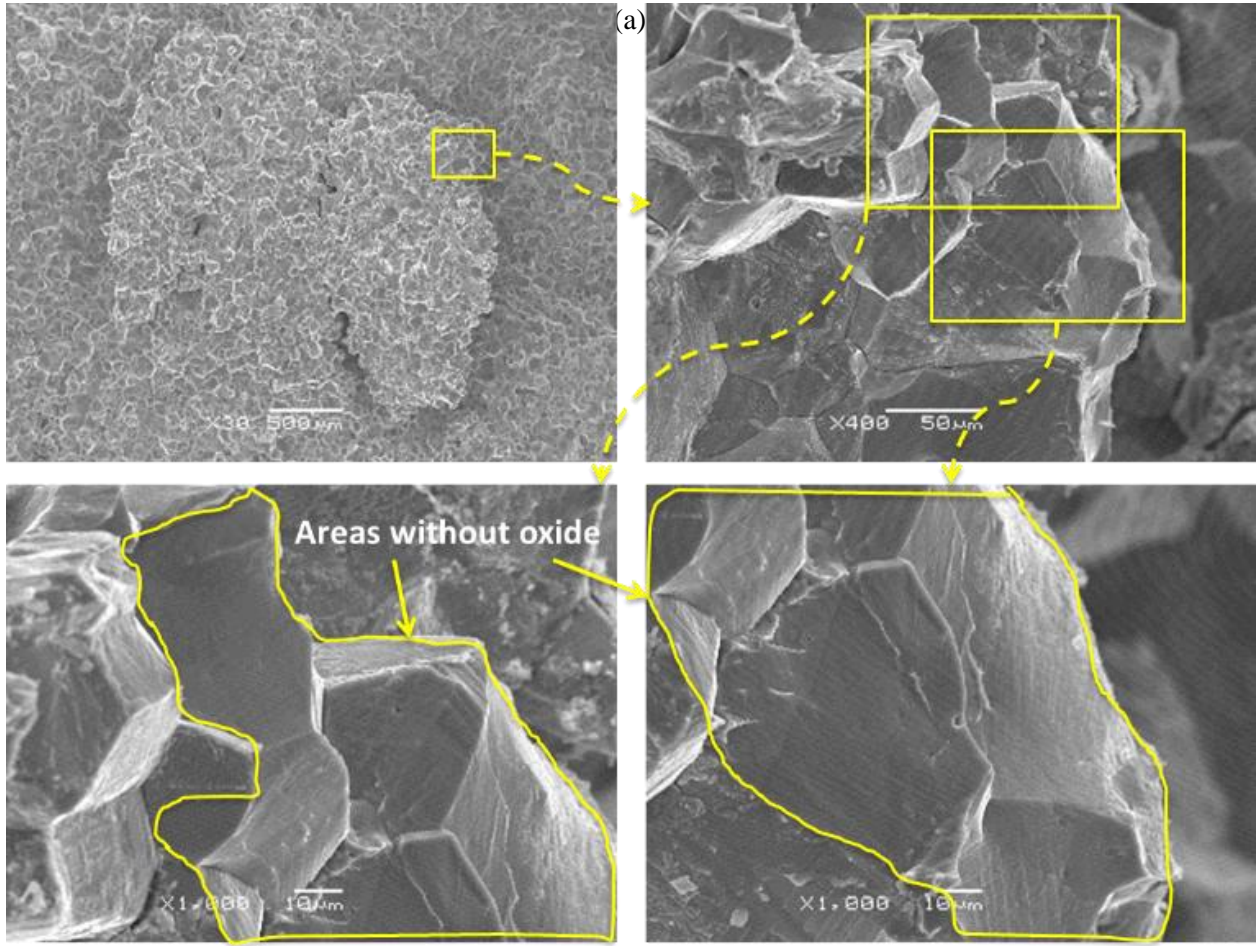
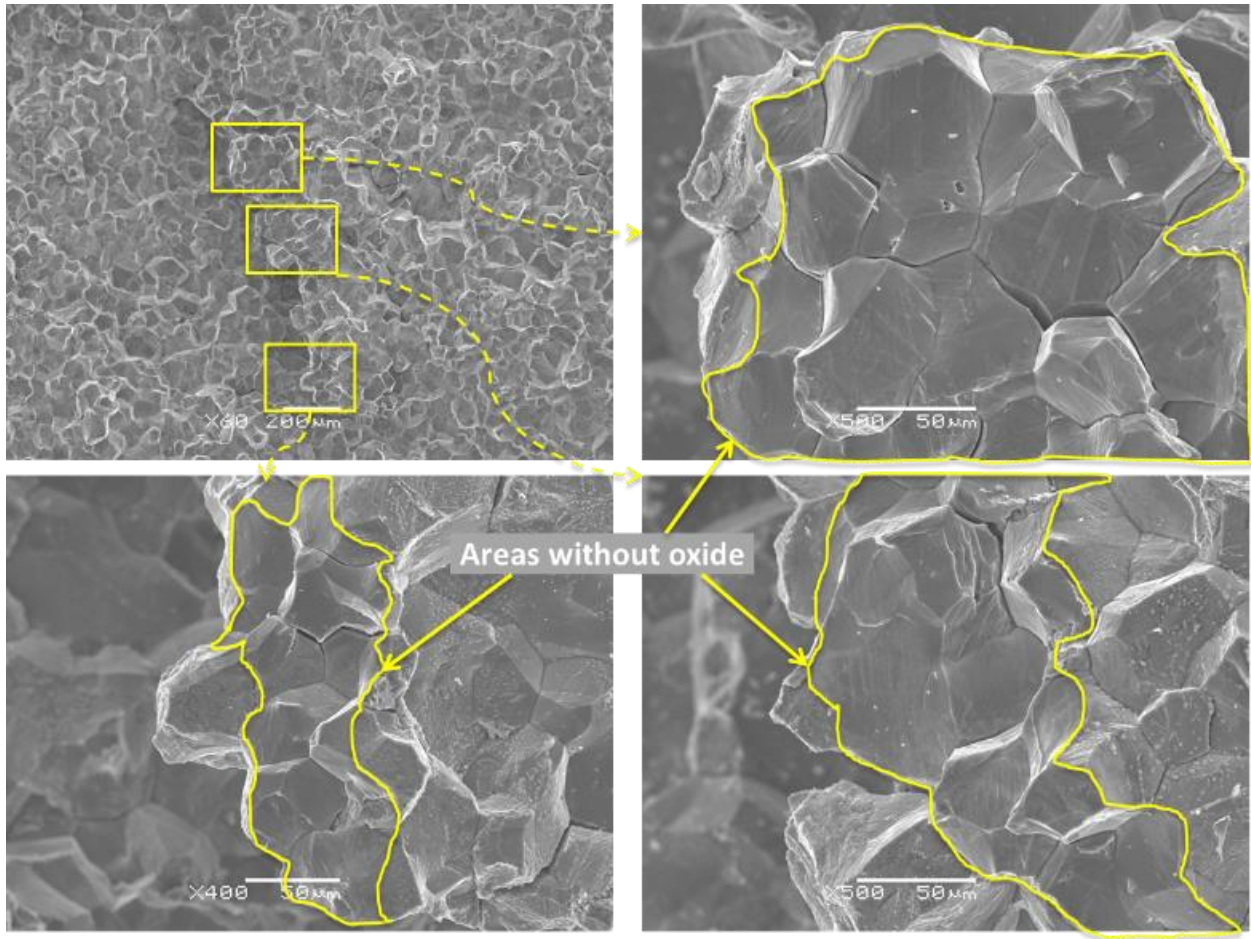


Figure 55. Fracture surface with marked ligaments on both sides of (a) specimen 4D2, (b) specimen 4D1.

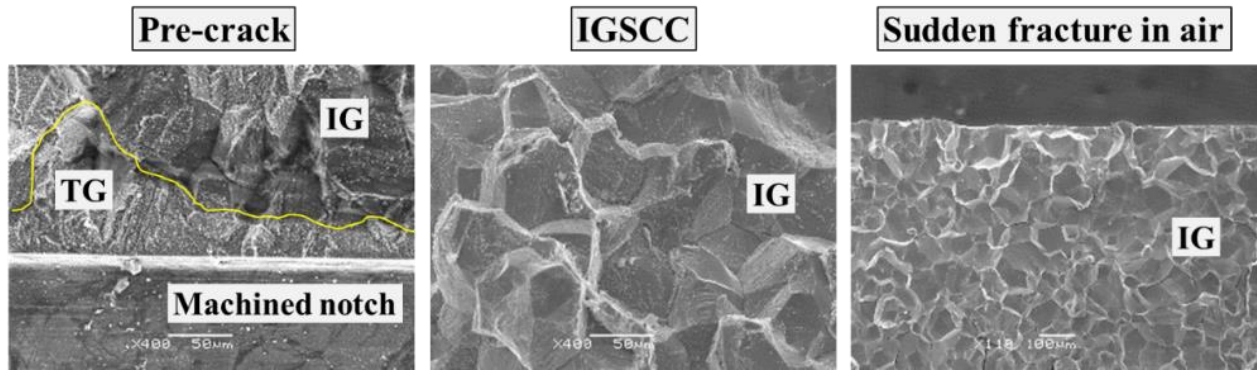


(a)

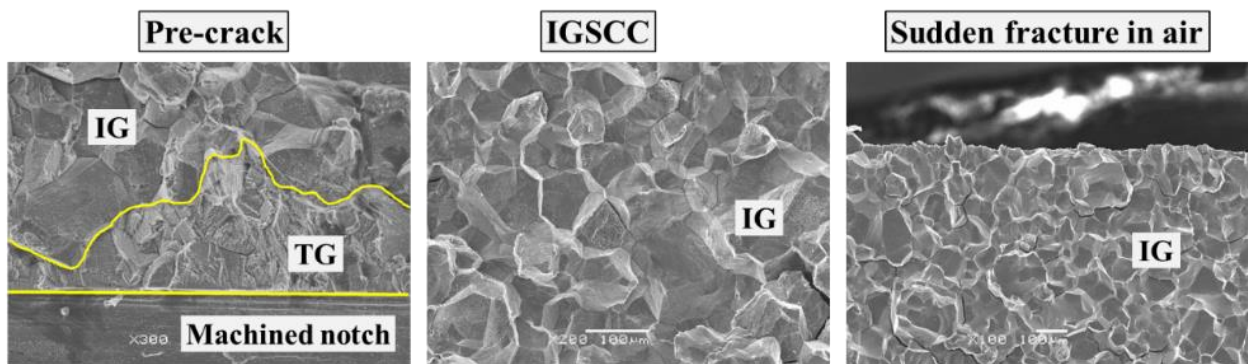


(b)

Figure 56. (a) Ligament #2 on the fracture surface of 4D2, (b) ligament #4 on the fracture surface of 4D1 (crack grew from bottom to top).



(a)

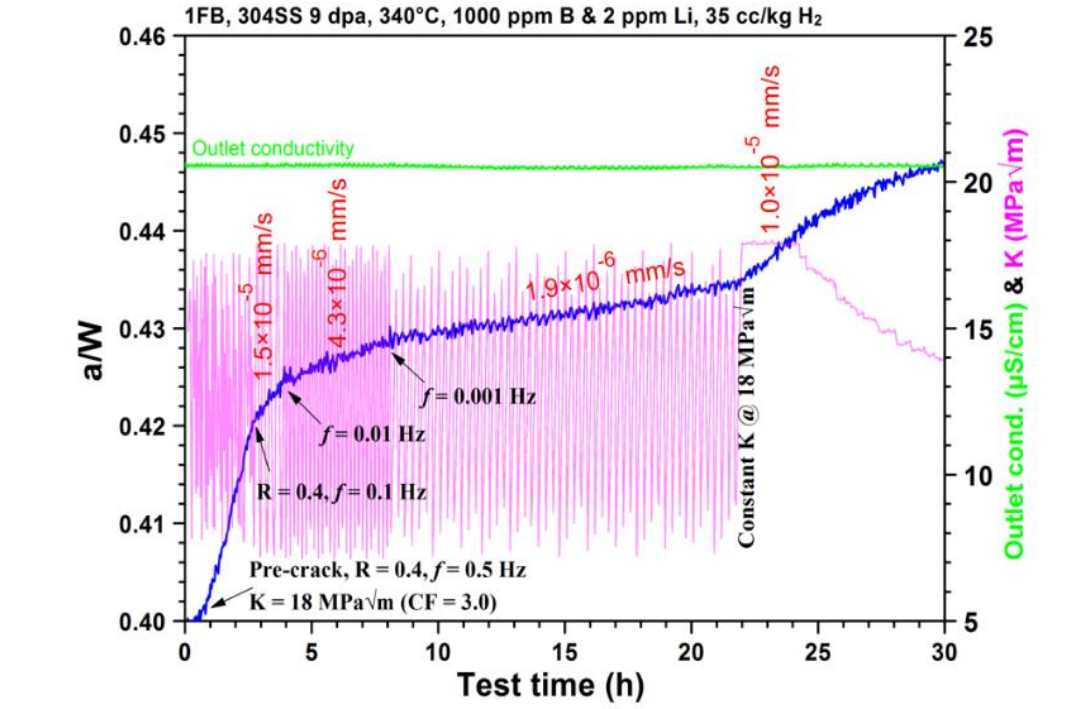


(b)

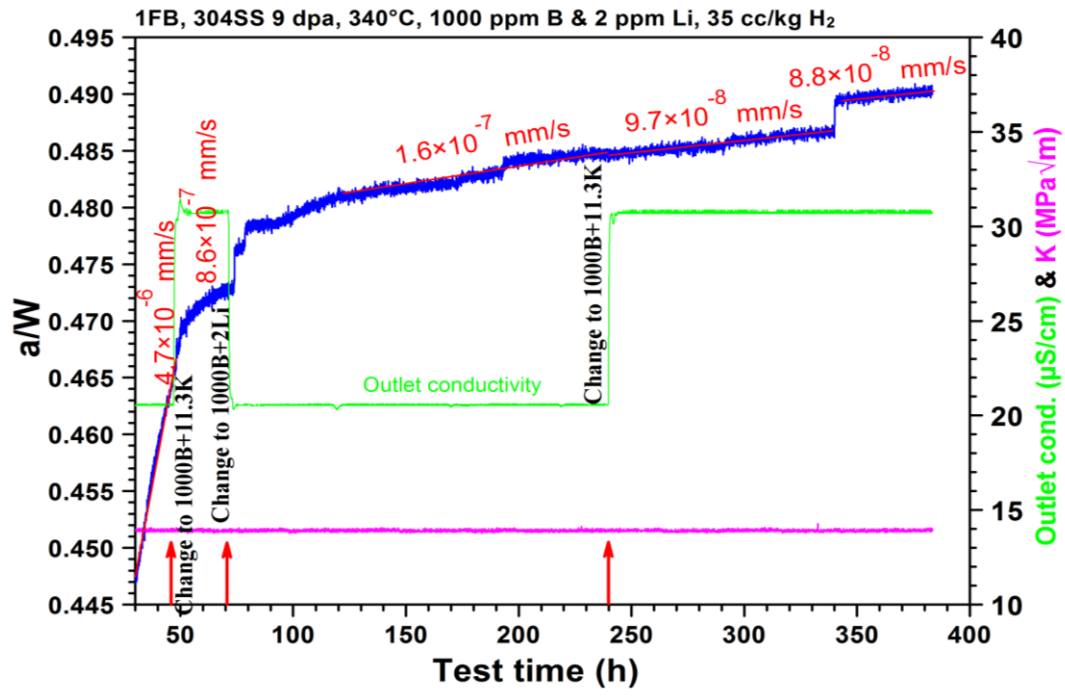
Figure 57. Pre-crack, IGSCC and sudden fracture in air regimes on the fracture surface of (a) 4D2, (b) 4D1 (crack grew from bottom to top).

5.3.4 CGR Testing of 1FB

After the testing experience with specimens 4D1 and 4D2, it was decided for specimens 1FB and 1FA to grow shorter cracks, where CGR data collected had been repeatable, and to keep the specimens intact after the test to investigate the crack structure by metallography in a future program (outside the scope of this thesis). The CGR test results for specimen 1FB are given in Figure 58. In this test, three water chemistry changes were conducted with no effect on CGR.



(a)

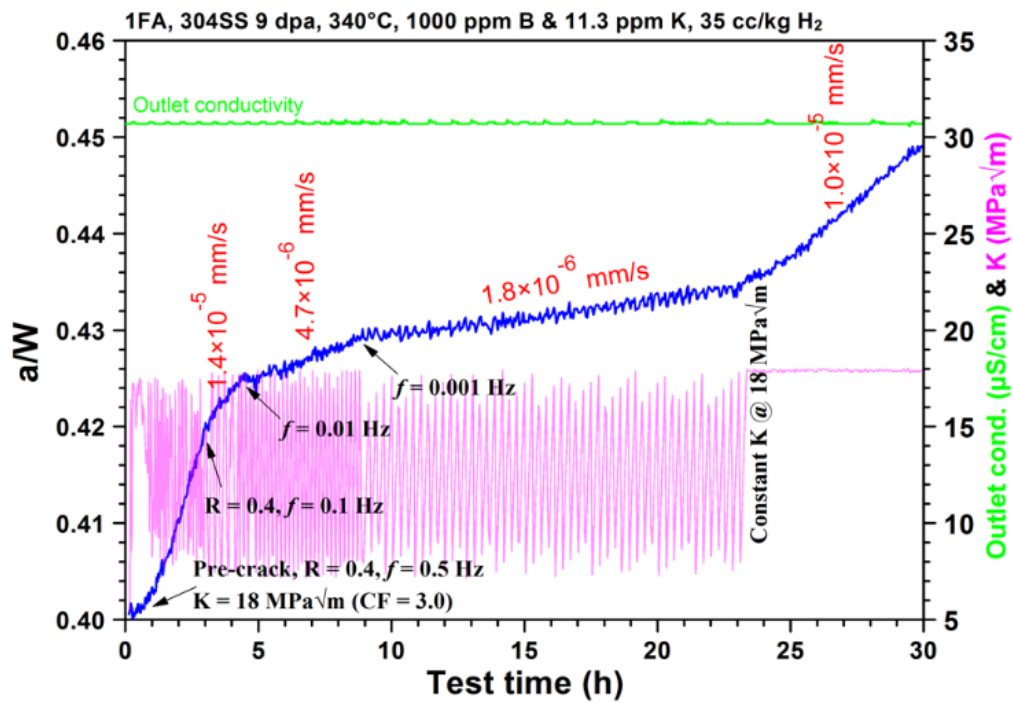


(b)

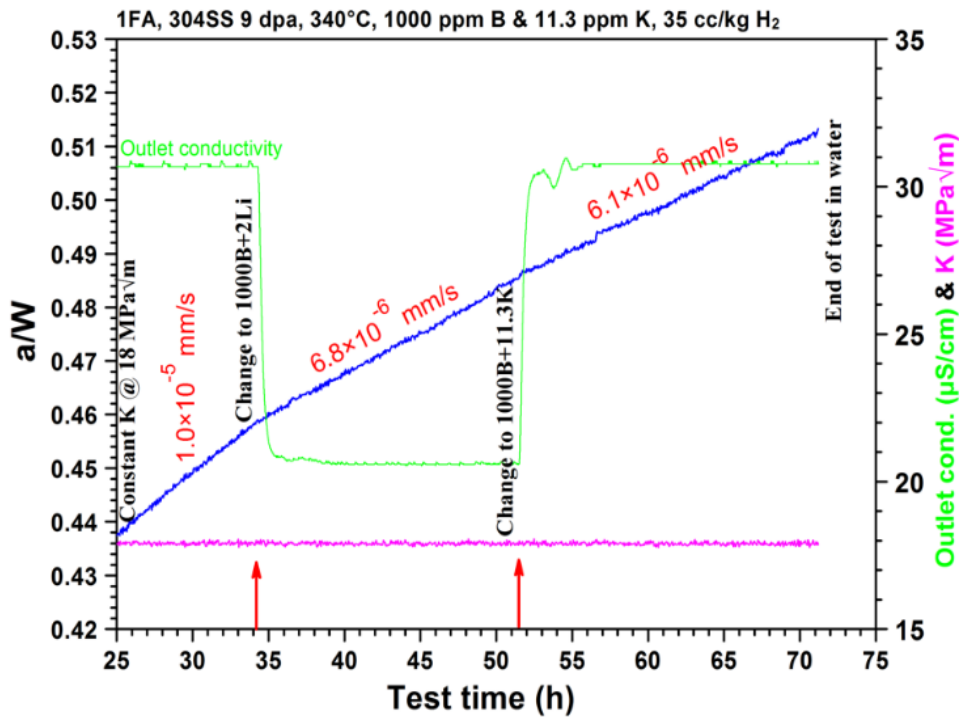
Figure 58. Crack length, outlet conductivity and K vs. test time of 1FB in 340°C hydrogenated water during (a) pre-cracking stage, (b) the water chemistry switch of Li – K – Li – K under BOC condition.

5.3.5 CGR Testing of 1FA

The CGR test results for specimen 1FA are given in Figure 59. Unlike previous tests which were all started using LiOH, this test was started using KOH water chemistry, specifically to investigate if this change would have any effects on the crack initiation or pre-cracking phases of the test. Two water chemistry changes were conducted during this test with no effect on crack growth rate. Two water chemistry changes were conducted during this test with no effect on crack growth rate.



(a)



(b)

Figure 59. Crack length, outlet conductivity and K vs. test time of 1FA in 340°C hydrogenated water during (a) pre-cracking stage, (b) the water chemistry switch of K – Li – K under BOC condition.

5.4 Discussion

During the post-test fractography of specimens 4D1 and 4D2, it was noticed that the fatigue regions of the specimen and the regions fractured at room temperature were intergranular. This deviates from the transgranular behavior that would typically be expected. This suggests that these materials may have substantial susceptibility to intergranular cracking. It also raises the question of whether IASCC was being observed in the specimen, if intergranular cracking was also occurring at ambient conditions. Fracture toughness tests conducted on the same materials at

similar temperatures in air did show ductile tearing, but the specimens also underwent intergranular cracking when being precracked by fatigue cycling at room temperature (Reference 53). Based on this and the extensive secondary cracking observed in the CGR portions of the test, it can be concluded that crack propagation by IASCC was indeed taking place.

The observation of ligaments on the fracture surface of 4D1 and 4D2 that were apparently intact longer than the surrounding cracked regions is a possible explanation of the apparent jumps in crack length. The DCPD system measures crack length by electrical resistance of the specimen, and so an intact ligament provides a conductive path that effectively causes a ‘short circuit’ in the DCPD measurement. When such a ligament fails later during the test, there is a step change in the resistivity resulting in an apparent crack jump. This explanation is supported by the work of Stigenberg, who studied the influence of crack branching on DCPD measurements (Reference 57).

Post-test fractography also confirmed that the final actual crack lengths correlated to the values measured by DCPD by within 15% of the crack length, which is satisfactory for IASCC CGR testing.

Crack growth rates at longer crack lengths were not found to be repeatable, and were affected to a greater extent by apparent crack length jumps and stalling cracks. This is likely due to the development of extensive crack branching. CGRs measured earlier in the tests had higher repeatability, and so these data were considered to be representative, while data from later in the tests of 4D1 and 4D2, where crack branching led to ligament formation and DCPD error, are not considered representative. The representative CGRs (that is, CGRs measured during portions of the test considered to be repeatable and representative of the material) are given in Table 8 along with the conditions wherein those CGRs were measured. CGRs measured under the same conditions show variation among different segments by as much as a factor of two. So, there would

need to be a difference greater than this between CGRs in KOH versus LiOH for any difference in CGRs between the environments to be considered significant. Comparing the CGRs in KOH to LiOH, no such difference is observed. Combining this with the observation of no changes during water chemistry changes during the testing allows it to be concluded that, for the conditions studied in this experiment, there is no significant impact of changing water chemistry from LiOH to KOH (or vice versa) on IASCC CGRs. There also seems to be no significant impact of EOC versus BOC conditions (changing boron content). There is of course a first-order correlation between the CGR and the stress intensity factor, K .

The lack of an effect of changing alkali ions on the CGR goes against the hypothesis put forth in subsection 5.1, expecting LiOH to create a more aggressive environment and enhancing cracking. It could be the case that these alkali ions do not participate in the fracture process. It is also possible that the effect is either below the limit of detection of these experiments (a factor of two) due to the inherent scatter in SCC CGR data, or, require longer experimental times for such a difference to develop. The length of these experiments was only hundreds of hours with testing conducted at high stress conditions intended to accelerate cracking, whereas power plant components operate for decades and would be exposed to such environmental conditions for orders of magnitude more time.

Table 8. Summary of the representative CGR results, and the environments they were measured in.

Specimen ID	Radiation damage	Li or K water chemistry	BOC or EOC condition	<i>K</i> (MPaVm)	CGR (mm/s)
4D2	15 dpa	LiOH	BOC	18	1.8×10^{-5}
	15 dpa	LiOH	BOC	14	6.6×10^{-6}
4D1	15 dpa	LiOH	EOC	18	1.9×10^{-5}
	15 dpa	LiOH	EOC	14	8.4×10^{-6}
	15 dpa	KOH	EOC	14	6.8×10^{-6}
	15 dpa	LiOH	EOC	14	5.4×10^{-6}
	15 dpa	KOH	EOC	14	7.7×10^{-6}
	15 dpa	KOH	EOC	14	7.7×10^{-6}
1FB	9 dpa	LiOH	BOC	18	1.0×10^{-5}
1FA	9 dpa	KOH	BOC	18	1.0×10^{-5}
	9 dpa	LiOH	BOC	18	6.8×10^{-6}
	9 dpa	KOH	BOC	18	6.1×10^{-6}
	9 dpa	KOH	BOC	18	6.1×10^{-6}

6.0 IASCC Crack Initiation Experiments

This project is supported by an award from the DOE-NE's Nuclear Science User Facility (NSUF) program under award 19-16567. While much of the testing work has been completed, there is still some scope remaining. Upon completion of the entire workscope, the results will be published in peer reviewed literature.

This work is being conducted with the collaboration of Lijin Dong, Gary Was, Abdullah Alsinglawi, and Kai Sun at the University of Michigan. Lucille Giannuzzi and Arash Parsi assisted with the generation of the FIB liftouts at Westinghouse Churchill Site.

6.1 Motivation and Experimental Objectives

The objective of this experiment is to investigate the IASCC initiation behavior of Type 347 stainless steel in lithium hydroxide and potassium hydroxide water chemistries across a range of irradiation damage and stress levels. One result of this objective will provide data supporting improved predictive capabilities of IASCC failures by assessing the radiation dose dependence of IASCC initiation. In power plant components like the baffle-former bolts examined in Section 4.0 the crack initiation step of IASCC is the rate limiting step, taking much longer than crack propagation to failure. The results of this study will also be directly beneficial to the U.S. nuclear industry by providing an understanding of IASCC susceptibility in potassium hydroxide water chemistry, which may provide cost savings and more secure supply chains to nuclear power plants. These objectives are consistent with the DOE's NE mission, which includes efforts to develop

technologies and other solutions that can improve the reliability, sustain the safety, and extend the life of current reactors.

6.2 Methodology

This experiment accomplished the research objectives by creating two sets of nominally equivalent sub-sized IASCC initiation test specimens from PWR-irradiated Type 347 baffle-former bolts, mechanically testing the specimens in simulated PWR conditions (with either LiOH and KOH additions), and conducting examinations of the specimens to determine IASCC initiation behavior and microstructural factors influencing this behavior. The use of Type 347 material in this study is important because most of the available data on IASCC initiation are based on cold-worked Type 316 from flux thimble tubes, which have not been observed to fail by IASCC during plant operation despite reaching high radiation damage levels. Specimens were fabricated at the hot cell facility at Westinghouse Churchill Site, while IASCC initiation testing was conducted at the University of Michigan.

6.2.1 Material and Specimen Manufacture

The IASCC initiation test specimens are small disks (Figure 60) which enable multiple specimens to be cut from the shank of a baffle-former bolt at the same location along its length. This resulted in sets of specimens with effectively equivalent radiation dose and service conditions. This specimen geometry was previously successfully implemented in IASCC testing of Type 316 stainless steel (Reference 58) providing new information on the specific sites at which cracks

initiated and the relation between deformation and cracking. Specimens from each set were tested in lithium hydroxide and in potassium hydroxide environments, which allowed for a direct comparison of the effects of these environments at each dpa level.

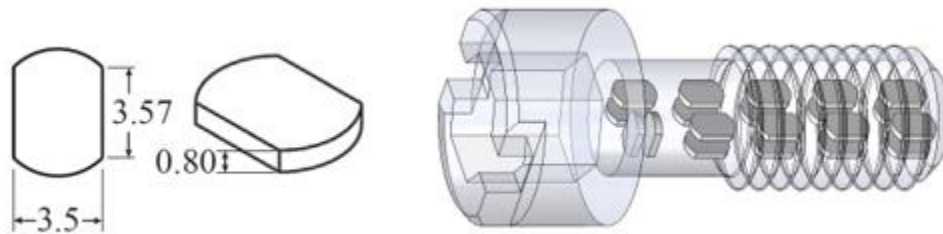


Figure 60. Left - Specimen Geometry (Dimensions in millimeters)
Right – Specimens Inside 12.7mm Diameter Baffle-former Bolt Shank (conceptual sketch)

The radiation dose varied in a predictable fashion along the axis of each baffle former bolt. Specimens of a range of fluences were created for testing, allowing the effects of radiation dose on IASCC initiation to be examined. The range of radiation damage and stress targeted by the tests are shown in Figure 61. By allowing many specimens to be cut from the same piece of bolt, heat-to-heat effects on the cracking behavior are eliminated. Because the radiation dose to such material increases as power plants age, this understanding will allow for improved prediction of IASCC-related degradation.

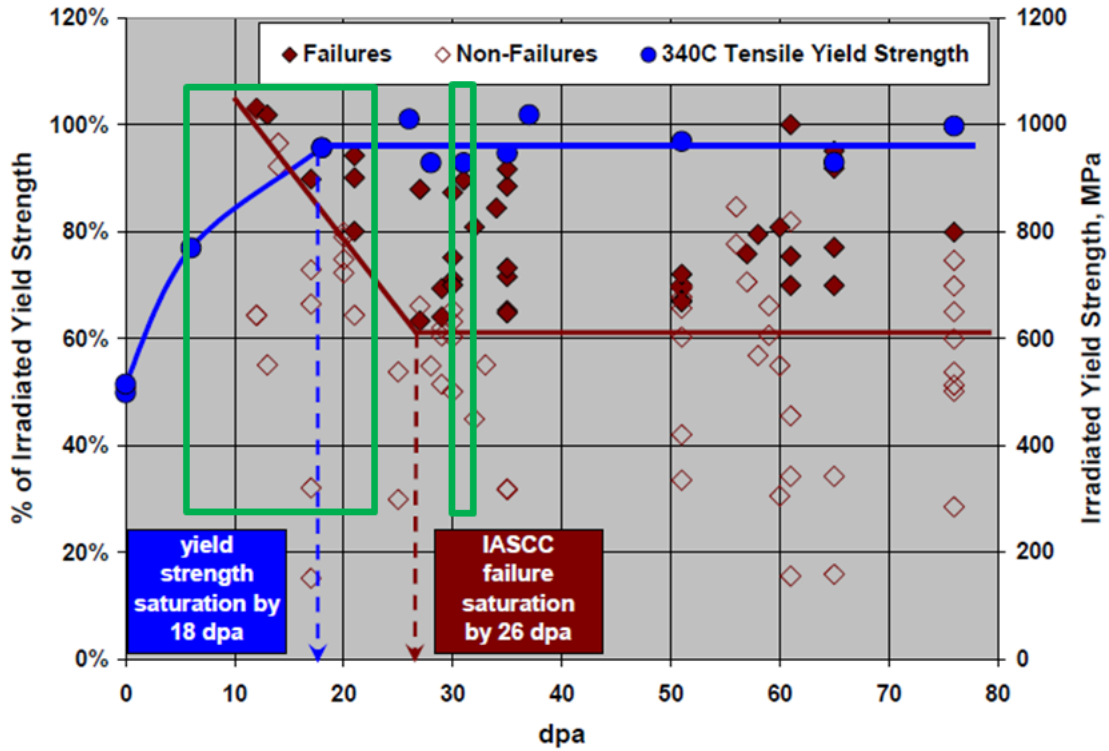


Figure 61. Areas to be investigated by this experiment shown in green boxes, relative to data generated by testing Type 316 O-rings irradiated in PWRs (Figure adapted from Reference 60)

The material used for testing was from baffle-former bolts extracted from commercial PWRs. The chemical composition of the bolts is shown in Table 9. These baffle-former bolts were in storage at the Westinghouse Churchill Hot Cell Facility in the High Level Cell. The materials were owned by Westinghouse, and existed as fractured (due to IASCC) bolts or whole bolts.

Table 9. Chemistry of Baffle-former Bolt Materials (from Reference 39)

Heat / Bolt	Fe	Ni	Cr	Mn	Mo	Nb	Si	C	P	S	N	Ti
N-R4C4	69.4	10	17.5	1.7	0.1	1.1	0.47	0.05	0.037	0.023	0.04	0.1
E-R4C6	66.9	10.9	19.2	1.7	0.1	0.8	0.47	0.05	0.034	0.020	0.04	0.2
W-R3C5	66.4	11.2	19.7	1.7	0.1	0.8	0.47	0.05	0.034	0.021	0.04	-
S-R5C7	66.8	10.9	19.6	1.7	0.1	0.8	0.47	0.05	0.034	0.020	0.04	-

These materials were previously characterized as part of failure analysis (Reference 59) and as part of industry research efforts (Reference 37). Such characterizations have included fractography (in the case of failed bolts), metallography, mechanical testing, and TEM.

The material considered for use in this project is shown in Table 10. This is limited to Westinghouse-owned Type 347SS baffle-former bolts that have been shipped to Westinghouse as part of various failure analysis efforts. The table indicates the radiation damage of each bolt in displacements per atom (dpa); these values are estimates based on neutron fluences calculated for comparable bolts.

The radiological activity of the baffle-former bolts used varied. Historically, they have been >>1000 R/hour on contact and were handled remotely at all times. This necessitated machining in a hot cell. The “M Cell” at the Churchill Hot Cell facility was chosen for this purpose.

Table 10. Identification of baffle-former bolts to be assessed for use in this project

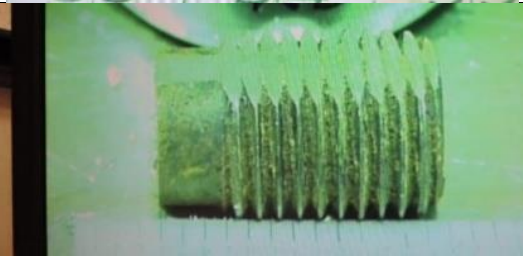
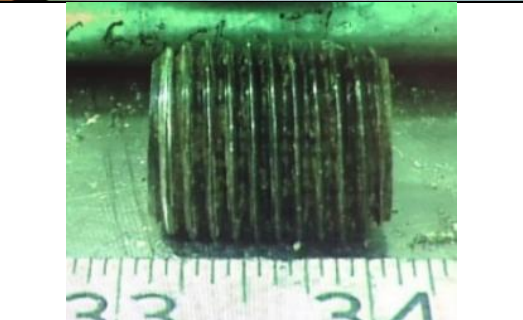
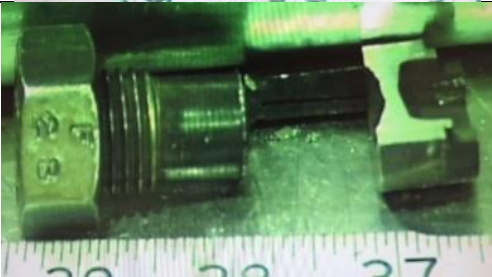
Plant	Bolt ID	dpa at head	Status	Photograph
D.C. Cook Unit 2	W-R3C5	22.5	Intact	 A photograph of a bolt with a hexagonal head and threaded shank, lying on a white surface. The bolt is oriented vertically.
D.C. Cook Unit 2	E-R4C6	23.1	Intact	 A photograph of a bolt with a hexagonal head and threaded shank, lying on a white surface. A ruler is visible below the bolt, showing markings for 33, 34, and 35. The bolt is oriented vertically.
D.C. Cook Unit 2	S-R5C7	23.2	Fractured at head-to-shank	 A close-up photograph of the threaded shank of a bolt, showing a clear fracture line between the head and the shank. The bolt is oriented vertically.
D.C. Cook Unit 2	S-R2C6	15.6	Fractured at head-to-shank, cut up into specimens	 A photograph of a bolt with a hexagonal head and threaded shank, lying on a white surface. A ruler is visible below the bolt, showing markings for 33 and 34. The bolt is oriented vertically.
D.C. Cook Unit 2	S-R6C6	23	Intact	 A photograph of a bolt with a hexagonal head and threaded shank, lying on a white surface. A ruler is visible below the bolt, showing markings for 33, 34, and 35. The bolt is oriented vertically. Handwritten text "S-R6C6 Bolt" is visible in the background.

Table 10. Identification of baffle-former bolts to be assessed for use in this project

Plant	Bolt ID	dpa at head	Status	Photograph
Salem Unit 1	D28	33	Fractured at head-to-shank. The nut attached to the threads is for specimen ID purposes.	
Salem Unit 1	F23	29	Fractured at head-to-shank. The nut attached to the threads is for specimen ID purposes.	

A Tormach PCNC 440 machine was used to machine the specimens. This was accomplished by milling the cross section of the four-point bend specimen into the baffle-former bolt and then using a fine saw blade to cut individual specimens free. Computer-aided drawing (CAD) sketches of the result of such a process on a bolt are shown in Figure 62. This process was slightly different from the proposed cutting diagram in Figure 60, and was considered an improvement because it allows six specimens to be cut from a single location along the bolt. In the project proposal, 24 tests were proposed. It was decided to cut 6 specimens from each of 5 locations to allow for a spare at each location should a sample become damaged during preparation; such a spare could also be used as a starting point for transmission electron microscopy (TEM) specimen preparation.

Practice machining was conducted on unirradiated material using the same model computer-numeric control (CNC) machine and same CNC program that was to be used for the

irradiated material (Figure 63). This process was found to consistently produce acceptably-sized specimens.

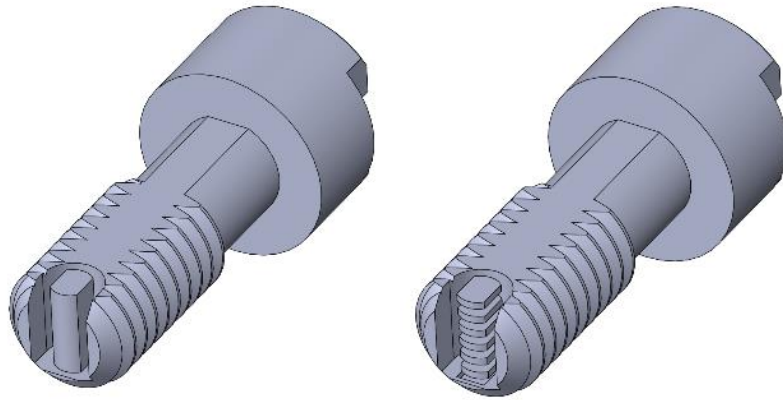


Figure 62. Baffle-former bolt (left) showing cross-section of 4-point bend specimen milled into the threaded end, and (right) the 4-point bend specimens cut free from the bolt.



Figure 63. Machining of 4-point bend samples from unirradiated practice bolt

To provide the range of radiation damage levels appropriate to the experiment, samples were cut from Salem Unit 1 bolt D28, D.C. Cook Unit 2 S-R2C6, and D.C. Cook Unit 2 S-R6C6 from the approximate locations shown in Figure 64, Figure 65, and Figure 66. This was achieved by installing the Tormach CNC machine into the M Cell (Figure 67). Machining was monitored by video camera installed inside the CNC machine; key steps of the machining process can be seen in Figure 68 and Figure 69.

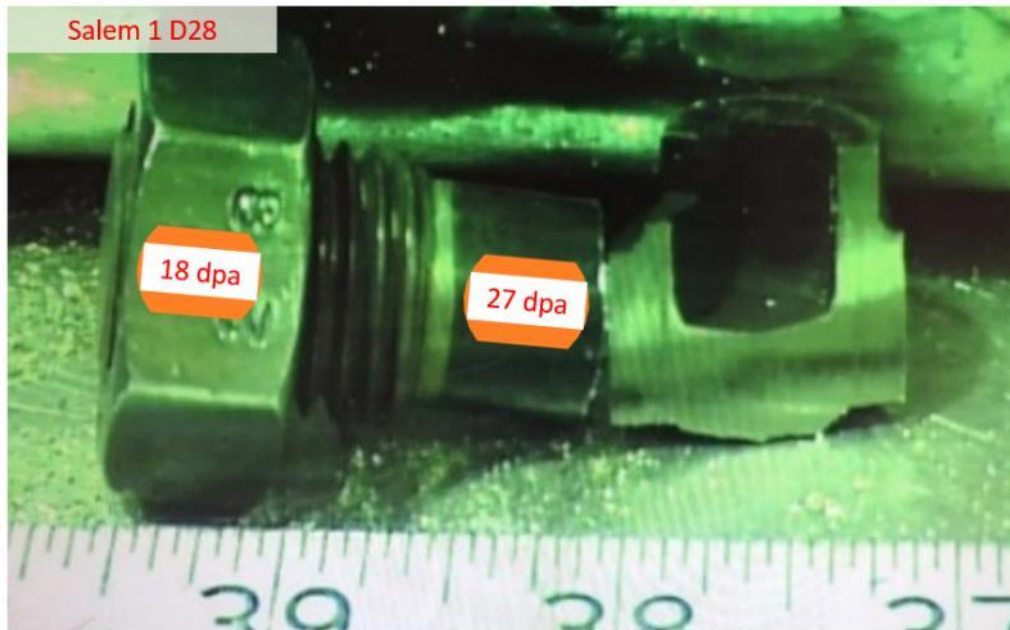


Figure 64. Approximate locations for specimen machining for Salem 1 bolt D28. The 18 dpa sampling location is at the end of the threaded portion of the bolt, obscured by the nut used for ID purposes.



Figure 65. Approximate locations for specimen machining for DC Cook 2 S-R6C6

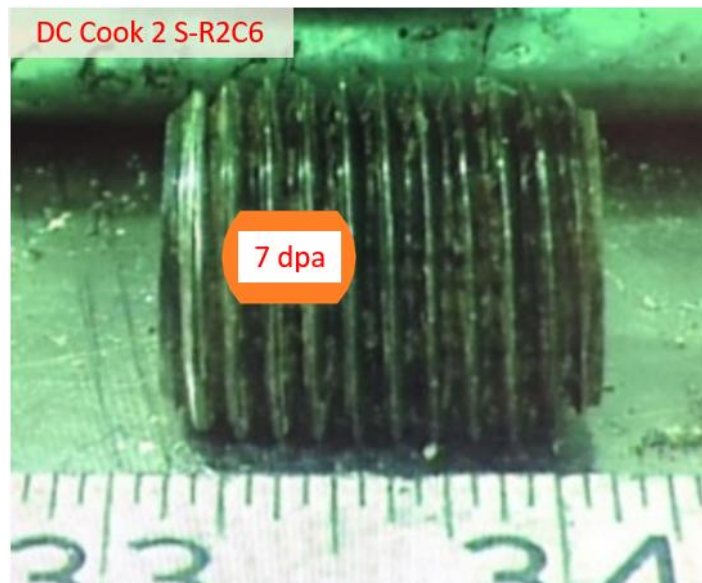


Figure 66. Approximate location for specimen machining for DC Cook 2 S-R2C6

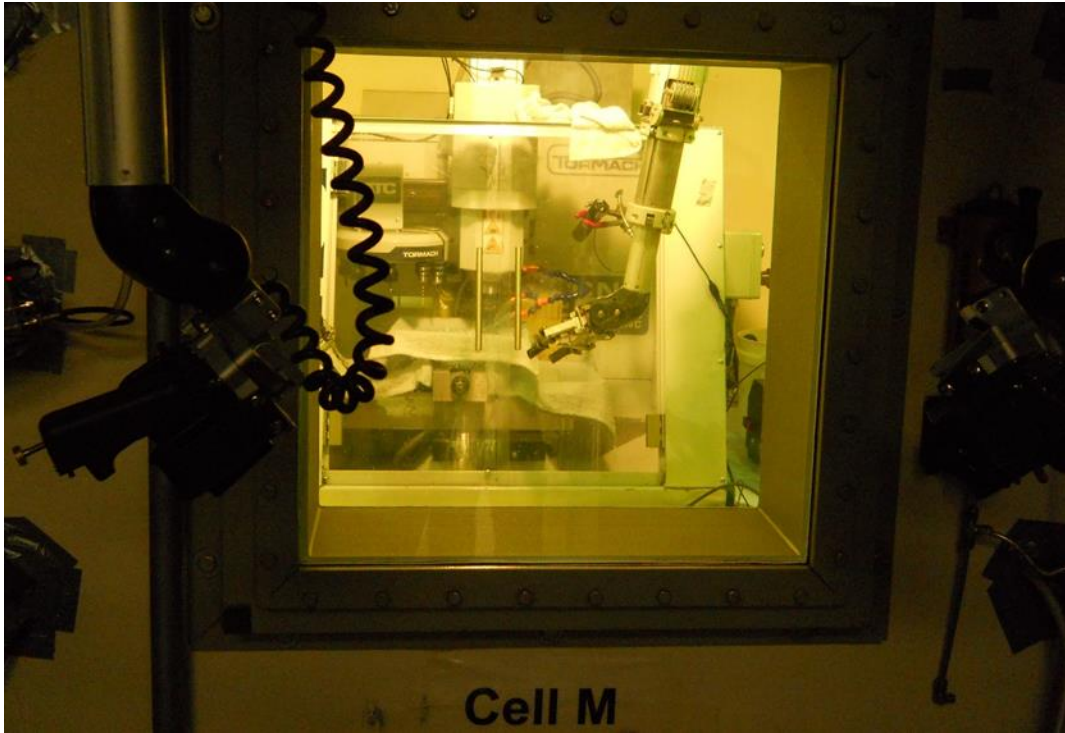


Figure 67. Tormach CNC Machine Installed in Cell M

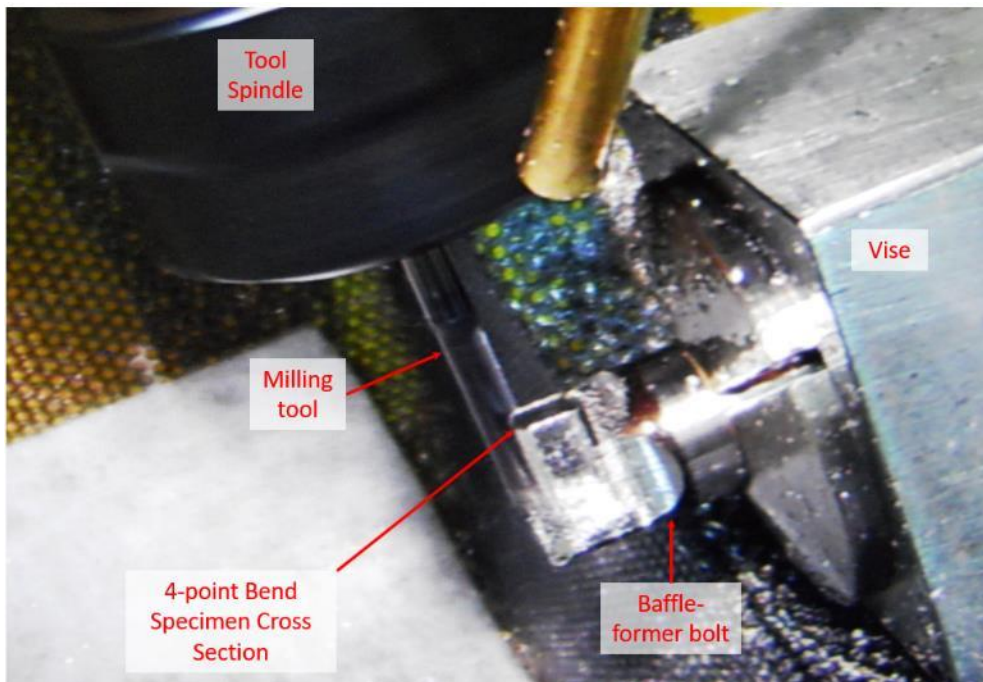


Figure 68. View within CNC machine, within M Cell, showing milling of 4-point bend cross section into threaded end of bolt

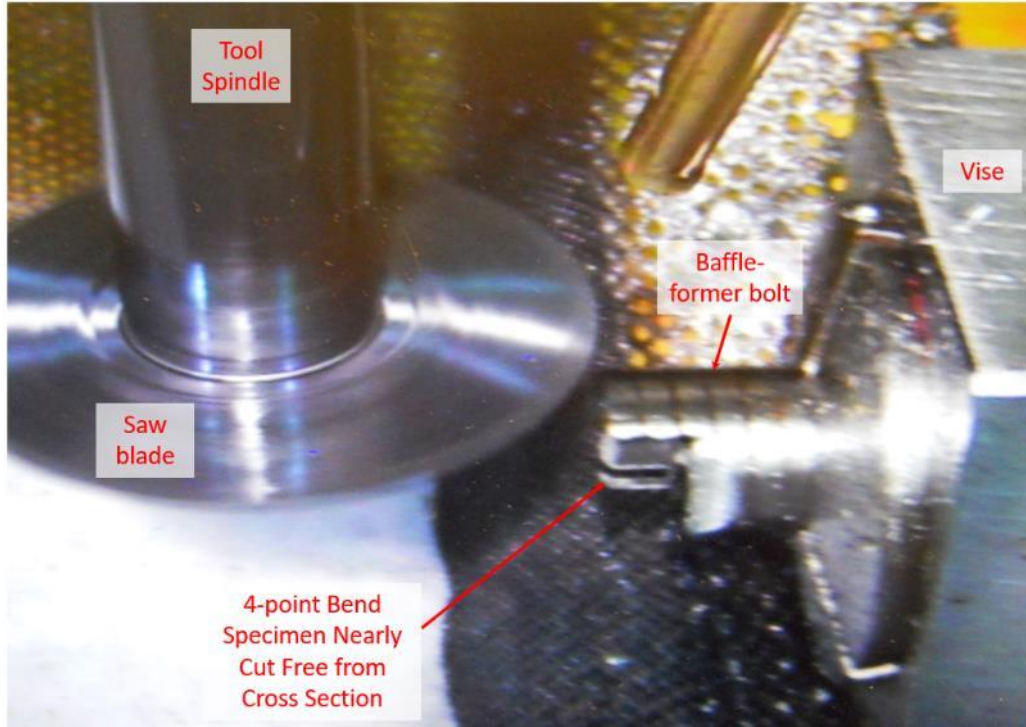


Figure 69. View within CNC machine, within M Cell, showing 4 point bend specimens being cut free from the bolt

After the 4-point bend specimens were cut free, the specimens were deburred. The specimens were then temporarily mounted in Konductomet® specimen holders, fastened in place using a small amount of Crystalbond. This allowed polishing of the specimens using typical metallographic polishing equipment. The specimens were polished to a final stage using oxide polishing suspension (OPS, colloidal silica).

After polishing, the specimens were electropolished to remove any residual cold work from the mechanical polishing process, and provide a high-quality surface to allow for examination of crack initiation sites. The specification ASTM B912 (Reference 62) gives a typical electropolishing solution recipe as a 1:1 mix of 96% sulfuric acid and 85% orthophosphoric acid, which was used for this project. The applied voltage was 5 volts, and applied current was 2 amps

for a current density of 4.6 amps/cm². As the OPS polish leaves a very minimal amount of residual cold work, 15 seconds of electropolishing was considered sufficient to remove it. This practice was in line with recommendations from the University of Michigan. On practice specimens, the effect of the 15 second electropolish treatment was observed to both clean the specimens and remove a small amount of material. Material removal was selective towards vertices, and so removal of material was apparent when the grain boundaries in the polished surface were not visible afterwards (Figure 70). Longer electropolishing times (45-60 seconds) appeared to show selective attack of stringer-like inclusions of the material (Figure 71), which is undesirable.

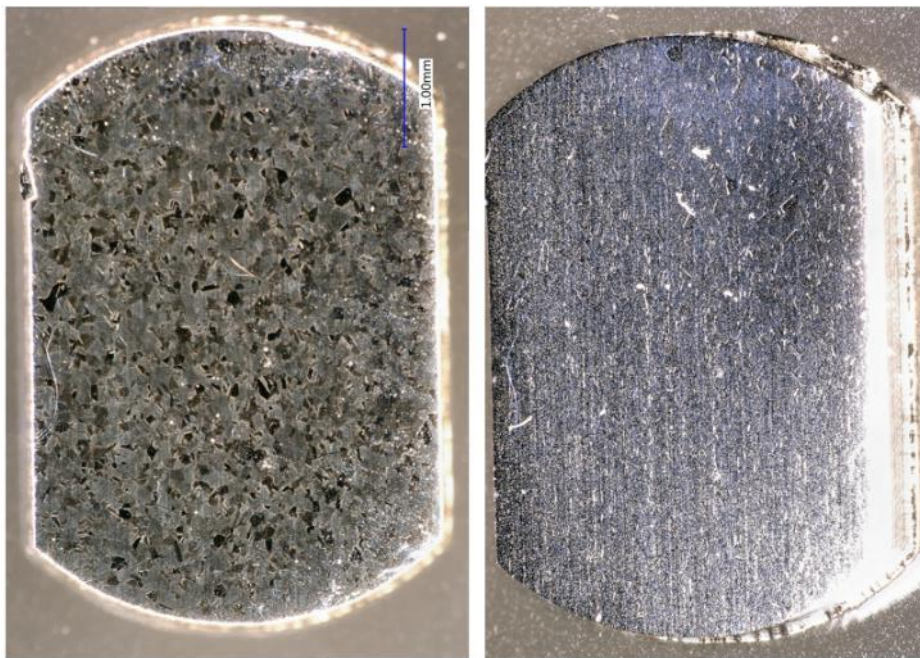


Figure 70. Effect of electropolishing showing difference between (left) as polished specimen and (right) specimen after 15 seconds of electropolishing

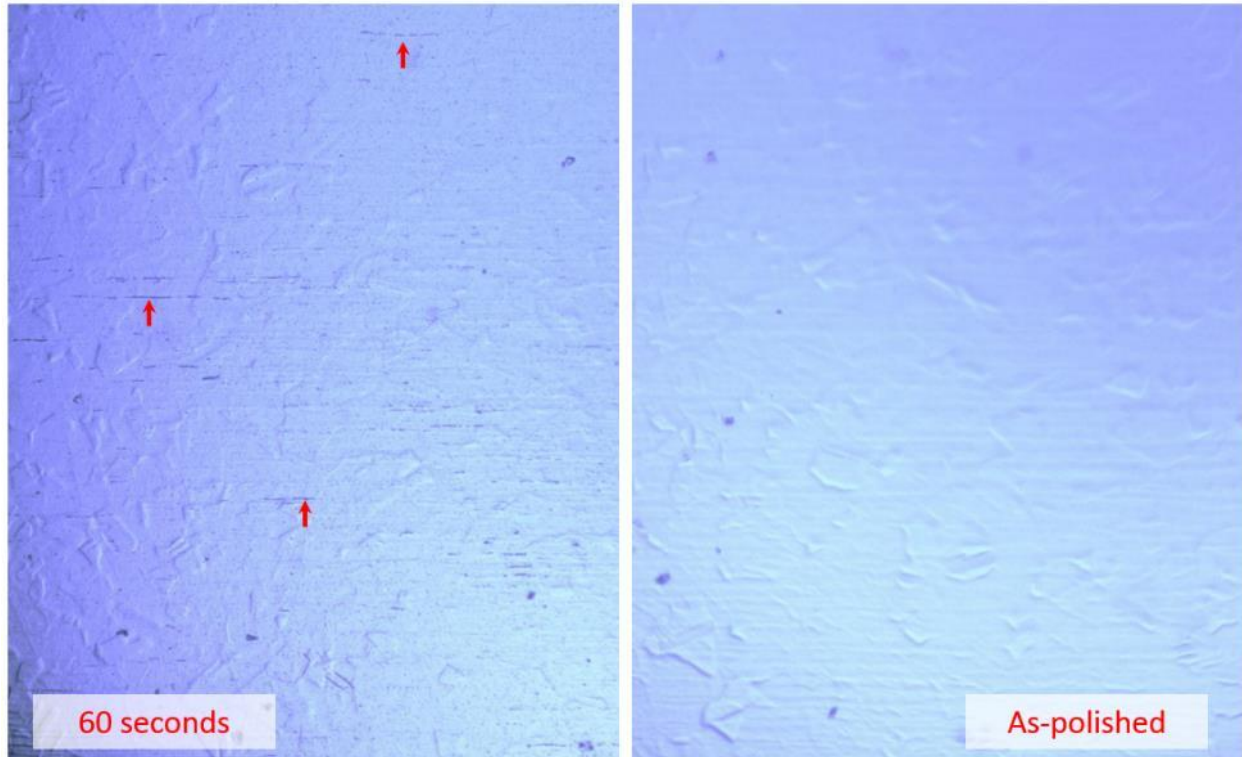


Figure 71. Effect of electropolishing showing difference between (right) as polished specimen and (left) specimen after 60 seconds of electropolishing, with the etching of stringers indicated by red arrows

The specimens remained in the Konductomet specimen holder during the electropolishing process. This allowed for easier handling of the specimens during the electropolishing. The specimens were then removed from the temporary mounts and cleaned in acetone. The specimens were then placed in membrane boxes, photographed in the open membrane box (to minimize handling), and then sealed in the membrane box.

Of the 6 pieces that were removed from each material location, 5 specimens were designated for 4-point bend testing while the 6th was used for preparing TEM specimens. This 6th 4-point bend specimen (of each material condition) was cut further into small pieces (roughly quarters), and one small piece was then mounted in Konductomet inside of a stainless steel tube (to allow for easier handling and breaking out of the larger metallographic mount), polished to

OPS, and electropolished (Figure 72). TEM samples were prepared by focused ion beam (FIB) preparation of TEM lamella using the Tescan LYRA-3 GMU FIB/SEM (dual beam FIB with an Orsay Physics Canion FIB column) in the Westinghouse Churchill Site Electron Optics laboratory. The ExpressLO LLC Nicola 800 *ex situ* liftout system was used for placing the cut lamella onto ExpressLO proprietary TEM grids.

First, to better identify grain boundaries, each sample was further polished using the ion beam at a current of 1 nA over a wide area (a view field of approximately 460 μm). Due to the differential milling rate of grains at different orientations, the grain structure became apparent (Figure 73). Areas of interest were selected, aligning a grain boundary with the center of where the specimen was to be extracted (Figure 74), and a carbon mask ($\sim 20\mu\text{m} \times 2\mu\text{m}$, 1 μm thick) was deposited over these areas to protect them from the ion beam. Trenches were then cut on both sides of the carbon deposits (Figure 75), surfaces polished (typically at or below 1 nA), and undercut (Figure 76). As is seen from the undercut lamella (Figure 77), it was usually possible to identify multiple grain boundaries and sometimes inclusions. The lamella surfaces were then further polished to remove redeposition after undercutting, and the final tabs milled away, which allowed the lamella to rest unattached at the bottom of its trench. The sample was then removed from the FIB/SEM and placed on the stage of the *ex situ* system. Once placed, the lamella was extracted from the trenches (Figure 78) and placed on a copper grid with numbered slots (Figure 79). Once all lamellas were transferred to a grid, it was placed back in the FIB/SEM and carbon was deposited on the edges to further secure the specimen (Figure 80). Final thinning to electron transparency was then completed. Each lamella was thinned at 30 kV and $\sim 100\text{-}120$ pA, followed by a final polish at 5 kV at 40-50 pA.

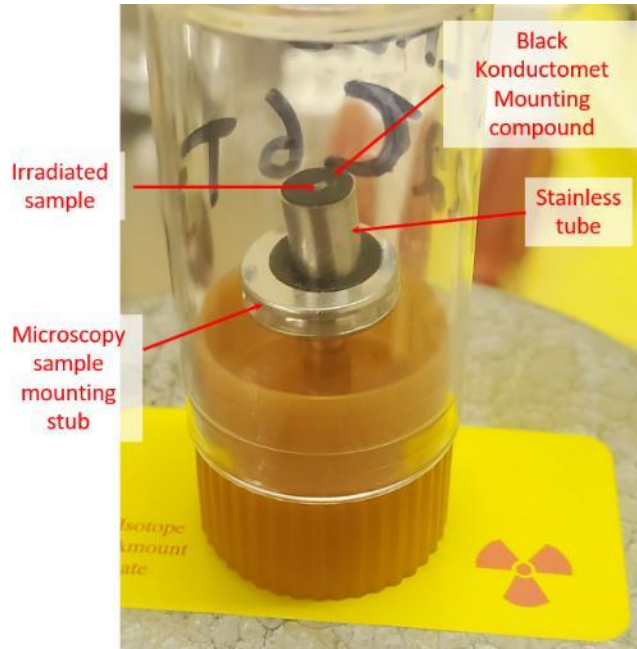


Figure 72. Sample for TEM Lamella Extraction in Protective Case

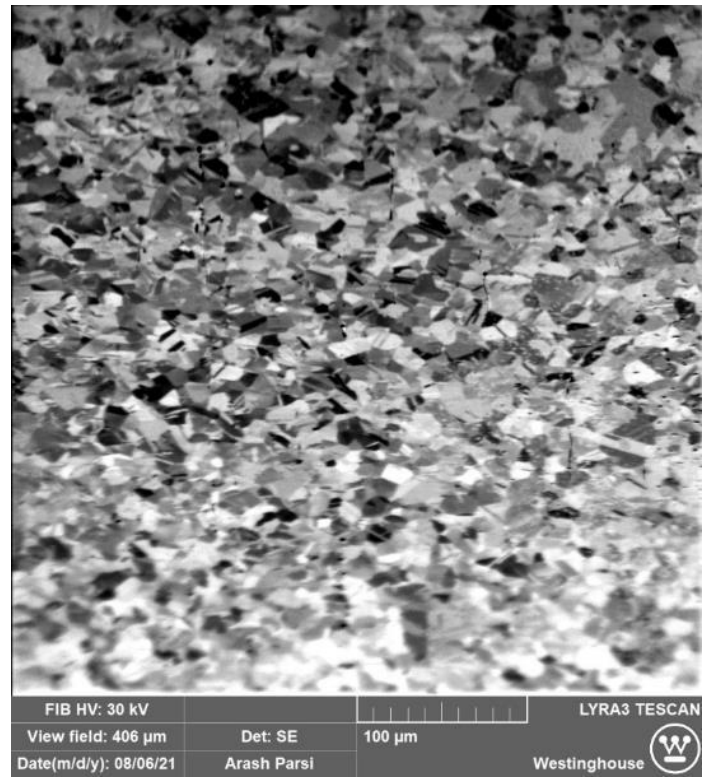
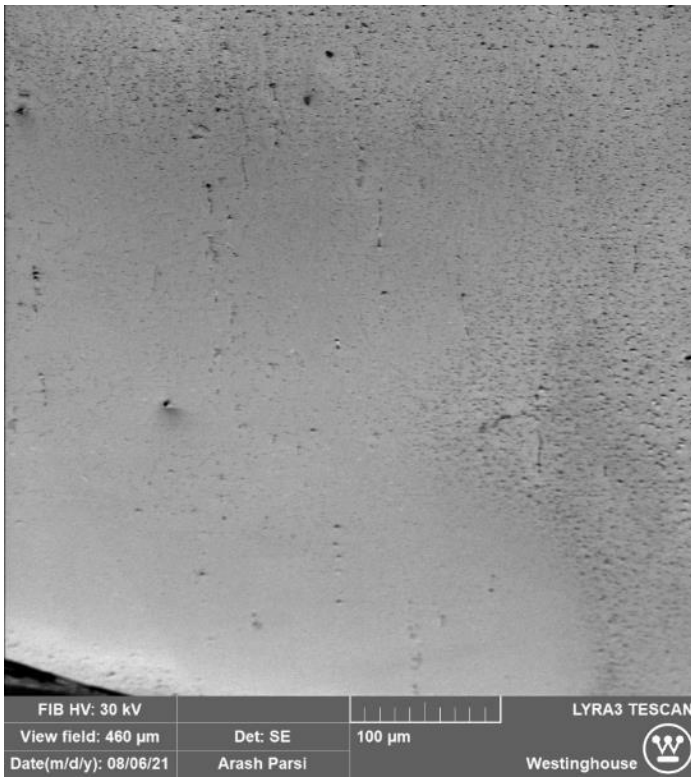


Figure 73. Specimen (left) before and (right) after wide-area ion beam polishing

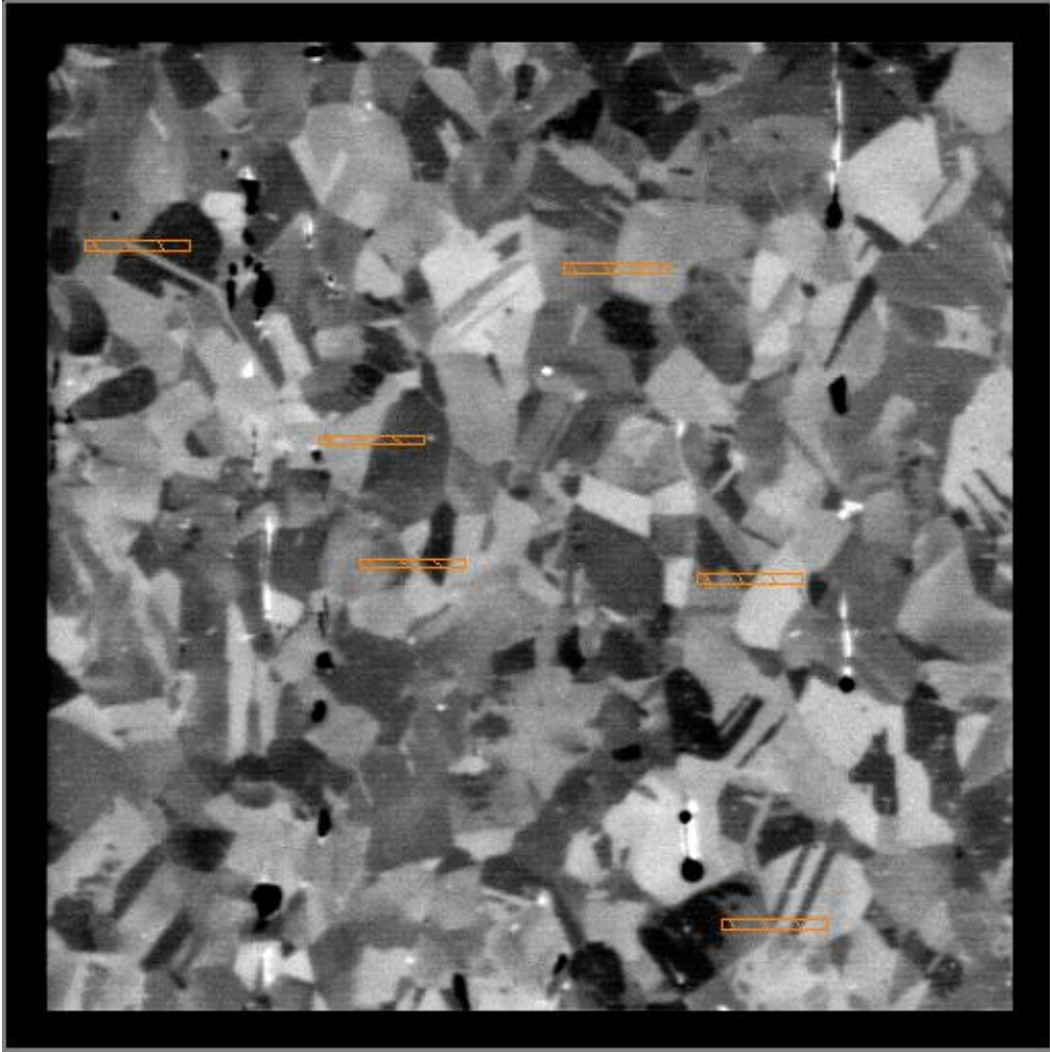


Figure 74. Selection of carbon deposition regions, attempting to center grain boundaries under the mask prior to ion milling for lamella preparation

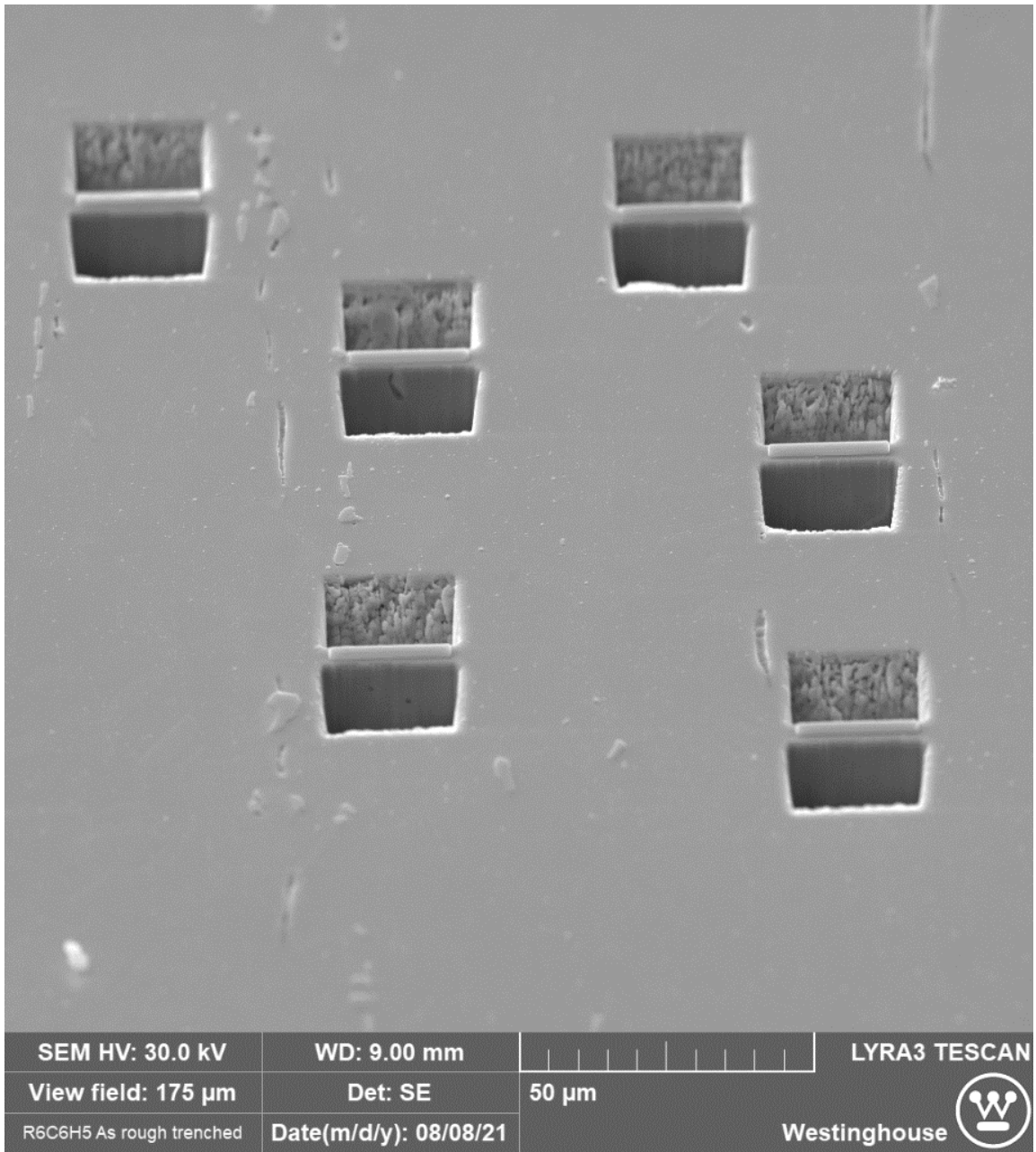


Figure 75. Trenches cut around carbon deposits

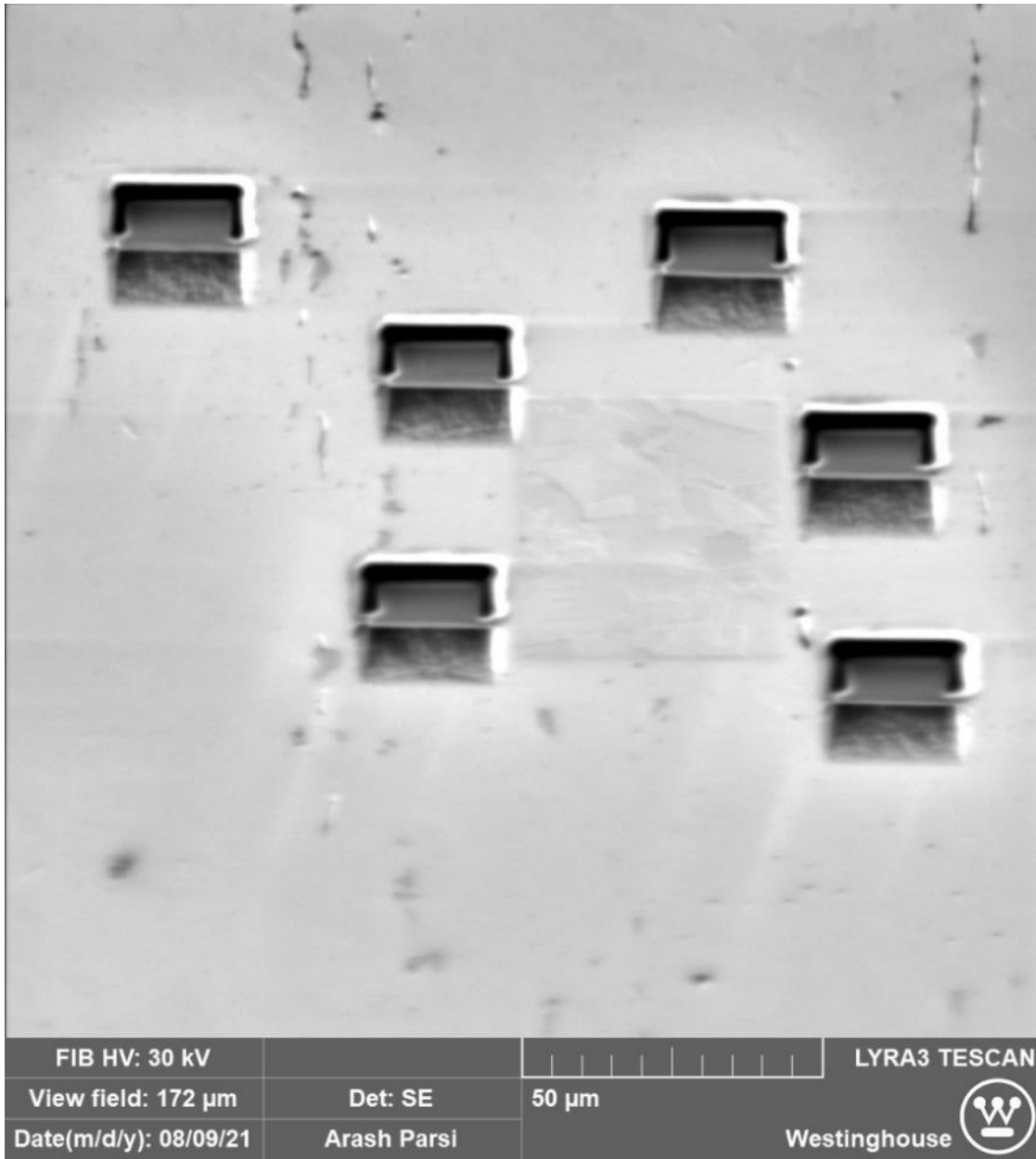


Figure 76. Six undercut lamellas

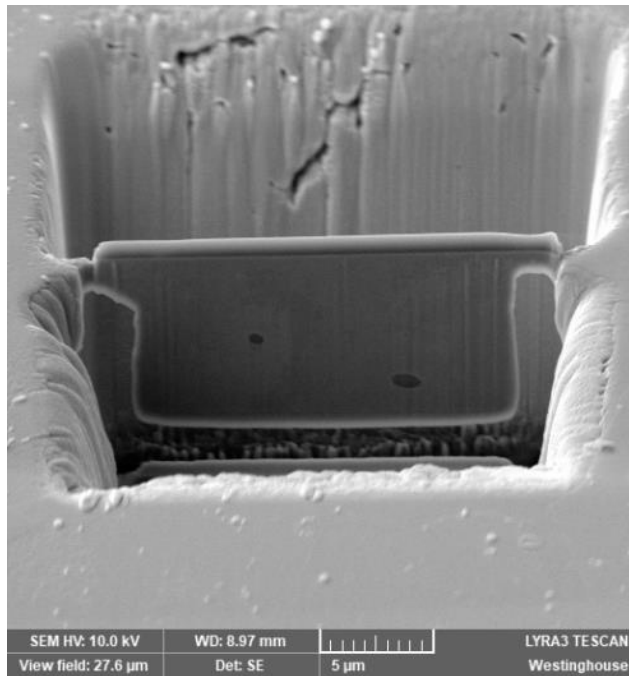


Figure 77. Undercut lamella containing some apparent inclusions

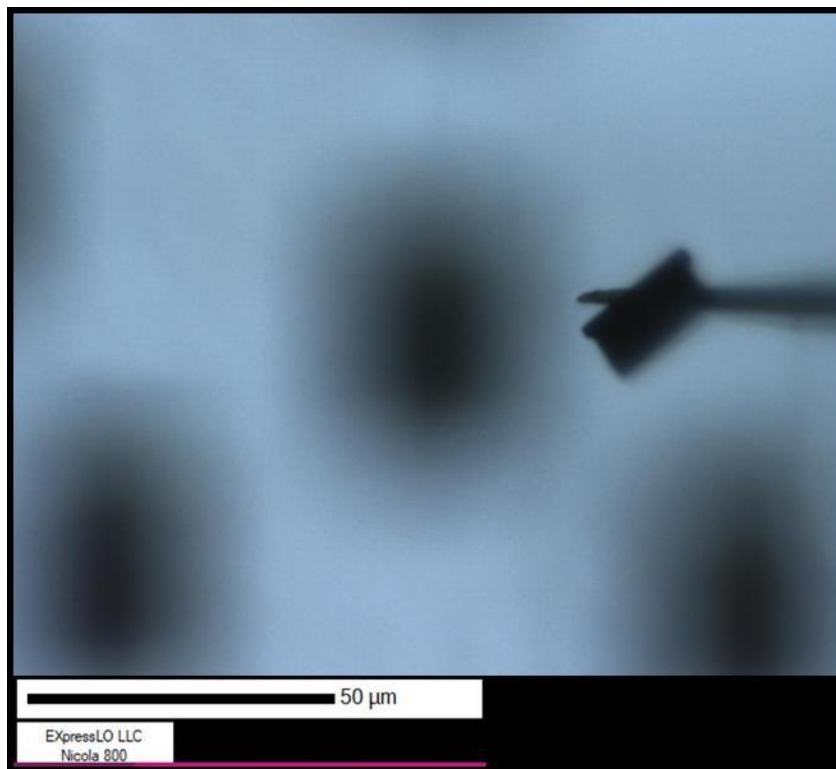


Figure 78. Lamella attached to lift-out needle prior to placement on grid (light optical image)

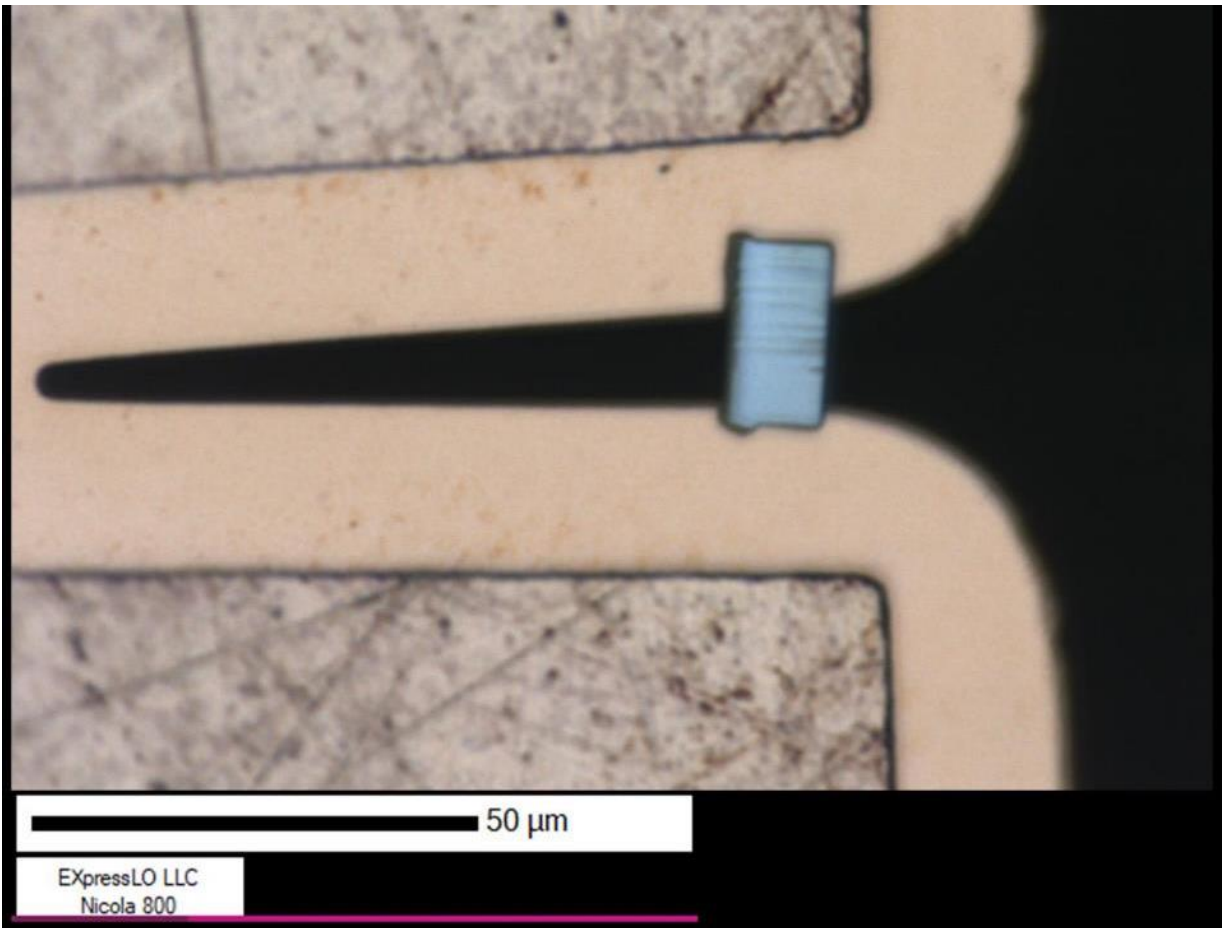


Figure 79. Lamella placed on grid (light optical image)

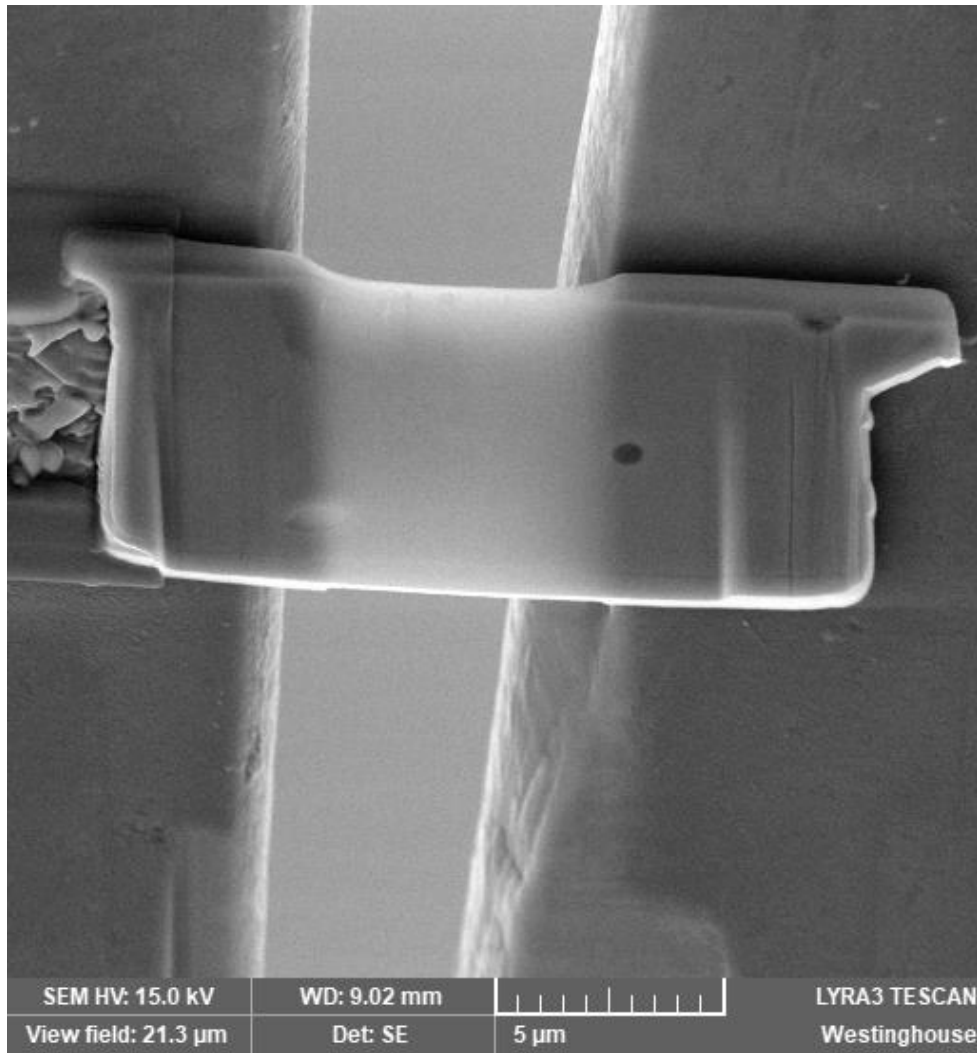


Figure 80. Lamella deposited on grid after final thinning (viewed via SEM)

The final length, width, and dose rates of each 4-point bend specimen is recorded in Table 11. The dose (dpa) in this table reflects the best-estimate for the as-machined location. As previously discussed, the five specimens with the best surface of the six were selected for testing, while the sixth was used for TEM specimen generation. TEM specimens shipped to University of Michigan are recorded in Table 12.

Table 11. Final Irradiated 4-point Specimen Identities, Dimensions, and Dose Rates

#	Specimen	Length (mm) [Target 5mm]	Width (mm) [Target 3.5mm]	Dose rate on contact (R/hr.)	Dose rate at 30 cm (mR/hr.)	Best Estimate on dose (dpa)
1	D28-H-1	5.05	3.49	16.2	83	26.4
2	D28-H-2	5.05	3.51	16.2	93	26.4
3	D28-H-3	5.05	3.49	15.6	90	26.4
4	D28-H-4	5.05	3.51	15.1	100	26.4
5	D28-H-5	5.05	3.51	16.1	90	26.4
6	D28-T-1	5.05	3.51	14.5	93	16.5
7	D28-T-2	5.05	3.51	14.1	84	16.5
8	D28-T-3	5.05	3.51	13.9	85	16.5
9	D28-T-4	5.05	3.52	14.8	81	16.5
10	D28-T-5	5.05	3.51	14.2	83	16.5
11	S-R6C6-H-1	5.05	3.48	5.6	33	18.4
12	S-R6C6-H-2	5.03	3.48	5.6	33	18.4
13	S-R6C6-H-3	5.03	3.47	5.5	34	18.4
14	S-R6C6-H-4	5.03	3.48	5.3	36	18.4
15	S-R6C6-H-6	5.08	3.52	5.2	34	18.4
16	S-R6C6-T-1	5.05	3.51	4.8	34	11.5
17	S-R6C6-T-2	5.07	3.49	4.76	35.8	11.5
18	S-R6C6-T-3	5.07	3.51	4.7	29.9	11.5
19	S-R6C6-T-5	5.07	3.51	4.75	32.7	11.5
20	S-R6C6-T-6	5.08	3.51	4.76	29.4	11.5
21	S-R2C6-T-1	5.07	3.52	3.1	24	7.8
22	S-R2C6-T-2	5.09	3.53	3.2	23	7.8
23	S-R2C6-T-4	5.07	3.54	3.5	26	7.8
24	S-R2C6-T-5	5.07	3.56	3.3	26	7.8
25	S-R2C6-T-6	5.11	3.56	3.6	24	7.8

Table 12. TEM Specimens Prepared from Baffle-former Bolt Material

Specimen used for Lamella Extraction	Irradiation Level (dpa)	Number of Lamella	Positions on Grid
D28-H-6	26	1 intact (1 damaged)	2, 3
S-R2C6-T-3	8	3	2, 3, 5
S-R6C6-H-5	18	3	2, 3, 5

The 4-point bend specimens were shipped from Westinghouse Churchill Site and received at the University of Michigan on October 27, 2020. The TEM specimens were shipped from Westinghouse Churchill Site and received at the University of Michigan on September 2nd, 2021. No difficulties or irregularities were encountered in either shipment.

6.2.2 IASCC Initiation Testing

The miniature 4-point specimens underwent IASCC initiation testing in a stainless steel refreshed water autoclave system capable of simulating the PWR primary water environment. The design of the test fixtures used to conduct these tests is shown in Figure 81. The shielded autoclave system used to conduct the testing on the radioactive samples is shown in Figure 82. The test is conducted in an interrupted mode, where each specimen is strained to a fraction of the irradiated yield stress at a strain rate of $4.3 \times 10^{-8} \text{ s}^{-1}$. Once the target fraction of the irradiated yield stress is achieved, the specimen is unloaded, removed from the autoclave, and inspected via a JEOL JSM-6480 SEM for the initiation of cracking. Targeted stress levels for each specimen were 40%, 50%, 60%, 70% and 80%, or until cracks initiated.

Testing was conducted at 320 degrees Celsius in all cases, with a hydrogen overpressure of 35 cc/kg to remove any free oxygen from the system. Water chemistry was maintained with either 2 ppm LiOH or 12.3 ppm KOH to maintain the same pH in the different water chemistries.

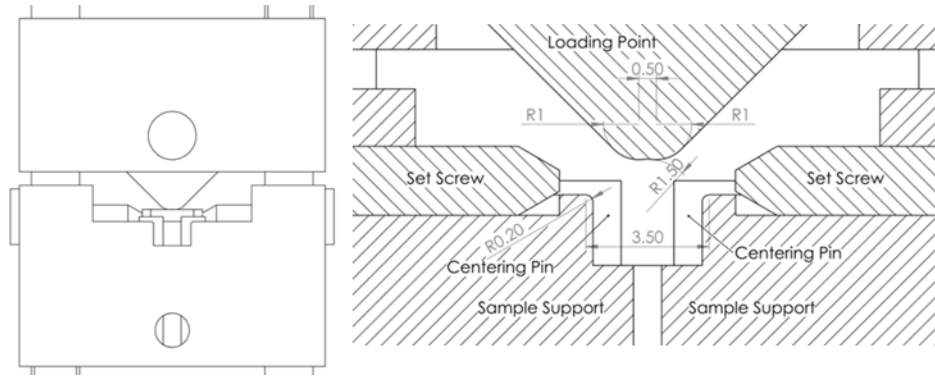


Figure 81. Design of test fixtures used for 4-point bend testing. The left image shows a CAD drawing of the overall fixture assembly with a specimen inserted, while the right image shows a cross-section of the fixture with the specimen removed. From Reference 58.

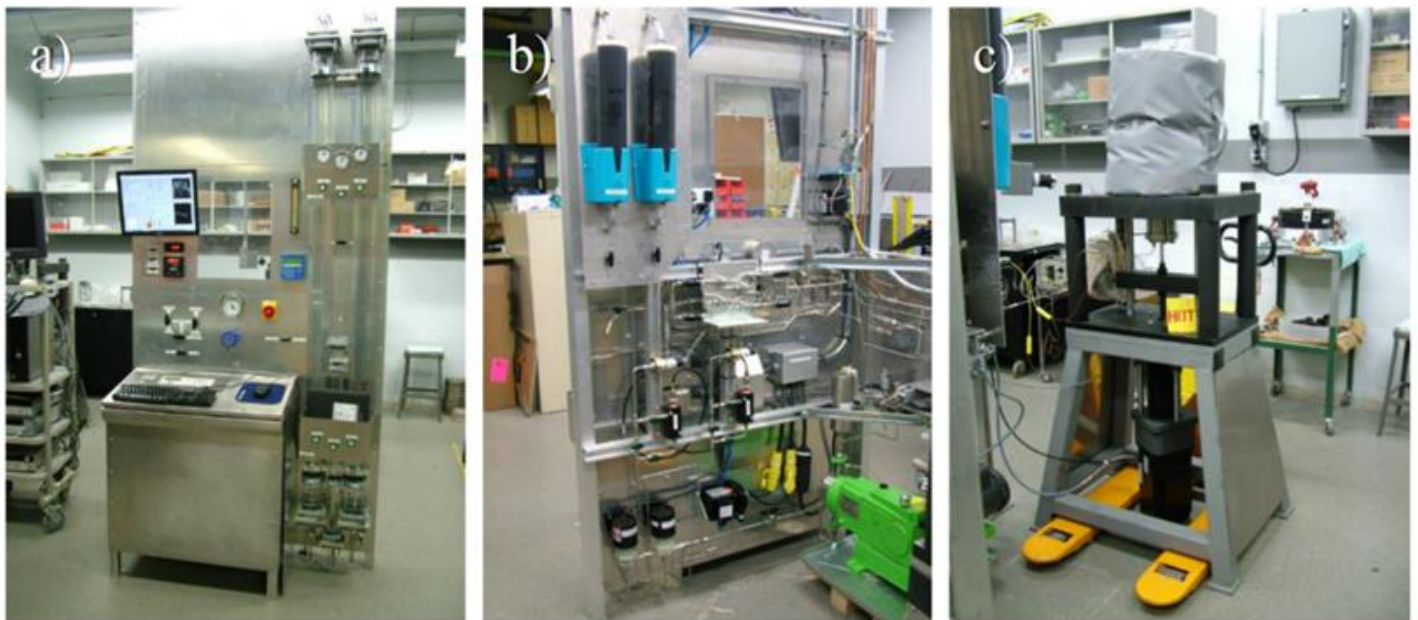


Figure 82. Shielded autoclave station at the University of Michigan, showing (a) the user controls, (b) the supporting piping and resin columns, and (c) the insulated autoclave system sitting atop the load frame. Photographs courtesy of University of Michigan

6.3 Results

As this work is still ongoing, these results are considered preliminary. The complete results will be published in a future peer-reviewed journal article. At present, testing of twelve specimens for crack initiation has been completed and analyzed. Six specimens have been tested in each water chemistry at this time, allowing a meaningful comparison to be made.

Figure 83 shows an example of the specimen surface of D-28-H3 after completion of testing. The oxidation of the surface is apparent, and cracking is readily visible in backscatter mode. Figure 84 shows the surfaces of the six samples tested in KOH water chemistry, with the region of uniform tensile stress and crack initiation locations shown. The resulting summary data on crack initiation for samples tested in KOH are given in Table 13.

Table 13. Results for specimens tested in KOH

Sample ID	D28-H-3		S-R6C6-H-4	S-R6C6-T-5	S-R6C6-T-3	S-R2C6-T-1	S-R2C6-T-2
Thickness (mm)	0.795		0.8	0.805	0.81	0.735-0.765	0.8
dpa	26.4		18.4	11.5	11.5	7.8	7.8
Yield stress (MPa)	1089		1082	1050	1050	996	996
Crack initiation Stress	0.6		0.6	0.6	0.8	0.6	0.8
Applied stress (% YS)	0.6	0.7	0.6	0.6	0.8	0.6	0.8
Number of cracks	9	13	3	10	3	40	5
Average crack length (μm)	24.7 \pm 2.0	45.6 \pm 1.5	16.2 \pm 1.2	10.7 \pm 0.21	9.0 \pm 0.32	45.8 \pm 0.54	8.23 \pm 0.5
Crack density (#cracks/ mm^2)	5.2	7.4	1.7	5.8	1.7	26.2	2.9
Crack length/unit area ($\mu\text{m}/\text{mm}^2$)	133.7 \pm 33.6	337.6 \pm 28.9	27.6 \pm 5.4	70.0 \pm 1.9	15.3 \pm 3.1	3338.8 \pm 227.8	23.5 \pm 2.5

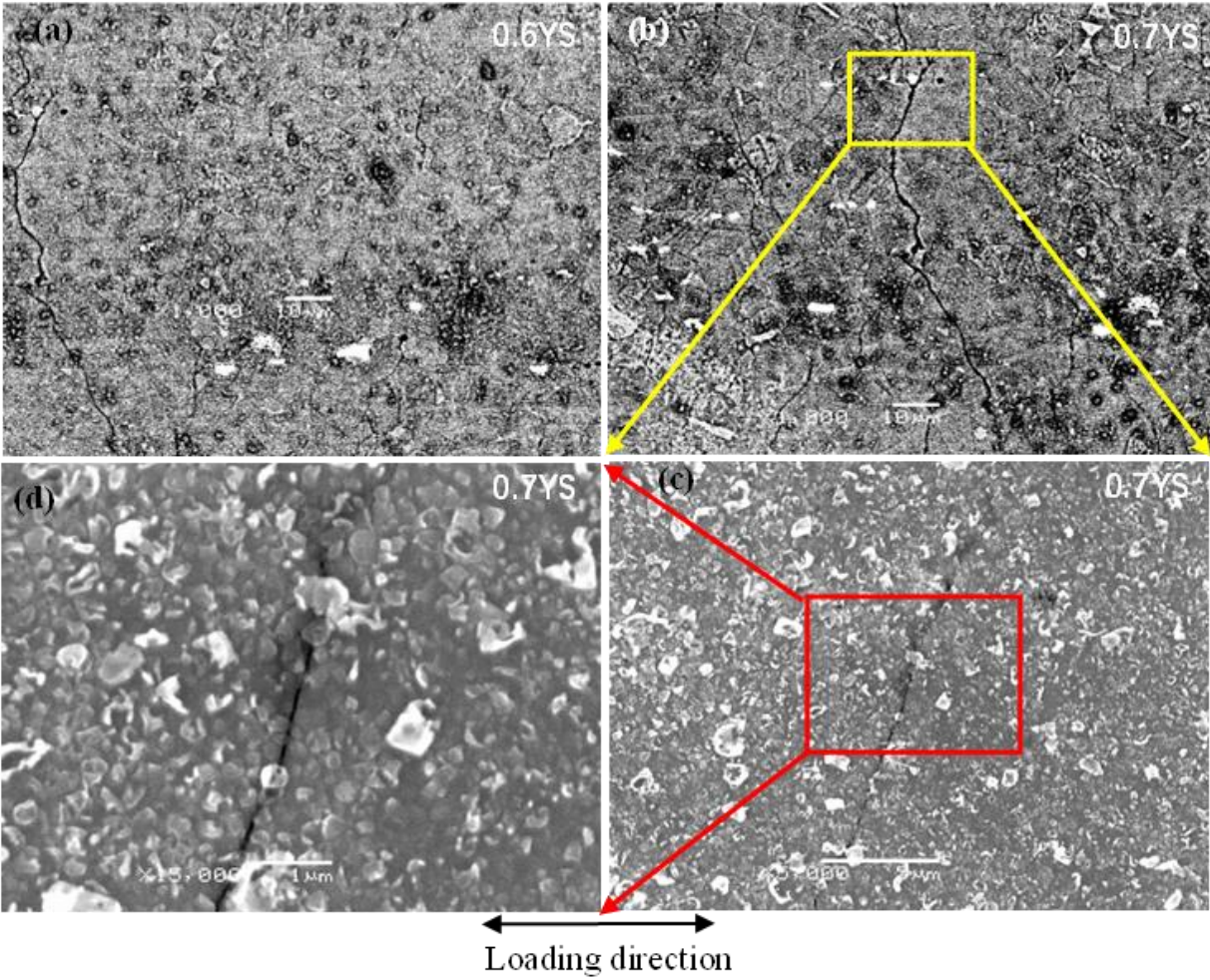


Figure 83. An example crack from specimen D28-H-3 at 26.4 dpa, viewed in back scatter mode after testing at 60% and 70% of the irradiated yield stress in KOH water chemistry

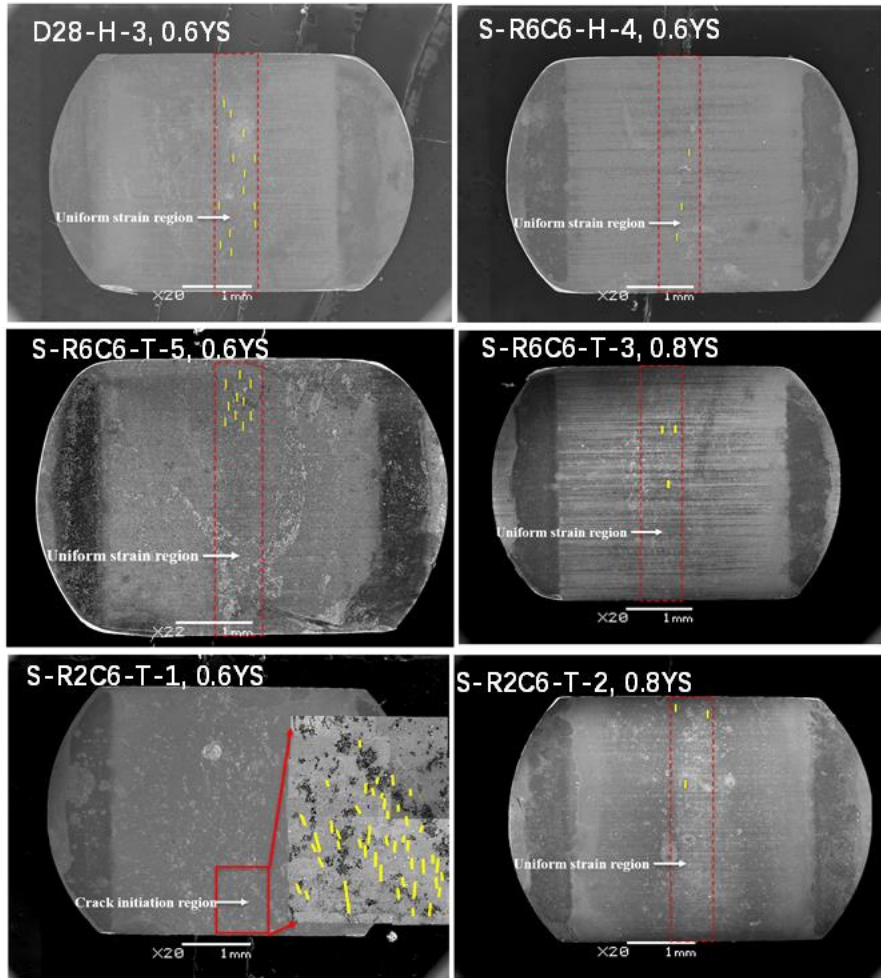


Figure 84. Images of 4-point bend specimens after testing in KOH water chemistry. The dashed red boxes indicate regions of uniform surface stress.

Figure 85 shows an example of the specimen surface of D-28-H1 after completion of testing. The oxidation of the surface is again apparent, and cracking is readily visible in backscatter mode. Figure 86 shows the surfaces of the six samples tested in LiOH water chemistry, with the region of uniform tensile stress and crack initiation locations shown. The resulting summary data on crack initiation for samples tested in LiOH are given in Table 14.

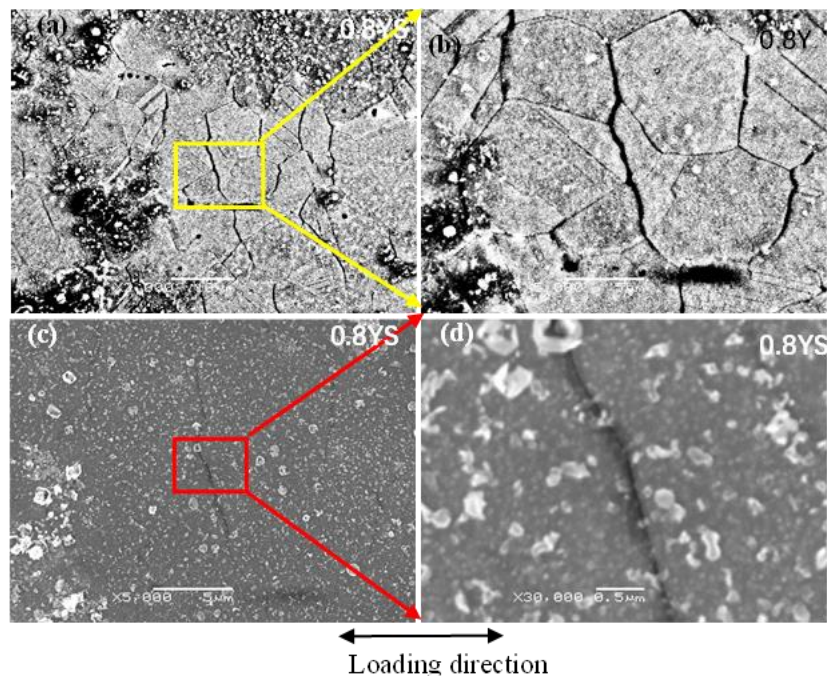


Figure 85. An example crack from specimen D28-H-1 at 26.4 dpa, viewed in back scatter mode (top) and secondary electron mode (bottom) after testing at 80% of the irradiated yield stress in LiOH water chemistry

Table 14. Results for Specimens Tested in LiOH

Sample ID	D28-H-2	D28-H-1	S-R6C6-H-3	S-R6C6-H-6	S-R6C6-T-2	S-R2C6-T-4
Thickness (mm)	0.82	0.81	0.785	0.804	0.835	0.785
dpa	26.4	26.4	18.4	18.4	11.5	7.8
Yield stress (MPa)	1089	1089	1082	1082	1050	996
Crack initiation Stress	0.8	0.8	0.6	0.6	0.8	0.7
Applied stress (% YS)	0.8	0.8	0.6	0.6	0.8	0.7
Number of cracks	3	5	4	4	3	4
Average crack length (μm)	10.6 \pm 0.28	32.3 \pm 0.88	8.75 \pm 0.50	10.25 \pm 0.57	13.7 \pm 0.42	11.3 \pm 0.48
Crack density (#cracks/ mm^2)	1.7	2.9	2.3	2.3	1.7	2.3
Crack length/unit area ($\mu\text{m}/\text{mm}^2$)	18.02 \pm 2.5	93.7 \pm 5.4	20.1 \pm 2.2	23.6 \pm 2.8	23.3 \pm 3.5	26 \pm 3.1

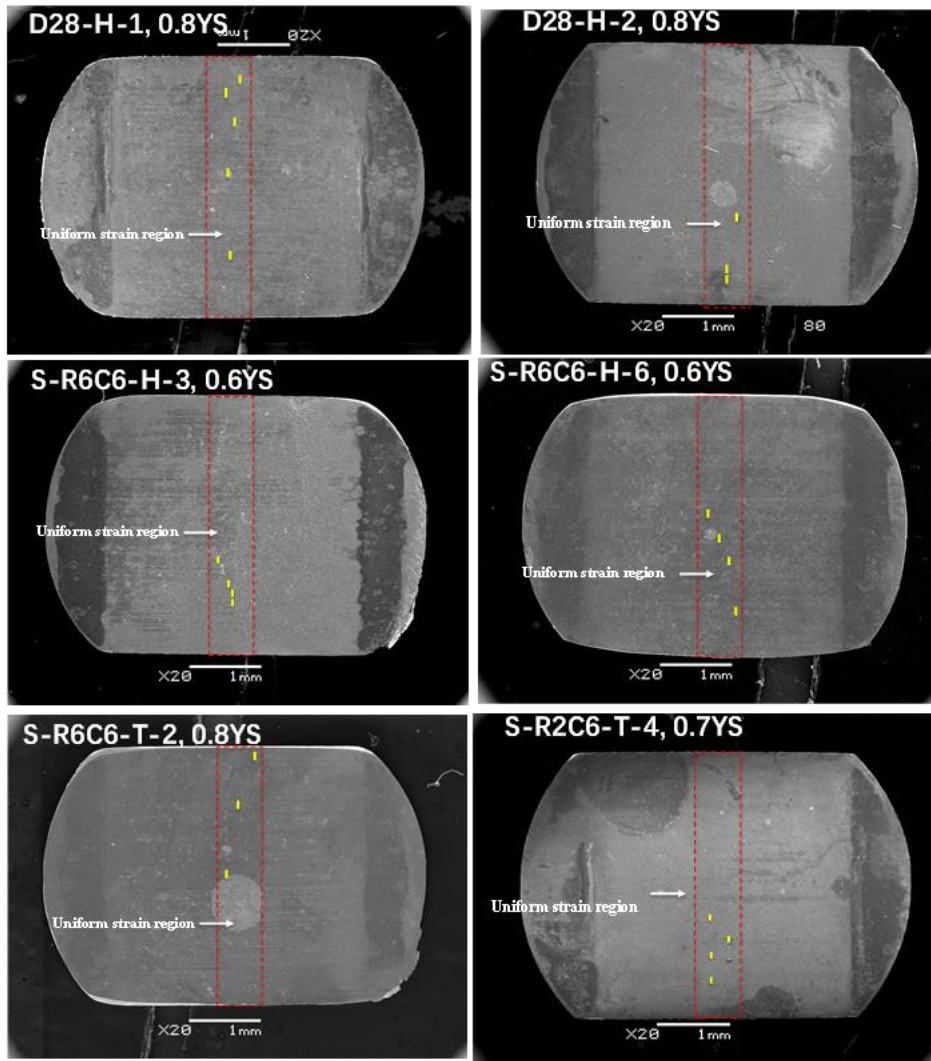


Figure 86. Images of 4-point bend specimens after testing in LiOH water chemistry. The dashed red boxes indicate regions of uniform surface stress.

Figure 87 summarizes the average crack length and crack length per unit area for the samples tested in KOH and LiOH water chemistries. While slight differences can be observed (note the difference in Y axis between the left and righthand plots), these are relatively minor in the context of SCC initiation testing, especially for a single specimen at each condition. The trends between the two data sets are in relatively good agreement. Figure 88 offers another graphical comparison between the KOH and LiOH data sets, this time for the crack initiation stress. Once

again, some differences exist, but the general level agreement is quite good for testing a single specimen for SCC initiation.

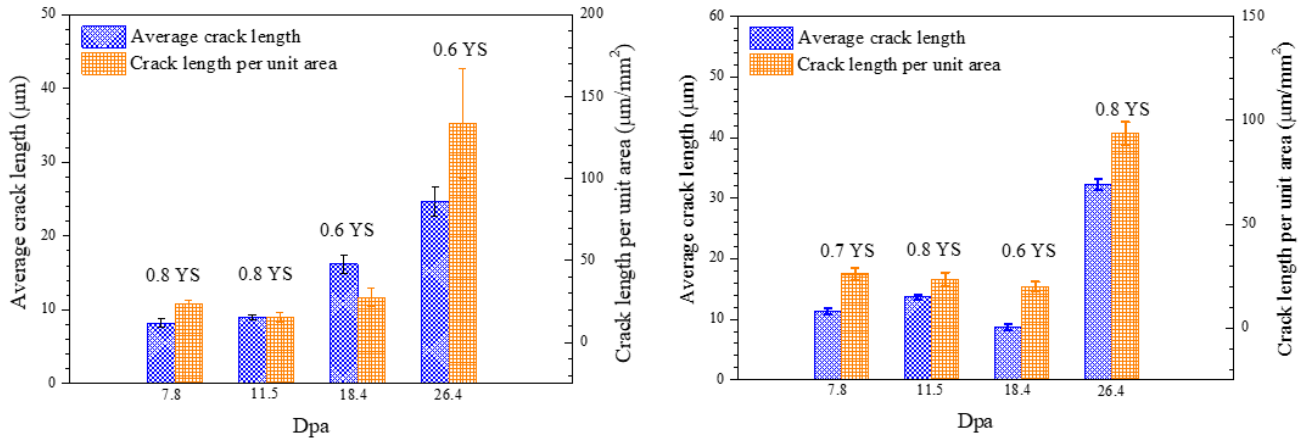


Figure 87. Average crack length (μm) and crack length per unit area ($\mu\text{m}/\text{mm}^2$) for samples tested in KOH water chemistry (left) and LiOH water chemistry (right)

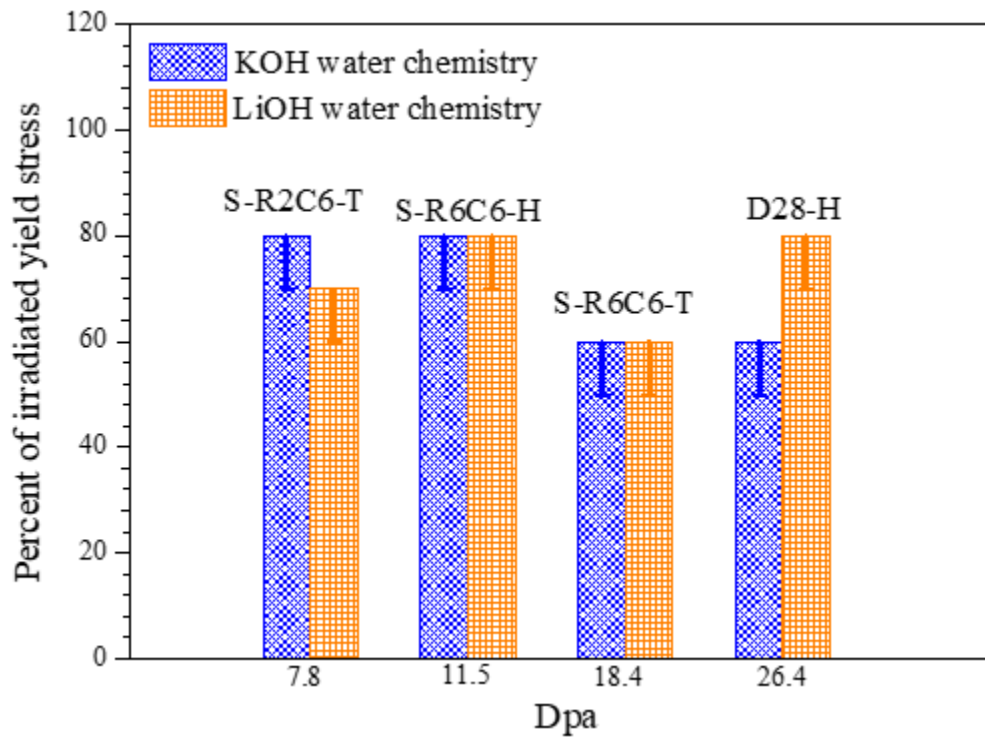


Figure 88. Comparison of crack initiation stress at the investigated dose rates for KOH and LiOH water chemistries

As mentioned previously, a benefit of this method of 4-point bend testing for crack initiation is the ability to identify specific microstructural features associated with crack initiation. In previous research, dislocations channels and manganese sulfide inclusions were identified as precursors for IASCC initiation (Reference 58). In this work however, while such features were present, these were not identified as necessary conditions for IASCC initiation. Oxidation of grain boundaries was observed as a precursor to crack initiation. An excellent example of this is given for specimen D28-H-2 in Figure 89. Here, the progression of grain boundary oxidation to crack initiation can be observed at a triple junction. At 60% of the irradiated yield stress, some oxidation of the grain boundaries can be clearly observed. At 70% of the irradiated yield stress this oxidation has become more severe, while at 80% of the irradiated yield stress crack initiation has occurred.

Figure 90 compares the data in this study to the available crack initiation data from other sources, including the O-ring testing documented in Reference 60. Note that the ‘tails’ on the data points associated with this work are related to the uncertainty in the testing process, where specimens are loaded in increments of 10% of the irradiated yield stress. Generally the data generated in this experiment follow the trend of the available crack initiation data, and all fall above the presently established threshold stress for IASCC initiation. In the author’s opinion, one notable difference between the data generated in this study and the literature data is that the crack initiation data generated by the four-point bend method do not exhibit the same scatter towards high irradiated yield stress as some of the other crack initiation data do. This may be due to the ‘slow strain rate test’ like loading of the four-point bend specimens, creating a stress state potentially more severe than the quasi-static loading targeted by other crack initiation testing methods, such as the O-ring method described in Reference 60.

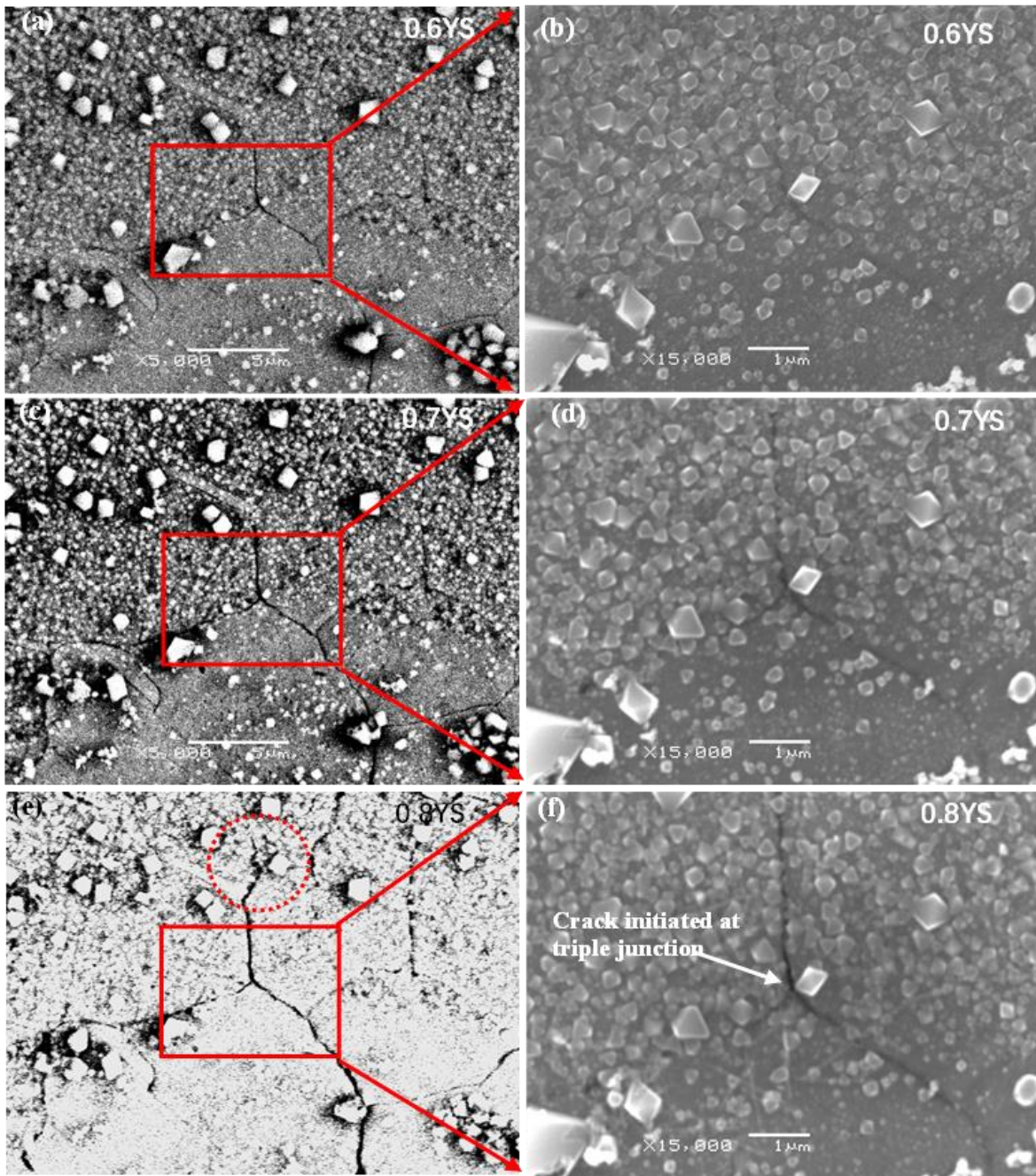


Figure 89. Images in (left) backscatter mode and (right) secondary electron mode of the progression of crack initiation at a location on sample D28-H-2

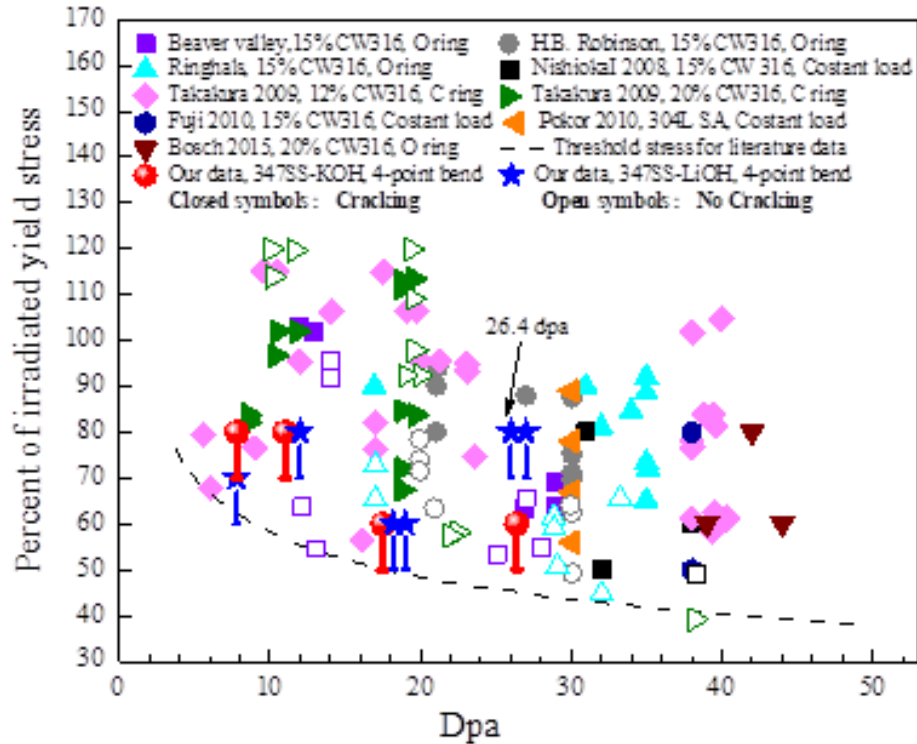


Figure 90. Comparison of data generated in this program to literature data

6.4 Discussion

While further work is in progress in this area, including TEM analysis of specimens during this experiment, the results to date have clear relevance to the topic of this thesis. While no significant difference in crack initiation behavior has been observed between the KOH and LiOH environments in the testing to date, the influence of stress and radiation damage are clear. Figure 87 clearly shows an increase in average crack length and crack length per unit area with increasing radiation damage in both environments, although the reason for this increase is not immediately obvious because saturation of mechanical properties is expected to be essentially complete by 10 dpa, and the largest increase in these measured parameters occurs after 18.4 dpa. The relationship

between stress and crack initiation behavior is quite obvious, as illustrated by Figure 88 and Figure 90 where a threshold stress is required to be exceeded for crack initiation to occur. As this work was the first to conduct testing of its kind on neutron-irradiated Type 347 stainless steel, and presently represents the largest IASCC initiation dataset on such material, it is important to demonstrate that it follows these expected trends which were largely developed on Type 316 stainless steel extracted from flux thimble tubes.

The lack of an effect of changing alkali ions on the crack initiation behavior also goes against the hypothesis put forth in subsection 5.1, expecting LiOH to create a more aggressive environment and enhancing cracking. It could be the case that these alkali ions do not participate in the fracture process. It is also possible that the effect is either below the limit of detection of these experiments due to the inherent scatter in SCC initiation data, or, requires longer experimental times for such a difference to develop. The length of these experiments was only hundreds of hours with testing conducted at high stress conditions intended to accelerate cracking, whereas power plant components operate for decades and would be exposed to such environmental conditions for orders of magnitude more time.

7.0 Proton-Irradiation of Additively Manufactured Materials

This experiment was conducted with the assistance of Ovidiu Toader and Gary Was at the University of Michigan. Funding assistance for the proton irradiation and mechanical testing were provided by NSUF under Rapid Turnaround Experiment (RTE) award number 19-2869.

7.1 Experimental Objectives

Additive manufacturing has the potential to be a transformative manufacturing technology, but appropriate applications must be identified. One concept for additive manufacturing is replacement of out-of-production hardware, such as replacement components for nuclear reactors. This experiment was intended to evaluate the SCC and IASCC susceptibility of Type 316 stainless steel produced by binder jet and laser powder bed fusion (LPBF) additive manufacturing methods for potential use as reactor structural materials.

The three materials selected for study in this experiment included wrought material (fabricated from plate material) as a control sample. LPBF material was selected as this additive manufacturing method can quickly produce dense metallic components, though significant residual stress and elemental segregation can be produced by the rapid laser melting and solidification occurring during this process, which results in a unique microstructure. The process is shown in Figure 91. Essentially, a layer of powder is melted by the laser on to the part being built, which is then lowered in the powder bed and a new layer of powder is spread over it for the melting operation to be repeated, until layer by layer a component is produced. The LPBF

microstructure consists of a series of small melt pools as shown in Figure 92, which can be compared to the more traditional wrought microstructure shown in Figure 41. Examining the LPBF microstructure at higher magnification (Figure 93) a honeycomb or cellular structure can be observed within the melt pools. Binder jet additive manufacturing produce deposits by sintering and infiltration method, and result in specimens that have very different microstructures as those made with LPBF, and do not contain as much residual stresses (Reference 63). This materials selection was intended to allow comparison of essentially the same material, with three different microstructures, to allow this variable to be investigated.

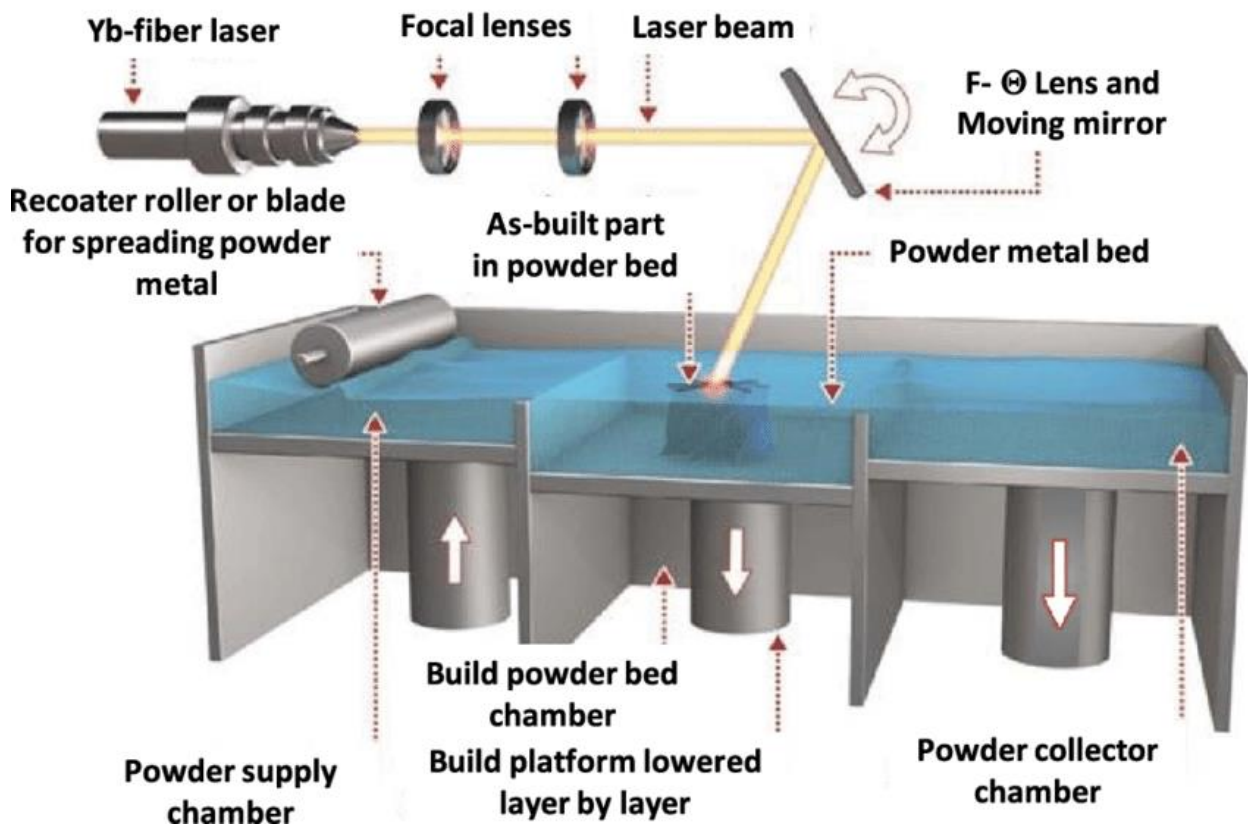


Figure 91. Illustration of the laser powder bed fusion (LPBF) process from Reference 63.

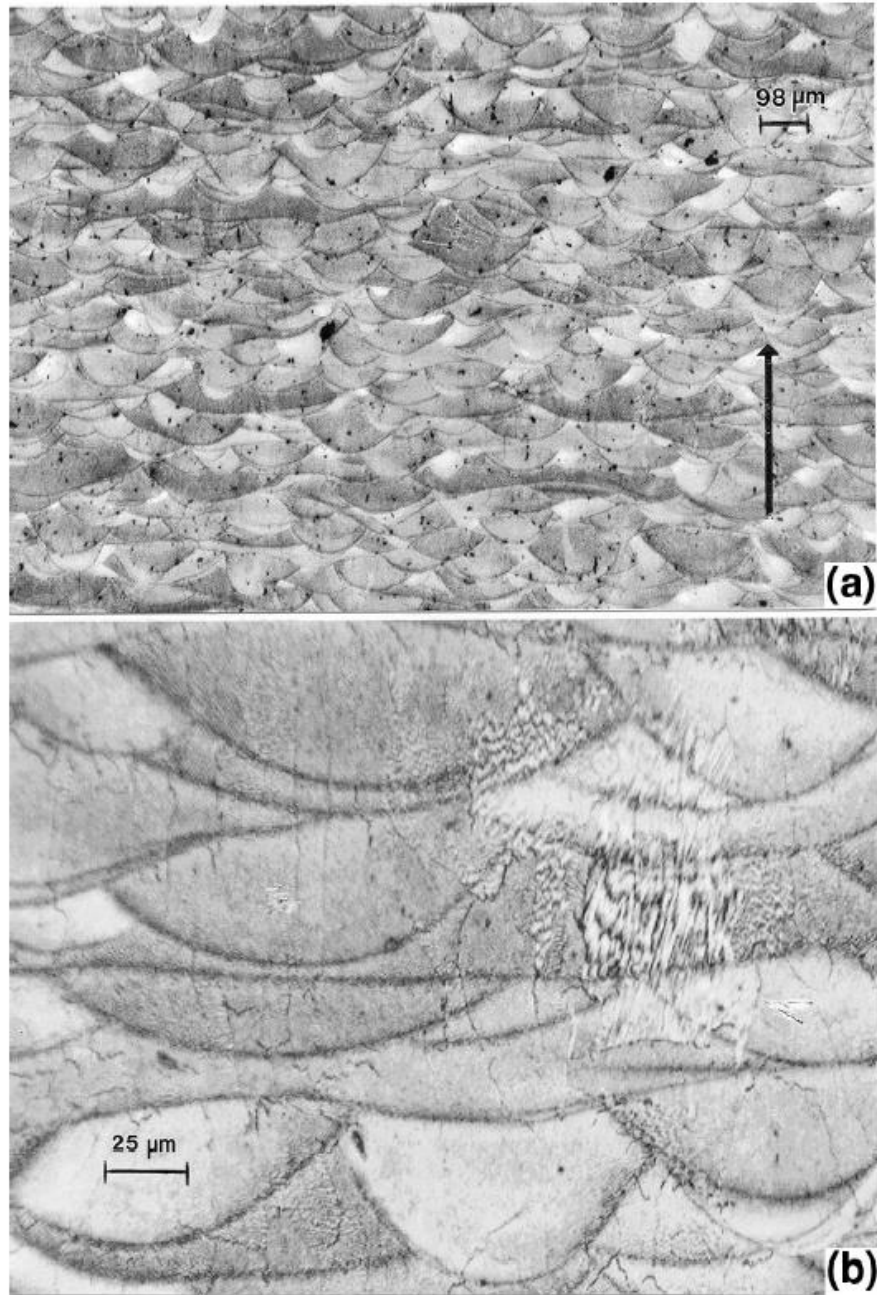


Figure 92. Etched metallographic cross-section of Inconel 718 fabricated by selective laser melting in an argon environment showing the melt pool structure resulting from rapid laser melting and cooling. Arrow indicates build direction. From Reference 65.

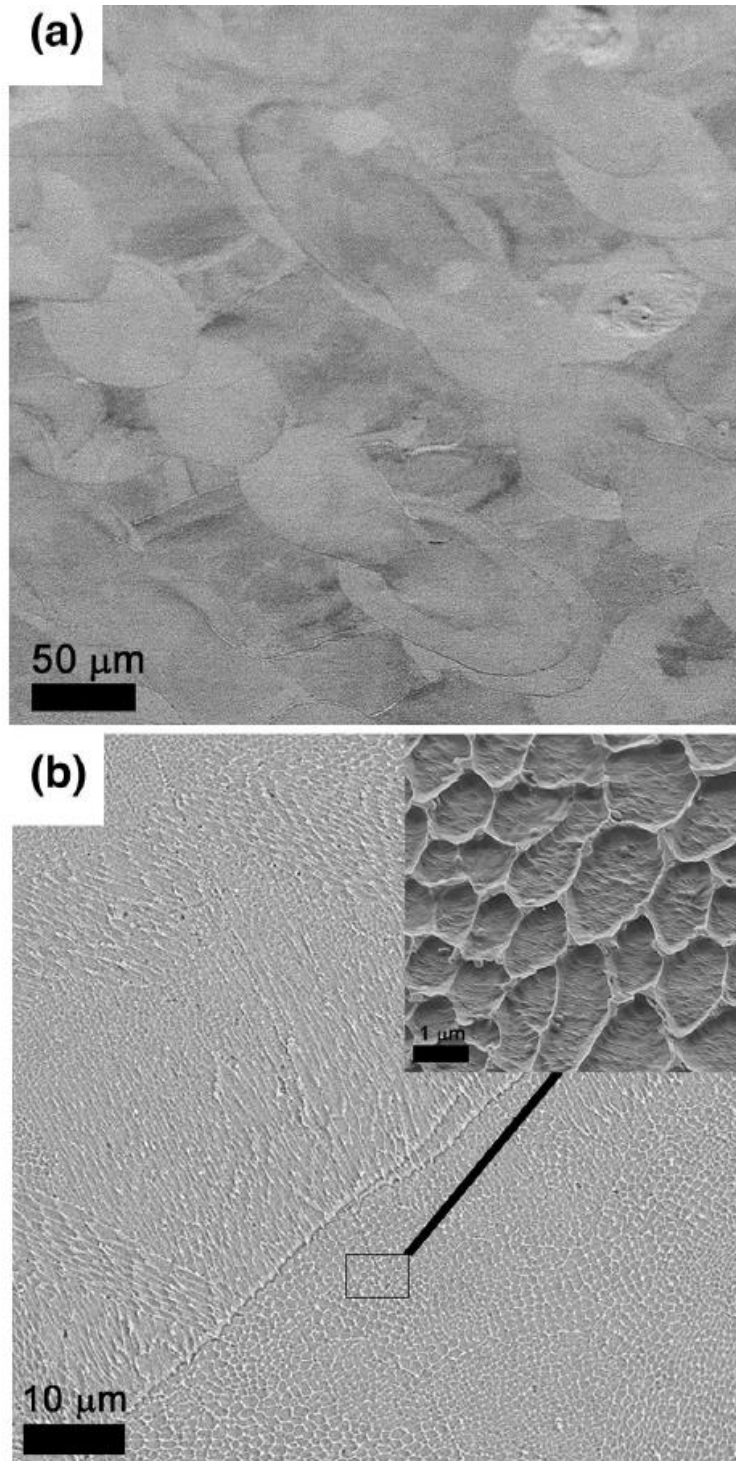


Figure 93. SEM images showing (a) the melt pool structure present in a LPBF Type 316L sample after etching with Vilella's reagent for thirty minutes and (b) the texture of the etched material at the intersection of two melt pools. From Reference 65.

7.2 Methodology

7.2.1 Material and Specimen Fabrication

Type 316 stainless steel wrought material in plate form was provided by Westinghouse to provide material for control samples. These samples were cut from the plate using a water jet cutter. LPBF material was provided by Pitt, utilizing the EOS M 290 system in Pitt's ANSYS Additive Manufacturing Research Laboratory to fabricate the samples. Samples were fabricated using the binder jet method were provided by ExOne, per sketches shown in Figure 94. They were then polished using a rotary tool and a diamond suspension until a mirror-like finish was achieved on the gauge sections of the SCC samples. The samples were not heat treated. The test matrix for the samples is given in Table 15.

Table 15. Test Matrix for SCC susceptibility test

Type 316 Stainless Steel Fabrication Method	Irradiated to 5 dpa, tested in inert environment	Irradiated to 5 dpa, tested in simulated PWR environment
Hot rolled plate (wrought)	X	X
Laser Powder Bed Fusion	X	X
Binder Jet	X	X

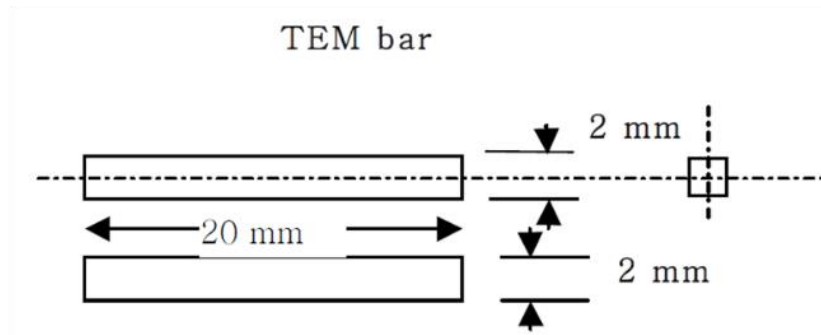
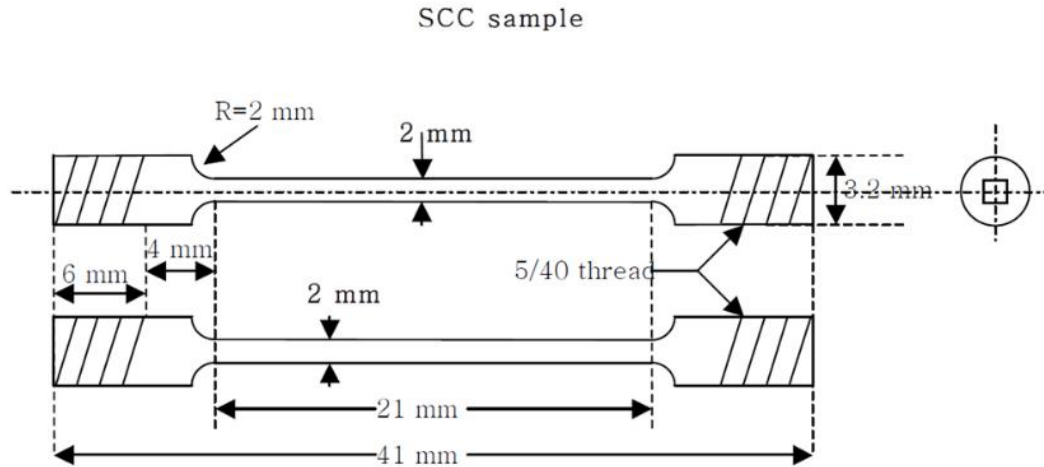


Figure 94. Dimensions of Samples

7.2.2 Sample Irradiation

Proton irradiation was conducted at the University of Michigan Ion Beam Laboratory (MIBL), in beamline 2. While not equivalent to neutron irradiation, protons have been confirmed to be a suitable surrogate for accelerated testing for certain phenomenon, including IASCC initiation, where the behavior of the surface layer of material is critical (References 67 and 68). This irradiation was conducted using 2 MeV protons to an irradiation damage level of 5 dpa at 360°C, maintaining vacuum below 1×10^{-7} torr. The irradiation was performed from November 9, 2020 to November 20, 2020 using 95 total beam hours with an average sample current of 28 μ A. The

proton beam was rastered over the irradiation area of the sample. The experiment was paused due to staffing (watchers) scheduling and availability, but the samples were cooled to under 200°C during all pauses. Specimen irradiation temperature was maintained using the heated stage design shown in Figure 95, and monitored using a thermal imaging system. The thermal imaging system was calibrated prior to the start of the irradiation. Three AOIs were set per sample to measure the sample temperature with the thermal imager.

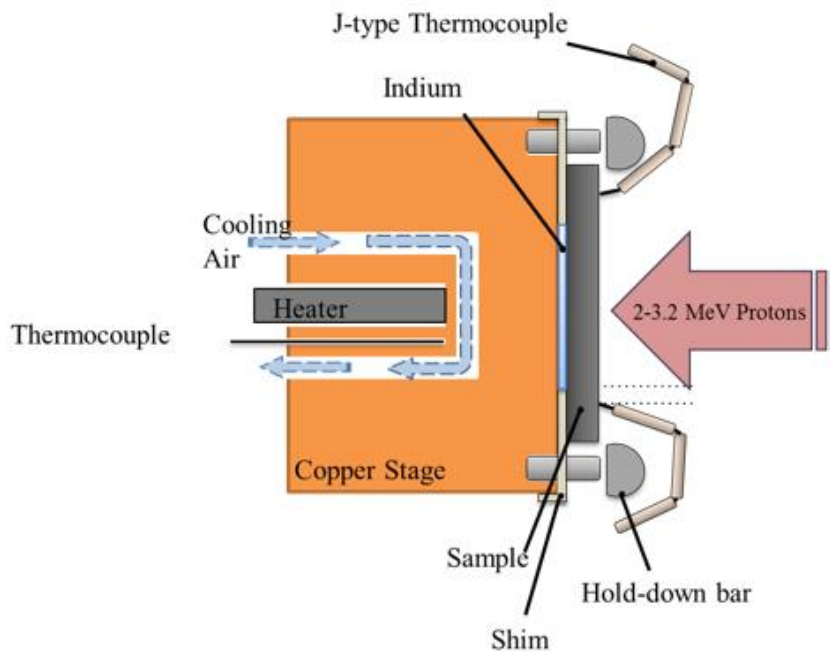


Figure 95. Stage Design

To understand the resulting depth of radiation damage, a calculation was performed using the Stopping Range of Ions in Matter (SRIM) code. A simulation (Figure 96) conducted using the achieved irradiation parameters indicates an irradiation damage depth of approximately 20 μm .

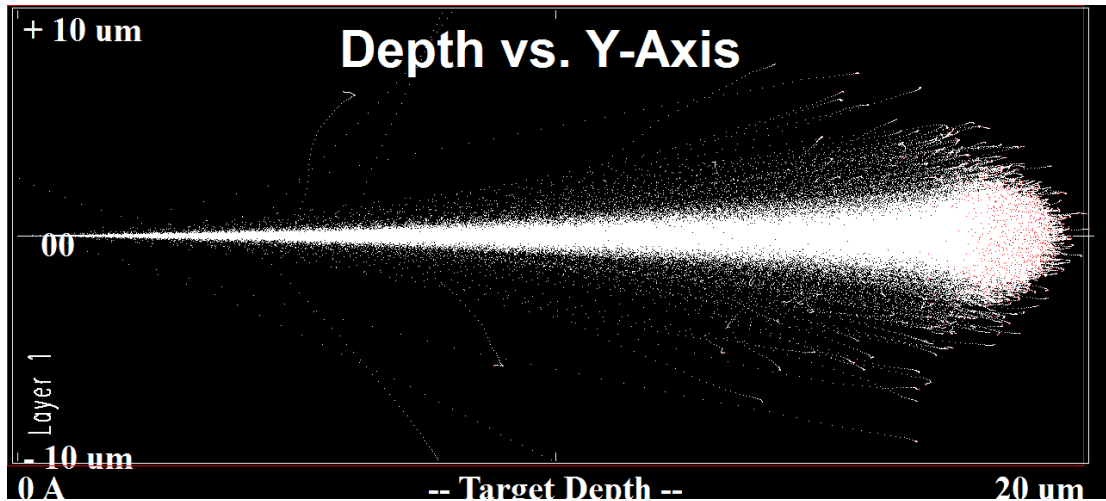


Figure 96. SRIM Results indicating depth of irradiation

In total, it is possible to fit eight tensile bars on the stage for irradiation, with eight TEM bars placed in the gap between the tensile bars, allowing for an effectively continuous metal surface to be irradiated (example shown with 4 tensile bars in Figure 97), which is important for proper irradiation and temperature control. So in addition to the six tensile specimens listed in Table 15, an additional tensile sample each of the binder jet and LPBF material, for a total of eight, were irradiated. The specimen distribution of the TEM bars followed that of the tensile specimens: that is, three LBPF, three binder jet, and two wrought TEM bars were irradiated in the same irradiation evolution as the eight tensile bars.

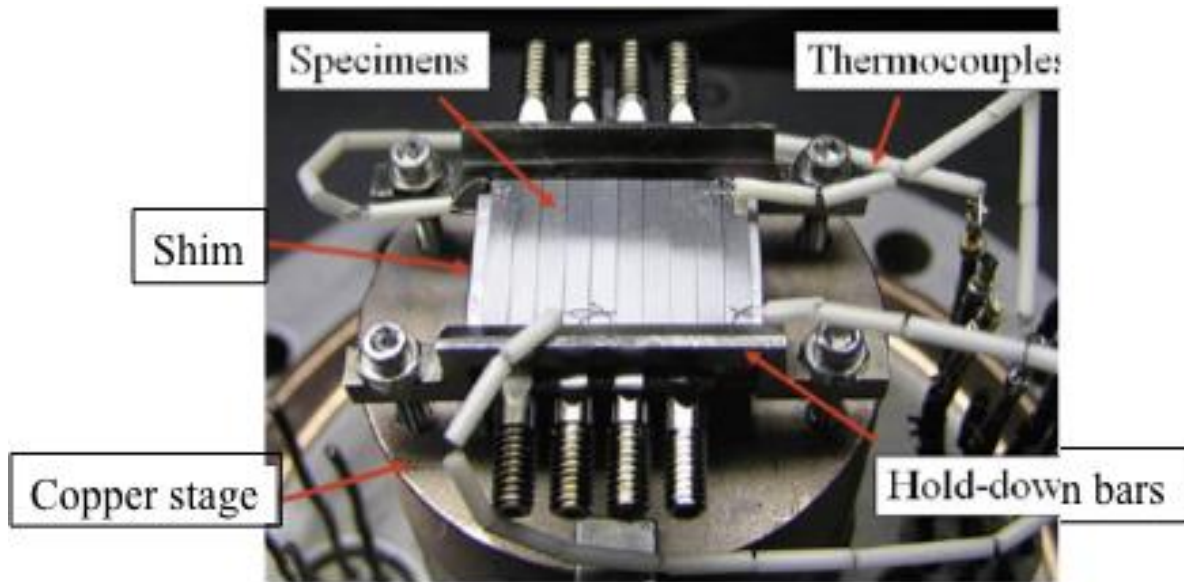


Figure 97. Tensile samples and TEM bars mounted on irradiation stage. Picture courtesy of the University of Michigan

7.2.3 Testing Procedure

To generate cracks within the tensile samples, constant extension rate tests (CERT) were performed in the Irradiated Materials Testing Complex at the University of Michigan in a stainless steel recirculating autoclave equipped with a loading frame capable of loading four tensile samples at once. One proton-irradiated tensile bar fabricated from each material type (wrought, LPBF, and binder jet) was tested in argon, and one of each material type was tested in simulated PWR water. As the proton irradiation only affects one of the four faces of the tensile samples, irradiated and unirradiated material is tested simultaneously on each sample.

Both CERT tests were conducted at 340°C. The strain rate for the test in argon was $\sim 1.5 \times 10^{-7}/s$ (minimal strain rate that can be achieved for the gauge length on the available test system) and it was $1 \times 10^{-7}/s$ for the test in PWR water. The simulated PWR water contained 1000 ppm B and 2 ppm Li, 35cc/kg H₂ with an outlet conductivity of $\sim 20 \mu S/cm$.

7.2.4 Sample Evaluation

Post-test examinations were performed at Westinghouse Churchill Site. For initial imaging, all samples were mounted on a stage with the irradiated side facing up. Later, to image the unirradiated side of the sample, each sample was rotated 180 degrees, so that the face of the sample opposite the irradiated face was imaged. The sample order was planned and recorded photographically (Figure 98), as each individual sample did not contain an identifier, and so it would be possible to mix up samples if care was not taken. The samples were mounted to the stage one at a time, and the labeled vials the samples were extracted from were kept in the same order as the samples on the microscopy stage. The samples were imaged primarily using a Tescan Lyra-3 GMU dual-beam SEM, although a Tescan Vega system was also used to image some of the specimens at times due to instrument availability.

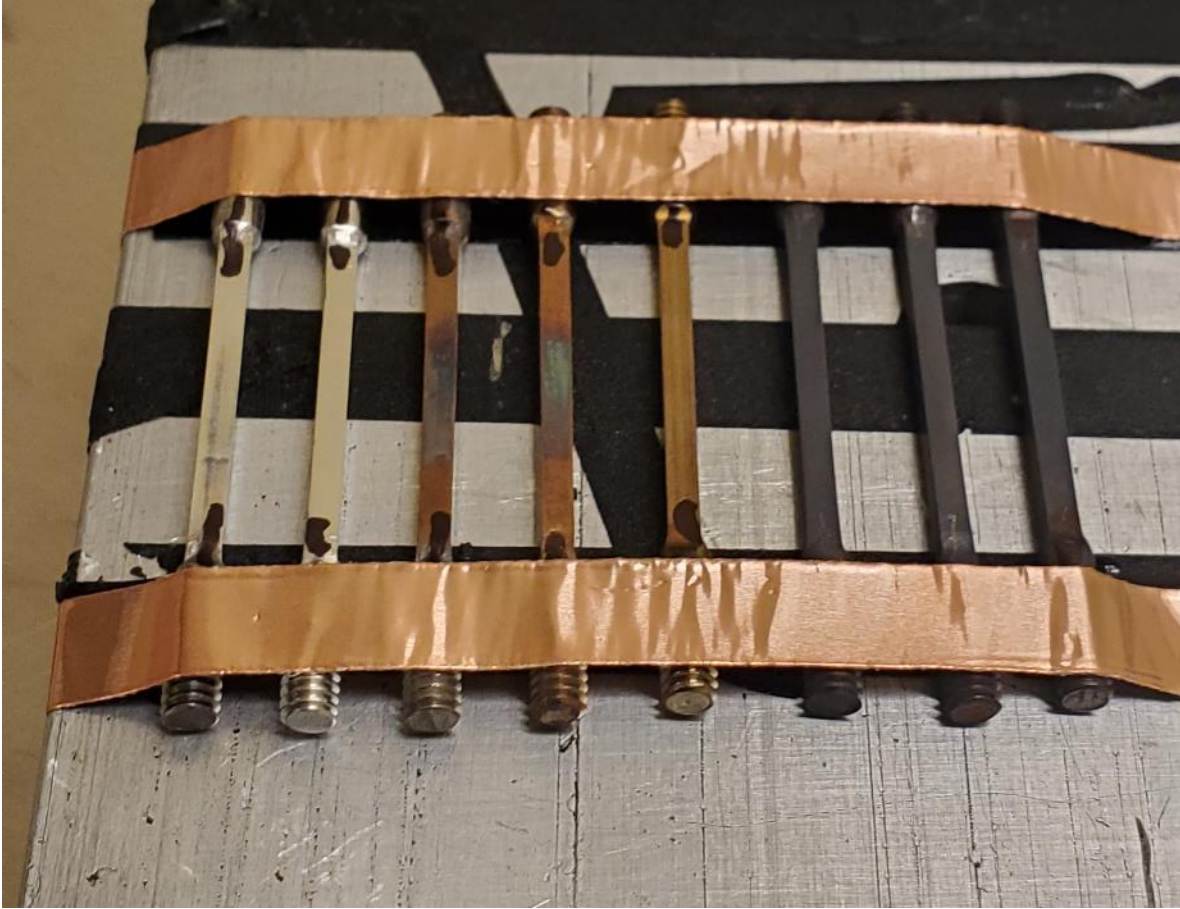


Figure 98. Sample mounting for automated image capture of gauge sections

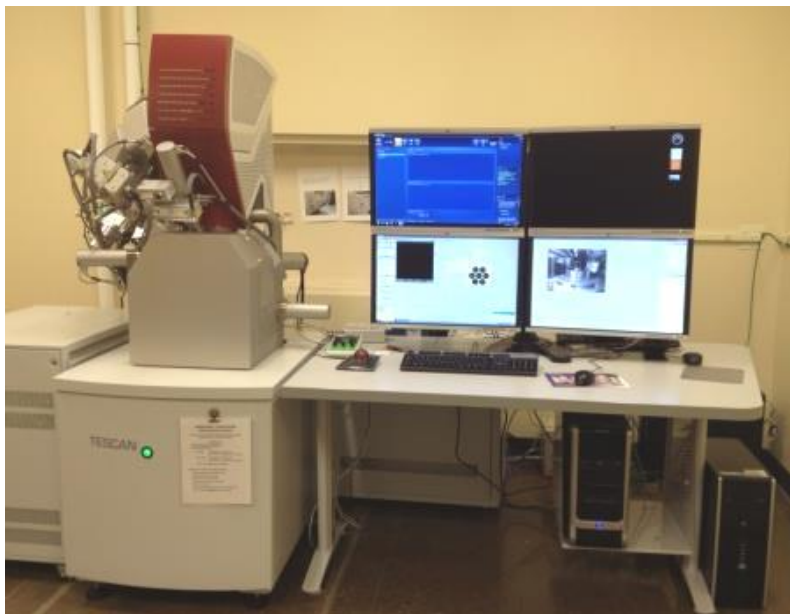


Figure 99. Tescan LYRA-3 at Westinghouse Churchill Site

Imaging was conducted 30 KeV and began by taking montages of each gauge section using the secondary electron detector. By utilizing the automated image capture system, large quantities of data were collected, typically overnight when the instrument would not otherwise have been in use. Additional higher-magnification images were taken at specific regions of interest. This instrument is also equipped with an Oxford Instruments X-Max N-80 silicon drift detector for Energy-dispersive X-ray Spectroscopy characterization.

Ultimately, upon examination of the specimens, it was found that the presence of cracking was not “binary.” It was initially expected that cracking either would, or would not, be present on material of a given condition. For example, the extent of cracking observed in unirradiated material was not anticipated. Therefore, to allow for meaningful comparison of samples, a quantitative method of evaluating cracking was required. The automated image capture process captured hundreds of images for each sample, which provided the basis for this quantitative method of cracking evaluation. A subset of these images were analyzed, with the center of the gauge section (where irradiation would have taken place as applicable) being the focus of this evaluation. At least 100 images analyzed for each mechanically-tested condition; that is, for the six samples strained to 4%, images from both the irradiated and unirradiated side of the sample were evaluated. This evaluation included measuring the length of cracking present on each image and noting the presence of defects.

7.3 RESULTS

7.3.1 Constant Extension Rate Tests

Figure 100 shows the stress-strain curve for the tests in argon and Figure 101 shows the stress-strain curve for the tests in PWR water. The small “noise”-like features seen on the curves are likely due to dynamic strain aging (DSA), which is common at this strain rate and temperature. The binder jet sample reached 4% earlier due to lower yield stress. All samples were unloaded when the binder sample reached 4% which caused the big drops for the reference and laser sample in the stress-strain curves. The wrought (reference) and LBPF samples were then strained further to reach 4% plastic strain. The yield strength values determined from these tests are given in Table 16.

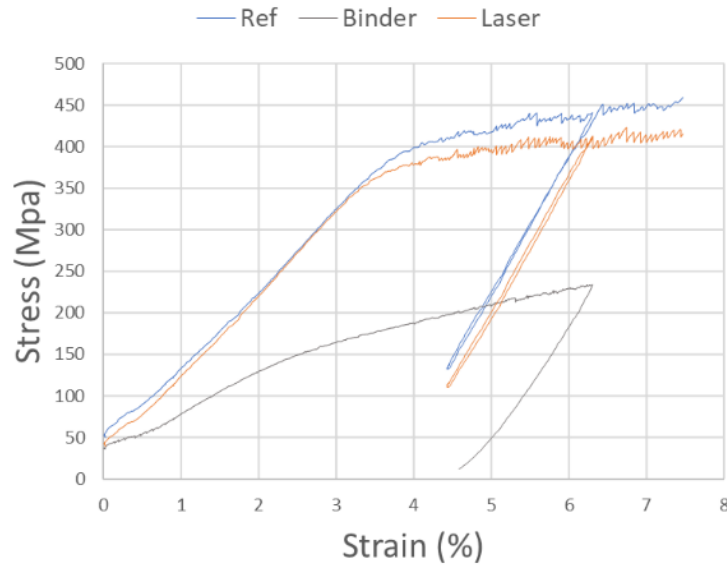


Figure 100. CERT Results in Argon

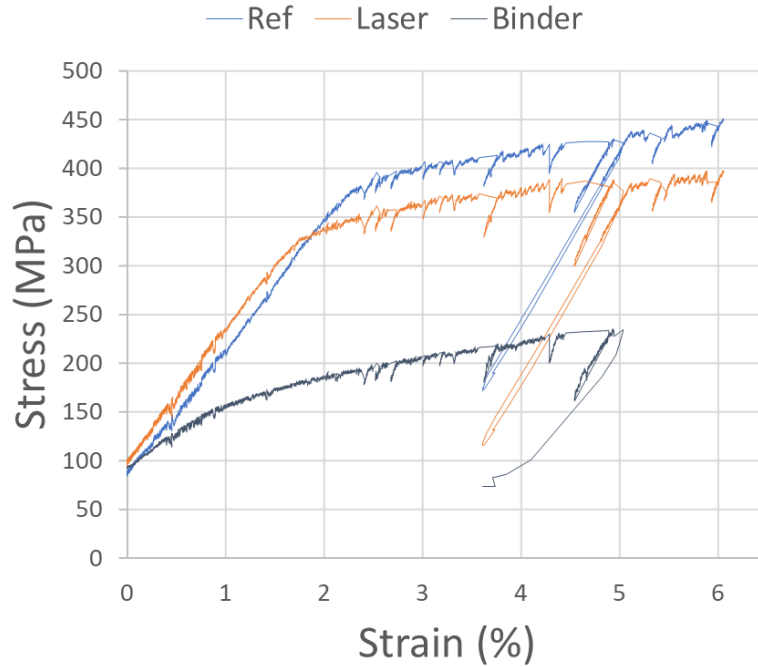


Figure 101. CERT Results in PWR water

Table 16. Yield strength determined from CERT

Environment	Material	Y.S. (0.2%), MPa	Plastic Strain (%)
ASTM A240 Type 316L*		170	-
PWR	Wrought	390	4.14±0.05
	LPBF	375	4.14±0.05
	Binder Jet	148	3.77±0.05
Argon	Wrought	385	3.95±0.05
	LPBF	333	4.05±0.05
	Binder Jet	140	3.76±0.05

*Note the CERT test is not intended to determine yield strength for comparison to ASTM criteria, but the comparison is instructive.

7.3.2 Sample Evaluation

The chemical composition of the samples was measured on the as-received surfaces of the gauge lengths, with results given in Table 17.

Table 17. EDS results on the as-received surface of the samples

Element	ASTM A240 Type 316 L	Binder Jet	LPBF	Wrought
Al	-	0.3	0.2	0.3
Si	0.75 max	0.7	0.5	0.6
Cr	16-18	15.1	17.0	16.9
Mn	2.0 max	0.7	1.3	2.0
Fe	Bal.	69.2	65.9	65.0
Ni	10-14	9.5	11.5	9.6
Mo	2-3	1.8	2.4	2.1

The first sample examined was the as-irradiated (but unstrained) binder jet sample. This sample had numerous defects in the sample surface, which may have been porosity from the binder jet printing process, or particles of material that were pulled out of the surface during polishing. These defects are large, on the order of 50 to 100 microns, and are related to the sample fabrication, rather than the irradiation. An example of the sample surface is given in Figure 102. No significant difference between the irradiated side of the sample and the unirradiated side of the sample was noticed.

The second sample examined was the as-irradiated LPBF sample (Figure 103). This material appears to have less porosity than the binder jet material, although some finer pores are present. These are on the scale of a few microns. Again, these are most likely due to porosity from the LPBF process. There are also a substantial number of scratches visible on the sample surface, oriented along the tensile axis of the specimen. For the strained samples, it is expected

that cracks would initiate perpendicular to the tensile direction and these scratches, so they should not significantly hamper the identification of cracks in the strained samples. No significant difference between the irradiated side of the sample and the unirradiated side of the sample was noticed.

The third sample evaluated was the irradiated binder jet sample strained to 4% in argon. This strain caused profuse cracking of the sample (Figure 104). This cracking was not limited to the center of the gauge region where the irradiation occurred, and was also present in quantity on the unirradiated side of the sample. This cracking was occasionally associated with defects, but as many more cracks appear away from defects, these do not seem to be the cause of the cracking. Some evidence of slip-step like features was observed.

The LPBF sample strained to 4% in argon had a few small cracks, and slip bands could clearly be observed (Figure 105). These features were present on both the irradiated and unirradiated side of the sample.

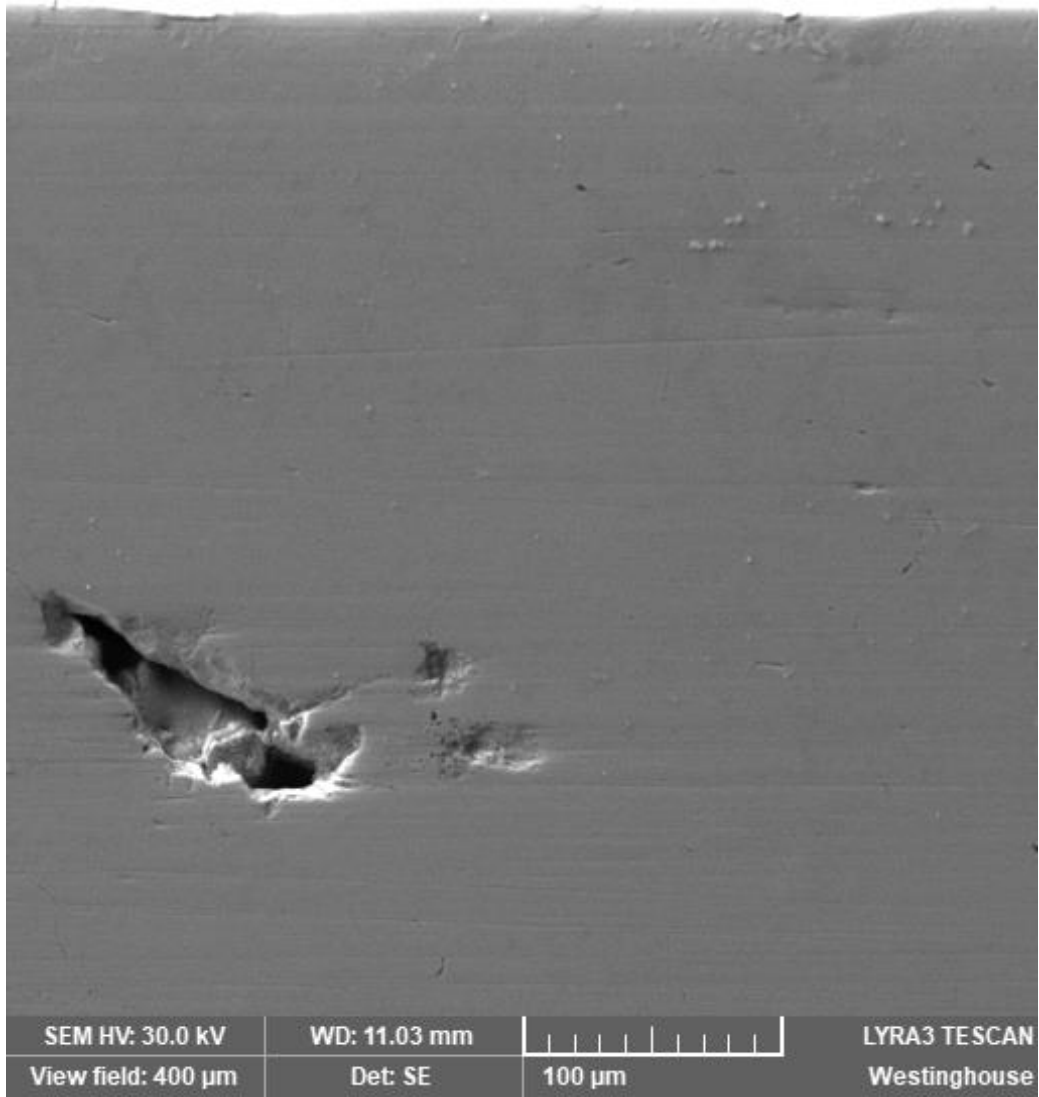


Figure 102. Example of image of surface of as-irradiated binder jet tensile sample

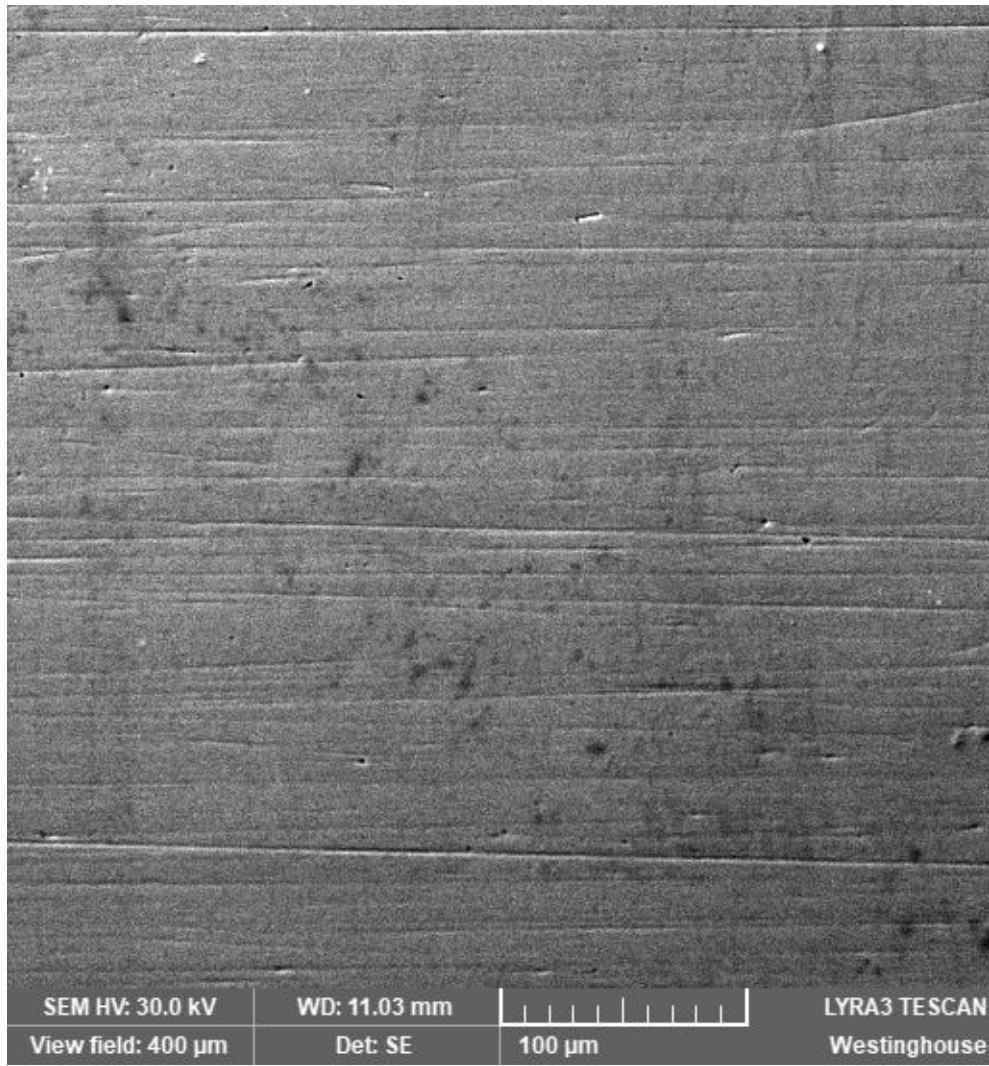


Figure 103. Example image of surface of as-irradiated LPBF tensile sample

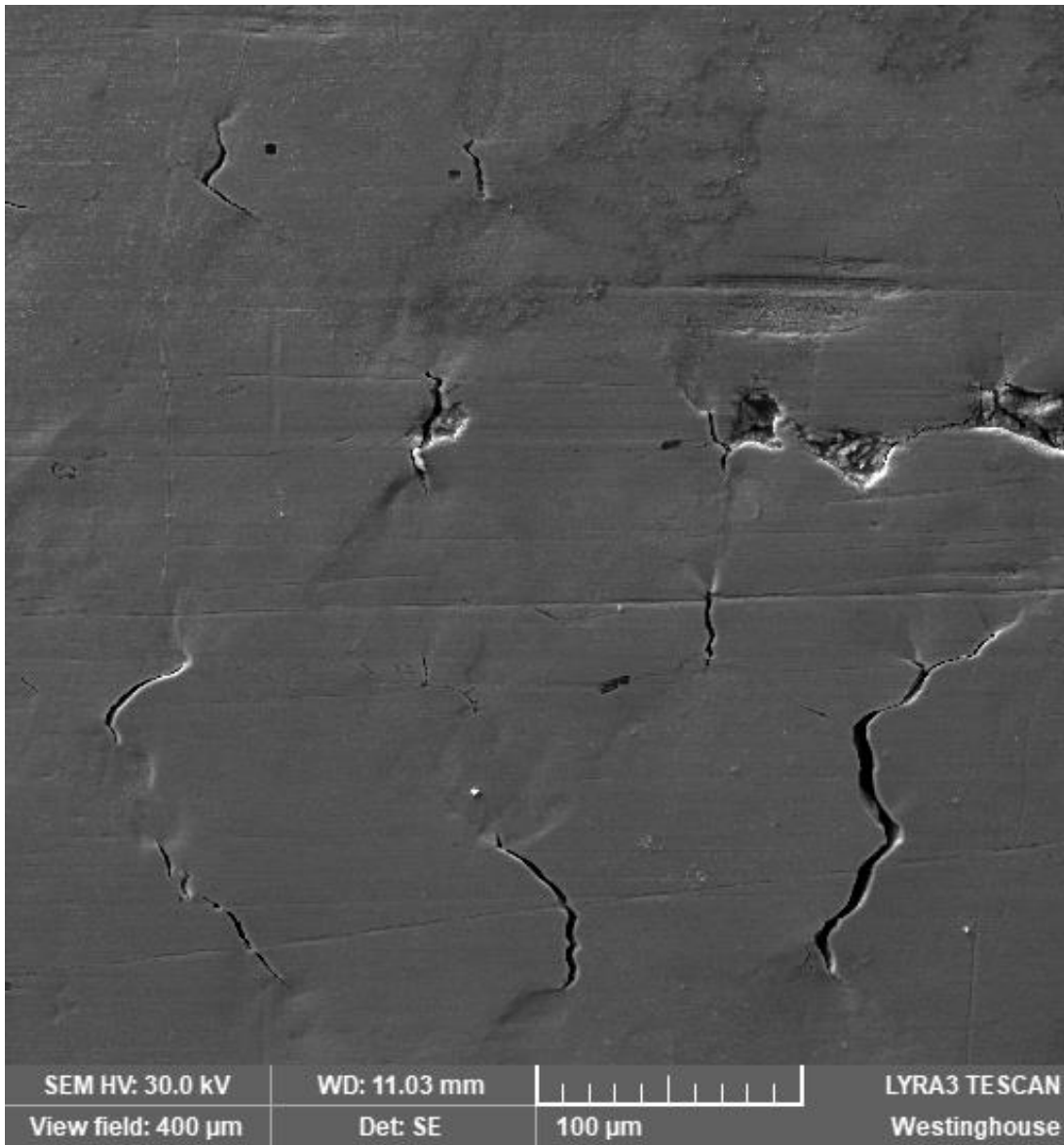


Figure 104. Example image of surface of irradiated binder jet CERT sample after 4% strain in argon. The strain direction was horizontal in this image.

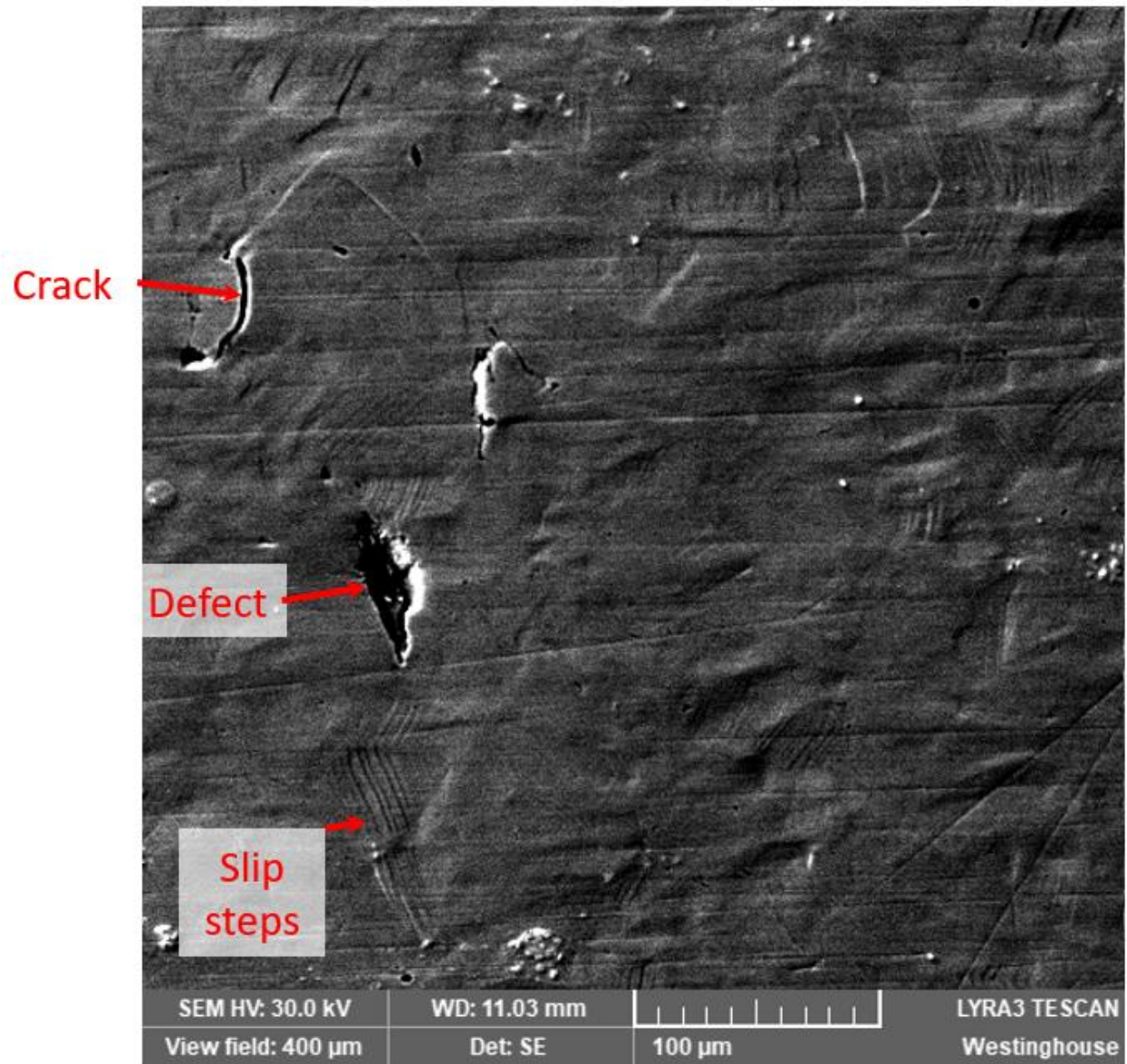


Figure 105. Example image of surface of LPBF sample strained to 4% in argon, with slip steps and cracks visible. The strain direction was horizontal in this image.

The irradiated wrought specimen strained to 4% in argon (Figure 106) had slip steps covering the majority of the specimen surface. Very few cracks were identified on this sample, though cracking was present on both the irradiated and unirradiated side of the specimen.

The irradiated binder jet sample strained to 4% in simulated PWR water is shown in Figure 107. Extensive cracking was present on both the irradiated and unirradiated side of the sample. The sample has hydrothermal deposits decorating the surface, however these appeared to be patchy rather than uniform. This prompted EDS mapping of an area of this sample (Figure 108 and Figure 109). This EDS mapping identified a network of regions of elemental segregation which were enriched in chromium, molybdenum, and to some extent, manganese, but depleted in nickel. This is again likely a result of the binder jet printing process, which relies on a sintering step to achieve full density. The network of regions of elemental segregation were likely former boundaries between individual particles. The initiation or growth of some of the cracks does appear to be associated with this compositional segregation, with some cracks bridging the chromium and molybdenum rich regions, and some cracks seeming to follow them. However, there are also many cracks which do not appear associated with this feature. Such elemental segregation at this scale was not in evidence in the wrought or LPBF samples.

The irradiated LPBF sample (Figure 110) had more uniform and dense hydrothermal deposits on the surface, and some amount of cracking. Cracking was observed both as larger (25 to 50 micron) sized cracks, and also some amount of fine scale cracking. This type of cracking was observed both close to the larger cracks (Figure 111) and isolated from larger cracks (Figure 112). These features were present on both the irradiated and unirradiated side of the sample.

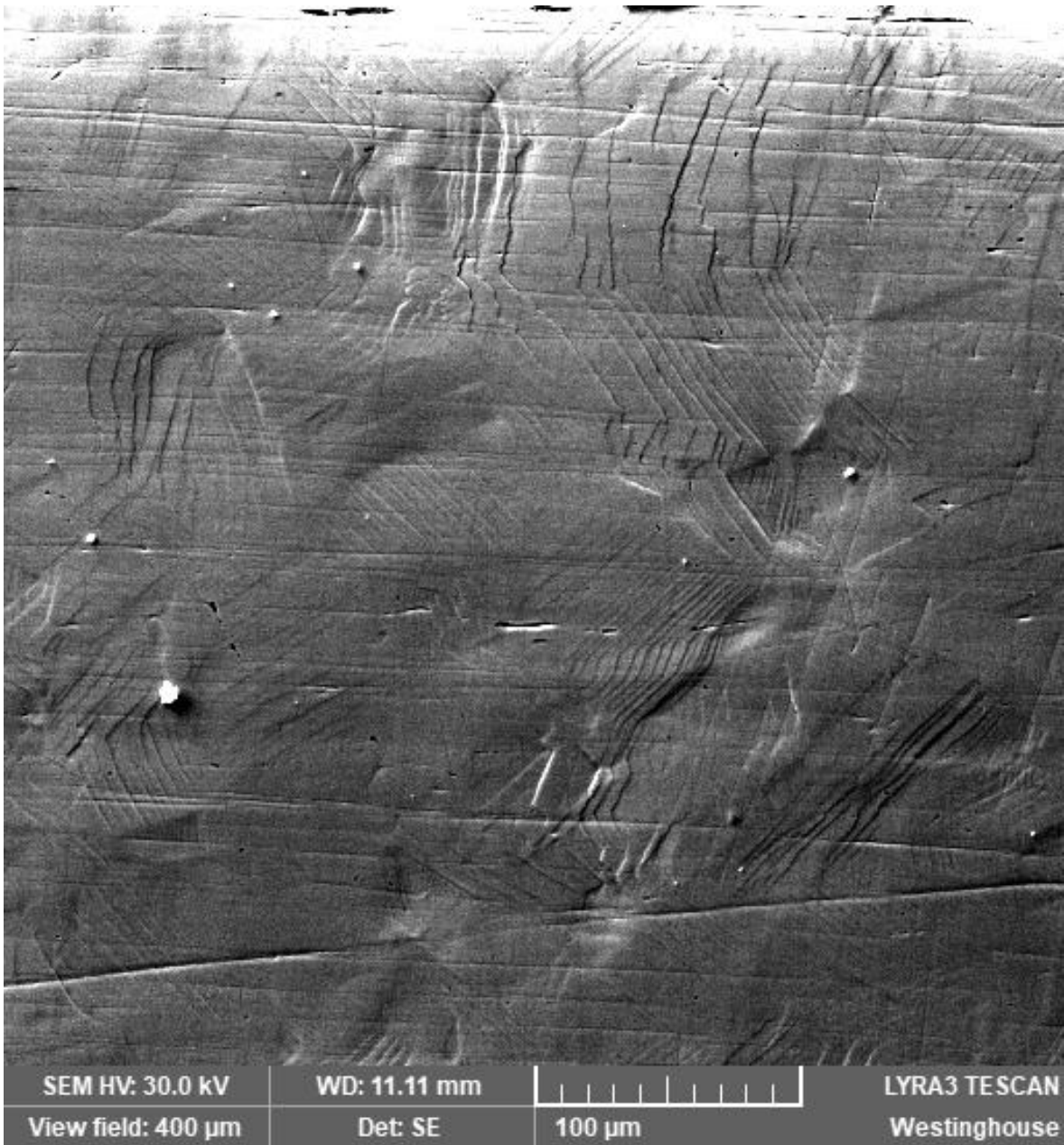


Figure 106. Example image of surface of wrought sample strained to 4% in argon, with slip steps visible. The strain direction was horizontal in this image.

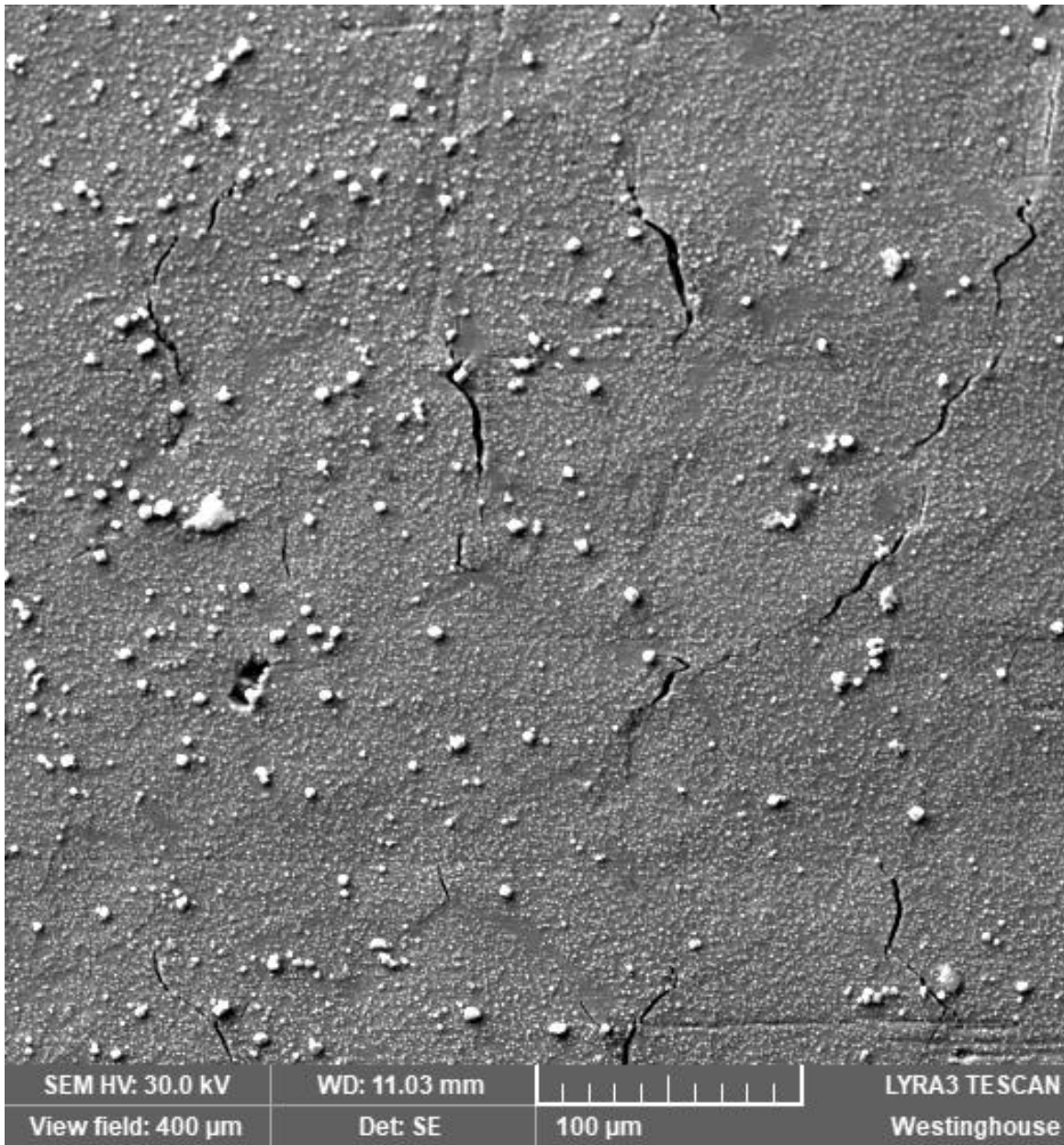


Figure 107. Example image of surface of binder jet sample strained to 4% in simulated PWR water, with hydrothermal oxide deposits decorating the surface and cracking observed. Strain direction was left to right in this image.

Electron Image 2

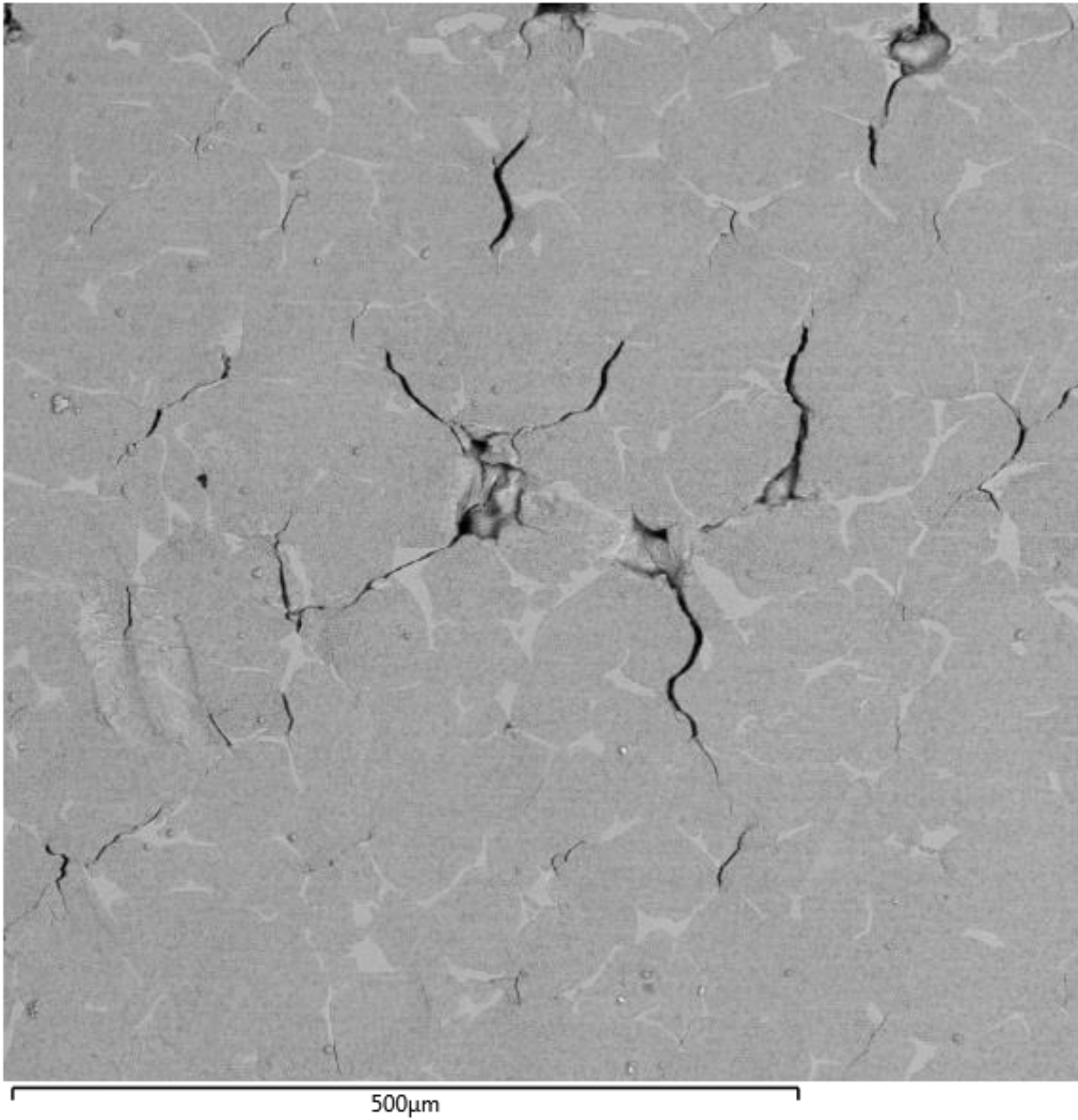


Figure 108. SEM image for EDS map of irradiated binder jet sample strained to 4% in simulated PWR water. This image was taken in backscatter mode.

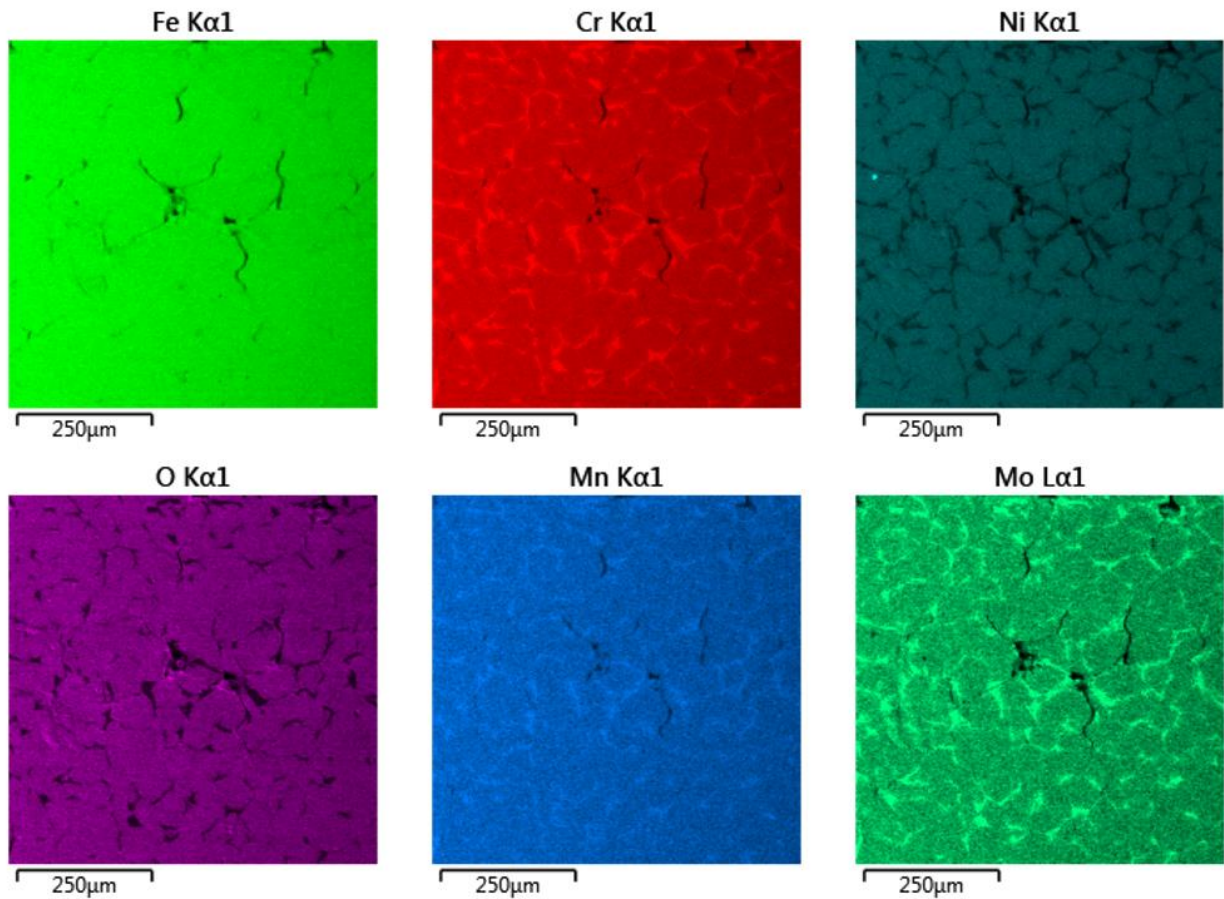


Figure 109. EDS maps of irradiated binder jet sample strained to 4% in simulated PWR water.

The irradiated wrought sample (Figure 113) showed largely uniform hydrothermal deposits, and some amount of cracking. These features were present on both the irradiated and unirradiated side of the sample.

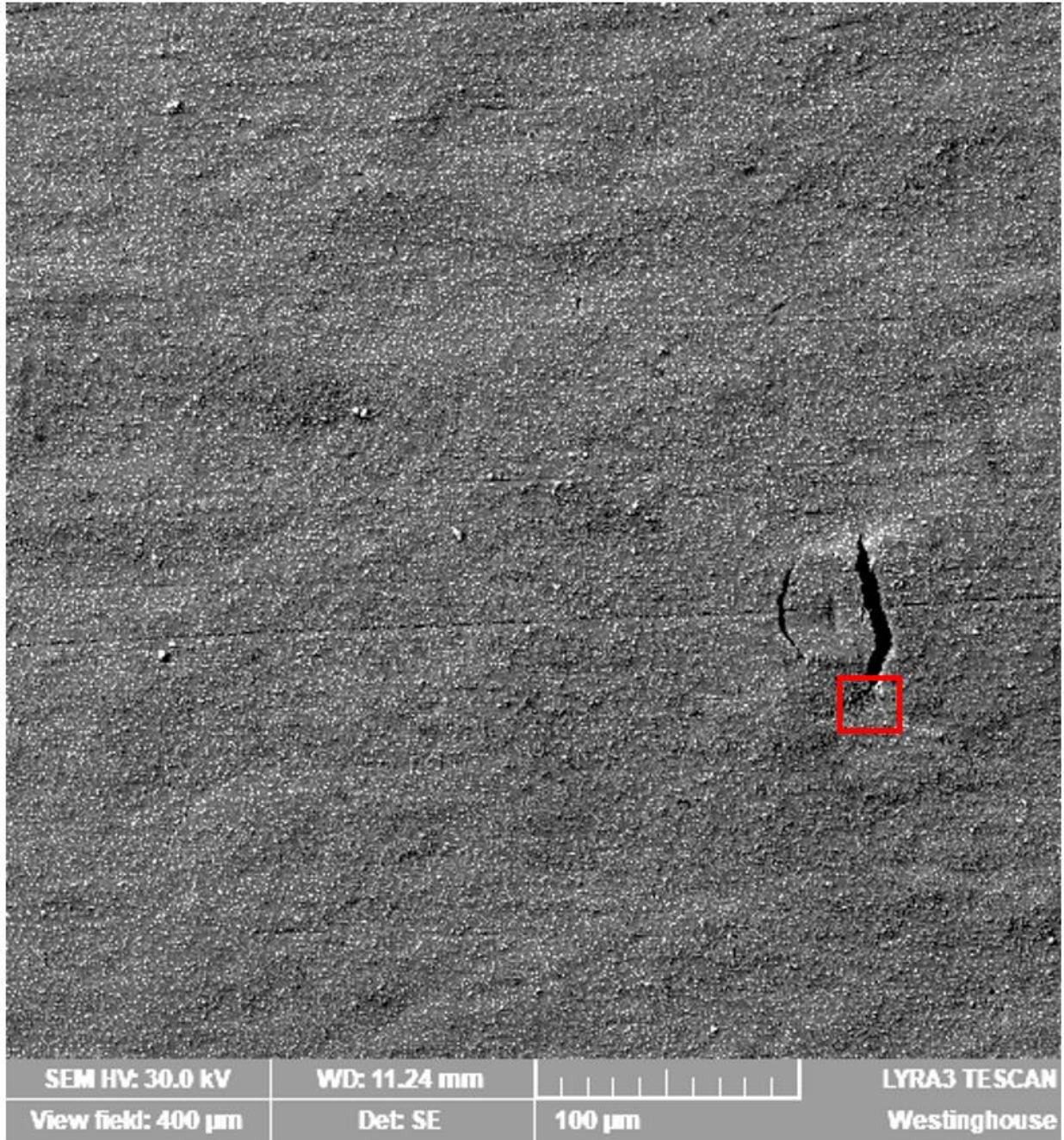


Figure 110. Example image of surface of LPBF sample strained to 4% in simulated PWR water. The red box indicates area of higher magnification shown in Figure 111. Strain direction was left to right in this image.

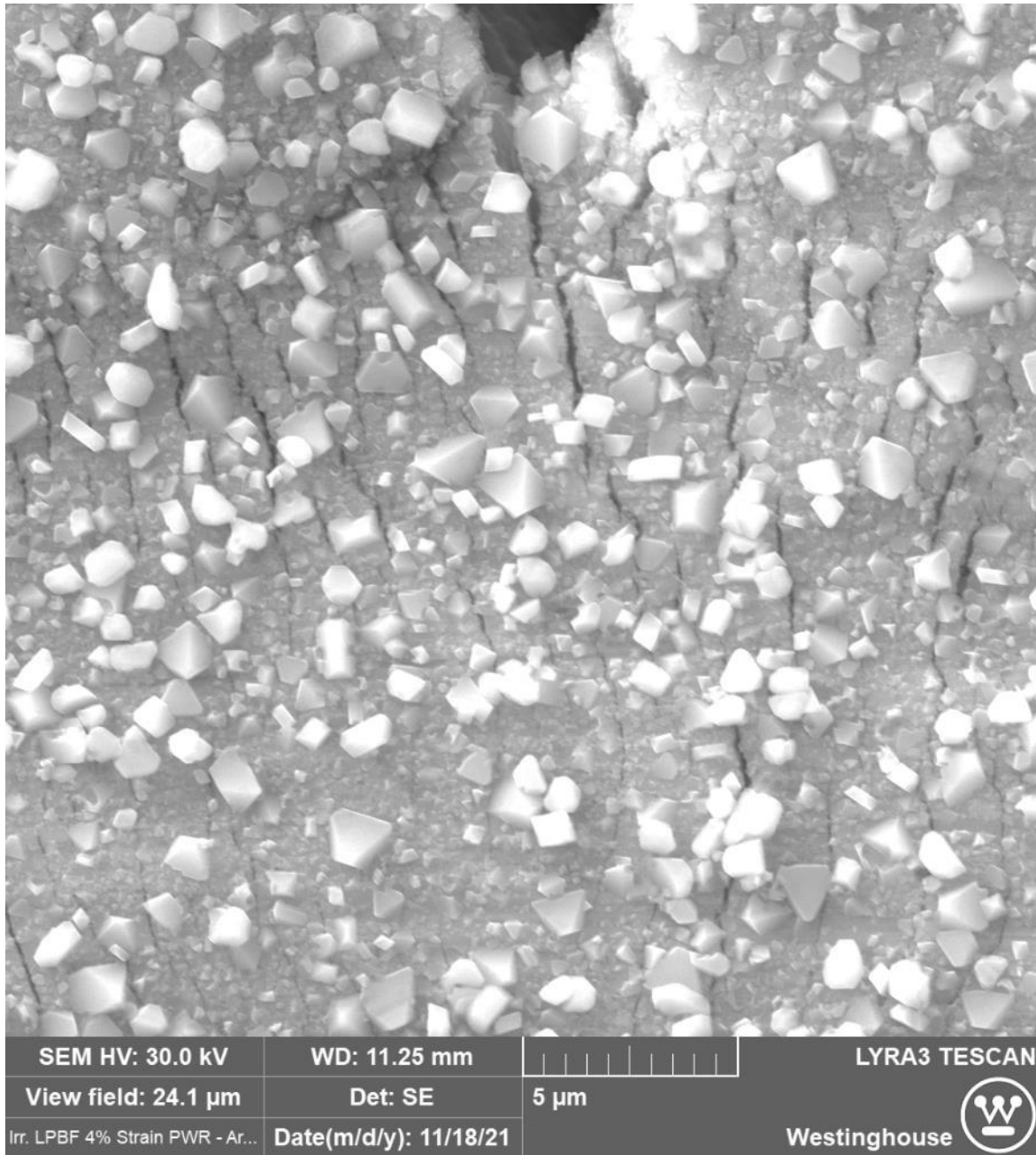


Figure 111. Enlarged image of region indicated in Figure 110 on the surface of LPBF sample strained to 4% in simulated PWR water, showing fine scale cracking emanating from crack tip of larger crack. Strain direction was left to right in this image.

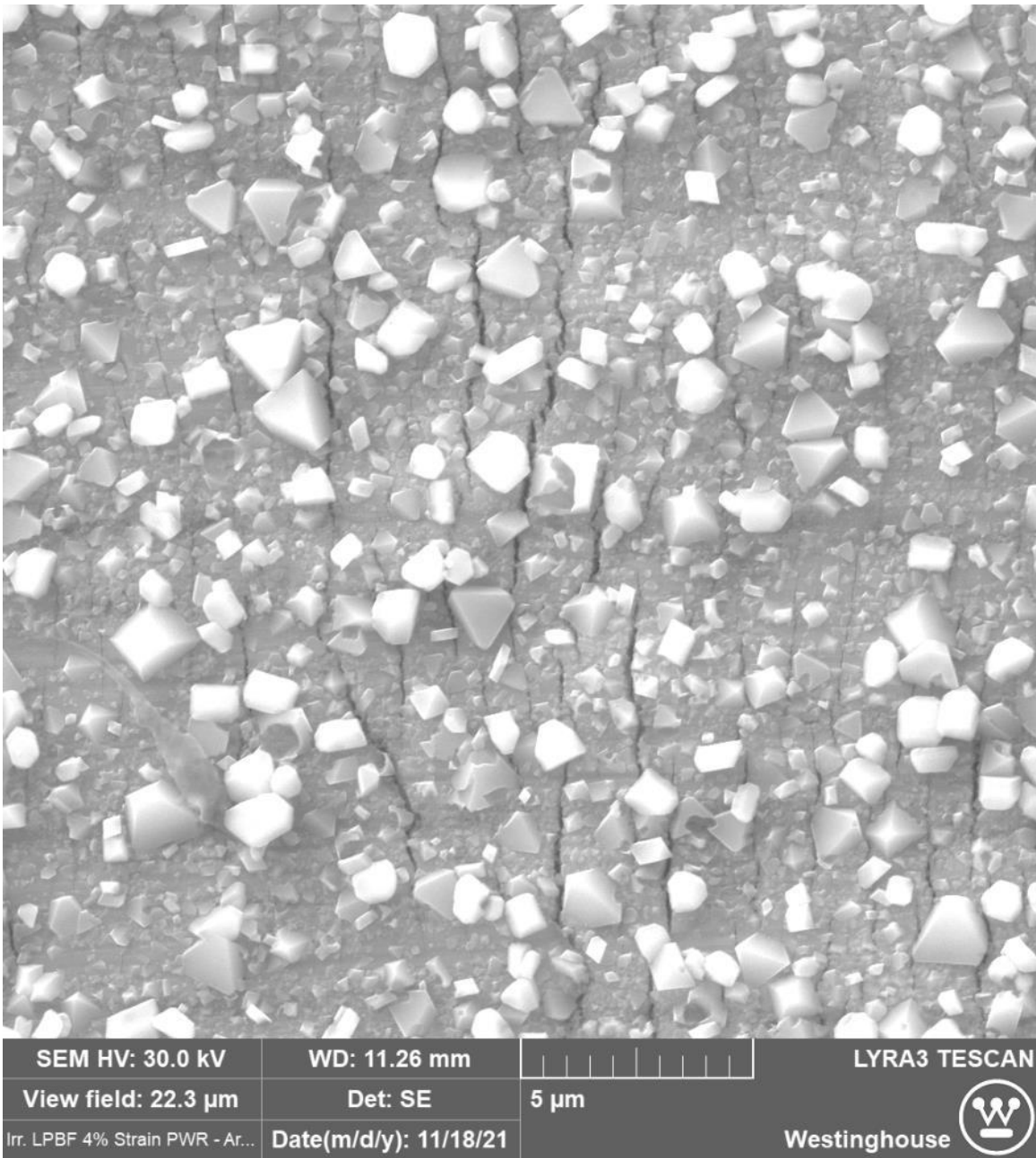


Figure 112. Example image of surface of LPBF sample strained to 4% in simulated PWR water showing isolated fine cracking. This region was far way from any larger cracks such as that visible in Figure 110. Strain direction was left to right in this image.

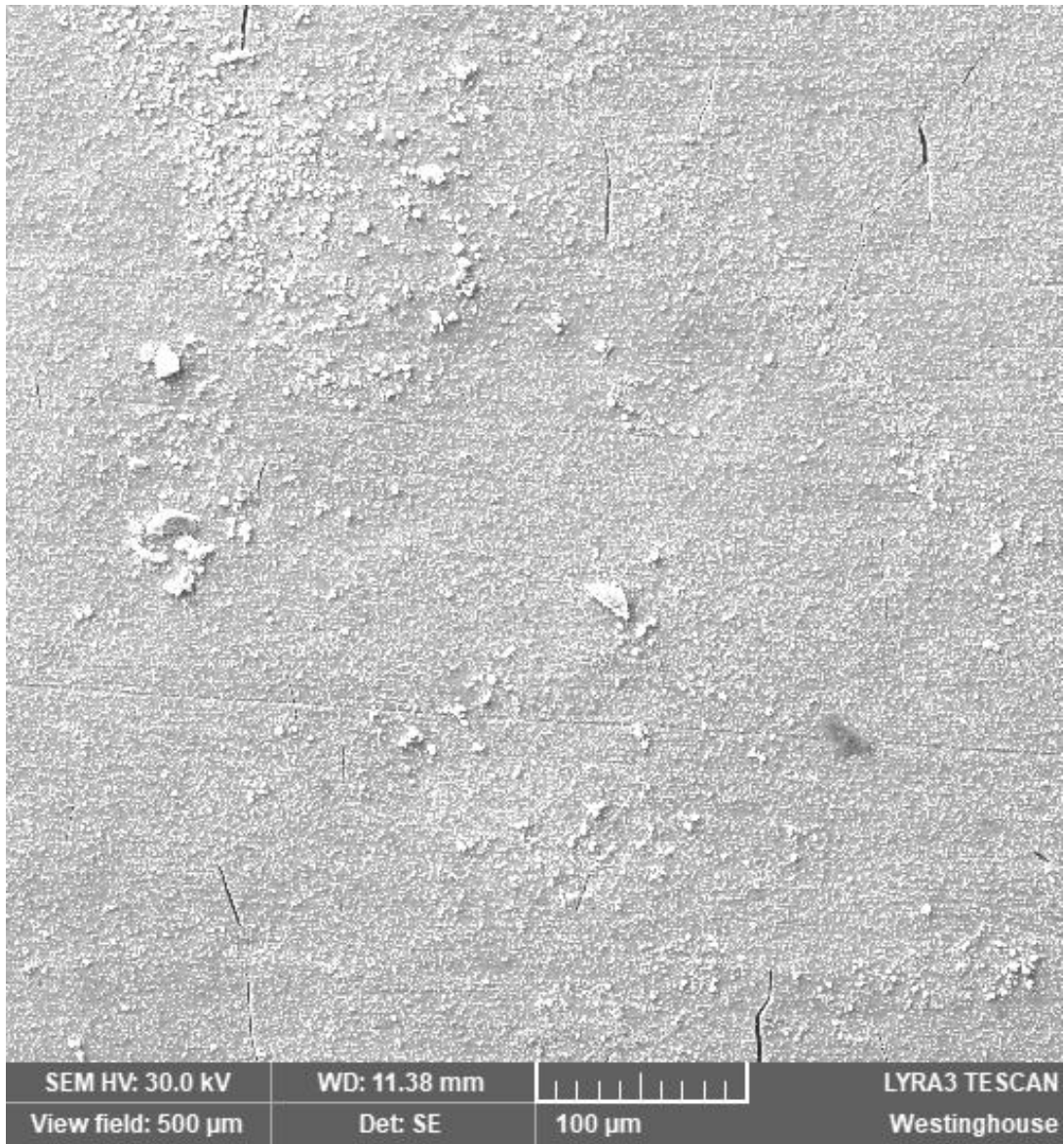


Figure 113. Example image of surface of wrought sample strained to 4% in simulated PWR water. Strain direction was left to right in this image.

In total, the evaluation of cracking constituted evaluating over 1300 images of the sample surfaces. This data was tabulated, and used to calculate a metric – microns of crack length per square millimeter of area – that has been utilized in previous evaluations of crack initiation behavior (Reference 58). This allows a normalized comparison of the samples across the various test conditions. The cracking metric was plotted for each specimen condition, as shown in Figure 114.

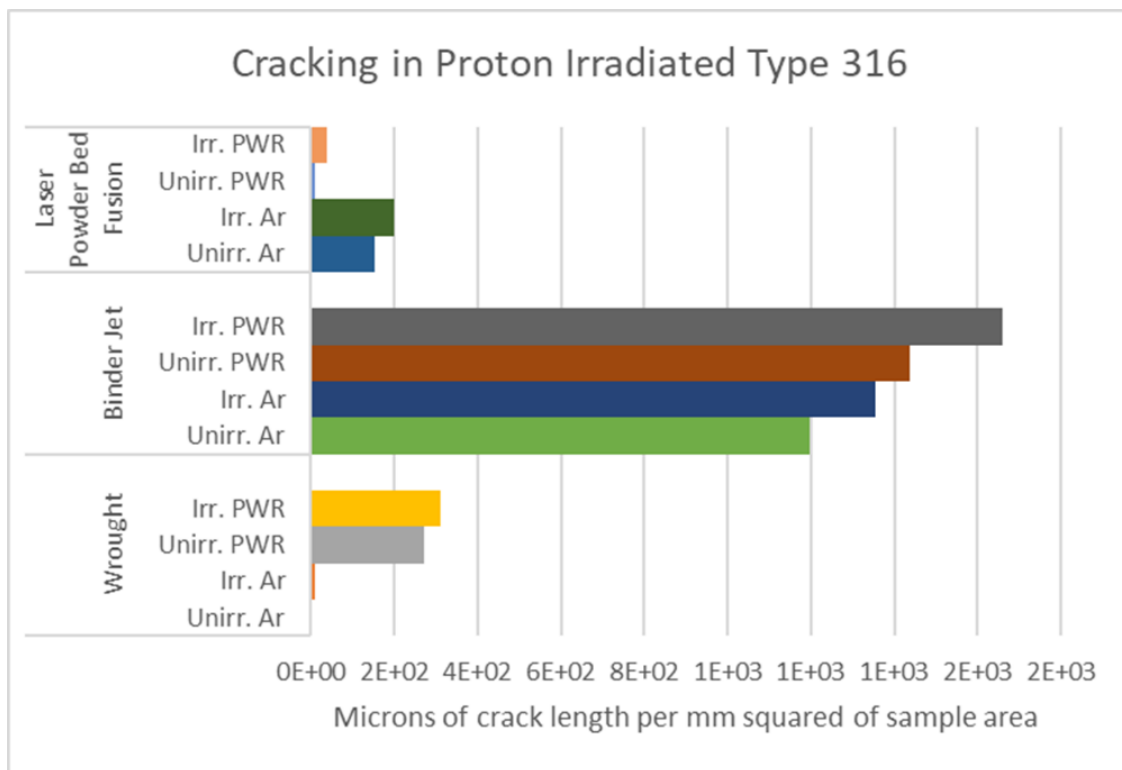


Figure 114. Results of quantitative sample cracking evaluation as a function of environment during straining and material type.

7.4 Discussion

All of the samples strained to 4% exhibited some amount of cracking, with the wrought material having the least cracking, the binder jet material having the most cracking, and the LPBF material similar to the wrought material results. The fact that CERT is a mechanically severe process is attested by the fact that unirradiated wrought material strained in argon and PWR water exhibited cracking. This test forces cracking to initiate through a severe stress state, which while not prototypic, is appropriate for a comparative screening test such as this.

By examining the crack initiation data (Figure 115), some trends can be observed. For example, in all cases, the addition of irradiation enhanced cracking relative to the comparable unirradiated condition. The influence of the PWR environment also clearly increased the propensity for crack formation in the binder jet and wrought materials. This trend of environmentally-enhanced cracking was also expected to extend to the LPBF material; it is believed fewer cracks were observed in the LPBF material strained in PWR water due to prolific hydrothermal deposits, which obscured much of the surface (Figure 116).

It is also clear that the binder jet material is highly susceptible to cracking, an order of magnitude more so than the other material. This appears to be related to the presence of defects (likely porosity) from the fabrication process, and substantial alloying element segregation. These fabrication defects are likely also responsible for the low yield strength of the binder jet material.

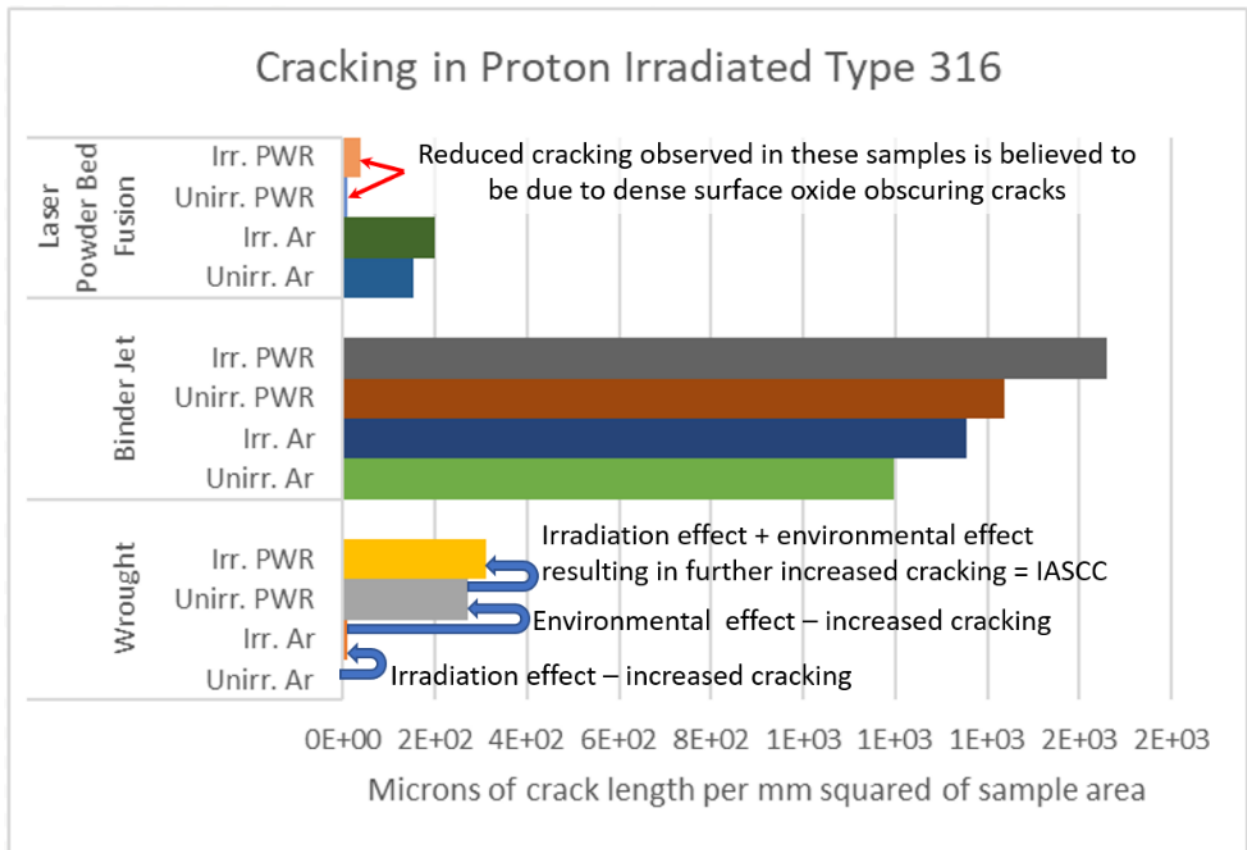


Figure 115. Trends in quantitative cracking evaluation results

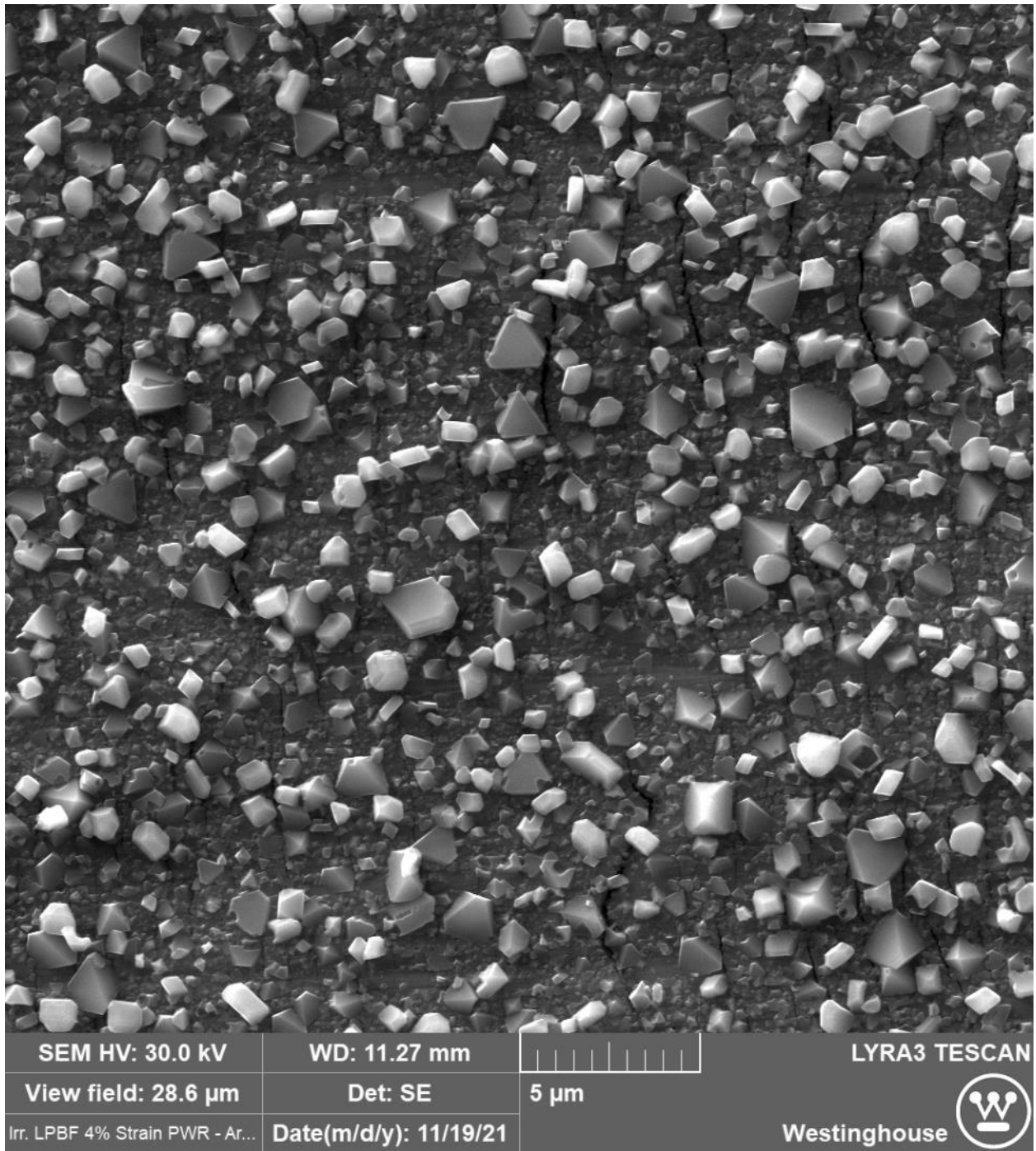


Figure 116. Oxide partially obscuring cracks on LPBF sample strained in PWR water

8.0 Summary and Conclusions

The hypothesis of this thesis is **“The extent of environmental assistance in causing cracking in irradiated austenitic stainless steel in light water reactor environments varies depending on the extent of irradiation damage to the material, the alkali ions in the water, and the stress applied to it.”** The experiments described in Sections 4.0 , 5.0 , 6.0 , and 7.0 were intended to investigate this hypothesis.

Section 4.0 investigated IASCC behavior through failure analysis of PWR power plant baffle-former bolts. While not a highly controlled experiment, careful analysis of the available data shows a clear trend of decreasing environmental influence on the fracture process with increasing levels of stress, which supports the hypothesis related to applied stress.

Section 5.0 investigated IASCC CGRs in well-controlled experiments where radiation dose, applied stress, and water chemistry could be controlled as variables. The specific objective was to determine if there was any difference in IASCC CGRs between the LiOH and KOH water chemistry, and none was observed for the conditions tested. The difference in behavior between 9 and 15 dpa specimens in this experiment was negligible. This is likely because at both radiation damage levels, the mechanical property change (irradiation embrittlement) has either reached saturation or is closely approaching it.

In Section 4.0 , the observation of transgranular IASCC was considered significant, while in 5.0 the *lack* of transgranular IASCC was considered significant. This is because in Section 4.0 it was shown that the stress state was driving the resulting crack morphology, while in Section 5.0 applied stress intensity factors were low and the susceptibility of the material studied (separate from material examined in other sections) was seemingly uniquely susceptible to intergranular fracture, showing the dominance of microstructural factors over the stress state.

Section 6.0 investigated IASCC initiation behavior in miniature 4-point bend specimens fabricated from baffle-former bolt materials. This is the first time such testing had been conducted on neutron-irradiated Type 347 stainless steel, and represents the largest IASCC initiation data set on this material. The performance of the Type 347 stainless steel appears comparable to the Type 304 and Type 316 stainless steel materials making up the majority of the available IASCC initiation data. This testing did not cover lower fluences (less than 7 dpa) where IASCC susceptibility onset occurs. Such testing could be conducted using the baffle-former bolt materials now in the DOE's material library.

The primary objective of this experiment was again to discern any difference in IASCC behavior between the LiOH and KOH water chemistry, and again none was observed for the conditions tested. While stress, water chemistry, and irradiation dose were controlled as variables, one of the potentially most valuable aspects of the experiment was the ability to determine microstructural features associated with crack initiation. While previous studies have implicated dislocation channels or manganese sulfide inclusions (Reference 58), this study showed that these features are not necessary for IASCC initiation, and suggest that grain boundary oxidation is a necessary precursor to IASCC initiation. The influence of radiation damage and applied stress on crack initiation were also apparent in the crack initiation behavior, supporting the hypothesis of this thesis document.

The results provided in Section 5.0 and 6.0 suggest that any difference in IASCC behavior between KOH and LiOH PWR environments either does not exist, or would have to develop over longer time scales. No prior data for IASCC CGR or initiation have been publicly published for neutron-irradiated 300-series austenitic stainless steels in KOH PWR water at the time of this writing. These results are contrary to the hypothesis as it relates to alkali ions, as no difference

between the KOH and LiOH environments was observed. This is contrary to the author's initial thinking that LiOH additions would result in a more aggressive environment, as lithium is both smaller (and so more mobile) and more reactive than potassium.

Section 7.0 departed from the previous sections in utilizing proton-irradiation, rather than neutron irradiated materials, and focusing on additively manufactured steels rather than the legacy materials of PWRs. This was to the author's knowledge the first testing of this kind conducted on binder jet additively manufactured material. While a different approach, the applicability to the theme of this work is clear. The crack initiation data clearly show that irradiation and the PWR water environment enhanced cracking, as well as the sensitivity of such cracking behavior to defects in the material microstructure.

The experimental works described in this document together form a comprehensive investigation of the hypothesis. The three primary variables to be investigated are stress, radiation dose, and alkali ion environment, although microstructure was inevitably also investigated to some extent. The studied range and effect of these three variables on IASCC phenomena as investigated throughout the completed experiments as shown in Table 18. Based on these works, the hypothesis given can be concluded to be partially correct. A revised form of the hypothesis is better supported by this work, particularly by removing the implication that alkali ions may affect IASCC behavior. Such an effect was not observed in the conducted experiments. The revised hypothesis statement would then be, **“The extent of environmental assistance in causing cracking in irradiated austenitic stainless steel in light water reactor environments varies depending on the extent of irradiation damage to the material and the stress applied to it.”**

This revised hypothesis is well-supported by the completed experimental work.

Table 18. Variables in IASCC Investigated in this Work

Experiment / Variable Investigated	Stress	Influence of Stress on IASCC behavior	Radiation Dose	Influence of Radiation dose on IASCC behavior	Environmental Variables	Influence of Environmental variable on IASCC behavior
Baffle-former bolt failure analysis	Low / High	High	1-27	Moderate	LiOH	N / A
IASCC CGR	14, 18 MPa √m	High	9, 15 dpa	Low/none	LiOH vs. KOH	No effect
IASCC Crack Initiation	20-80% σ_Y	High	7 – 33 dpa	Moderate	LiOH vs. KOH	No effect
Crack initiation testing of additively manufactured 316SS	In excess of yield	High	0, 5 dpa	High	PWR environment vs. inert environment	High

Bibliography

1. Mehos, Mark, Hank Price, Robert Cable, David Kearney, Bruce Kelly, Gregory Kolb, and Frederick Morse. 2020. Concentrating Solar Power Best Practices Study. National Renewable Energy Laboratory. NREL/TP-5500-75763.
<https://www.nrel.gov/docs/fy20osti/75763.pdf>.
2. Ingram, G. K., & Hong, Y. (Eds.). (2011). Climate change and land policies : Climate change and land policies.
3. B.W. Brook, A. Alonso, D.A.Meneley, J. Misak, T. Blee, J.B. van Erp, "Why nuclear energy is sustainable and has to be part of the energy mix," Sustainable Materials and Technologies 1–2 (2014) 8–16
4. Report from Office of Nuclear Reactor Regulation (NRR) Office, "Degradation of Baffle-former Bolts in Pressurized-Water Reactors," NRC ADAMS Accession Number ML16225A341, October 20, 2016.
<https://www.nrc.gov/docs/ML1622/ML16225A341.pdf>
5. U.S. Government Accountability Office Report, GAO-13-716, "Managing Critical Isotopes: Stewardship of Lithium-7 Is Needed to Ensure a Stable Supply," October 17, 2013. <https://www.gao.gov/products/GAO-13-716>
6. Effect of Boron Concentration on Alloy 690 Corrosion Product Release Rates -Results at 325°C and 285°C. EPRI, Palo Alto, CA: 2001. 1011744.
<https://www.epri.com/#/pages/product/1011744/?lang=en-US>
7. "Fundamentals of Radiation Materials Science," Gary Was, 2nd Edition, Springer, 2017.
8. "SCC in LWR's – Good Practices and Lessons Learned," IAEA Nuclear Energy Series, No. NP-T-3.13, International Atomic Energy Agency, Vienna, 2011.
9. R.B. Rebak, "Industrial Experience on the Caustic Cracking of Stainless Steels and Nickel Alloys – A Review," Corrosion 2006 Conference and Exposition, San Diego, CA, March 12-March 16, 2006.
10. Barry Gordon, "The Effect of Chloride and Oxygen on the Stress Corrosion Cracking of Stainless Steels: Review of Literature, Materials Performance," Vol. 19, No 4., pp. 29-38, April 1980.

11. Michael R. Ickes, "Stress Corrosion Cracking of an Austenitic Stainless Steel Pipe Weld," 19th International Conference on Environmental Degradation of Materials in Nuclear Power Systems - Water Reactors, August 28-22, 2019, Boston, Massachusetts.
12. O. Raquet, E. Herms, F. Vaillant, T. Couvant, "SCC Of Cold-Worked Austenitic Stainless Steels In PWR Conditions," *Advances in Materials Science*, Vol. 7, No. 1 (11), March 2007.
13. BWR Core Shroud Boat Sample Metallurgical Testing Summary, D. Sommerville et al., EPRI International LWR Material Reliability Conference, Chicago, IL, August 2016.
14. P. Scott, "A Review of Irradiation Assisted Stress Corrosion Cracking," *Journal of Nuclear Materials*, 211, 101-122, April 26, 1994.
15. Materials Reliability Program: PWR Internals Material Aging Degradation Mechanism Screening and Threshold Values (MRP-175). EPRI, Palo Alto, CA: 2005. 1012081.
16. McMurtrey, Was, et al., "Relationship between localized strain and irradiation assisted stress corrosion cracking in an austenitic alloy," *Materials Science and Engineering A* 528 (2011) 3730–3740, 26 January 2011.
17. Koji Fukuya, Hiromasa Nishioka, Katsuhiko Fujii, Terumitsu Miura, Tadahiko Torimaru, "An EBSD examination of SUS316 stainless steel irradiated to 73 dpa and deformed at 593 K," *Journal of Nuclear Materials* 417 (2011) 958–962, 1 January 2011.
18. NUREG/CR-7027, "Degradation of LWR Core Internal Materials due to Neutron Irradiation," December 2010.
19. Evaluation of Plant Data to Determine Effects of Zinc on Primary Water Stress Corrosion Cracking in Pressurized Water Reactors. EPRI, Palo Alto, CA: 2005. 1011775.
20. S. Hettiarachchi, "BWR Field Experiences with NobleChem," ICONE 9, April 8-12, Nice, France, 2001.
21. Chih-Kuang Lin and I-Lon Lan, "Environmental Effects on the Fatigue Behavior of an Austenitic Stainless Steel," Department of Mechanical Engineering, National Central University.
22. NUREG/CR-6909, Rev. 1, "Effect of LWR Coolant Environments on the Fatigue Life of Reactor Materials," March 2014.
23. S.S. Raiman, D.M. Bartels, G.S. Was, "Radiolysis driven changes to oxide stability during irradiation-corrosion of 316L stainless steel in high temperature water," *Journal of Nuclear Materials* 493 (2017) 40-52, <https://doi.org/10.1016/j.jnucmat.2017.05.042>

24. J. Garnier, P. Dubuisson, C. Pokor, E. Lemaire, N. Monteil, J.-P. Massoud, ‘Relaxation and Irradiation Creep of PWR Baffle Bolt Materials,’ Fontevraud 7 Conference: Contribution of Materials Investigations and Operating Experience to Light Water NPPs’ Safety, Performance and Reliability, 26 – 30 September 2010, Avignon, France.
25. A.K. Vasudevan and K. Sadananda, “Role of Slip Mode on Stress Corrosion Cracking Behavior,” Metallurgical and Materials Transactions A, Volume 42A, February 2011—405, DOI: 10.1007/s11661-010-0471-4
26. M.N. Gussev, J.T. Busby, L. Tan, F.A. Garner, “Magnetic phase formation in irradiated austenitic alloys,” Journal of Nuclear Materials 448 (2014) 294–300, <http://dx.doi.org/10.1016/j.jnucmat.2014.02.005>
27. Stress Corrosion Cracking Testing Guidelines: With Emphasis on High Temperature Water. EPRI, Palo Alto, CA: 2020. 3002018265. <https://www.epri.com/research/programs/061144/results/3002018265>
28. Garner Frank A. (2020). Radiation-Induced Damage in Austenitic Structural Steels Used in Nuclear Reactors. In: Konings, Rudy JM and Stoller Roger E (eds.) Comprehensive Nuclear Materials 2nd edition, vol. 3, pp. 57–168. Oxford: Elsevier. <http://dx.doi.org/10.1016/B978-0-12-803581-8.12067-3>
29. H.M. Chung, J.E. Sanecki, and F.A. Garner, “Radiation-Induced Instability Of Mns Precipitates And Its Possible Consequences On Irradiation-Induced Stress Corrosion Cracking Of Austenitic Stainless Steels,” Effect of Radiation on Materials: 18th Symposium, ASTM, 1999

Start of Section 4.0 References

30. Michael R. Ickes, Joshua McKinley, Jung-Kun Lee, Jean M. Smith, Andrew M. Ruminski, Michael A. Burke, “Irradiation-assisted stress corrosion cracking of Type 347 and Type 316 steels irradiated in commercial pressurized water reactors,” Journal of Nuclear Materials, Volume 536, 1 August 2020. <https://doi.org/10.1016/j.jnucmat.2020.152182>
31. MRP-2018-025, “2018 Biennial Report of Recent MRP-227-A Reactor Internals Inspection Results,” July 19, 2018, <https://www.nrc.gov/docs/ML1820/ML18204A161.pdf>
32. MRP-2014-009, “Biennial Report of Recent MRP-227-A Reactor Internals Inspection Results,” May 12, 2014. <https://www.nrc.gov/docs/ML1522/ML15223A460.pdf>
33. MRP 2016-008, “Biennial Report of MRP-227-A Reactor Internals Inspection Results,” May 18, 2016. <https://www.nrc.gov/docs/ML1614/ML16144A789.pdf>

34. Strebin R., Orr R., Kaye J., Fadeff S., "Nickel-59 and Nickel63 Determination in Aqueous Samples," Pacific Northwest Laboratory, Richland, WA - DOE Methods Compendium RP300; Référence Eichrom RP300.
35. Westinghouse Science and Technology Department Report STD-MR-01-0012, "Ginna Hot Cell Testing Report," November 26, 2001.
36. F. Somville, R. Gerard, R-W. Bosch, D. Bertolis, S. Vissers, "Ageing Management of Baffle Former Bolts in Belgian Nuclear Power Plants," Fontevraud 8, Contribution of Materials Investigations and Operating Experience to LWRs' Safety, Performance and Reliability, September 14 - 18, 2014, Avignon, France.
37. Materials Reliability Program: Hot Cell Testing of Baffle/Former Bolts Removed From Two Lead PWR Plants (MRP-51), EPRI, Palo Alto, CA: 2001. 1003069.
<https://www.epri.com/#/pages/product/00000000001003069/?lang=en-US>
38. Materials Reliability Program: Determination of Operating Parameters of Extracted Bolts (MRP-52), EPRI, Palo Alto, CA: 2001. 1003076.
<https://www.epri.com/#/pages/product/00000000001003076/?lang=en-US>
39. J.K. McKinley, R.G. Lott, J.B. Hall, K. Kalchik, "Examination of Baffle-Former Bolts from D.C. Cook Unit 2," International BWR and PWR Materials Reliability Conference and Exhibition, July 18, 2012.
40. Materials Reliability Program: Characterization of Decommissioned PWR Vessel Internals Material Samples—Tensile and SSRT Testing (MRP-129), EPRI, Palo Alto, CA, and U.S. Department of Energy: 2004. 1008205.
<https://www.epri.com/#/pages/product/00000000001008205/?lang=en-US>
41. T. Couvant, "Corrosion Sous Contrainte en Milieu Primaire REP de L'acier Inoxydable Austenitique Ecroui 304L," Thesis of Ecole des Mines de Saint-Etienne, 2003.
42. O. Raquet, E. Herms, F. Vaillant, T. Couvant, J.M. Boursier, "SCC of Cold-worked Austenitic Stainless Steels in PWR conditions," Proceedings of the 12th International Conference on Environmental Degradation of Materials in Nuclear Power System – Water Reactors, 2005.
43. T. Couvant, L. Legras, F. Vaillant, J.M. Boursier, Y. Rouillon, "Effect of Strain Hardening on Stress Corrosion Cracking of AISI 304L Stainless Steel in PWR Primary Environment at 360°C," Proceedings of the 12th International Conference on Environmental Degradation of Materials in Nuclear Power System – Water Reactors, 2005.

44. T. Couvant, L. Legras, A. Herbelin, A. Musienko, G. Ilbevare, et al., “Development of Understanding of The Interaction between Localized deformation and SCC of Austenitic Stainless Steels Exposed to Primary Environment,” American Nuclear Society. 14th International Conference on Environmental Degradation of Materials in Nuclear Power Systems- Water Reactors, Sep. 2010, Virginia Beach, United States.
45. F. Vaillant, L. Tribouilloy-Buisse, T. Couvant, “Stress Corrosion Cracking Propagation of Cold-worked Austenitic Stainless Steels in PWR Environment,” 14th International Conference on Environmental Degradation of Materials in Nuclear Power Systems, Whistler, British Columbia, August 19 - 23, 2007.
46. L. Tribouilloy, F. Vaillant, J-M. Olive, M. Puiggali, L.Legras, T. Couvant, J-M. Boursier, Y Rouillon, C. Amzallag, “Stress Corrosion Cracking on Cold-Worked Austenitic Stainless Steels in PWR Environment,” 13th International Conference on Environmental Degradation of Materials in Nuclear Power Systems, Whistler, British Columbia, August 19-23, 2007.
47. Mike Ickes and Mike Burke, Pressurized Water Reactor Owner’s Group Report PWROG-15105-NP, “PA-MS-C-1288 PWR RV Internals Cold Work Assessment,” April 2016, <https://www.nrc.gov/docs/ML1622/ML16222A300.pdf>
48. Materials Reliability Program: Characterization of Decommissioned PWR Vessel Internals Material Samples—Tensile and SSRT Testing (MRP-129), EPRI, Palo Alto, CA, and U.S. Department of Energy: 2004. 1008205.
<https://www.epri.com/#/pages/product/000000000001008205/?lang=en-US>
49. M.D. McMurtrey, G.S. Was, L. Patrick, D. Farkas, “Relationship between localized strain and irradiation assisted stress corrosion cracking in an austenitic alloy,” Materials Science and Engineering A 528 (2011) 3730–3740, 26 January 2011, doi:10.1016/j.msea.2011.01.073
50. E.A. West, G.S. Was, “Strain incompatibilities and their role in intergranular cracking of irradiated 316L stainless steel,” Journal of Nuclear Materials, Volume 441, 2013, pp. 623–632. <http://dx.doi.org/10.1016/j.jnucmat.2012.10.021>
51. T. Magnin, A. Chambreuil, B. Bayle, “The Corrosion-enhanced Plasticity Model for Stress Corrosion Cracking in Ductile FCC Alloys,” Acta Materialia, Vol. 44, No. 4, pp. 1457-1470, 1996.

Start of Section 5 (IASCC CGR) References

52. Kai Chen, Michael R. Ickes, Michael A. Burke, Gary S. Was, “The effect of potassium hydroxide primary water chemistry on the IASCC behavior of 304 stainless steel,” Available online 9 October 2021, <https://doi.org/10.1016/j.jnucmat.2021.153323>

53. Materials Reliability Program: Fracture Toughness Testing of Decommissioned PWR Core Internals Material Samples (MRP-160): Proprietary Version. EPRI, Palo Alto, CA and U.S. Department of Energy, Washington, D.C.: 2005. 1012079.
<https://www.epri.com/#/pages/product/000000000001012079/?lang=en-US>
54. Materials Reliability Program: Characterization of Decommissioned PWR Vessel Internals Material Samples – Material Certification, Fluence, and Temperature (MRP-128), EPRI, Palo Alto, CA, and U.S. Department of Energy, Washington, D.C.: 2004. 1008202. <https://www.epri.com/#/pages/product/000000000001008202/?lang=en-US>
55. Materials Reliability Program: Characterization of Decommissioned PWR Vessel Internals Material Samples—Transmission Electron Microscopy Evaluation (MRP-201), EPRI, Palo Alto, CA. 2006, 1013417.
<https://www.epri.com/#/pages/product/000000000001013417/?lang=en-US>
56. Xiang (Frank) Chen, Randy K. Nanstad, Mikhail A. Sokolov, “Application of Direct Current Potential Drop for the J-integral vs. Crack Growth Resistance Curve Characterization,” <https://www.osti.gov/servlets/purl/1207046>
57. Margareta Stigenberg, “The Influence of Crack Branching on the Potential Drop Monitoring Technique and on the Stress Intensity Factor in a CT Specimen,” Uppsala University, Tekniska Hogskolan, Teknikum, Institutionen for Teknologi, ISSN 0346-8887.

Start of Section 6 (IASCC Initiation) References:

58. Kale J. Stephenson and Gary S. Was, “The Role of Dislocation Channeling in IASCC Initiation of Neutron Irradiated Stainless Steel,” *Journal of Nuclear Materials* 481, 214-225, September 28, 2016. <https://doi.org/10.1016/j.jnucmat.2016.09.001>
59. J.K. McKinley, R.G. Lott, J.B. Hall, K. Kalchik, “Examination of Baffle-former Bolts from D.C. Cook Unit 2,” 16th International Conference on Environmental Degradation of Materials in Nuclear Power Systems – Water Reactors, August 11-15, 2013, Asheville, North Carolina, USA.
60. Materials Reliability Program: Characterizations of Type 316 Cold Worked Stainless Steel Highly Irradiated Under PWR Operating Conditions (International IASCC Advisory Committee Phase 3 Program Final Report) (MRP-214). EPRI, Palo Alto, CA and the International IASCC Advisory Committee: 2007. 1015332.
<https://www.epri.com/#/pages/product/000000000001015332/?lang=en-US>
61. J.M. Smith, M.R. Ickes, M.A. Burke, A.M. Ruminski, K.J. Amberge, “Hot Cell Testing of Type 347 Stainless Steel Baffle-to-Former Bolts Removed from U.S. PWRs,” Fontevraud 9 Conference: Contribution of Materials Investigations and Operating

Experience to Light Water NPPs' Safety, Performance and Reliability, 17 – 20
September 2018, Avignon, France.

62. ASTM Standard B912-02, “Standard Specification for Passivation of Stainless Steels Using Electropolishing,” American Society of Testing and Materials International, 2018

Section 7 references

63. Saereh Mirzababaei, Somayeh Pasebani, “A Review on Binder Jet Additive Manufacturing of 316L Stainless Steel,” *J. Manuf. Mater. Process.* 2019, 3, 82; doi:10.3390/jmmp3030082
64. Özel, Tuğrul & Altay, Ayça & Kaftanoğlu, Bilgin & Senin, Nicola & Leach, Richard & Donmez, M. (2019). Focus Variation Measurement and Prediction of Surface Texture Parameters Using Machine Learning in Laser Powder Bed Fusion. *Journal of Manufacturing Science and Engineering.* 142. 011008. 10.1115/1.4045415].
65. L. E. Murr, “A Metallographic Review of 3D Printing/Additive Manufacturing of Metal and Alloy Products and Components,” *Metallography, Microstructure, and Analysis* (2018) 7:103–132, <https://doi.org/10.1007/s13632-018-0433-6>
66. J. R. Trelewicz, G. P. Halada, O. K. Donaldson, G. Manogharan, “Microstructure and Corrosion Resistance of Laser Additively Manufactured 316L Stainless Steel,” *JOM*, Vol. 68, No. 3, 2016, DOI: 10.1007/s11837-016-1822-4.
67. G.S. Was, J.T. Busby, T. Allen, E.A. Kenik, A. Jenssen, S.M. Bruemmer, J. Gan, A.D. Edwards, P.M. Scott, P.L. Andresen, “Emulation of neutron irradiation effects with protons: Validation of principle,” *Journal of Nuclear Materials* 300 (2002) 198–216.
68. Idaho National Laboratory Report INL/EXT-17-43130, “Roadmap for the Application of Ion Beam Technologies to Challenges of the Advancement and Implementation of Nuclear Energy Technologies,” September 2017, <https://www.osti.gov/servlets/purl/1408762>
69. General Electric Global Research Report, “Environmental Cracking and Irradiation Resistant Stainless Steels by Additive Manufacturing,” March 30, 2018. <https://www.osti.gov/servlets/purl/1431212>